IntechOpen

Morphodynamic Model for Predicting Beach Changes Based on Bagnold's Concept and Its Applications

Authored by Takaaki Uda, Masumi Serizawa and Shiho Miyahara

Morphodynamic Model for Predicting Beach Changes Based on Bagnold's Concept and Its Applications

Edited by Takaaki Uda, Masumi Serizawa and Shiho Miyahara

Published in London, United Kingdom

IntechOpen

Supporting open minds since 2005

Morphodynamic Model for Predicting Beach Changes Based on Bagnold's Concept and Its Applications
http://dx.doi.org/10.5772/10.5772/66722
Edited by Takaaki Uda, Masumi Serizawa and Shiho Miyahara

Contributors
Takaaki Uda, Masumi Serizawa and Shiho Miyahara

© The Editor(s) and the Author(s) 2018
The rights of the editor(s) and the author(s) have been asserted in accordance with the Copyright, Designs and Patents Act 1988. All rights to the book as a whole are reserved by INTECHOPEN LIMITED. The book as a whole (compilation) cannot be reproduced, distributed or used for commercial or non-commercial purposes without INTECHOPEN LIMITED's written permission. Enquiries concerning the use of the book should be directed to INTECHOPEN LIMITED rights and permissions department (permissions@intechopen.com).
Violations are liable to prosecution under the governing Copyright Law.

BY-NC

Individual chapters of this publication are distributed under the terms of the Creative Commons Attribution – NonCommercial 4.0 International which permits use, distribution and reproduction of the individual chapters for non-commercial purposes, provided the original author(s) and source publication are appropriately acknowledged. More details and guidelines concerning content reuse and adaptation can be found at http://www.intechopen.com/copyright-policy.html.

Notice
Statements and opinions expressed in the chapters are these of the individual contributors and not necessarily those of the editors or publisher. No responsibility is accepted for the accuracy of information contained in the published chapters. The publisher assumes no responsibility for any damage or injury to persons or property arising out of the use of any materials, instructions, methods or ideas contained in the book.

First published in London, United Kingdom, 2018 by IntechOpen
eBook (PDF) Published by IntechOpen, 2019
IntechOpen is the global imprint of INTECHOPEN LIMITED, registered in England and Wales, registration number: 11086078, The Shard, 25th floor, 32 London Bridge Street
London, SE19SG – United Kingdom
Printed in Croatia

British Library Cataloguing-in-Publication Data
A catalogue record for this book is available from the British Library

Additional hard and PDF copies can be obtained from orders@intechopen.com

Morphodynamic Model for Predicting Beach Changes Based on Bagnold's Concept and Its Applications
Edited by Takaaki Uda, Masumi Serizawa and Shiho Miyahara
p. cm.
Print ISBN 978-1-78984-945-5
Online ISBN 978-1-78984-946-2
eBook (PDF) ISBN 978-1-83881-268-3

We are IntechOpen, the world's leading publisher of Open Access books

Built by scientists, for scientists

3,900+
Open access books available

116,000+
International authors and editors

120M+
Downloads

Our authors are among the

151
Countries delivered to

Top 1%
most cited scientists

12.2%
Contributors from top 500 universities

WEB OF SCIENCE™

Selection of our books indexed in the Book Citation Index in Web of Science™ Core Collection (BKCI)

Interested in publishing with us?
Contact book.department@intechopen.com

Numbers displayed above are based on latest data collected.
For more information visit www.intechopen.com

Meet the editors

In 1973, Dr. Takaaki Uda became a research engineer at the Coastal Engineering Division, PWRI, Ministry of Construction, Japan, after finishing his master course at Tokyo Institute of Technology. He attained his doctor degree from Tokyo Institute of Technology in 1983, and became the head of the Coastal Engineering Division. Since then he has worked as a coastal engineer focusing on field work. He became director of the River Department at the same institute in 1997, and further served as General Coordinator of Research, National Institute for Land, Infrastructure and Management, Japan, from April 2001. He then became Executive Director of PWRC in August 2002, and has been a visiting professor at Nihon University since 2007. Based on his carrier, he published the book Japan's Beach Erosion.

In 1983, Dr. Masumi Serizawa became a coastal engineer at the Port and Coastal Engineering Division, Pacific Consultants International Co., Ltd., Japan, after finishing his Bachelor of Engineering course of Yokohama National University, Japan. In 1995, he founded Coastal Engineering Laboratory Co., Ltd. in Tokyo. Since then he has been working as the head of this consultant company focusing on the numerical simulation of beach changes. He attained his doctor degree from Nihon University in 2012.

In 2005, Shiho Miyahara finished her Bachelor of Science in Engineering course at Shimane University, Japan. In 2009, she became a research engineer at the Coastal Engineering Laboratory Co., Ltd., Japan. Since then, she has been working as a research engineer focusing on the numerical simulation of beach changes.

Contents

Preface XIII

Chapter 1 1
Introductory Chapter: Morphodynamic Model for Predicting Beach Changes Based on Bagnold's Concept and Its Applications
by Takaaki Uda, Masumi Serizawa and Shiho Miyahara

Chapter 2 9
Derivation of the BG Model
by Takaaki Uda, Masumi Serizawa and Shiho Miyahara

Chapter 3 21
Eight Types of BG Models and Discretization
by Takaaki Uda, Masumi Serizawa and Shiho Miyahara

Chapter 4 57
Prediction of Typical Beach Changes Owing to Human Activities
by Takaaki Uda, Masumi Serizawa and Shiho Miyahara

Chapter 5 85
Beach Changes on Coast Subject to Waves and Seaward or Shoreward Strong Currents
by Takaaki Uda, Masumi Serizawa and Shiho Miyahara

Chapter 6 103
Formation of Sand Spit and Bay Barrier
by Takaaki Uda, Masumi Serizawa and Shiho Miyahara

Chapter 7 131
Interaction of Sandy Islands
by Takaaki Uda, Masumi Serizawa and Shiho Miyahara

Chapter 8 149
Formation of Cuspate Foreland
by Takaaki Uda, Masumi Serizawa and Shiho Miyahara

Chapter 9 171
Segmentation and Merging of Closed Water Bodies by Wind Waves
by Takaaki Uda, Masumi Serizawa and Shiho Miyahara

List of Symbols 191

Preface

Beach erosion is caused by an imbalance in the sediment budget of a coast, with the exception of ground subsidence or sea level rise. The causes of beach erosion could be classified mainly into four types: (1) obstruction of longshore sand transport, (2) beach changes associated with the formation of wave-shelter zones, (3) decreased fluvial sediment supply, and (4) offshore sand mining or dredging. To solve these erosion problems, it is important to predict beach changes. In the prediction of beach changes triggered by the imbalance in longshore sand transport, a long-term prediction in an extensive area is often required. The time scale changes yearly to decadal time scales, and the calculation domain even reaches up to 10–100 km. Although the One-line model or N-line model is a popular tool to predict such beach changes, further advanced 3D beach change models, so-called process-based models, have been developed. In these models, the depth changes on 2D horizontal grids are predicted using the sand transport formulae expressed by local hydrodynamic parameters, i.e., oscillatory velocity due to waves, nearshore current velocity, and tidal current velocity.

In these process-based models, computational load is much larger than that of the One-line model, because recurrent calculations of not only wave field but also nearshore current are required so that application to the long-term prediction in an extensive calculation domain is limited. The authors have developed models for predicting beach changes applicable to various problems on real coasts. One of them is the contour-line-change model to predict long-term beach changes caused by the imbalance in longshore sand transport, which is a kind of N-line model. Because the calculation of the nearshore current is not needed in this model, and the computational load is small, it has an advantage in the prediction of long-term topographic changes on an extensive coast. However, the handling of boundary conditions becomes difficult when offshore coastal structures are constructed in a complicated manner, and in this regard the so-called 3D model has an advantage. Taking this point into account, the authors developed a morphodynamic model (BG model) by applying the concept of the equilibrium slope and the energetics approach, in which depth changes on 2D horizontal grids are calculated. This book is composed of nine chapters. First chapter is the introductory chapter.

In Chapter 2, the BG model is introduced, and the fundamental aspects of the model are explained; the BG model is based on three concepts: (1) the contour line becomes orthogonal to the wave direction at any point at the final stage, (2) similarly, the local beach slope coincides with the equilibrium slope at any point, and (3) a restoring force is generated in response to the deviation from the statically stable condition, and sand transport occurs because of this restoring force.

In Chapter 3, eight types of the BG models are introduced. Type 1 is a model using wave parameters at the breaking point. In Type 2, the effect of longshore sand transport due to the effect of the longshore gradient of breaker height is included. In Type 3, the intensity of sand transport P is assumed to be proportional to the third power of the amplitude of the bottom oscillatory velocity due to waves, and in Type 4, P is given by the wave energy dissipation rate due to wave breaking at a

local point. In Type 5, wave power is calculated using a coordinate system different from that for the calculation of beach changes to predict the topographic changes of an island or a cuspate foreland in a shallow water body when waves are randomly incidental from every direction. In Type 6, the height of wind waves is first predicted using Wilson's formula, and then sand transport fluxes are calculated. Type 7 is a model for predicting the formation of the ebb tidal delta under the combined effect of waves and ebb tidal currents with an analogy of the velocity distribution of ebb tidal currents to the wave diffraction coefficient. In Type 8, the effect of the nearshore currents induced by forced wave breaking is incorporated into the model by calculating the nearshore currents, taking both the wave field and the current velocity at a local point into account.

In Chapter 4, beach changes related to human activities, such as the effect of the construction of groynes and detached breakwaters on a coast with prevailing longshore sand transport, and offshore sand mining are predicted using the Types 1 and 2 BG model.

In Chapter 5, beach changes on a coast subject to waves and seaward or shoreward strong currents are predicted using the Types 7 and 8 BG model. The formation of an ebb tidal delta subject to strong ebb tidal currents is studied first, taking the Imagire-guchi inlet connecting Lake Hamana with the Pacific Ocean as an example, and then the prediction of the formation of a dynamically stable ebb tidal delta is predicted. Regarding beach changes on a coast subject to waves and shoreward strong currents, Type 8 is applied to the Kaike coast, where an artificial reef was constructed in place of a detached breakwater, resulting in the occurrence of strong shoreward currents over the artificial reef.

In Chapter 6, the formation of a sand spit and a bay barrier is predicted using the Types 5 and 3 BG model, covering three topics: (1) formation of a bay barrier in flat shallow sea and the merging of bay mouth sand spits, (2) elongation of a sand spit on a seabed with different water depths, and (3) deformation of a sandbar formed at the tip of the Futtsu cuspate foreland.

In Chapter 7, the formation of land-tied islands, when waves are incident to several islands composed of sand from two opposite directions, is first investigated, and their topographic changes are predicted using the Type 5 BG model. In addition, the interaction among multiple circular sandy islands on a flat shallow seabed is investigated, taking the islands in Hingham Bay near Boston Harbor as an example, and topographic changes are predicted using the Type 5 BG model.

In Chapter 8, the formation of a cuspate foreland when waves are incident from two opposite directions is investigated, taking a cuspate foreland extending at the north-east end of Graham Island in British Columbia, Canada, and the cuspate forelands formed at the tip of Hon Bip Island, Vienam, as examples. The formation of such a cuspate foreland is predicted using the Type 4 BG model. Then the development of multiple sand spits with rhythmic shapes in a shallow water body is investigated, taking the Sea of Azov in Russia as an example. Furthermore, the development of sand spits and cuspate forelands with rhythmic shapes is predicted, assuming that the waves are obliquely incident at angles of 60° relative to the direction normal to the shoreline or at angles of ±60° with the change in probability.

In Chapter 9, the segmentation and merging of an elongated shallow water body with a large aspect ratio by wind waves are predicted using the Type 6 BG model.

The deformation of a circular lake by wind waves is also studied when a straight seawall cutting a part of the water body is constructed in a lake. Finally, the formation of oriented lakes is predicted using the Type 6 BG model. The ample examples of numerical calculations using the BG model are believed to be useful for enhancing the applicability of the BG model to solve many kinds of problems.

Takaaki Uda, Masumi Serizawa and Shiho Miyahara
Public Works Research Center,
Coastal Engineering Laboratory Co., Ltd.,
Tokyo, Japan

Chapter 1

Introductory Chapter: Morphodynamic Model for Predicting Beach Changes Based on Bagnold's Concept and Its Applications

Takaaki Uda, Masumi Serizawa and Shiho Miyahara

1. Introduction

Beach erosion is caused by an imbalance in the sediment budget of a coast, with the exception of ground subsidence associated with the excessive extraction of groundwater or sea level rise. Seasonal variations on beaches due to the occurrence of storms and calm waves are commonly observed, but the long-term stability of a beach is governed by longshore sand transport [1]. When the amount of sand supplied from rivers and sea cliffs decreases compared with the longshore sand transport of a coast, the inevitable result is beach erosion. Similarly, artificial removal of coastal sediment by dredging or mining results in beach erosion on neighboring coasts. The anthropogenic causes of beach erosion could be mainly classified into four types: (1) obstruction of longshore sand transport, (2) beach changes associated with the formation of wave-shelter zones, (3) decreased fluvial sediment supply, and (4) offshore sand mining or dredging [2]. When a breakwater, jetty, or groyne is extended offshore on a coast with predominant longshore sand transport, part or all of the longshore sand transport is obstructed, causing erosion downcoast and accretion upcoast. Even if waves are incident from the direction normal to the shoreline, longshore sand transport is induced from outside to inside the wave-shelter zone near a large port breakwater, resulting in erosion outside the wave-shelter zone and accretion inside. The dredging of sand deposited behind an oblique breakwater soon induces longshore sand transport from outside to inside the wave-shelter zone, resulting in erosion in the adjacent area. The effect of offshore mining may be extensive, depending on wave conditions, even though sand is not removed directly from the shoreline. Sand movement due to longshore sand transport occurs at depths less than the depth of closure, h_c, which is roughly equal to 10 m on well-exposed beaches. Since sand is continually being exchanged up to this depth, the removal of sand from a depth less than h_c leads to the same results as sand mining near the shoreline.

To solve these erosion problems or prevent the shoreline of a coast from receding earlier, it is important to predict beach changes. In the prediction of beach changes triggered by the imbalance in longshore sand transport, a long-term prediction in an extensive area is often required. The time scale changes yearly to decadal time scales, and the calculation domain reaches even up to 10–100 km. The One-line

IntechOpen

model is the most popular tool to predict such beach changes, which represents beach topography by the shoreline position, and beach changes are solved using the total longshore sand transport formula [3–5] described by wave parameters at the breaking point, and the continuity equation of sand [6–9]. This has been applied to many problems with small computational load. The N-line model is an improvement over the One-line model, and beach topography is represented by multiple contour lines. The change in successive locations of each contour line is calculated using longshore and cross-shore sand transport formulae, and the continuity equation of sand [9–15].

Recently, further advanced 3D beach change models, so-called process-based models, have been developed [16–26]. Furthermore, Nam et al. [26] reviewed the previous studies, which included the application of the model for predicting the beach changes around coastal structures. In these models, the depth changes on 2D horizontal grids are predicted using the sand transport formulae expressed by local hydrodynamic parameters, i.e., oscillatory velocity due to waves, nearshore current velocity, and tidal current velocity.

Regarding the sand transport formulae in the process-based models, a number of formulae have been proposed [17, 27–39]. Since recurrent calculations of not only wave field but also nearshore current are required in these process-based models, computational load is much larger than that of the One-line or N-line model, so that application to the long-term prediction in an extensive calculation domain is difficult.

On the basis of these previous studies, the authors have developed models for predicting beach changes applicable to various problems on real coasts [2]. One of them is the contour-line-change model [40] to predict long-term beach changes caused by the imbalance in longshore sand transport, which is a kind of N-line model, and in this model a sand transport equation similar to that by Hanson and Larson [14] is employed. Because the calculation of the nearshore current is not needed in this model as in 3D process-based models, and the computational load is small, it has an advantage in the prediction of long-term topographic changes in an extensive coast where many coastal structures have been constructed. This model then was improved to predict the temporal and spatial changes in the grain size of bed material [41–43]. The authors applied this model to many coasts in Japan to work out the countermeasures against beach erosion [2, 44–51]. However, this model has weak points.

First, in this model, the handling of boundary conditions becomes difficult when offshore coastal structures are constructed in a complicated manner, because tracking the subsequent positions of the contour lines is needed. In this regard, the so-called 3D model has an advantage. Taking this point into account, the authors developed a morphodynamic model (hereafter, "the BG model" named after Bagnold [52, 53]) by applying the concept of the equilibrium slope and the energetics approach, in which depth changes on 2D horizontal grids are calculated instead of tracking the subsequent positions of the contour lines [54, 55]. Second, the application of the contour-line-model to the prediction of topographic changes on a coast with a large shoreline curvature, such as a sand spit, was difficult.

In several previous studies, prediction of the deformation of a sand spit was tried by introducing the curvilinear coordinates along the curved shoreline in the One-line model [56–58], but their application to the prediction of topographic changes around a sand spit with a complicated form was limited. Taking this into account, the BG model was further improved to predict the 3D topographic changes around a sand spit or an isolated sand bar. Ashton et al. [59, 60] showed that sand spits may develop from infinitesimal perturbations on the shoreline under the conditions that the incident wave angle exceeds approximately 45° relative

to the direction normal to the shoreline. The BG model could be applied to these phenomena. In this book, the BG model is introduced with its applications.

In this book, however, we have not introduced the applications of the BG model to the prediction of beach changes on a coast with sand of mixed grain size because of the limits of space. On real coasts, spatial changes in the longitudinal profile associated with changes in the composition of each grain size may occur. The longitudinal slope gradually becomes gentle with increasing content of fine sand, for example, in the wave-shelter zone. These changes in the local slope in and around the wave-shelter zone can also be predicted [61, 62], taking the equilibrium slope corresponding to each grain size and its composition into account. Their applications are shown in [63–65].

Author details

Takaaki Uda[1*], Masumi Serizawa[2] and Shiho Miyahara[2]

1 Public Works Research Center, Tokyo, Japan

2 Coastal Engineering Laboratory Co., Ltd., Tokyo, Japan

*Address all correspondence to: uda@pwrc.or.jp

IntechOpen

© 2018 The Author(s). Licensee IntechOpen. Distributed under the terms of the Creative Commons Attribution - NonCommercial 4.0 License (https://creativecommons.org/licenses/by-nc/4.0/), which permits use, distribution and reproduction for non-commercial purposes, provided the original is properly cited. BY–NC

References

[1] Komar PD. Beach Processes and Sedimentation. London: Prentice Hall International; 1998. 544 p

[2] Uda T. Japan's Beach Erosion—Reality and Future Measures. 2nd ed. Singapore: World Scientific; 2017. 530 p

[3] Komar PD, Inman DL. Longshore sand transport on beaches. Journal of Geophysical Research. 1970;**75**:5914-5927

[4] CERC. Shore Protection Manual, Vicksburg, Mississippi, US Army Coastal Engineering Research Center, Corps of Engineers; 1984

[5] Kamphuis JW. Introduction to Coastal Engineering and Management. Singapore: World Scientific; 2000. 437 p

[6] Pelnard-Considere R. Essai de Theorie de l'Evolution des Formes de Ravage en Plages de Sables et de Galets. Societe Hydrotechnique de France, IV'eme Journee de L'Hydraulique Question III, Rapport, 1; 1956, 74-1-10 (in French)

[7] Hanson H, Kraus NC. GENESIS: Generalised model for simulating shoreline change, Technical Report CERC-89-19. Vicksburg, USA: Coastal Engineering Research Station, US Army Corps of Engineers; 1989. 185 p

[8] Dabees MA, Kamphuis JW. ONELINE, a numerical model for shoreline change. In: Proceedings of ASCE 27th International Conference on Coastal Engineering, ASCE, Vicksburg, USA; 1998. pp. 2668-2681

[9] Hanson H, Aarninkhof S, Capobianco M, Jimenez JA, Larson M, Nicholls R, et al. Modelling coastal evolution on early to decadal time scales. Journal of Coastal Research. 2003;**19**:790-811

[10] Bakker WT. The dynamics of a coast with a groyne system. In: Proceedings of 11th Coastal Engineering Conference (ASCE); 1969. pp. 1001-1020

[11] Perlin M, Dean RG. A Numerical Model to Simulate Sediment Transport in the Vicinity of Coastal Structures, Misc. Report, No. 83-10. Coastal Engineering Research Center, US Army Corps of Engineers; 1983. 119 p

[12] Steetzel HJ, de Vroeg JH. Application of a multilayer approach for morphological modelling. In: Coastal Sediments '99, ASCE, Vicksburg; 1999. pp. 2206-2218

[13] Steetzel HJ, de Vroeg H, van Rijn LC, Stam JM. Long-term modelling of the Holland coast using a multi-layer model. In: Proceedings of 27th International Conference on Coastal Engineering, ASCE, Sydney, Australia; 2000. pp. 2942-2955

[14] Hanson H, Larson M. Simulating coastal evolution using a new type N-line model. In: Proceedings of 27th International Conference on Coastal Engineering, ASCE, Vicksburg; 2000. pp. 2808-2821

[15] Dabees MA, Kamphuis JW. NLINE, efficient modeling of 3D beach change. In: Proceedings of 27th International Conference on Coastal Engineering, Sydney, Australia, ASCE; 2000. pp. 2700-2713

[16] Watanabe A, Maruyama K, Shimizu T, Sakakiyama T. Numerical prediction model of three-dimensional beach deformation around a structure. Coastal Engineering Journal (Japan). 1986;**29**:179-194

[17] Watanabe A. 3-Dimensional numerical model of beach evolution. In: Proceedings of Conference on Coastal Sediments '87, ASCE; 1987. pp. 802-817

[18] Watanabe A. Numerical model of beach topography change. In: Horikawa

K, editor. Nearshore Dynamics and Coastal Processes. Tokyo, Japan: University of Tokyo Press; 1988. pp. 241-243

[19] Sato S, Kabiling M. A numerical simulation of beach evolution based on a nonlinear dispersive wave-current model. In: Proceedings of 24th Conference on Coastal Engineering; 1994. pp. 2557-2570

[20] Roelvink D, Boutmy A, Stam JM. A simple method to predict long-term morphological changes. In: Proceedings of 26th International Conference on Coastal Engineering, Copenhagen, ASCE, New York; 1998. pp. 3224-3237

[21] Leont'yev IO. Modelling of morphological changes due to coastal structures. Coastal Engineering. 1999;**38**:143-166

[22] Gelfenbaum G, Roelvink JA, Meijs M, Buijsman M, Ruggiero P. Process-based morphological modeling of Gray Harbor inlet at decadal timescales. In: Proceedings of Coastal Sediments '03; 2003

[23] Lesser GR, Roelvink JA, van Kester JATM, Stelling GS. Development and validation of a three-dimensional morphological model. Coastal Engineering. 2004;**51**(8-9):883-915

[24] Brøker I, Zyserman J, Madsen EØ, Mangor K, Jensen J. Morphological modelling: a tool for optimisation of coastal structures. Journal of Coastal Research. 2007;**23**(5):1148-1158

[25] Kuroiwa M, Shibutani Y, Matsubara Y, Kuchiishi T, Abualtyef M. Numerical model of 3D morphodynamics after offshore nourishment. In: Proceedings of 31st International Conference on Coastal Engineering, No. 32, Paper #: sediments. 55; 2010. http://journals.tdl.org/ICCE/

[26] Nam PT, Larson M, Hanson H, Hoan LX. A numerical model of beach morphological evolution due to waves and currents in the vicinity of coastal structures. Coastal Engineering. 2011;**58**(9):863-876

[27] Bijker EW. Longshore transport computation. Journal of the Waterways and Harbors Division. 1971;**97**(WW4):687-701

[28] van Rijn LC. Sediment transport, part I: bed load transport. Journal of the Hydraulics Division. 1984;**110**(10):1431-1456

[29] van Rijn LC. Sediment transport, part II: suspended load transport. Journal of the Hydraulics Division. 1984;**110**(11):1613-1641

[30] Bailard JA. An energetics total load sediment transport model for a plane sloping beach. Journal of Geophysical Research. 1981;**86**(C11):10938-10954

[31] Dibajinia M, Watanabe A. Sheet flow under nonlinear waves and currents. In: Edge BL, editor, 23rd International Conference on Coastal Engineering, ASCE, Venice, Italy; 1992. pp. 2015-2028

[32] Soulsby DH. Dynamics of Marine Sands: A Manual for Practical Applications. London, England: Thomas Telford Publications; 1997. 249 p

[33] Ribberink JS. Bed-load transport for steady flows and unsteady oscillatory flows. Coastal Engineering. 1998;**34**:59-82

[34] Watanabe A, Sato S. A sheet-flow transport rate formula for asymmetric, forward-leaning waves and currents. In: Proceedings of 29th International Conference on Coastal Engineering, Lisbon, Portugal; 2004. pp. 1703-1714

[35] Camenen B, Larson M. A general formula for non-cohesive bed load sediment transport. Estuarine, Coastal and Shelf Science. 2005;**63**:249-260

[36] Camenen B, Larson M. A unified sediment transport formulation for coastal inlet application, Coastal Inlets Research Program, Final Report ERDC/CHL CR-07-1, US Army Corps of Engineers, Washington, DC; 2007

[37] Camenen B, Larson M. A total load formula for the nearshore. In: Proceedings of Coastal Sediments '07 Conference, ASCE, Reston, VA; 2007. pp. 56-67

[38] Ribberrink JS, van der A DA, Buijsrogge RH. SANTOSS Transport Model–A New Formula for Sand Transport Under Waves and Currents, Report SANTOSS_UT_IR3. Enschede, The Netherlands: University of Twente; 2010

[39] Van der A DA, Ribberrink JS, van der Werb JJ, O'Donoghue T, Buijsrogge RH, Kranenburg WM. Practical sand transport formula for non-breaking waves and currents. Coastal Engineering. 2013;**76**:26-42

[40] Serizawa M, Uda T, San-nami T, Furuike F, Kumada K. Improvement of contour-line change model in terms of stabilization mechanism of longitudinal profile. In: Coastal Sediments '03; 2003. pp. 1-15

[41] Uda T, Kumada T, Serizawa M. Predictive model of change in longitudinal profile in beach nourishment using sand of mixed grain size. In: Proceedings of 29th ICCE; 2004. pp. 3378-3390

[42] Kumada T, Uda T, Serizawa M, Noshi Y. Model for predicting changes in grain size distribution of bed materials. In: Proceedings of 30th ICCE; 2006. pp. 3043-3055

[43] Uda T, Serizawa M. Model for predicting topographic changes on coast composed of sand of mixed grain size and its applications (Chapter 16). In: Angermann, L. editor. Numerical Simulations-Examples and Applications in Computational Fluid Dynamics, INTEC; 2010. pp. 327-358. http://www.intechopen.com/articles/show/title/model-for-predicting-topographic-changes-on-coast-composed-of-sand-of-mixed-grain-size-and-its-appli

[44] Kumada T, Uda T, Serizawa M. Quantitative evaluation of controlling effect of headland on longshore sand transport using a model for predicting changes in contour lines and grain size. In: Coastal Sediments '07; 2007. pp. 2446-2459

[45] Yoshioka A, Uda T, Aoshima G, Furuike K, Ishikawa T. Field experiment of beach nourishment considering changes in grain size and prediction of beach changes. In: Proceedings of 31st ICCE; 2008. pp. 2694-2706

[46] Nishitani M, Uda T, Serizawa M, Ishikawa T. Measurement and prediction of deformation of conveyor belts carrying gravel and fine sand off Shimizu coast. In: Proceedings of 31st ICCE; 2008. pp. 2570-2582

[47] Kumada T, Uda T, Matsu-ura T, Sumiya M. Field experiment on beach nourishment using gravel at Jinkoji coast. In: Proceedings 32nd ICCE, sediment.100; 2010. pp. 1-13. http://journals.tdl.org/ICCE/article/view/1076/pdf_178

[48] Miyahara S, Uda T, Furuike K, Serizawa M, San-nami T, Ishikawa T. Effect of sand bypassing at Sakuma Dam in Tenryu River as a measure against erosion of Tenryu River delta coast. In: Proceedings of 32nd ICCE, sediment.106; 2010. pp. 1-12. http://journals.tdl.org/ICCE/article/view/1049/pdf_165

[49] Furuike K, Uda T, Serizawa M, San-nami T, Ishikawa T. Quantitative prediction of sand discharge into a submarine canyon off Morito River on Seisho coast, Japan. In: Proceedings

of 32nd ICCE, sediment.107; 2010. pp. 1-13. http://journals.tdl.org/ICCE/article/view/1050/pdf_166

[50] Ishikawa T, Uda T, Furuike K, Yoshioka A. Regional sediment management considering volume of sand and grain size. In: Coastal Sediments '11; 2011. pp. 2033-2046

[51] Ishikawa T, Uda T, San-nami T, Furuike K. Verification of effect of gravel nourishment on Hamamatsu-shinohara coast, Japan. In: Coastal Sediments '15, CD-Rom, No. 47; 2015. pp. 1-14

[52] Inman DL, Bagnold RA. Littoral processes. In: Hill MN, editor. The Sea. Vol. 3. New York: Wiley; 1963. pp. 529-533

[53] Bagnold RA. Mechanics of marine sedimentation. In: Hill MN, editor. The Sea. Vol. 3. New York: Wiley; 1963. pp. 507-528

[54] Serizawa M, Uda T, San-nami T, Furuike K. Three-dimensional model for predicting beach changes based on Bagnold's concept. In: Proceedings of 30th ICCE; 2006. pp. 3155-3167

[55] Serizawa M, Uda T, San-nami T, Furuike K, Ishikawa T. BG-model predicting three-dimensional beach changes based on Bagnold's concept and applications. In: Proceedings of 4th International Conference on Asian and Pacific Coasts 2007; 2007. pp. 1165-1179

[56] Jiménez JA, Sánchez-Arcilla A. Modelling of barrier-spit system evolution at decadal scale. In: Coastal Sediments '99. Reston, VA: American Society of Civil Engineers; 1999. pp. 1724-1738

[57] Jiménez JA, Sánchez-Arcilla A. A long-term (decadal scale) evolution model for microtidal barrier systems. Coastal Engineering. 2004;**51**:749-764

[58] Watanabe S, Serizawa M, Uda T. Predictive model of formation of a sand spit. In: Proceedings of 29th ICCE; 2004. pp. 2061-2073

[59] Ashton A, Murray AB, Arnault O. Formation of coastline features by large-scale instabilities induced by high angle waves. Nature. 2001;**414**:296-300

[60] Ashton A, Murray AB. High-angle wave instability and emergent shoreline shapes: 1. Modeling of sand waves, flying spits, and capes. Journal of Geophysical Research. 2006;**111**:F04011. DOI: 10.1029/2005JF000422

[61] Serizawa M, Uda T, San-nami T, Furuike K, Ishikawa T, Kumada T. Model for predicting beach changes on coast with sand of mixed grain size based on Bagnold's concept. In: Coastal Sediments '07; 2007. pp. 314-326

[62] Noshi Y, Uda T, Serizawa M, Kumada T, Kobayashi A. Model for predicting bathymetric and grain size changes based on Bagnold's concept and equilibrium slope corresponding to grain size composition. In: Proceedings of 32nd ICCE, sediment.15; 2010. pp. 1-13. http://journals.tdl.org/ICCE/article/view/1075/pdf_177

[63] Ishikawa T, Uda T, San-nami T, Hosokawa J. Verification of shore protection effect of beach nourishment on Chigasaki coast. In: Proceedings of the 7th International Conference on Asian and Pacific Coasts (APAC 2013) Bali, Indonesia, September 24-26, 2013; 2013. pp. 1-8

[64] Ishikawa T, Uda T, Miyahara S, Serizawa M, Fukuda M, Hara Y. Recovery of sandy beach by gravel nourishment—example of Ninomiya coast in Kanagawa Prefecture, Japan. In: Proceedings of 34th ICCE; 2014. pp. 1-15. https://journals.tdl.org/icce/index.php/icce/article/view/7107/pdf_411

[65] Uda T, Ishikawa T, San-nami T, Hosokawa J, Sasaki T, Furuike K. Shore protection by gravel nourishment on Chigasaki-naka coast and preventive measure against gravel diffusion to nearby beach. In: Proceedings of Civil Engineers, Japan, Vol. 70, No. 2; 2014. pp. I_702-I_707 (in Japanese)

Chapter 2

Derivation of the BG Model

Takaaki Uda, Masumi Serizawa and Shiho Miyahara

Abstract

The BG model (a model for predicting 3D beach changes based on the Bagnold's concept) was introduced, and the fundamental aspects of the model were explained. The BG model is based on the concepts such as (1) the contour line becomes orthogonal to the wave direction at any point at the final stage, (2) similarly, the local beach slope coincides with the equilibrium slope at any point, and (3) a restoring force is generated in response to the deviation from the statically stable condition, and sand transport occurs owing to this restoring force. The same concept has been employed in the contour-line-change model and N-line model. In these studies, the movement of certain contour lines was traced, but in the BG model, 3D beach changes were directly calculated.

Keywords: BG model, derivation, physical meaning

1. Introduction

The BG model is based on the concepts such as (1) the contour line is orthogonal to the wave direction at any point at the final stage, (2) similarly, the local beach slope coincides with the equilibrium slope at any point, and (3) a restoring force is generated in response to the deviation from the statically stable condition, and sand transport occurs owing to this restoring force. The same concept has been employed not only in the contour-line-change model [1] but also in the N-line model [2–7]. In these studies, the movement of certain contour lines was traced, but in the BG model, the depth change on the 2D horizontal grids was directly calculated. Falqués et al. [8, 9] developed a medium- to long-term model for beach morphodynamics named Q2D-morfo. In their model, similar expressions regarding crossshore and longshore sand transport equations as the BG model were employed. In particular, they used the beach slope measured on a real coast as the equilibrium slope, similar to the BG model, and the prediction of beach changes bounded by two groynes was carried out, but the prediction period was as short as 35 days [8]. van den Berg et al. [10] predicted the development of a sand wave associated with large-scale beach nourishment due to shoreline instability under the oblique wave incidence at a large angle using the model proposed by Falqués et al. [8]. Larson et al. [11] proposed the crossshore sand transport equation in the swash zone using the concept of the equilibrium slope and predicted the foreshore evolution. Similarly, Larson and Wamsley [12] proposed crossshore and longshore sand transport formulae in the swash zone, and they used the similar equations as the BG model. Their equations were also employed in the 3D beach change model in the swash zone by Nam et al. [13].

2. Derivation of the BG model

In the derivation of the sand transport equation of the BG model, we referred Bagnold [14] and the previous studies after Bagnold (Inman and Bagnold [15], Bowen [16], Bailard and Inman [17], and Bailard [18]). Bagnold [14] derived the sand transport equation for a unidirectional steady flow with an explicit expression of the seabed slope by applying the energetics approach. Inman and Bagnold [15] assumed that sand transport in a wave field is the sum of the components caused by shoreward flow during the motion of incoming waves and those caused by seaward flow during the motion of outgoing waves and defined the slope satisfying zero net onshore or offshore sediment transport as the equilibrium slope. Their equilibrium slope is the slope when upslope effect due to the asymmetry in action of incoming and outgoing waves and downslope effect due to the gravity balance each other.

Regarding the sand transport equation under waves, Bowen [16], Bailard and Inman [17], and Bailard [18] formulated the instantaneous sand transport flux on the basis of the sand transport equation for a unidirectional steady flow by Bagnold [14], assuming that the wave dissipation rate is proportional to the third power of the instantaneous velocity. Then, the net sand transport formula was derived by integrating the instantaneous sand transport flux over one wave period. Furthermore, they derived the equilibrium slope equation using the wave velocity parameters. Out of these studies, the sand transport flux formula by Bailard and Inman [17] considers both bed load and suspended load, and this formula has been extensively used in the models for predicting beach changes. Kabiling and Sato [19] calculated the wave and nearshore current field using the Boussinesq equation and predicted 3D beach changes using the Bailard formula. Long and Kirby [20] also carried out the numerical simulation of beach changes using the Bailard formula and Boussinesq equation. However, the application of their model to the long-term prediction of the topographic changes in an extensive calculation domain is limited because the recurrent calculations in solving the time-dependent equation of the wave field are time consuming. On a real coast, a longitudinal profile maintains its stable form as a whole, as a result of the wave action for a long period of time, apart from the short-period seasonal variation of the beach, suggesting the existence of an equilibrium slope on a real coast. In contrast, in their studies, the beach slope does not necessarily agree with the equilibrium slope after long-term prediction, even though an equilibrium slope exists, and it is difficult to explain the phenomena really observed on a coast.

In this study, we return to the starting point of Bagnold's basic study, and simple sand transport equations are derived. Then, a model for predicting 3D beach changes by applying the concept of the equilibrium slope introduced by Inman and Bagnold [15] and the energetics approach of Bagnold [14] is developed [21].

Figure 1 shows the definitions of the variables. Consider Cartesian coordinates (x, y) and the seabed elevation $Z(x, y, t)$ with reference to the still water level as a variable to be solved, where t is the time. Assume that waves are obliquely incident on a coast with a slope of $\tan\beta$. n and s are the local coordinates taken along the directions normal (shoreward) and parallel to the contour lines, respectively. The n-axis makes an angle of θ_n measured counterclockwise from the x-axis, $\vec{e_n}$ is the unit vector normal to the contour lines (shoreward), $\vec{e_s}$ is the unit vector parallel to the contour lines, $\vec{e_w}$ is the unit vector in the wave direction, and θ_w is the wave direction measured counterclockwise from the x-axis. α is the angle between the wave direction and the direction normal to the contour lines. These unit vectors are expressed as

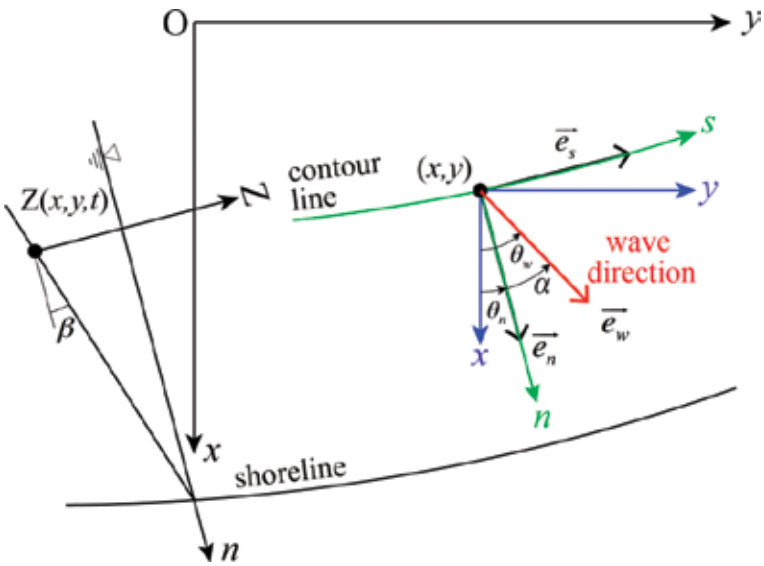

Figure 1.
Setup of the coordinate system and definition of variables.

$$\vec{e_n} = (\cos\theta_n, \sin\theta_n) \tag{1}$$

$$\vec{e_s} = (-\sin\theta_n, \cos\theta_n) \tag{2}$$

$$\vec{e_w} = (\cos\theta_w, \sin\theta_w) \tag{3}$$

The components of the sand transport vector $\vec{q}$ are expressed as Eq. (4), the direction and magnitude of which give the direction of sand transport and a volumetric expression for the sand transport rate per unit width normal to the direction of sand transport and per unit time, respectively. In addition, $\vec{q}$ can be expressed as the vector sum of the crossshore and longshore components in each direction of n and s as in Eq. (5), and by taking the inner products of $\vec{e_n}$ and $\vec{q}$ and of $\vec{e_s}$ and $\vec{q}$, the crossshore and longshore components of sand transport, q_n and q_s, are given by Eqs. (6) and (7), respectively.

$$\vec{q} = \left(q_x, q_y\right) \tag{4}$$

$$\vec{q} = q_n\vec{e_n} + q_s\,\vec{e_s} \tag{5}$$

$$q_n = \vec{e_n}\cdot\vec{q} \tag{6}$$

$$q_s = \vec{e_s}\cdot\vec{q} \tag{7}$$

When the gradient vector of Z is defined as Eq. (8), $\vec{\nabla Z}$ becomes a vector, the direction and the absolute value of which are along n-axis and $\tan\beta$, respectively, with the component form of the expression in Eq. (9) in (x, y) coordinates. Furthermore, Eqs. (10)–(15) are satisfied.

$$\vec{\nabla Z} = \tan\beta\ \vec{e_n} \tag{8}$$

$$\vec{\nabla Z} = (\tan\beta\cos\theta_n, \tan\beta\sin\theta_n) = (\partial Z/\partial x, \partial Z/\partial y) \tag{9}$$

$$\left|\vec{\nabla Z}\right| = \sqrt{(\partial Z/\partial x)^2 + (\partial Z/\partial y)^2} = \tan\beta \tag{10}$$

$$\tan\beta\ \vec{e_s} = (-\partial Z/\partial y, \partial Z/\partial x) \tag{11}$$

$$\theta_n = \tan^{-1}\left(\frac{\partial Z}{\partial y} \Big/ \frac{\partial Z}{\partial x}\right) \tag{12}$$

$$\alpha = \theta_w - \theta_n \tag{13}$$

$$\begin{aligned}\cos\alpha &= \vec{e_w}\cdot\vec{e_n} \\ &= \left(\vec{e_w}\cdot\vec{\nabla Z}\right)/\left|\vec{\nabla Z}\right| \\ &= [\cos\theta_w(\partial Z/\partial x) + \sin\theta_w(\partial Z/\partial y)]/\tan\beta\end{aligned} \tag{14}$$

$$\begin{aligned}\sin\alpha &= \vec{e_w}\cdot\vec{e_s} \\ &= \left(\vec{e_w}\cdot\tan\beta\,\vec{e_s}\right)/\tan\beta \\ &= [-\cos\theta_w(\partial Z/\partial y) + \sin\theta_w(\partial Z/\partial x)]/\tan\beta\end{aligned} \tag{15}$$

The fluid motion due to waves near the sea bottom becomes oscillatory, and a sand particle moves back and forth in the crossshore direction. Sand transport in a wave field is assumed to be the sum of the components caused by shoreward flow during the motion of incoming waves and those caused by seaward flow during the motion of outgoing waves, as suggested in [15], and the sand transport equation for a unidirectional steady flow introduced by Bagnold [14] can be applied to each component.

Assuming that tan β is infinitesimal, the flow makes a sand particle move in the direction of the flow, and gravity causes downslope action; the sand transport flux of a unidirectional flow is expressed by Eq. (16) as a linear approximation in terms of tan β [15–18].

$$\vec{q_u} = a_0\,\vec{e_u} - a_1\,\vec{\nabla Z} \qquad (a_0>0,\quad a_1>0) \tag{16}$$

Here, the subscript u denotes the unidirectional flow, $\vec{q_u} = \left(q_{ux}, q_{uy}\right)$ is the sand transport vector, the direction and magnitude of which give the direction of sand transport and a volumetric expression for the sand transport rate per unit width normal to the direction of sand transport and per unit time, respectively, $\vec{e_u}$ is the unit vector in the direction of the flow, $\vec{\nabla Z} = \tan\beta\ \vec{e_n} = (\partial Z/\partial x, \partial Z/\partial y)$ is the gradient vector of Z, and tan β is the seabed slope. The sign of the coefficients a_0 and a_1 is always positive. The first and second terms in Eq. (16) represent the action produced by the flow and the downslope action due to gravity, respectively. In the equation in [17] based on the bedload equation of Bagnold [14], the coefficients a_0 and a_1 are described in terms of the angle of the internal friction of sand and the flow velocity. On the other hand, the sand transport equations in [16, 18] based on the suspended load equation of Bagnold [14] can be expressed in the same form as Eq. (16), although the coefficients a_0 and a_1 are described in terms of the falling velocity of a sand particle and the flow velocity. Thus, Eq. (16) is satisfied for not only the bedload but also suspended load, that is, total load.

The net sand transport flux due to waves, $\vec{q} = \left(q_x, q_y\right)$, is the sum of the components due to incoming and outgoing waves, as shown in Eq. (17), when the time-averaged sand transport rate in a period involving the action of incoming and outgoing waves is expressed by Eqs. (18) and (19).

$$\vec{q} = \vec{q^+} + \vec{q^-} \tag{17}$$

$$\vec{q^+} = a_0^+ \vec{e_w^+} - a_1^+ \vec{\nabla Z} \quad \left(a_0^+ > 0, a_1^+ > 0\right) \tag{18}$$

$$\vec{q^-} = a_0^- \vec{e_w^-} - a_1^- \vec{\nabla Z} \quad \left(a_0^- > 0, a_1^- > 0\right) \tag{19}$$

Here, the subscripts + and – denote the values corresponding to incoming and outgoing waves, respectively, and $\vec{e_w^+}$ and $\vec{e_w^-}$ are the unit vectors in the directions of the shoreward and seaward flows of waves, respectively. Modifying Eq. (17) under the assumption that the directions of waves propagating shoreward and seaward are opposite, as given by Eq. (20), defining the slope satisfying zero net onshore or offshore sediment transport when waves are incident from the direction normal to the slope as the equilibrium slope, $\tan\beta_c$ (Eq. (21)), and defining the coefficient A by Eq. (22), the sand transport flux is given by Eq. (23).

$$\vec{e_w^-} = -\vec{e_w^+} \tag{20}$$

$$\tan\beta_c = \left(\frac{a_0^+ - a_0^-}{a_1^+ + a_1^-}\right) \tag{21}$$

$$A = \left(a_1^+ + a_1^-\right) \tag{22}$$

$$\vec{q} = A\left[\tan\beta_c \vec{e_w} - \vec{\nabla Z}\right] \tag{23}$$

Here, $\vec{e_w} = \vec{e_w^+}$ is the unit vector in the wave direction θ_w (Eq. (3)). Bowen [16], Bailard and Inman [17], and Bailard [18], based on the Bagnold's concept, formulated the equilibrium slope of Eq. (21) using the oscillatory flow velocity due to waves, the angle of the internal friction of sand, and the falling velocity of a sand particle. Hardisty [22, 23] also formulated the equilibrium slope using the wave parameters on the basis of the same concept. Furthermore, Dean [24, 25] formulated the equilibrium profile in terms of energy dissipation rate due to wave breaking, and Larson et al. [26] gave a theoretical formulation of the equilibrium profile, the derivative of which is equal to the equilibrium slope, with the combination of wave parameters.

In this study, we used the seabed slope measured on real coasts as the equilibrium slope instead of using the formulated results of the equilibrium slope. The measured slope is assumed to be given a priori because the real seabed topography includes every effect of past events, and it has a stable form, except for seasonal short-period variations, in the long term.

Applying the energetics approach [14] and assuming that the coefficient A in Eq. (23) is proportional to the wave energy dissipation rate Φ, the total longshore sand transport rate is obtained by integrating Eq. (23) over the depth. This has the same form as the CERC-type formula given by Komar and Inman [27], and the coefficient A is determined as Eq. (24) from the equivalence of both results as mentioned later. Finally, the fundamental equation of sand transport flux due to waves is given by Eq. (26).

$$A = C_0 \frac{K_1 \Phi}{\tan\beta_c} \tag{24}$$

$$C_0 = \frac{1}{(\rho_s - \rho)g(1-p)} \tag{25}$$

$$\vec{q} = C_0 \frac{K_1 \Phi}{\tan\beta_c} \left[\tan\beta_c \, \vec{e_w} - \vec{\nabla Z} \right] \tag{26}$$

Here, K_1 is the coefficient of longshore sand transport, Φ is the wave energy dissipation rate per unit time and unit seabed area, C_0 is the coefficient through which the sand transport rate expressed in terms of the immersed weight is related to the volumetric sand transport rate, ρ_s and ρ are the sand and water densities, respectively, g is the acceleration of gravity, and p is the porosity of the sediment.

3. Physical meaning of the sand transport equation of the BG model

3.1 Statically stable condition

When we set $\vec{q} = \vec{0}$ in Eq. (26), Eq. (27) is derived as a statically stable condition.

$$\vec{\nabla Z} = \tan\beta_c \, \vec{e_w} \tag{27}$$

This equation demonstrates that the directions of the vectors on both sides of Eq. (27) and their absolute values are equivalent. When $\tan\beta$ and $\vec{e_n}$ are set to the seabed slope and the unit vector normal to the contour lines (shoreward), respectively, the relation $\vec{\nabla Z} = \tan\beta \, \vec{e_n}$ holds. Thus, Eq. (27) is equivalent to the following relationships being satisfied.

$$\vec{e_n} = \vec{e_w}, \ \tan\beta = \tan\beta_c \tag{28}$$

Finally, the conditions required for the formation of a statically stable beach are (1) the contour line is orthogonal to the wave direction at any point and (2) the local beach slope coincides with the equilibrium slope at any point. This concept was also employed in the model for predicting a statically stable beach [28]. According to Eq. (26), a restoring force is generated in response to the deviation from the statically stable condition, and sand transport occurs owing to this restoring force.

3.2 Topographic changes

Topographic changes can be determined from the mass conservation equation.

$$\frac{\partial Z}{\partial t} = -\nabla \bullet \vec{q} = -\frac{\partial q_x}{\partial x} - \frac{\partial q_y}{\partial y} \tag{29}$$

When the sand transport fluxes in Eq. (26) are expressed by the components in (x, y) coordinates and are substituted into Eq. (29), the following two-dimensional diffusion equation is obtained, assuming that the coefficient A, equilibrium slope, and wave direction are constant:

$$\frac{\partial Z}{\partial t} = A\left(\frac{\partial^2 Z}{\partial x^2} + \frac{\partial^2 Z}{\partial y^2}\right) \tag{30}$$

The left term and the terms in the parenthesis on the right represent the rate of topographic changes and the spatial curvature of the topography, respectively. In other words, beach changes cause the smoothing of an uneven topography, and in a

closed system of sand transport, a statically stable beach is obtained such that the direction of the contours at any point becomes orthogonal to the wave direction, and the local slope is equivalent to the equilibrium slope. These characteristics are the same as those of the contour-line change model [1].

3.3 Dynamically stable beach

In addition to the formation of a statically stable beach, a stable beach can also be dynamically stable, which occurs when the divergence of the sand transport flux in Eq. (30) becomes 0. The dynamically stable beach topography satisfies the Laplace equation, and the relationship between the dynamically stable topography and the sand transport flux has an analogy with the two-dimensional potential flow in fluid dynamics [29].

3.4 Crossshore sand transport

Using Eqs. (6) and (26), the crossshore component of sand transport q_n is obtained as

$$q_n = \vec{e_n} \cdot \vec{q} = C_0 \frac{K_1 \Phi}{\tan\beta_c} \left(\tan\beta_c \cos\alpha - \tan\beta \right) \tag{31}$$

Here, n is the coordinate in the crossshore direction and $\vec{e_n}$ is the unit vector in the cross-shore direction, as defined by Eq. (1). α is the angle between the wave direction and the direction normal to the contour lines, as in Eq. (13). When waves are incident from the direction normal to the shoreline, Eq. (31) becomes

$$q_n = C_0 \frac{K_1 \Phi}{\tan\beta_c} \left(\tan\beta_c - \tan\beta \right) \tag{32}$$

Eq. (32) has the characteristics that crossshore sand transport diminishes when waves are incident from the direction normal to the shoreline, and the local slope is equal to the equilibrium slope ($\tan\beta = \tan\beta_c$). Shoreward transport is generated when the local slope is smaller than the equilibrium slope and vice versa (**Figure 2**). This represents the balance between the upslope flow asymmetry and the downslope component of gravity [15–18].

Figure 2(a) shows the stabilization mechanism of a beach profile based on sand movement during one wave period, a sand particle moves from point 1 to point 2 during incoming waves and from point 2 to point 3 during outgoing waves, and it returns to the same position after one wave period. The net movement of the sand particle is zero, resulting in the formation of a stable beach profile. The seabed slope $\tan\beta$ under this condition is equivalent to the equilibrium slope $\tan\beta_c$. **Figure 2(b)** shows the movement of a sand particle in the case that the local slope is larger than the equilibrium slope $\tan\beta_c$. Because of the increase in the effect of gravity, the sand particle moves seaward as from point 1 to point 2 and then to point 3, resulting in net seaward sand transport and the beach attains a stable slope. To the contrary, when the local slope is gentler than the equilibrium slope, the sand particle is transported landward because of the decrease in the effect of gravity, as schematically shown in **Figure 2(c)**. In **Figure 2**, an extremely simple condition that a sand particle sets on the slope is assumed as an imaginary case to enhance the understanding of the physical meaning of sand movement. In fact, a sand body to be transported due to waves was conceptually regarded as "a sand particle," instead of the method of tracking one sand particle.

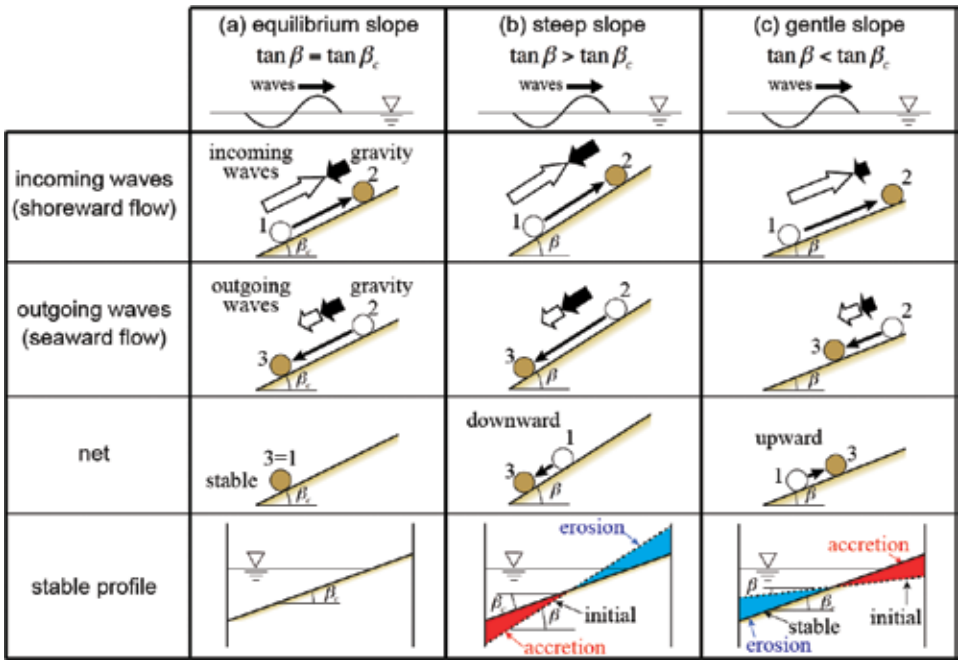

Figure 2.
Stabilization mechanism of the beach profile based on the sand movement during the one wave period.

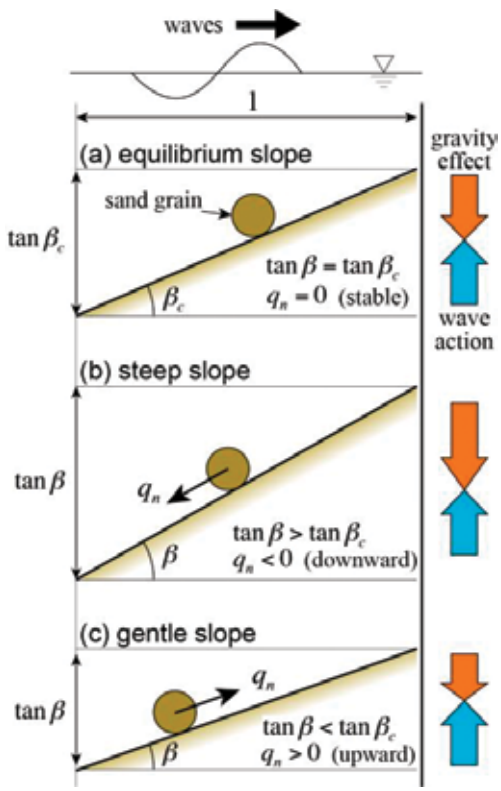

Figure 3.
Equilibrium between the gravity effect and the wave action.

Figure 3 shows a summary of the movement of a sand particle. Crossshore sand transport is zero when the local seabed slope is equivalent to the equilibrium slope, similar to the stabilization mechanism of the longitudinal profile described by Serizawa et al. [1]. Offshore (shoreward) sand transport occurs when the local slope is larger (smaller) than the equilibrium slope.

When waves are obliquely incident to the shoreline, the equilibrium slope $\tan\beta_c'$ can be obtained as Eq. (33) after setting $q_n = 0$ in Eq. (31). Here, the breaker angle α_b is substituted into α as an approximation.

$$\tan\beta_c' = \tan\beta|_{q_n=0} = \tan\beta_c \cos\alpha \approx \tan\beta_c \cos\alpha_b \tag{33}$$

Although $\tan\beta_c'$ is smaller than $\tan\beta_c$ by a factor of $\cos\alpha_b$, the approximation of $\cos\alpha_b \approx 1$ holds, because α_b normally takes a value within 20°, and $\tan\beta_c'$ can be regarded as $\tan\beta_c$.

3.5 Longshore sand transport

Using Eqs. (7) and (26), the longshore component of sand transport q can be expressed as

$$q_s = \vec{e_s} \cdot \vec{q} = C_0 K_1 \Phi \sin\alpha \tag{34}$$

Here, s and $\vec{e_s}$ are the coordinate and the unit vector in the longshore direction, as defined in Eq. (2), respectively. This equation shows that the longshore sand transport q_s becomes 0 when the wave direction coincides with the direction normal to

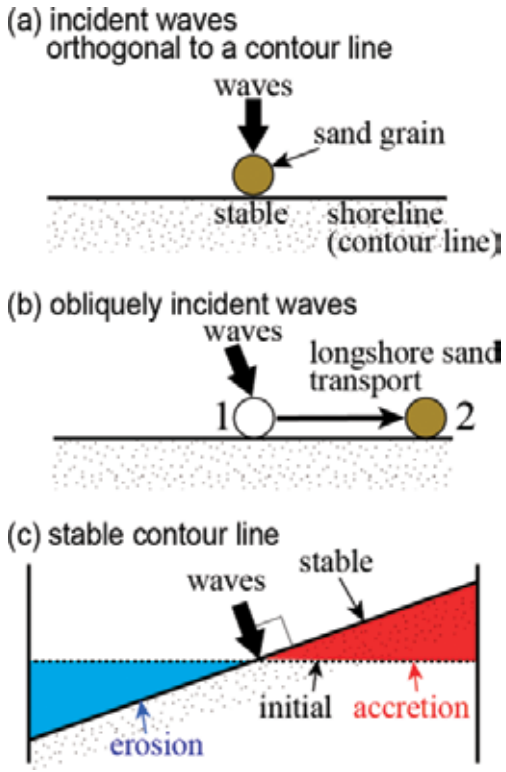

Figure 4.
Formation of stable contour lines.

the contour lines. Under other conditions, longshore sand transport is induced, as schematically shown in **Figure 4**.

When the total sand transport Q_s is calculated by integrating Eq. (34) in the crossshore direction, it coincides with the CERC-type formula [1], as in Eq. (35), under the assumptions that the integral of Φ in the crossshore direction is equal to the energy flux per unit length of the coastline at the breaking point and that α is approximately given by the breaker angle α_b.

$$\begin{aligned} Q_s &= \int q_s dn = C_0 K_1 \int \Phi \sin\alpha \, dn \\ &= C_0 K_1 (EC_g)_b \cos\alpha_b \sin\alpha_b \\ &\left(\alpha \approx \alpha_b, \int \Phi dn = (EC_g)_b \cos\alpha_b\right) \end{aligned} \tag{35}$$

Here, $(EC_g)_b$ and α_b are the wave energy flux at the breaking point and the breaker angle, respectively. This CERC-type formula [30] has been employed in the one-line model in practical engineering [31, 32]. Thus, the integral of the longshore component of sand transport in the BG model in the crossshore direction is equivalent to the total longshore sand transport, so both bedload and suspended sediment transport are automatically included in the total sand transport. The fundamental equations of the BG model are compatible with the CERC total sand transport formula, which has often been employed in the prediction of beach changes in the practical applications.

Author details

Takaaki Uda[1*], Masumi Serizawa[2] and Shiho Miyahara[2]

1 Public Works Research Center, Tokyo, Japan

2 Coastal Engineering Laboratory Co., Ltd., Tokyo, Japan

*Address all correspondence to: uda@pwrc.or.jp

IntechOpen

© 2018 The Author(s). Licensee IntechOpen. Distributed under the terms of the Creative Commons Attribution - NonCommercial 4.0 License (https://creativecommons.org/licenses/by-nc/4.0/), which permits use, distribution and reproduction for non-commercial purposes, provided the original is properly cited. BY–NC

References

[1] Serizawa M, Uda T, San-nami T, Furuike F, Kumada K. Improvement of contour-line change model in terms of stabilization mechanism of longitudinal profile. In: Coastal Sediments '03. World Sceintific Publication Co.; 2003. pp. 1-15

[2] Hanson H, Aarninkhof S, Capobianco M, Jimenez JA, Larson M, Nicholls R, et al. Modelling coastal evolution on early to decadal time scales. Journal of Coastal Research. 2003;**19**:790-811

[3] Perlin M, Dean RG. A numerical model to simulate sediment transport in the vicinity of coastal structures, Misc. Report, No. 83-10. Coastal Engineering Research Center, U.S. Army Corps of Engineers; 1983. p. 119

[4] Steetzel HJ, de Vroeg JH. Application of a multilayer approach for morphological modelling. In: Coastal Sediments' 99. Vicksburg: ASCE; 1999. pp. 2206-2218

[5] Steetzel HJ, de Vroeg H, van Rijn LC, Stam JM. Long-term modelling of the Holland coast using a multi-layer model. In: Proceedings of the 27th International Conference on Coastal Engineering. Sydney, Australia: ASCE; 2000. pp. 2942-2955

[6] Hanson H, Larson M. Simulating coastal evolution using a new type N-line model. In: Proceedings of the 27th International Conference on Coastal Engineering. Vicksburg: ASCE; 2000. pp. 2808-2821

[7] Dabees MA, Kamphuis JW. Efficient modeling of 3D beach change. In: Proceedings of the 27th International Conference on Coastal Engineering. Sydney, Australia: ASCE; 2000. pp. 2700-2713

[8] Falqués A, Garnier R, Ojeda E, Ribas F, Guillen J. Q2D-morfo: A medium to long term model for beach morphodynamics. River, Coastal and Estuarine Morphodynamics. 2007;**1-2**: 71-78

[9] Falqués A, van den Berg N, Calvete D. The role of cross-shore profile dynamics on shoreline instability due to high-angle waves. In: Proceedings of 31st ICCE; 2008. pp. 1826-1838

[10] van den Berg N, Falqués A, Ribasz F. Long-term evolution of nourished beaches under high angle wave conditions. Journal of Marine Systems. 2011;**88**(1):102-112

[11] Larson M, Kubota S, Erikson L. Swash zone sediment transport and foreshore evolution: Field experiment and mathematical modeling. Marine Geology. 2004;**212**:61-79

[12] Larson M, Wamsley TV. A formula for longshore sediment transport in the swash. In: Proceedings of Coastal Sediment'07. ASCE; 2007. pp. 1924-1937

[13] Nam PT, Larson M, Hanson H, Hoan LX. A numerical model of beach morphological evolution due to waves and currents in the vicinity of coastal structures. Coastal Engineering. 2011; **58**(9):863-876

[14] Bagnold RA. Mechanics of marine sedimentation. In: Hill MN, editor. The Sea. Vol. 3. New York: Wiley; 1963. pp. 507-528

[15] Inman DL, Bagnold RA. Littoral processes. In: Hill MN, editor. The Sea. Vol. 3. New York: Wiley; 1963. pp. 529-533

[16] Bowen AJ. Simple models for nearshore sedimentation: Beach profiles and longshore bars. In: The Coastline of Canada, The Geological Survey of

Canada, McCann SB, Paper 80(10); 1980. pp. 1-11

[17] Bailard JA, Inman DL. An energetics bedload model for a plane sloping beach: Local transport. Journal of Geophysical Research. 1981;**86**(C3):2035-2043

[18] Bailard JA. An energetics total load sediment transport model for a plane sloping beach. Journal of Geophysical Research. 1981;**86**(C11):10938-10954

[19] Kabiling M, Sato S. Two-dimensional nonlinear dispersive wave-current model and three-dimensional beach deformation model. Coastal Engineering in Japan. 1993;**36**(2): 195-212

[20] Long W, Kirby JT. Cross-shore sediment transport model based on the Boussinesq equations and an improved Bagnold formula. In: Proceedings of Coastal Sediments '03. Clearwater Beach: ASCE; 2003

[21] Serizawa M, Uda T, San-nami T, Furuike K. Three-dimensional model for predicting beach changes based on Bagnold's concept. In: Proceedings of 30th ICCE; 2006. pp. 3155-3167

[22] Hardisty J. A note on negative beach slopes and flow asymmetry. Marine Geology. 1985;**69**:203-206

[23] Hardisty J. A morphodynamic model for beach gradients. Earth Surface Processes and Landforms. 1986; **11**:327-333

[24] Dean RG. Equilibrium beach profiles: Characteristics and applications. Journal of Coastal Research. 1991;7(1):53-84

[25] Dean RG, Dalrymple RA. Coastal Processes with Engineering Applications. New York, NY: Cambridge University Press; 2002. p. 474

[26] Larson M, Kraus NC, Wise RA. A equilibrium beach profiles under breaking and non-breaking waves. Coastal Engineering. 1999;**36**:59-85

[27] Komar PD, Inman DL. Longshore sand transport on beaches. Journal of Geophysical Research. 1970;**75**: 5914-5927

[28] Sakai K, Uda T, Serizawa M, Kumada T, Kanda Y. Model for predicting three-dimensional sea bottom topography of statically stable beach. In: Proceedinsg of 30th ICCE; 2006. pp. 3184-3196

[29] Uda T, Serizawa M, San-nami T, Furuike K. Model for predicting dynamically stable beach based on analogy with two-dimensional potential flow. In: Proceedings of 30th ICCE; 2006. pp. 3911-3923

[30] CERC. Shore Protection Manual. Vicksburg, Mississippi: U.S. Army Coastal Engineering Research Center, Corps of Engineers

[31] Komar PD. Beach Processes and Sedimentation. London: Prentice Hall International; 1998. p. 544

[32] Horikawa K, editor. Nearshore Dynamics and Coastal Processes. Tokyo: University of Tokyo Press; 1988. p. 522

Chapter 3

Eight Types of BG Models and Discretization

Takaaki Uda, Masumi Serizawa and Shiho Miyahara

Abstract

Eight types of the BG models are introduced in this chapter. The Type 1 is a model using wave parameters at the breaking point. In the Type 2, the effect of longshore sand transport due to the effect of the longshore gradient of breaker height is included with an additional term given by Ozasa and Brampton. In the Type 3, the intensity of sand transport P is assumed to be proportional to the third power of the amplitude of the bottom oscillatory velocity u_{m} due to waves, and in the Type 4, P is given by the wave energy dissipation rate due to wave breaking at a local point. In the Type 5, wave power is calculated using the coordinate system different from that for the calculation of beach changes to predict the topographic changes of an island or a cuspate foreland in a shallow water body under the action of waves randomly incident from every direction. In the Type 6, the height of wind waves is predicted using Wilson's formula using the wind fetch distance and wind velocity, and then sand transport fluxes are calculated. The Type 7 is a model for predicting the formation of the ebb-tidal delta under the combined effect of waves and ebb-tidal currents with an analogy of the velocity distribution of ebb-tidal currents to the wave diffraction coefficient, which can be calculated by the angular spreading method for irregular waves. In the Type 8, the effect of the nearshore currents induced by forced wave breaking is incorporated into the model by calculating the nearshore currents, taking both the wave field and the current velocity at a local point into account.

Keywords: eight types of BG models, discretization method

1. Introduction

Eight types of the BG models to be used in the following chapters are introduced (**Table 1**). The Type 1 is a model using wave parameters at the breaking point. In the Type 2, the effect of longshore sand transport due to the effect of the longshore gradient of breaker height is included with an additional term given by Ozasa and Brampton [1], whereas the sand transport equations with the coefficients of longshore and cross-shore sand transport are employed. In the Type 3, the intensity of sand transport, P, is assumed to be proportional to the third power of the amplitude of the bottom oscillatory velocity, u_{m}, due to waves predicted in the calculation of the plane wave field. In the Type 4, P is given by the wave energy dissipation rate due to wave breaking at a local point. To calculate the wave field, a numerical simulation method using the energy balance equation is employed. In the Type 5, wave power is calculated using the coordinate system different from that

Type	External force	Characteristics	Application	Chapter
1	Waves	Most fundamental model using wave parameters at breaking point	Prediction of typical beach changes in coastal engineering	3
2	Waves	The effect of longshore sand transport due to the effect of the longshore gradient of breaker height was included with an additional term given by Ozasa and Brampton [1]	Prediction of beach changes by human activities	3
3	Waves	The intensity of sand transport P is assumed to be proportional to the third power of the amplitude of the bottom oscillatory velocity, u_m, due to waves predicted in the calculation of the plane wave field	Formation of sand spit and bay barrier	5
4	Waves	The intensity of sand transport P is given by the wave energy dissipation rate due to wave breaking at a local point	Formation of cuspate foreland	7
5	Waves	The wave power is calculated using the coordinate system different from that for the calculation of beach changes under the action of waves randomly incident from every direction	Formation of sand spit and bay barrier and interaction of sandy islands on flat shallow seabed owing to waves	5 and 6
6	Wind waves developed in closed water body	The height of wind waves is predicted using Wilson's formula given the wind fetch distance and wind velocity	Segmentation and merging of closed water bodies by wind waves	8
7	Waves and ebb-tidal currents	A model for predicting the formation of the ebb-tidal delta under the combined effect of waves and ebb-tidal currents with an analogy of the velocity distribution of ebb-tidal currents to the wave diffraction coefficient	Formation of dynamically stable ebb-tidal delta	4
8	Waves and nearshore currents	The effect of the nearshore currents induced by forced wave breaking is incorporated into the model, taking both the wave field and the current velocity at a local point into account	Beach changes around artificial reef	4

Table 1.
Eight types of BG models and their applications.

for the calculation of beach changes in order to predict the topographic changes of an island or a cuspate foreland in a shallow water body under the action of waves randomly incident from every direction. In the Type 6, the height of wind waves is predicted using Wilson's formula given the wind fetch distance and wind velocity, and the segmentation of a closed water body is predicted. The Type 7 is a model for predicting the formation of the ebb-tidal delta under the combined effect of waves and ebb-tidal currents with an analogy of the velocity distribution of ebb-tidal currents to the wave diffraction coefficient, which is calculated by the angular

spreading method for irregular waves. In the Type 8, the effect of the nearshore currents induced by forced wave breaking is incorporated into the model by calculating the nearshore currents, taking both the wave field and the current velocity at a local point into account.

2. Eight types of BG models

2.1 Type 1 BG model

A simple, practical Type 1 BG model is derived here using wave parameters at the breaking point on the basis of Eq. (26) in Chapter 1. The energy dissipation ratio Φ is evaluated by the energy flux of waves at the breaking point as in the contour-line change model [2]. Assume that waves are obliquely incident to a coast with a uniform slope of $\tan\overline{\beta}$. Φ is given by the wave energy flux transported per unit width of the shoreline, $(EC_g)_b \cos\alpha_b$, divided by the cross-shore distance $R = (h_c + h_R)/\tan\overline{\beta}$ between the depth of closure, h_c, and the berm height, h_R, corresponding to the wave run-up height (**Figure 1**). Then, assuming $\tan\overline{\beta} \approx \tan\beta_c \cos\alpha_b$ (Eq. (32) in Chapter 1), Φ becomes $(EC_g)_b \cos^2\alpha_b/(h_c + h_R)/\tan\beta_c$. Furthermore, introducing the depth distribution of the sand transport intensity $\varepsilon(Z)$ and transforming $1/(h_c + h_R)$ into $\varepsilon(Z)$, the coefficient A of Eq. (23) in Chapter 1 is expressed in terms of the wave energy flux at the breaking point, and the sand transport flux is reduced to

$$\vec{q} = \frac{G}{\tan\beta_c}\left[\tan\beta_c \vec{e_w} - \vec{\nabla}Z\right]. \tag{1}$$

Eq. (1) can be written in components as Eqs. (2a) and (2b), and G in Eq. (1) is expressed by Eqs. (3) and (4):

$$q_x = \frac{G}{\tan\beta_c}\left[\tan\beta_c \cos\theta_w - \partial Z/\partial x\right] \tag{2a}$$

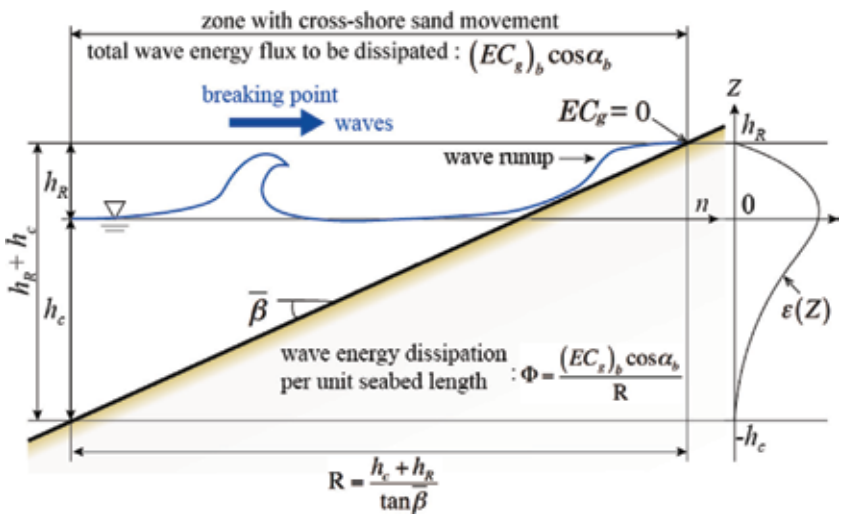

Figure 1.
Zone with cross-shore sand movement and dissipation of wave energy.

$$q_y = \frac{G}{\tan\beta_c}\left[\ \tan\beta_c \sin\theta_w - \partial Z/\partial y\ \right] \tag{2b}$$

$$G = C_0 K_1 P \tag{3}$$

$$P = \Phi = \varepsilon(Z)\left(EC_g\right)_b \cos^2\alpha_b \tan\beta_c \tag{4}$$

$$\int_{-h_c}^{h_R} \varepsilon(Z)\, dZ = 1 \tag{5}$$

$$\varepsilon(Z) = \begin{cases} \dfrac{2}{h_c^3}\left(\dfrac{h_c}{2} - Z\right)(Z + h_c)^2 & (-h_c \le Z \le h_R) \\ 0 & (Z < -h_c, h_R < Z) \end{cases} \tag{6}$$

Here, $\varepsilon(Z)$ is defined so that the integral over the depth between $Z = -h_c$ and h_R is equal to 1, as given by Eq. (5), and the depth distribution of the longshore sand transport, Eq. (6), given by Uda and Kawano [3] is used. This distribution takes a peak value on the shoreline ($Z = 0$), and it monotonically decreases landward and seaward. In addition, when it is given by a uniform distribution, Eq. (7) can be used:

$$\varepsilon(Z) = \begin{cases} 1/(h_c + h_R) & (-h_c \le Z \le h_R) \\ 0 & (Z < -h_c, h_R < Z) \end{cases} \tag{7}$$

The wave energy flux at the breaking point $(EC_g)_b$ can be calculated by small-amplitude wave theory in shallow water using the breaker height H_b, where H_b is given by the following relation:

$$\left(EC_g\right)_b = C_1 (H_b)^{\frac{5}{2}} \tag{8a}$$

$$C_1 = \frac{\rho g}{k_1}\sqrt{g/\gamma} \qquad (\gamma \approx 0.8) \tag{8b}$$

$$k_1 = \begin{cases} 8 & \text{for regular waves} \\ (4.004)^2 & \text{for irregular waves} \end{cases} \tag{8c}$$

Here, γ is the ratio of the breaker height to the water depth. $k_1 = (4.004)^2$ in Eq. (8c) is a constant in the relationship between the wave energy E and the significant wave height when the probability of the wave height of irregular waves is assumed to be given by the Rayleigh distribution [4]. Furthermore, regarding the breaker angle α_b in Eq. (4), the following approximation is assumed:

$$\begin{aligned} \alpha_b \approx \alpha &= \theta_w - \theta_n \\ &= \theta_w - \tan^{-1}\left(\frac{\partial Z}{\partial y} \Big/ \frac{\partial Z}{\partial x}\right) \end{aligned} \tag{9}$$

Here, α is the angle between the wave direction at each point θ_w and the direction (shoreward positive) normal to the contours θ_n as expressed by Eq. (12) in Chapter 1. In a numerical simulation, the mean beach slope of the coast before the construction of the structures is given as the equilibrium slope to consider the long-term prediction of beach changes, similarly to the contour-line change model [2]. Here, the measured slope is employed as the equilibrium slope to make the prediction of beach changes on real coasts possible. The measured slope is given a priori because the real seabed topography includes every effect of past events, and it has a stable form, except for seasonal short-period variations, in the long term.

In the calculation, the coastal domain is discretized using 2D elements with widths Δx and Δy. The calculation points of the seabed elevation Z and sand transport rates $\vec{q} = (q_x, q_y)$ are set in staggered meshes with a difference of 1/2 mesh. The explicit finite-difference method is used in the calculation. **Figure 2** shows the flowchart for numerical simulation using the Type 1.

Given the initial seabed topography, the distribution of H_b, α_b, h_c, and h_R, and the equilibrium slope, sand transport fluxes and the change in seabed elevation after time Δt are calculated using Eq. (2) and Eq. (28) in Chapter 1, respectively. These procedures are repeated recurrently. As the boundary conditions, sand transport is set to 0 along the outer boundaries of the calculation domain and the boundary along the structures. Here, a lower minimum of 0.5 was set for $|\cos\alpha_b|$ in the calculation of P value in Eq. (4) to avoid the occurrence of a local discontinuity in the topography.

In the calculation of beach changes in the wave-shelter zone behind an offshore breakwater, the wave diffraction coefficient K_d and the direction of diffracted waves θ_d are predicted using the angular spreading method for irregular waves [5, 6], and $(EC_g)_b$ in the case of no offshore structure is reduced by multiplying by the square of the coefficient K_d so that a relation of $(EC_g)_b' = K_d^2(EC_g)_b$ is satisfied. On the other hand, the direction of the diffracted waves θ_d is used as the wave

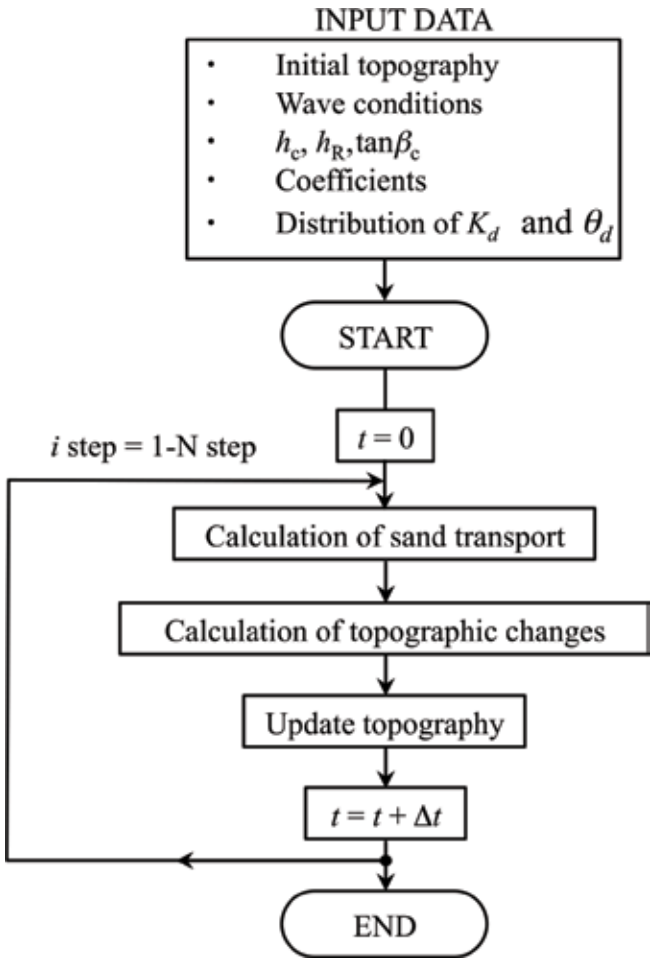

Figure 2.
Flowchart for numerical calculation using Typ. 1 BG model.

direction θ_w to evaluate the wave energy flux at any point. In addition, the effect of the longshore sand transport induced by a longshore change in the breaker height as given by Ozasa and Brampton [1] can be included using the method in [5], although the term expressing this effect is not included in the sand transport equation of the Type 1 BG model. In the method, the wave direction, θ_w, in the wave-shelter zone is modified in response to the ratio of the coefficients of longshore sand transport, K_2/K_1, and the longshore gradient of the wave height H_b multiplied by K_d. When modified wave directions are employed in the sand transport equation, the additional effect given by Ozasa and Brampton [1] in the CERC-type longshore sand transport formula can be implicitly included [5].

2.2 Type 2 BG model

In the Type 1 BG model, the fundamental equation for sand transport is expressed in terms of the wave energy at the breaking point. In the Type 2 BG model, the equation in the Type 1 is improved to an equation including the coefficients of longshore and cross-shore sand transports and the additional term given by Ozasa and Brampton [1] to evaluate the effect of the longshore gradient of the breaker height.

We use the Cartesian coordinates (x, y), in which the x- and y-axes are taken in the cross-shore (shoreward positive) and longshore directions, respectively. For the sand transport equation, Eq. (10), expressed in terms of the wave energy at the breaking point, is used with the variables given by Eq. (11) together with Eq. (4):

$$q_x = \frac{G_x}{\tan\beta_c}\left[\ \tan\beta_c \cos\theta_w - \partial Z/\partial x\ \right] \qquad (-h_c \le Z \le h_R) \tag{10a}$$

$$q_y = \frac{G_y}{\tan\beta_c}\left[\ \tan\beta_c\left(\sin\theta_w - \frac{1}{\tan\overline{\beta}}\frac{K_2}{K_y}\frac{\partial H_b}{\partial y}\right) - \partial Z/\partial y\ \right] \qquad (-h_c \le Z \le h_R) \tag{10b}$$

$$G_x = C_0 K_x P \tag{11a}$$

$$G_y = C_0 K_y P \tag{11b}$$

Here, θ_w is the wave angle measured counterclockwise from the x-axis. K_x and K_y are the coefficients of cross-shore and longshore sand transport, respectively, K_2 is the coefficient of the term given by Ozasa and Brampton [1], and $\tan\overline{\beta}$ is the seabed slope at the breaker point. Here, we assume $\tan\overline{\beta} = \tan\beta_c$. $\varepsilon(Z)$ is the depth distribution of the intensity of longshore sand transport, as defined by Eq. (6) or (7) in the Type 1. Beach changes are obtained by solving the continuity equation. The flowchart for numerical simulation using the Type 2 is the same as that in the Type 1, as shown in **Figure 2**.

Note that the x- and y-axes must be taken shoreward from an offshore point and in longshore direction, respectively, although the sand transport equations of the Type 1 do not depend on the directions of the orthogonal coordinates (x, y). Regarding h_R and h_c, the K_d value is also multiplied to cover the reduction in wave height if necessary.

2.3 Type 3 BG model

The Type 3 BG model is employed in the calculation of the formation of a sand spit and a bay barrier to be described in Chapter 5. Although the sand transport

equations in the Types 1 and 2 BG model are expressed by using the wave energy flux at the breaking point, the sand transport equation in the Type 3 is expressed using local wave parameters which can be evaluated from the calculation of the plane wave field. Because a sand spit and cuspate foreland may change their configuration significantly, their effects on the wave refraction, wave breaking, and the wave-sheltering effect must be calculated by the recurrent calculations to evaluate the time changes in the wave field. The additional term given by Ozasa and Brampton [1] is also incorporated into the fundamental equation of the BG model to evaluate the longshore sand transport due to the effect of the longshore gradient of the wave height with the inclusion of two coefficients to evaluate the cross-shore and longshore sand transports. The fundamental equation is given by

$$\vec{q} = C_0 \frac{P}{\tan\beta_c} \left\{ \begin{array}{l} K_n \left(\tan\beta_c \vec{e_w} - |\cos\alpha| \overrightarrow{\nabla Z} \right) \\ + \left\{ (K_s - K_n)\sin\alpha - \dfrac{K_2}{\tan\overline{\beta}} \dfrac{\partial H}{\partial s} \right\} \tan\beta \vec{e_s} \end{array} \right\} \quad (12)$$

$$(-h_c \le Z \le h_R)$$

$$P = \rho\, u_m^3 \quad (13)$$

$$u_m = \frac{H}{2}\sqrt{\frac{g}{h}}. \quad (14)$$

Here, $\tan\beta\ \vec{e_s} = (-\partial Z/\partial y, \partial Z/\partial x)$, K_s and K_n are the coefficients of longshore sand transport and cross-shore sand transport, respectively, $\partial H/\partial s = \vec{e_s} \cdot \overrightarrow{\nabla H}$ is the longshore gradient of the wave height H measured parallel to the contour lines, and $\overrightarrow{\nabla H} = (\partial H/\partial x, \partial H/\partial y)$. $\tan\overline{\beta}$ is the characteristic slope of the breaker zone, and h is the water depth. Furthermore, $\tan\overline{\beta} = \tan\beta_c$ is assumed. u_m is the amplitude of the seabed velocity due to the orbital motion of waves given by Eq. (14).

The intensity of sand transport P in Eq. (12) is assumed to be proportional to the wave energy dissipation rate Φ based on the energetics approach of Bagnold [7]. In the Type 1, P is formulated using the wave energy at the breaking point, but here it is combined with the wave characteristics at a local point. Bailard and Inman [8] used the relationship $\Phi_t = \tau u_t = \rho C_f u_t^3$ for the instantaneous wave energy dissipation rate Φ_t to derive their sand transport equation, where τ is the bottom shear stress, u_t is the instantaneous velocity, and C_f is the drag coefficient. We basically follow their study but assume that Φ is proportional to the third power of the amplitude of the bottom oscillatory velocity u_m due to waves instead of the third power of the instantaneous velocity. The intensity of sand transport P is then given by Eq. (13), and its coefficient is assumed to be included in the coefficients of longshore and cross-shore sand transports, K_s and K_n in Eq. (12), respectively. u_m can be calculated by small-amplitude wave theory in shallow water using the wave height H at a local point in Eq. (14), which can be obtained by the numerical calculation of the plane wave field. h_c is assumed to be proportional to the wave height H at a local point and is given by Eq. (15), referring to the relationship given by Uda and Kawano [3]:

$$h_c = KH \qquad (K = 2.5) \quad (15)$$

In the numerical simulation of beach changes, the sand transport equation and the continuity equation are solved on the x-y plane by the explicit finite-difference method employing a staggered mesh scheme.

The wave field is calculated using the energy balance equation given by Mase [9], in which the directional spectrum $D(f, \theta)$ of the irregular waves is the variable to be solved, with the energy dissipation term due to wave breaking in [10]. Here, f and θ are the frequency and wave direction, respectively. In this method, wave refraction, wave breaking, and wave diffraction in the wave-shelter zone can be calculated with a small calculation load. The energy dissipation term due to wave breaking Φ, which is incorporated into the energy balance equation of Eq. (16), is given by Eq. (17):

$$\frac{\partial}{\partial x}(DV_x) + \frac{\partial}{\partial y}(DV_y) + \frac{\partial}{\partial \theta}(DV_\theta) = F - \Phi \tag{16}$$

$$\Phi = (K/h)\, DC_g \left[1 - (\Gamma/\gamma)^2 \right] \qquad (\Phi \geq 0) \tag{17}$$

Here, D is the directional spectrum, (V_x, V_y, V_θ) is the energy transport velocity in the (x, y, θ) space, F is the wave diffraction term in [9], K is the coefficient of the wave-breaking intensity, h is the water depth, C_g is the wave group velocity ($C_g \approx \sqrt{gh}$ in shallow-water wave theory), Γ is the ratio of the critical breaker height to the water depth on the horizontal bed, and γ is the ratio of the wave height to the water depth. As the spectrum of the incident waves, a combination of the Bretschneider-Mitsuyasu-type frequency spectrum and the Mitsuyasu-type directional function is used as in Goda [11]. **Figure 3** shows the flowchart for numerical simulation using the Type 3.

To prevent the location where the berm develops from being excessively seaward compared with that observed in the experiment or the field, a lower limit is considered for h in Eq. (17). As a result of this procedure, wave decay near the berm top is reduced, resulting in a higher landward sand transport rate. In the calculation of the wave field on land, the imaginary depth h' between the minimum depth h_0 and h_R is considered as follows, similarly to the 3D model of Shimizu et al. [12]:

$$h' = \left(\frac{h_R - Z}{h_R + h_0} \right)^r h_0 \qquad (r = 1) \qquad (-h_0 \leq Z \leq h_R). \tag{18}$$

In addition, at locations whose elevation is higher than h_R, the wave energy is set to 0. Similarly to the Type 1, beach changes are obtained by solving the continuity equation. In the calculation of the formation of a bay barrier in [13], the sand transport equation without Ozasa and Brampton's term in Eq. (12) is employed, i.e., $K_2 = 0$, and in the calculation of the P value in Eq. (12), Eq. (13) multiplied by the coefficient F expressed by Eq. (20) is employed:

$$P = F \cdot \rho\, u_m^3 \tag{19}$$

$$F = \frac{\tan \beta_w}{\tan \beta_c} \tag{20}$$

$$\tan \beta_w = \vec{e_w} \bullet \vec{\nabla} Z \qquad (\tan \beta_w \geq 0) \tag{21}$$

Here, $\tan\beta_w$ is the seabed slope measured along the direction of wave propagation. In Eq. (19), F is introduced so that the wave dissipation rate can respond to the seabed slope when the wave dissipation in the surf zone is considered.

Eq. (12) shows that the sand transport flux can be expressed as the sum of the component along the wave direction and the components due to the effect of gravity normal to the contours and the effect of longshore currents parallel to the

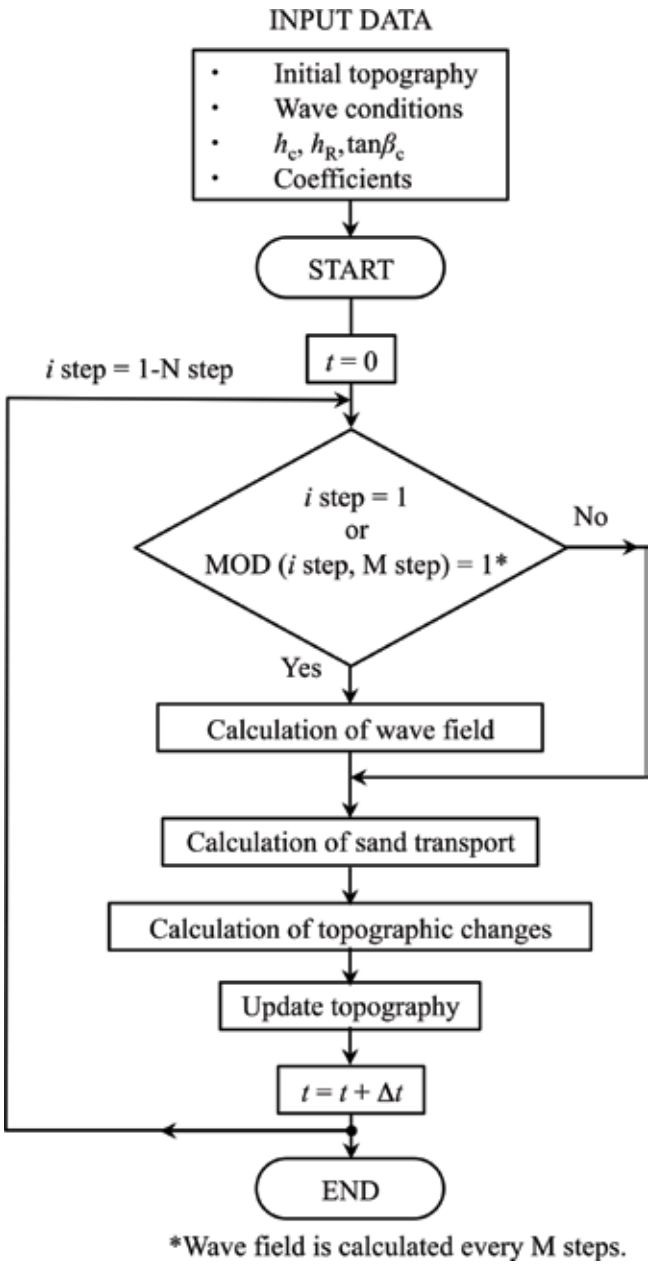

Figure 3.
Flowchart for numerical calculation using the Typ. 3 BG model.

contours. To investigate the physical meaning of Eq. (12), neglecting the additional term given by Ozasa and Brampton [1], that is, assuming $K_2 = 0$ in Eq. (12), Eqs. (22) and (23) are derived for the cross-shore and longshore components of sand transport, q_n and q_s, respectively. Furthermore, under the condition that the seabed slope is equal to the equilibrium slope, Eq. (23) reduces to Eq. (24):

$$q_n = \vec{e_n} \bullet \vec{q} = C_0 K_n P |\cos\alpha| \left(\frac{\cos\alpha}{|\cos\alpha|} - \frac{\tan\beta}{\tan\beta_c} \right) \tag{22}$$

$$q_s = \vec{e_s} \bullet \vec{q} = C_0 K_s P \sin\alpha \left\{ \frac{\tan\beta}{\tan\beta_c} + \frac{K_n}{K_s}\left(1 - \frac{\tan\beta}{\tan\beta_c}\right)\right\} \tag{23}$$

$$q_s \approx C_0 K_s P \sin\alpha \qquad (\because \tan\beta \approx \tan\beta_c) \tag{24}$$

In Eq. (22), the cross-shore sand transport q_n becomes 0 when the local seabed slope is equal to the equilibrium slope, and the longshore sand transport q_s becomes 0 when the wave direction coincides with the normal to the contour lines, as shown in Eqs. (23) and (24). When a discrepancy from these conditions arises, sand transport is generated by the same stabilization mechanism as that given by the sand transport equation in the Type 1.

Comparing Eqs. (22) and (24) in the Type 3 with Eqs. (31) and (34) in Chapter 1, which are the fundamental equations for the cross-shore and longshore components of sand transport in the Type 1, the sand transport equations in the Type 1 have a single coefficient, whereas the equations in the Type 3 are expressed using two coefficients, i.e., the intensities of cross-shore and longshore sand transports can be independently determined. The equilibrium slope $\tan\beta'_c$, which gives q_n = 0 under the condition of oblique wave incidence, satisfies the relation $\tan\beta'_c = \tan\beta_c \cos\alpha$ in the Type 1, as in Eq. (33) in Chapter 1, and $\tan\beta'_c$ is affected by α. On the other hand, in the Type 3, the relation $\tan\beta'_c = \tan\beta_c$ stands after setting q_n = 0 in Eq. (22). Thus, $\tan\beta'_c$ is independent of α. This is a result of multiplying $\vec{\nabla Z}$ in the sand transport equation of Eq. (13) in the Type 3 by the coefficient $|\cos\alpha|$, assuming that the effect of gravity is proportional to the magnitude of the cross-slope velocity component that is generated by waves, similarly to the bedload equation of Dronkers [14].

Taking the above into account, the first term in the parentheses in Eq. (12) gives the sand transport in the case that the rates of longshore and cross-shore sand transports are equal (K_s = K_n), and the second term is the additional longshore sand transport in the case that the rates are different (K_s > K_n). The physical meaning of the second term is that longshore sand transport is generated by the small angular shift that occurs when the wave direction is incompletely reversed in the oscillatory movement due to waves, and the second term also models the additional longshore sand transport due to the effect of longshore currents, which is only partially included in the first term.

2.4 Type 4 BG model

This model is used for the calculation of the development of sand spits and cuspate forelands with rhythmic shapes and the formation of a cuspate foreland in Chapter 7. Although the intensity of sand transport P in the Type 3 was assumed to be proportional to the third power of the amplitude of the bottom oscillatory velocity, u_m, due to waves, as shown in Eq. (13), P was given by the wave energy dissipation rate Φ_b due to wave breaking at a local point in the Type 4, which can be determined by the calculation of the plane wave field:

$$P = \Phi_b \tag{25}$$

To calculate the wave field, the numerical simulation method using the energy balance equation given by Mase [9], in which the directional spectrum of irregular waves is the variable to be solved, is employed, similarly to the Type 3, with an additional term of energy dissipation due to wave breaking [10], similarly to Eq. (16). Φ_b in Eq. (25) is calculated using Eq. (26), which defines the sum of the energy dissipation of each component wave due to breaking:

$$P = \Phi_{\mathrm{b}} = f_D E = K\sqrt{g/h}\left[1 - (\Gamma/\gamma)^2\right]E \qquad (P \geq 0) \tag{26}$$

Here, f_D is the energy dissipation rate, E is the wave energy, K is a coefficient expressing the intensity of wave dissipation due to breaking, h is the water depth, Γ is the ratio of the critical wave height to the water depth on a flat bottom, and γ is the ratio of the wave height to the water depth H/h. In addition, similarly to the calculation in the Type 3, a lower limit is set for the water depth h in Eq. (18) in the calculation of the plane wave field. To calculate the wave field in the wave run-up zone, an imaginary depth is assumed, similarly to the Type 3. Furthermore, the wave energy at locations with elevations higher than h_{R} is set to 0. The flowchart for numerical simulation using the Type 4 is the same as that in the Type 3, as shown in **Figure 3**.

When investigating the physical meaning of Eq. (12) in the Type 3, the effect of the additional term given by Ozasa and Brampton [1] was neglected. Here, the effect of the additional term is included, and Eq. (27) is derived for the longshore component of sand transport, q_s, along with Eq. (22) for the cross-shore component of sand transport, q_n. In addition, under the condition that the seabed slope is equal to the equilibrium slope, Eq. (27) reduces to Eq. (28):

$$\begin{aligned} q_s &= \vec{e_s} \bullet \vec{q} \\ &= C_0 K_s P\left\{\frac{\tan\beta}{\tan\beta_{\mathrm{c}}}\left(\sin\alpha - \frac{K_2}{K_s}\frac{1}{\tan\overline{\beta}}\frac{\partial H}{\partial s}\right) + \sin\alpha\frac{K_n}{K_s}\left(1 - \frac{\tan\beta}{\tan\beta_{\mathrm{c}}}\right)\right\} \end{aligned} \tag{27}$$

$$q_s = C_0 K_s P\left(\sin\alpha - \frac{K_2}{K_s}\frac{1}{\tan\overline{\beta}}\frac{\partial H}{\partial s}\right) \qquad (\because \tan\beta \approx \tan\beta_{\mathrm{c}}) \tag{28}$$

The cross-shore sand transport q_n is the same as Eq. (22) in the Type 3, whereas the longshore sand transport q_s given by Eqs. (27) and (28) has the additional term of Ozasa and Brampton [1]. When the total sand transport Q_s is calculated by integrating Eq. (28) in the cross-shore direction, it coincides with the CERC-type formula [15] with the additional term [1] as in Eq. (29) [4]. Here, the relation $P = \Phi_{\mathrm{b}}$ (Eq. (25)) is employed, α is approximately given by the breaker angle α_b, and the longshore gradient of the breaker height is used in place of the longshore gradient of the wave height in the Ozasa and Brampton's term together with the assumption that the integral of Φ in the cross-shore direction is equal to the energy flux per unit length of the coastline at the breaking point:

$$\begin{aligned} Q_s &= \int q_s dn \\ &= C_0 K_s \int\left\{P\left(\sin\alpha - \frac{K_2}{K_s}\frac{1}{\tan\overline{\beta}}\frac{\partial H}{\partial s}\right)\right\}dn \\ &= C_0 K_s \int\left\{\Phi_{\mathrm{b}}\left(\sin\alpha - \frac{K_2}{K_s}\frac{1}{\tan\overline{\beta}}\frac{\partial H}{\partial s}\right)\right\}dn \quad (\because P = \Phi_{\mathrm{b}}) \\ &= C_0 K_s\left\{\sin\alpha_{\mathrm{b}} - \frac{K_2}{K_s}\frac{1}{\tan\overline{\beta}}\frac{\partial H_{\mathrm{b}}}{\partial s}\right\}\int \Phi_{\mathrm{b}}\, dn \quad \left(\because \alpha \approx \alpha_{\mathrm{b}}, \frac{\partial H}{\partial s} \approx \frac{\partial H_{\mathrm{b}}}{\partial s}\right) \\ &= C_0 K_s (EC_g)_{\mathrm{b}}\cos\alpha_{\mathrm{b}}\left\{\sin\alpha_{\mathrm{b}} - \frac{K_2}{K_s}\frac{1}{\tan\overline{\beta}}\frac{\partial H_{\mathrm{b}}}{\partial s}\right\} \\ &\qquad \left(\because \int \Phi_{\mathrm{b}}\, dn \approx (EC_g)_{\mathrm{b}}\cos\alpha_{\mathrm{b}}\right) \end{aligned} \tag{29}$$

2.5 Type 5 BG model

To predict the topographic changes of an island or a cuspate foreland in a shallow water body under the action of waves randomly incident from every direction, the wave power P is calculated using a coordinate system different from that for the calculation of beach changes, assuming that waves propagate in a straight line by neglecting the effect of the wave refraction. Since the wave field itself significantly changes with time in response to the deformation of the topography, the calculation of the wave power P and beach changes is carried out recurrently every time step. This model is employed in the numerical simulation of the elongation and merging of bay mouth sand spits in Chapter 5 and the interaction of islands in Chapter 6.

The sand transport equation employed is Eq. (30), which uses the expression of the wave energy evaluated at the breaking point. The variables in Eq. (30) are given by Eqs. (31)–(36) along with Eqs. (5), (7), (8), and (9) in the Type 1 BG model:

$$\vec{q} = C_0 \frac{K_s P}{\tan\beta_c} \left\{ \tan\beta_c \, \vec{e_w} - |\cos\alpha| \, \overrightarrow{\nabla Z} \right\} \quad (-h_c \le Z \le h_R) \tag{30}$$

$$P = \varepsilon(Z) \left(EC_g\right)_b \tan\beta_w \quad (P \ge 0) \tag{31}$$

$$\tan\beta_w = dZ/dx_w \quad (\tan\beta_w \ge 0) \tag{32}$$

$$I_\varepsilon(Z) = \begin{cases} 1 & (Z < -h_c) \\ \int_Z^{h_R} \varepsilon(Z)\, dZ = \dfrac{h_R - Z}{h_c + h_R} & (-h_c \le Z \le h_R) \\ 0 & (Z > h_R) \end{cases} \tag{33}$$

$$P = \left(EC_g\right)_b \left(-\frac{dI_\varepsilon}{dx_w} \right) \quad (P \ge 0) \tag{34}$$

$$I_\varepsilon{}^{(i+1)} = \min\left(\text{Eq.}(33)\Big|^{Z=Z^{(i+1)}}, \; I_\varepsilon{}^{(i)} \right) \tag{35}$$

$$P^{(i+1/2)} = \left(EC_g\right)_b \left(\frac{I_\varepsilon{}^{(i)} - I_\varepsilon{}^{(i+1)}}{\Delta x_w} \right) \tag{36}$$

Here, K_s is the longshore and cross-shore sand transport coefficients, and the index i in Eqs. (35) and (36) is the mesh number along the x_w-axis, and min denotes the selection of the smaller of either value in the parentheses. In the calculation, the local beach slope measured along the wave ray is used as the beach slope in Eq. (31), as shown in Eq. (32).

For the calculation of the P value, another coordinate system different from that for the calculation of beach changes is used as in [16], in which the x_w- and y_w-axes are taken along the wave direction and the direction normal to the wave direction, respectively (**Figure 4**). The fixed coordinate system (x, y) is used for the calculation of beach changes with a rectangular calculation domain ABCD, whereas the P value is calculated in the rectangular domain A′B′C′D′ including the domain ABCD with the coordinate system (x_w, y_w). In the calculation of the wave field, wave refraction is neglected, and waves are assumed to propagate in a straight line while maintaining the wave incident angle. The distance along the x_w-axis is subdivided by a mesh of Δx_w, and a cumulative function of $\varepsilon(Z)$, $I_\varepsilon(Z)$, is introduced as in Eq. (33). Here, $\varepsilon(Z)$ is assumed to have a uniform distribution (Eq. (7)), and $I_\varepsilon(Z)$ takes a value of unity in the zone deeper than h_c, decreases with the water depth, and becomes 0 in the zone higher than h_R.

Using Eq. (33), Eq. (31) is transformed into Eq. (34). Thus, the P value can be determined from the derivative of $I_\varepsilon(Z)$ at a point along the x_w-axis using Eq. (34). $I_\varepsilon(Z)$ is calculated along the x_w-axis from the starting point of wave incidence in the direction of wave propagation; $I_\varepsilon(Z)$ at the $(i + 1)^{\text{th}}$ point can be calculated from Eq. (35) with the given value of $I_\varepsilon(Z)$ at the i^{th} point when the initial value of $I_\varepsilon(Z)$ at the offshore end is given and the mesh location is denoted by $x_w{}^{(i)} = i\Delta x_w$.

Furthermore, the P value at the $(i + 1/2)^{\text{th}}$ point is calculated from Eq. (36), which is derived from Eq. (34). Note that in calculating $I_\varepsilon(Z)$ at the $(i+1)^{\text{th}}$ point, the smaller value calculated from Eq. (35) given the elevation $Z(i+1)$ at the $(i+1)^{\text{th}}$ point and $I_\varepsilon(Z)$ at the i^{th} point is adopted. As a result, the value of $I_\varepsilon(Z)$ corresponding to the minimum water depth (maximum Z) between the offshore end and a designated point along the x_w-axis can be adopted.

Using this procedure, the depth distribution along the x_w-axis between the offshore end and a certain point is automatically taken into account in the calculation of the P value. For example, when there is a location with an elevation higher than h_R, the P value in the shoreward zone is automatically reset as 0 regardless of the elevation and water depth. This procedure becomes important when the beach profile along the x_w-axis has several uneven shapes.

Consider the case where the x_w-axis passes through their tips of two sand spits. The wave energy is reduced when waves pass through near the tip of the first sand spit, resulting in the reduction of the wave energy reaching the second sand spit. Using this procedure, the wave-sheltering effect due to the existence of multiple sand spits can be automatically evaluated, in contrast to the method where the P value is calculated by substituting the local elevation Z into $\varepsilon(Z)$ in Eq. (31). Moreover, the P value on an impermeable breakwater is set to 0 to take the wave-sheltering effect of the breakwater into account. The P value integrated from a location on land whose elevation exceeds h_R to an offshore end along the x_w-axis is always equivalent to $(EC_g)_b$ regardless of the seabed topography. Because $(EC_g)_b$ corresponds to the entire power of the incident waves, the exact satisfaction of this condition is reasonable.

The calculation of the P value is independently carried out along each the x_w-axis. The P value calculated at point (x_w, y_w) is memorized, and the P value at point (x, y) necessary for the calculation of beach changes is interpolated from the

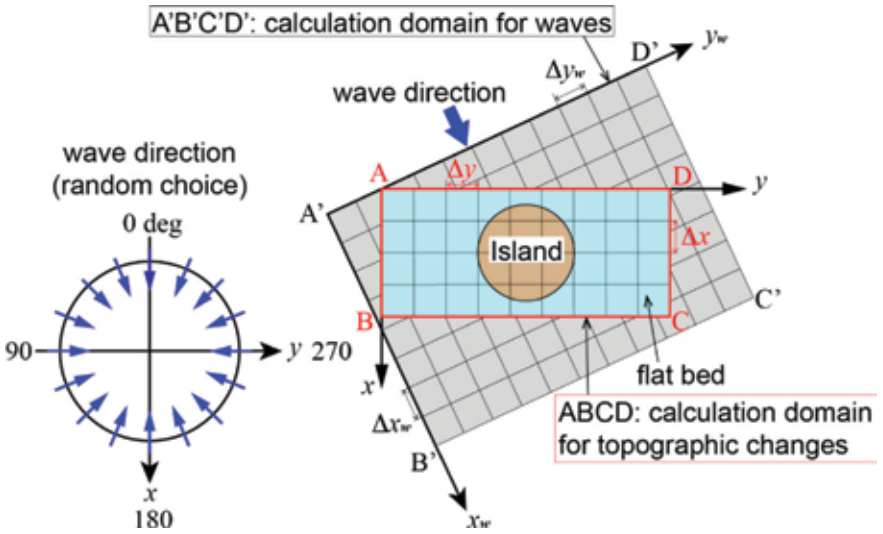

Figure 4.
Definition of coordinate system around an island.

memorized value at point (x_w, y_w). The mesh intervals Δx_w and Δy_w are the same as Δx and Δy. Here, Δx and Δy are the mesh intervals of the coordinate system for the calculation of beach changes, and we assume the equivalent condition of $\Delta x = \Delta y$. The beach changes are calculated by explicitly solving the continuity equations on the staggered meshes using the sand transport fluxes obtained from Eq. (30). **Figure 5** shows the flowchart for numerical simulation using the Type 5 BG model.

The incident wave direction at each time step in the calculation of beach changes is selected to be a value determined randomly so as to satisfy the probability distribution function of the incident wave direction, although the incident wave height is assumed to be constant. For example, in Chapter 5, the energy distribution for multidirectional irregular waves with a directional spreading parameter of $S_{max} = 10$ is used, and in Chapter 6, the wave incidence with the direction ranging between 0 and 360° with the same probability is employed as the probability distribution function of the wave direction. The P value, which is subject to change with the propagation of waves, is recalculated at every time step in the calculation of the beach changes.

2.6 Type 6 BG model

The Type 6 is employed in the numerical simulation of the segmentation of a closed water body, as mentioned in Chapter 8. The height of wind waves in a closed body is predicted using Wilson's formula on the basis of the fetch distance and wind velocity, and then sand transport fluxes are calculated. To calculate the topographic changes in a lake under the action of wind waves randomly incident from all directions, the wave power P is calculated using a coordinate system different from that for the calculation of beach changes. Since the wave field itself significantly changes with time in response to the deformation of the topography, the calculation of the height of the wind waves and beach changes was carried out recurrently every time step.

As the sand transport equation, Eq. (37) is used, which is expressed using the wave energy at the breaking point, similarly to the Type 5. The variables in Eq. (37) are given by Eqs. (38)–(41) along with the relations of Eqs. (6)–(8) in the Type 1 and Eqs. (31) and (32) in the Type 5. Although the P value in Eq. (31) was calculated from Eqs. (33)–(36) in the Type 5, the P value was evaluated directly from Eq. (31) in the Type 6:

$$\vec{q} = C_0 \frac{K_s P}{\tan\beta_c} \left\{ \tan\beta_c \, \vec{e_w} - |\cos\alpha| \, \vec{\nabla Z} \right\} \qquad (-h_c \le Z \le h_R) \tag{37}$$

$$F^{(i+1)} = F^{(i)} + r\Delta x_w \tag{38}$$

$$r = \begin{cases} 1 & (Z \le 0) \\ 0 & (Z > 0) \end{cases} \tag{39}$$

$$F^{(i)} = 0 \quad \text{if} (Z \ge 0 \text{ and } dZ/dx_w \le 0) \tag{40}$$

$$\begin{aligned} H_{1/3} &= f(F, U) \\ &= 0.30 \left\{ 1 - \left[1 + 0.004 \left(gF/U^2 \right)^{1/2} \right]^{-2} \right\} \left(U^2/g \right) \end{aligned} \tag{41}$$

Here, F is the local fetch distance and U is the wind velocity. The index i in Eq. (38) is the mesh number along the x_w-axis. Prior to the calculation of beach changes, the significant wave height at a point is calculated using Wilson's equation

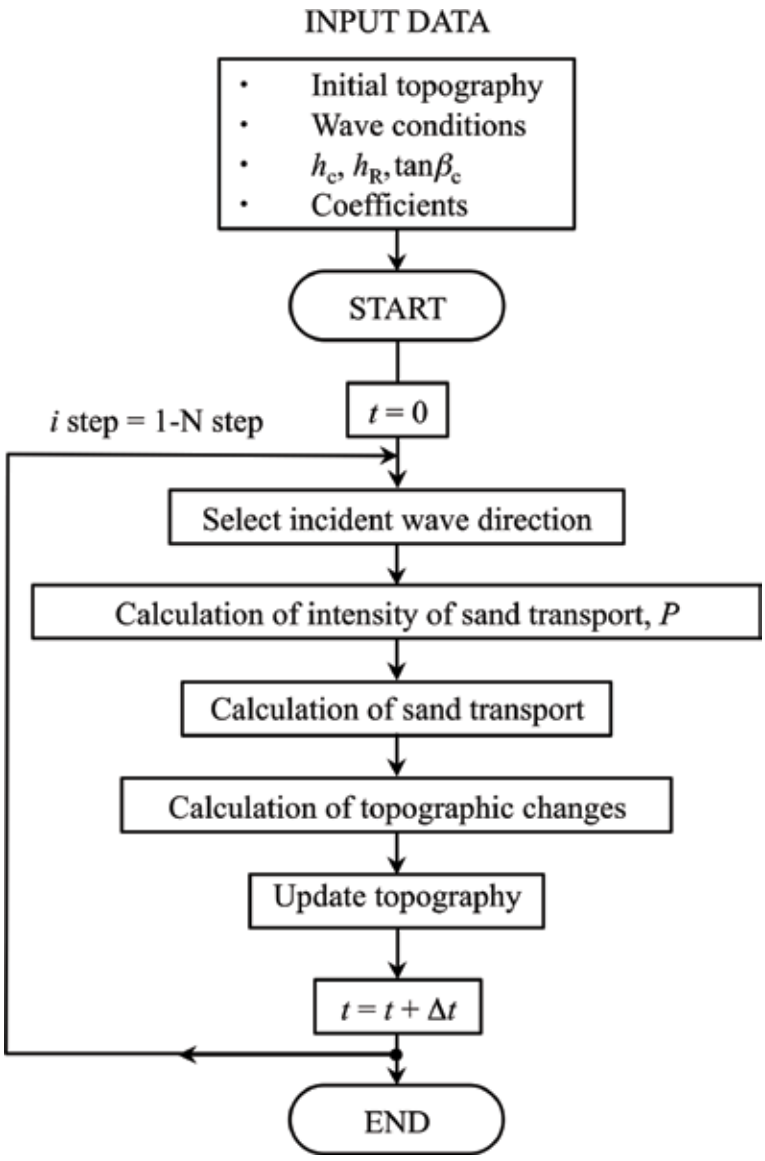

Figure 5.
Flowchart for numerical calculation using Typ. 5 BG model.

(Eq. (41)), described in Wilson [17] and Goda [18], given the local fetch F at a point and wind velocity U.

In this calculation, a fixed coordinate system (x, y) is adopted for the calculation of beach changes with the rectangular calculation domain ABCD, as shown in **Figure 6**, whereas another coordinate system (x_w, y_w) is set corresponding to the wave direction, and the wave height is calculated in the rectangular domain A′B′C′D′ including the domain ABCD.

Neglecting the wave refraction effect, waves are assumed to propagate in the same direction as the wind. The x_w-axis is subdivided by mesh intervals of Δx_w. The fetch F is added from upwind to downwind along the x_w-axis using Eq. (38). When a grid point is located on land and the downslope condition of $dZ/dx_w \leq 0$ is satisfied, the local fetch is reset to $F = 0$ (Eq. (40)). Also we reset F to 0 on structures. When the grid point is located in the lake, F is recalculated. By this

procedure, the wave-sheltering effect by a sand spit or a structure on wind-wave development is taken into account. Then, the significant wave height is calculated with Wilson's [17] equation (Eq. (41)) using the wind fetch F and wind velocity U [18], and this wave height is assumed to be equal to the breaker height. Simultaneously, the wave power P was calculated and assigned to each grid point in the coordinate system (x_w, y_w). The calculation of the P value is independently carried out along each x_w-axis, similarly to the Type 5. The beach changes are calculated by explicitly solving the continuity equations on the staggered meshes using the sand transport fluxes obtained from Eq. (37). The flowchart for numerical simulation using the Type 6 is shown in **Figure** 7.

The wind direction at each time step in the calculation of beach changes is selected to be a value determined randomly so as to satisfy the probability distribution function of the wind direction, although the wind velocity is assumed to be constant. For example, in Chapter 8, wind is assumed to blow uniformly from all directions between 0 and 360°, that is, a symmetric circular distribution, together with the calculation with asymmetric probability distribution of occurrence of wind direction. In every time step of the calculation of beach changes, the wind direction is reset randomly, and the distribution of the P value is recalculated.

2.7 Type 7 BG model

Tung et al. [19] predicted the evolution of ebb-tidal deltas using the Delft 3D model. In their model, the full equations of waves and nearshore and tidal currents were solved to predict three-dimensional bathymetric changes. Beck and Kraus [20] have also carried out the numerical simulation of the development of an ebb-tidal delta by solving the equations of waves and nearshore and ebb-tidal currents. For practical applications, however, the development of a model by which bathymetric changes can be more easily predicted and used to investigate measures against beach erosion is also desirable. Therefore, the model described below was developed [21, 22].

A model for predicting the formation of ebb-tidal deltas under the combined effect of waves and ebb-tidal currents was developed on the basis of the BG model

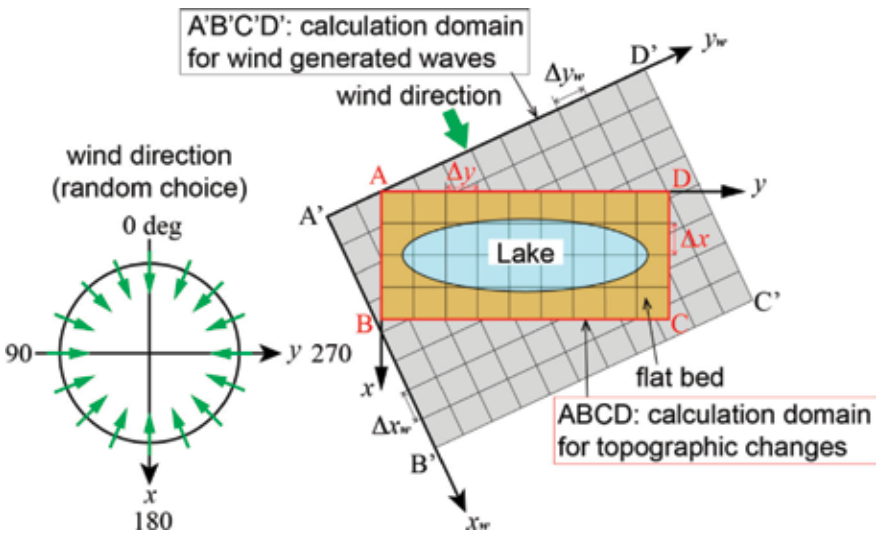

Figure 6.
Definition of two coordinate systems around a lake.

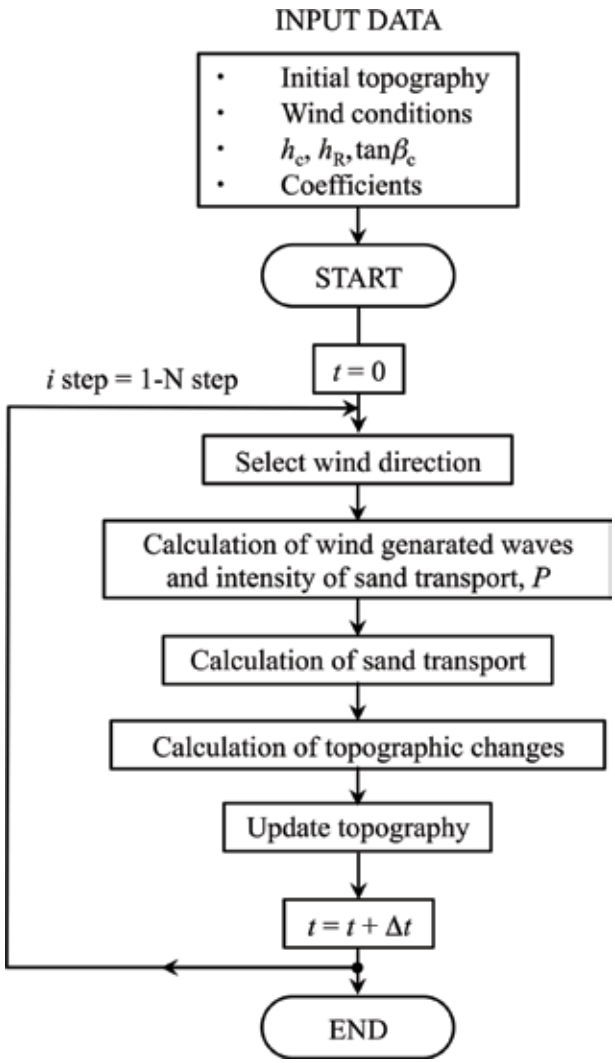

Figure 7.
Flowchart for numerical calculation using Typ. 6 BG model.

[23] with an analogy of the velocity distribution of ebb-tidal currents to the wave diffraction coefficient, which was calculated using the angular spreading method for irregular waves [5, 6].

Assume that the total sand transport $\vec{q}$ is a linear sum of the sand transport due to waves $\vec{q_w}$ and that due to ebb-tidal currents $\vec{q_R}$,

$$\vec{q} = \vec{q_w} + \vec{q_R}. \tag{42}$$

For the equation of sediment transport due to waves, the equation in the Type 1 is improved to take the differences in the intensity of cross-shore and longshore sand transports into account. Consider the Cartesian coordinates (x, y), where the x- and y-coordinates are taken to be the cross-shore distance (positive for shoreward) and longshore distance parallel to the shoreline, respectively. Assume that waves are obliquely incident to a coast with a slope of $\tan\beta$. Then, the net sand transport flux due to waves $\vec{q_w} = (q_{wx}, q_{wy})$ is written as

$$q_{wx} = \frac{G_{wx}}{\tan\beta_c}\left[\ \tan\beta_c \cos\theta_w - \frac{\partial Z}{\partial x}\ \right], \tag{43a}$$

$$q_{wy} = \frac{G_{wy}}{\tan\beta_c}\left[\ \tan\beta_c \sin\theta_w - \frac{\partial Z}{\partial y}\ \right]. \tag{43b}$$

Here, G_{wx} and G_{wy} are given by

$$G_{wx} = C_0 K_x P \tag{44a}$$

$$G_{wy} = C_0 K_y P \tag{44b}$$

Here, q_x is the cross-shore component of the sediment transport flux (positive for shoreward), and q_y is the longshore component of sediment transport flux. K_x and K_y are the coefficients of cross-shore and longshore sand transports, respectively. $\tan\beta_c$ is the equilibrium slope for which zero net cross-shore transport occurs when waves are incident from the direction normal to the slope.

Regarding Eq. (43), Serizawa et al. [21] used the sediment transport equation in the Type 1. This implicitly assumes that the coefficients of cross-shore and longshore sand transports are equivalent. Here, to take the difference in the intensities of cross-shore and longshore sand transport into account, the coefficients of cross-shore and longshore sand transports, K_x and K_y, are determined independently. This equation is the same as the sand transport equation in the Type 2 BG model without the additional term given by Ozasa and Brampton [1].

Regarding the sand transport flux $\vec{q_R} = (q_{Rx}, q_{Ry})$ due to ebb-tidal currents, Eq. (45) of Bailard and Inman [8] is employed, which was derived in terms of the seabed slope from the bedload transport formula of Bagnold [7] by a linear approximation:

$$q_{Rx} = \frac{G_R}{\tan\phi}\left[\ \tan\phi \cos\theta_R - \frac{\partial Z}{\partial x}\ \right] \tag{45a}$$

$$q_{Ry} = \frac{G_R}{\tan\phi}\left[\ \tan\phi \sin\theta_R - \frac{\partial Z}{\partial y}\ \right] \tag{45b}$$

Here, the subscript R denotes the ebb-tidal currents, θ_R is the angle between the direction of the ebb-tidal currents and the x-axis, and $\tan\phi$ is the angle of repose of the sand. In the original equation of Bailard and Inman [8], the coefficient G_R in Eq. (45) is expressed in terms of the instantaneous velocity, the angle of repose of the sand, and a friction factor, but here sand transport due to currents is assumed to satisfy an equation of the same form as Eq. (45), and all these effects are included in the coefficient G_R in Eq. (45). The first and second terms in the parentheses in Eq. (45) correspond to the action of currents and the downslope action due to gravity, respectively.

In fact, the sand transport due to ebb-tidal currents is comprised of bedload and suspended load, and Eq. (45), therefore, should be expressed by the ratio of ebb-tidal currents to the falling velocity as in [24, 25]. However, in this study, it was assumed that Eq. (45) could be employed as the total load formula, and G_R is given by

$$G_R = \begin{cases} C_0 K_R F_w K_V^3 & (-h_{c2} \le Z \le h_{R2}) \\ 0 & (Z < -h_{c2}, h_{R2} < Z) \end{cases} \tag{46}$$

$$F_w = \frac{(EC_g)_{\mathrm{bo}}}{h_{\mathrm{c}} + h_{\mathrm{R}}} \tag{47}$$

$$K_V = \frac{V}{V_0} = K_{V1}\left(\frac{h_0}{h}\right) \tag{48}$$

$$K_{V1} = \left(\frac{V_1}{V_0}\right). \tag{49}$$

Here, K_R is the coefficient of sand transport due to ebb-tidal currents, and K_V is the ratio of the ebb-tidal current velocity to V_0, V/V_0, where V is the velocity of the ebb-tidal currents and V_0 is a reference velocity at the inlet. F_w is a characteristic value of the intensity of wave action and is given by the wave energy flux at the breaking point of the reference point, $(EC_g)_{\mathrm{b0}}$, divided by the sum of h_{c} and h_{R}, as in Eq. (47). V_1 is the flow velocity of the ebb-tidal currents on the plane bottom. K_{V1} is the ratio of the velocity to the flow velocity at the inlet on the plane bottom. In addition, h_0 and h in Eq. (48) are the reference depth on the plane bottom and water depth, respectively. h_{c2} and h_{R2} are the lower and upper limit depths of bathymetric changes due to ebb-tidal currents, respectively.

Regarding the reason why G_R is given as Eq. (46), G_R in Eq. (45) represents the work done by the ebb-tidal currents in sand movement and is proportional to the energy dissipation rate of the ebb-tidal currents [7, 24]. Here, the action of the ebb-tidal currents is evaluated in macroscopically, and Eq. (45) is assumed to have the same form as Eq. (43); G_R is expressed by the intensity of the ebb-tidal currents relative to the wave intensity $(EC_g)_{\mathrm{b0}}$ and is assumed to be zero outside the zone between the upper and lower limit depths of bathymetric changes due to the ebb-tidal currents. Furthermore, G_R is assumed to be proportional to the third power of the velocity ratio so that the energy dissipation rate is proportional to the third power of the velocity [7, 24].

When the distribution of K_{V1}, as expressed by Eq. (49), on a flat bottom is given, the effect of a change in current velocity associated with a depth change is evaluated using Eq. (48) so that the mass conservation of the fluid is satisfied. K_{V1} is calculated by applying the angular spreading method for irregular waves [5, 6], taking into consideration the fact that the jet-like velocity distribution of ebb-tidal currents at an inlet is very similar to the distribution of the wave diffraction coefficient at the opening of offshore breakwaters. Finally, the coefficient of sand transport due to ebb-tidal currents K_R in Eq. (46) becomes a coefficient including the ratio of the action due to the currents to the wave action. In the calculation, the mean beach slope before the construction of artificial structures is assumed to be the equilibrium slope, considering the long-term beach changes. Although the actions of waves and ebb-tidal currents both simultaneously occur in a tidal inlet, it is assumed that there is no sand supply during the ebb-tidal currents. **Figure 8** shows the flowchart for numerical simulation using the Type 7.

2.8 Type 8 BG model

When an artificial reef (submerged breakwater) is constructed on a coast with detached breakwaters, strong shoreward currents are generated by the forced wave breaking, producing rip currents at the opening between the artificial reef and the existing detached breakwaters. The effects of these currents are not considered in the Type 3, which employs only the wave field without calculating the nearshore currents, although the effect of longshore currents is implicitly considered in the sand transport equation described using the local wave characteristics. Here, the

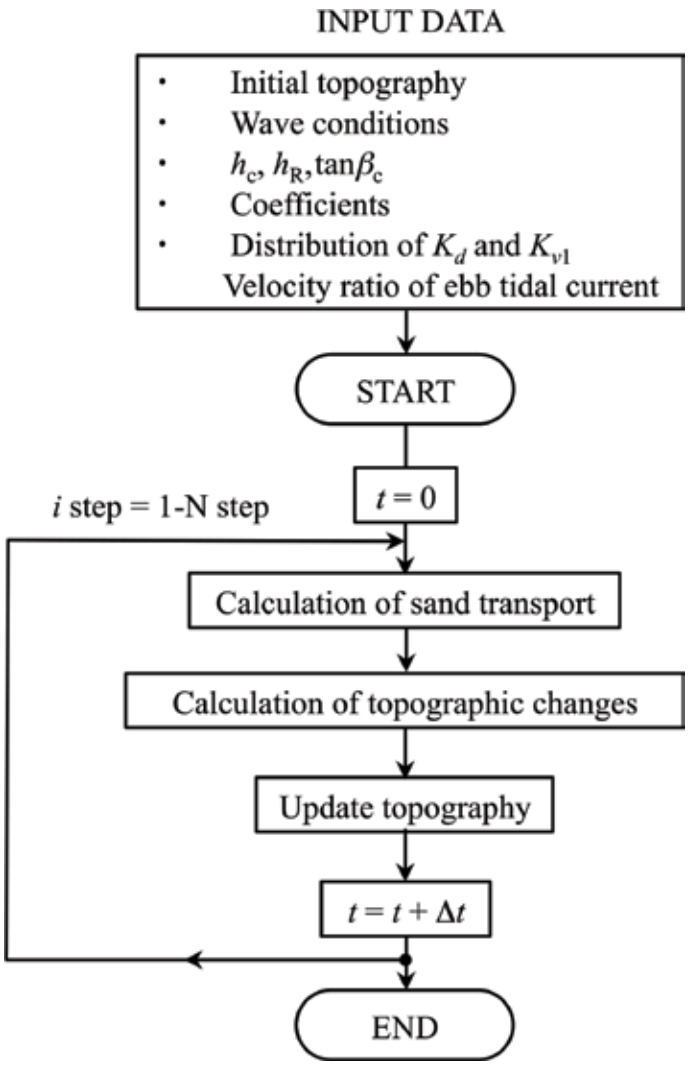

Figure 8.
Flowchart for numerical calculation using Typ. 7 BG model.

effect of the nearshore currents induced by forced wave breaking is incorporated into the model by calculating the nearshore currents. Zanuttigh [26] and Kuroiwa et al. [27] predicted the topographic changes around the low-crested structures by numerical simulation using the so-called 3D model. In this study, an improved BG model is proposed to predict the topographic changes around the artificial reefs. In this study, the sand transport equation based on the concept of the equilibrium slope is employed.

The Type 3 BG model is improved by taking both the wave field and the current velocity at a local point into account. The fundamental equations of the model are given by Eqs. (50)–(54) in the Cartesian coordinates (x, y), assuming that the sand transport flux $\vec{q} = (q_x, q_y)$ is a linear sum of the component due to waves, $\vec{q_w} = (q_{wx}, q_{wy})$, and that due to currents, $\vec{q_c} = (q_{cx}, q_{cy})$:

$$\vec{q} = \vec{q_w} + \vec{q_c} \quad (-h_c \le Z \le h_R) \tag{50}$$

$$\vec{q_w} = C_0 \frac{P_w}{\tan\beta_c} \left(\tan\beta_c \, \vec{e_w} - b_1 \, \overrightarrow{\nabla Z} \right) \tag{51}$$

$$P_w = K_w \cdot \rho \, {u_m}^3 \tag{52}$$

$$\vec{q_c} = C_0 \frac{P_c}{\tan\phi} \left(\tan\phi \, \vec{e_c} - b_2 \, \overrightarrow{\nabla Z} \right) \tag{53}$$

$$P_c = K_c \cdot \rho \, {u_m}^2 V \tag{54}$$

Here, $\vec{q}$ is the total sand transport, $\vec{q_w}$ is the sand transport due to waves, $\vec{q_c}$ is the sand transport due to currents, $\vec{e_c}$ is the unit vector in the current direction, and u_m is the amplitude of the seabed velocity due to the orbital motion of waves defined by Eq. (14) in the Type 3 BG model. $b_1 = |\cos\alpha_1| = \left|\vec{e_w} \bullet \overrightarrow{\nabla Z}\right| \Big/ \left|\overrightarrow{\nabla Z}\right|$, α_1 is the angle between the wave direction and the direction normal to the contour lines, V is the velocity of the currents, K_w and K_c are the coefficients of sand transport due to waves and currents, respectively, $b_2 = |\cos\alpha_2| = \left|\vec{e_c} \bullet \overrightarrow{\nabla Z}\right| \Big/ \left|\overrightarrow{\nabla Z}\right|$, α_2 is the angle between the direction of the currents and the direction normal to the contour lines, and $\tan\phi$ is the slope of the angle of repose of sand. Here, b_2 is assumed to be 0 in the calculation.

The sand transport equations of Eqs. (51) and (53) were derived on the basis of Bagnold's concept as the sand transport equation in the Type 7 BG model. Eq. (51), expressing the effect due to waves, is the same as the equation when assuming that the coefficient of cross-shore sand transport is equivalent to that of longshore sand transport, and the Ozasa and Brampton's term [1] is excluded from the sand transport equation in the Type 3.

In Eq. (53), the wave power by which sand transport is caused by nearshore current is assumed to have the form of ${u_m}^2 V$, referring the previous studies on 3D beach change models in the nearshore zone [4, 12, 28–31]. In the calculation of beach changes, the wave field and nearshore currents are calculated first, and then beach changes are predicted.

Similarly to the calculation in the Type 3 BG model, the wave field is calculated using the energy balance equation [9] with the energy dissipation term due to wave breaking [10]. As the directional spectrum of the incident waves, the combination of the Bretschneider-Mitsuyasu-type frequency spectrum and the Mitsuyasu-type directional function is used [11]. To calculate the nearshore currents, the upwind finite-difference scheme is used for the 2-D momentum equation [4], along with the lateral diffusion term of Larson and Kraus [32]. Because recurrent feedback calculations are necessary in response to the topographic changes in this calculation, the energy balance equation method is used to reduce the calculation load.

In the calculation of the wave field on land, the imaginary depth is assumed between h_R and the shoreline. In this case, the imaginary depth h' can be obtained from Eq. (18) using the minimum depth h_0 and h_R. In particular, in the calculation in Chapter 4, h_0 is assumed to be 1 m. The wave energy is set to be 0 in the area with an elevation higher than the berm height. Although h_c is assumed to be $2.5H$, where H is the wave height at a local point, the increment due to the effect of the strong rip currents is evaluated as

$$h_c' = \{1 + a(V/u_m)\} h_c. \tag{55}$$

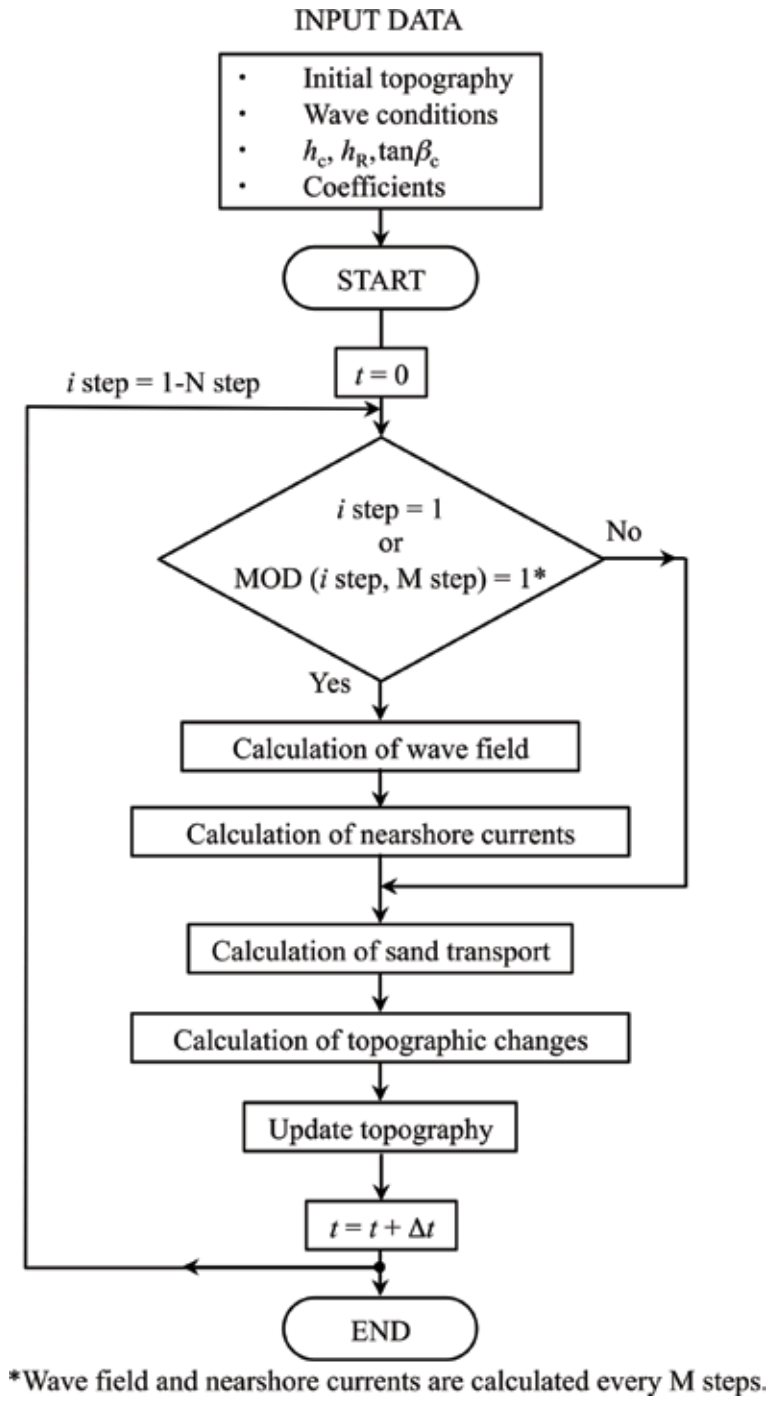

Figure 9.
Flowchart for numerical calculation using Typ. 8 BG model.

Here, V is the velocity of the nearshore currents, and in the calculation in Chapter 4, a coefficient of 0.5 is employed. Similar to the calculation in the Type 1 BG model, beach changes are obtained by solving the continuity equation. **Figure 9** shows the flowchart for the Type 8.

3. Discretization method

3.1 Discretization of mass conservation equation

Beach changes can be calculated using the mass conservation equation (Eq. (28) in Chapter 1). In the calculation, the coastal domain is discretized using 2D elements with widths Δx and Δy, as schematically shown in **Figure 10**. The calculation points of the seabed elevation Z and sand transport rates are set in staggered meshes with a difference of 1/2 mesh, and the equations are solved by the explicit finite-difference method.

First, the calculation point of the elevation Z at $(x_i, y_j) = (i\Delta x, j\Delta y)$ is taken at the center of the cell, as shown in **Figure 11**, and $Z_{(i,j)} = Z(x_i, y_j, t)$ $(1 \le i \le N_x,$ $1 \le j \le N_y)$ is evaluated at each point. Here, the subscripts i and j are the cell numbers taken in the x- and y-directions, and N_x and N_y are the numbers of cells in the x- and y-directions, respectively. Then, $q_{x\ (i-1/2,j)}$ $(1 \le i \le N_x + 1, 1 \le j \le N_y)$ and $q_{y\ (i,j-1/2)}$ $(1 \le i \le N_x, 1 \le j \le N_y + 1)$ are set at points $((i - 1/2)\Delta x,\ j\Delta y)$ and $(i\Delta x,\ (j - 1/2)\Delta y)$, which are separated from the points $Z_{(i,j)}$ by 1/2 mesh in the x- and y-directions, respectively.

When the sand transport flux $\vec{q} = (q_x, q_y)$ is calculated, the seabed elevation $Z'_{(i,j)} = Z(x_i, y_j, t + \Delta t)$ after time Δt can be calculated using Eq. (56), which is the discretized form of Eq. (29) in Chapter 1:

$$Z'_{(i,j)} = Z_{(i,j)} + \left\{ q_{x\ (i-1/2,j)} - q_{x\ (i+1/2,j)} \right\} \left(\frac{\Delta t}{\Delta x} \right) + \left\{ q_{y\ (i,j-1/2)} - q_{y\ (i,j+1/2)} \right\} \left(\frac{\Delta t}{\Delta y} \right) \tag{56}$$

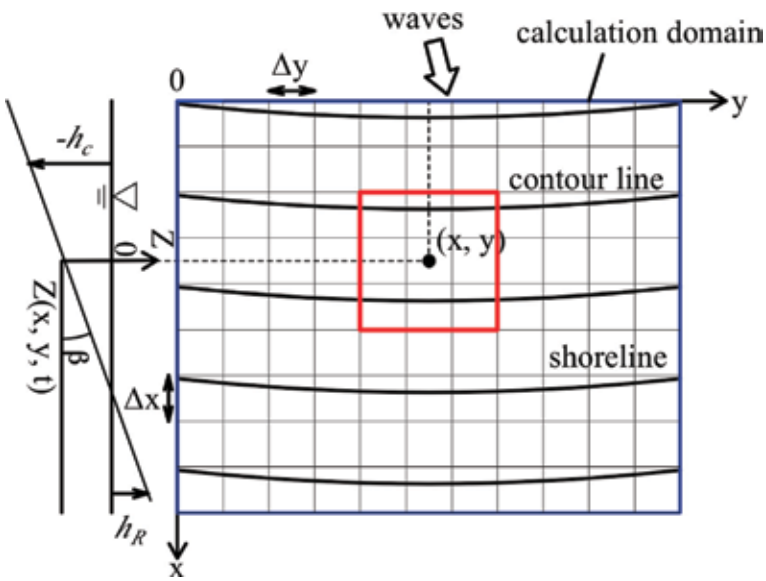

Figure 10.
Calculation domain and meshes.

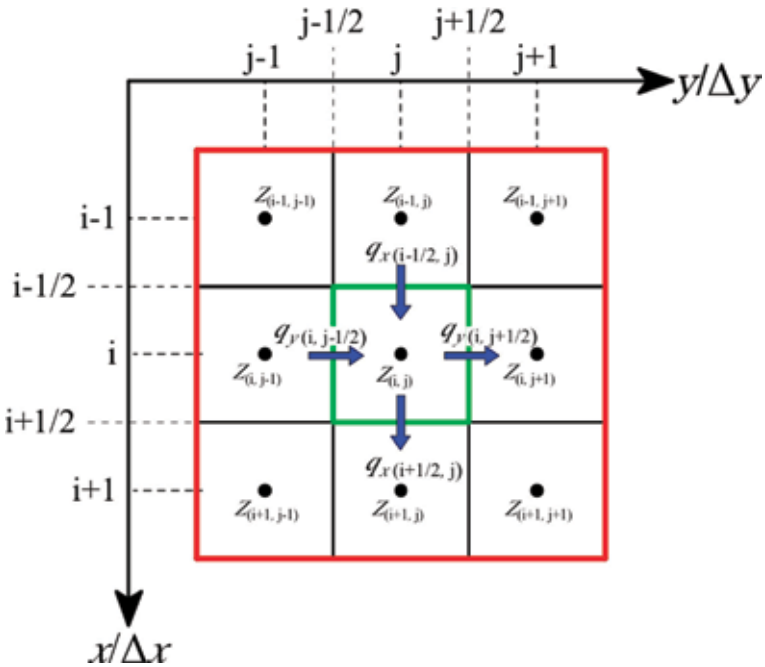

Figure 11.
Arrangement of variables in discretization.

In the calculation of Eq. (56) in a closed system, sand transport is set to 0 along the outer boundaries of the domain as the boundary conditions. A free boundary condition of $dq_x/dx = 0$ or $dq_y/dy = 0$ is often set, where sand freely enters or passes through the boundary. In this case, the value at the boundary is evaluated to be the same value as the sand transport evaluated at an inner point.

As a boundary condition of the structure, sand transport is set to 0 along the boundary. In the calculation of the Type 1 BG model, given the initial seabed topography, the distribution of H_b, α_b, h_c, and h_R, and the equilibrium slope, sand transport fluxes (q_x, q_y) are calculated using the equations given later, and the change in seabed elevation after time Δt is calculated using Eq. (56). These procedures are repeated recurrently.

3.2 Discretization of sand transport equation

All the BG models except the Types 2 and 7 are expressed as

$$\vec{q} = A_1 \vec{e_w} + A_2 \vec{\nabla Z} + A_3 \tan\beta \ \vec{e_s}, \tag{57}$$

where $\vec{e_w}$, $\vec{\nabla Z}$, and $\tan\beta \ \vec{e_s}$ are given by Eqs. (3), (9), and (11) in Chapter 1. When using the vector expression of Eq. (57), the coefficients of the sand transport equation of the Type 1 (Eq. (58)) are given by Eq. (59):

$$\vec{q} = C_0 \frac{K_1 P}{\tan\beta_c} \left[\tan\beta_c \vec{e_w} - \vec{\nabla Z} \right] \tag{58}$$

$$A_1 = C_0 K_1 P \tag{59a}$$

$$A_2 = -\frac{A_1}{\tan\beta_c} \tag{59b}$$

$$A_3 = 0 \tag{59c}$$

Similarly, the coefficients of the sand transport equation of the Type 3 in Eq. (60) are given by Eq. (61):

$$\vec{q} = C_0 \frac{P}{\tan\beta_c} \left\{ \begin{array}{l} K_n \left(\tan\beta_c \, \vec{e_w} - |\cos\alpha| \, \vec{\nabla} Z \right) \\ + \left\{ (K_s - K_n)\sin\alpha - \dfrac{K_2}{\tan\overline{\beta}} \dfrac{\partial H}{\partial s} \right\} \tan\beta \, \vec{e_s} \end{array} \right\} \tag{60}$$

$$(-h_c \le Z \le h_R)$$

$$A_1 = C_0 K_n P \tag{61a}$$

$$A_2 = -\frac{|\cos\alpha|}{\tan\beta_c} A_1 \tag{61b}$$

$$A_3 = \frac{1}{K_n \tan\beta_c} \left\{ (K_s - K_n)\sin\alpha - \frac{K_2}{\tan\overline{\beta}} \frac{\partial H}{\partial s} \right\} A_1 \tag{61c}$$

Since the sand transport equations of the various types can be written as the form in Eq. (57), the sand transport flux of Eq. (57) can be written as x- and y-component expressions for use in the calculation procedure as follows:

$$q_x = A_1 \cos\theta_w + A_2(\partial Z/\partial x) - A_3(\partial Z/\partial y) \tag{62a}$$

$$q_y = A_1 \sin\theta_w + A_2(\partial Z/\partial y) + A_3(\partial Z/\partial x) \tag{62b}$$

Using Eq. (62), the four components of the sand transport equation in Eq. (56) are expressed as follows:

$q_{x\ (i-1/2j)}$ is calculated as

$$\begin{aligned} q_{x\ (i-1/2j)} &= A_{1(i-1/2j)} \ \cos\theta_{w(i-1/2j)} \\ &+ A_{2(i-1/2j)} \ (\partial Z/\partial x)_{(i-1/2j)} \\ &- A_{3(i-1/2j)} \ (\partial Z/\partial y)_{(i-1/2j)}, \end{aligned} \tag{63}$$

where

$$(\partial Z/\partial x)_{(i-1/2j)} = \frac{Z_{(ij)} - Z_{(i-1j)}}{\Delta x}, \tag{64}$$

$$\begin{aligned} (\partial Z/\partial y)_{(i-1/2j)} &= \frac{1}{2} \left\{ \ (\partial Z/\partial y)_{(i-1j)} + (\partial Z/\partial y)_{(ij)} \ \right\} \\ &= \frac{Z_{(i-1j+1)} - Z_{(i-1j-1)} + Z_{(ij+1)} - Z_{(ij-1)}}{4\Delta y}. \end{aligned} \tag{65}$$

$q_{x\ (i+1/2j)}$ is calculated as

$$q_{x\ (i+1/2j)} = [\text{Eq.}(63)]^{i=i+1}. \tag{66}$$

$q_{y\ (ij-1/2)}$ is calculated as

$$\begin{aligned} q_{y\ (ij-1/2)} &= A_{1(ij-1/2)} \ \sin\theta_{w(ij-1/2)} \\ &+ A_{2(ij-1/2)} \ (\partial Z/\partial y)_{(ij-1/2)} \\ &+ A_{3(ij-1/2)} \ (\partial Z/\partial x)_{(ij-1/2)}, \end{aligned} \tag{67}$$

where

$$(\partial Z/\partial y)_{(i,j-1/2)} = \frac{Z_{(i,j)} - Z_{(i,j-1)}}{\Delta y}, \tag{68}$$

$$\begin{aligned}(\partial Z/\partial x)_{(i,j-1/2)} &= \frac{1}{2}\left\{ (\partial Z/\partial x)_{(i,j-1)} + (\partial Z/\partial x)_{(i,j)} \right\} \\ &= \frac{Z_{(i+1,j-1)} - Z_{(i-1,j-1)} + Z_{(i+1,j)} - Z_{(i-1,j)}}{4\Delta x}.\end{aligned} \tag{69}$$

Finally, $q_{y\ (i,j+1/2)}$ is calculated as

$$q_{y\ (i,j+1/2)} = [\text{Eq.}(67)]^{j=j+1}. \tag{70}$$

3.3 Procedure to estimate sand transport near berm top and depth of closure

In the estimation of the intensity of sand transport near the berm top and at the depth of closure, the intensity of sand transport is linearly reduced to 0 by multiplying by the reduction ratio near h_R or h_c to prevent sand from being deposited in the zone higher than h_R and the beach from being eroded in the zone deeper than h_c [33]. In this method, the evaluation method for sand transport on an exposed rock bed in the 3-D beach change model proposed by Ikeno et al. [34] was employed as in [35]. The sand transport fluxes $\vec{q} = (q_x, q_y)$ are reduced by multiplying by a coefficient μ as in Eq. (71), where μ is given by Eq. (72). ΔZ_0 is the thickness of the sand layer from which the reduction in sand transport begins, and ΔZ is given by Eq. (73) near h_R and by Eq. (74) near h_c (**Figure 12**). On a fixed bed comprising a coral reef, Eq. (74) is employed near the depth of the solid bed.

$$\vec{q}' = \mu\ \vec{q} \tag{71}$$

$$\mu = \mu(Z) = \frac{\Delta Z}{\Delta Z_0} \qquad (0 \le \mu \le 1) \tag{72}$$

$$\Delta Z = h_R - Z \qquad (\text{near } Z = h_R) \tag{73}$$

$$\Delta Z = Z - (-h_c) \qquad (\text{near } Z = -h_c) \tag{74}$$

The calculation points of the sand transport and seabed elevation have a 1/2 mesh difference because of the staggered meshes with a 1/2 mesh interval. Here, on the basis of the direction of sand transport, the Z value at a point immediately downcoast and upcoast of the calculation point of sand transport is used in Eqs. (73) and (74), respectively. For example, in the calculation of the x-component in Eq. (74), the Z value at a point immediately upcoast of the calculation point of sand transport is used and is calculated using Eq. (75) as in **Figure 13**:

$$q'_{x\ (i-1/2,j)} = \mu_{iup}\ q_{x\ (i-1/2,j)} (\text{near } Z = -h_c) \tag{75a}$$

$$\mu_{iup} = \frac{\Delta Z_{iup}}{\Delta Z_0} = \frac{Z_{(iup,j)} - (-h_c)}{\Delta Z_0} \tag{75b}$$

$$iup = \begin{cases} i-1 & \left(q_{x\ (i-1/2,j)} \ge 0\right) \\ i & \left(q_{x\ (i-1/2,j)} < 0\right) \end{cases} \tag{75c}$$

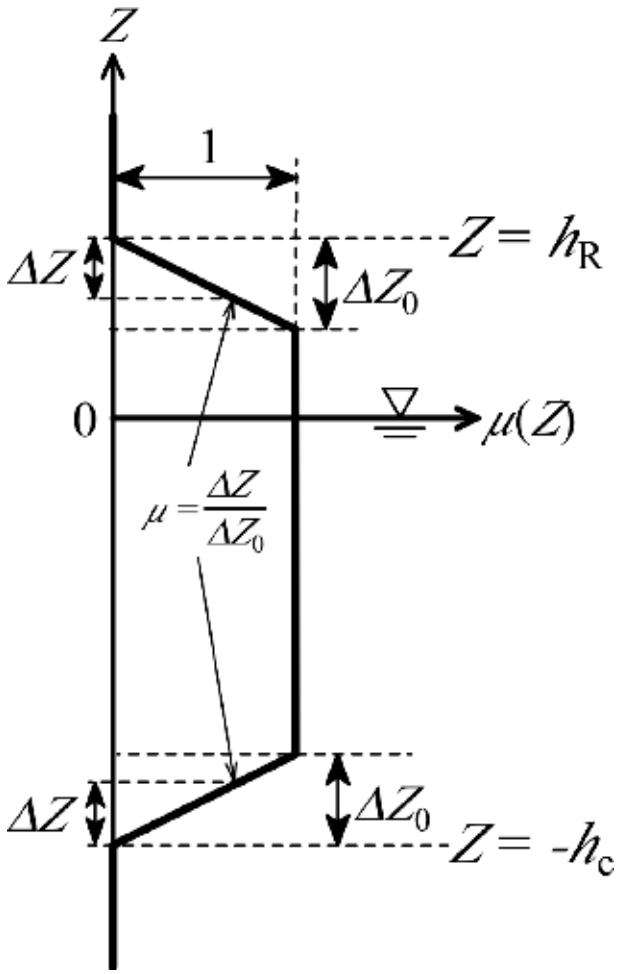

Figure 12
Reduction coefficient μ of sand tranport rate near berm height h_R and depth of closure h_c.

Here, the subscript *iup* represents the location of the Z value at a point immediately updrift of q_x (**Figure 13**). A similar method can be used for the y-component of q. In the calculation of the x-component in Eq. (73), the Z value at a point immediately downcoast of the calculation point of sand transport is used and calculated using Eq. (76) (**Figure 14**).

$$q'_{x\ (i-1/2,j)} = \mu_{idown}\, q_{x\ (i-1/2,j)} (\text{near } Z = h_R) \tag{76a}$$

$$\mu_{idown} = \frac{\Delta Z_{idown}}{\Delta Z_0} = \frac{h_R - Z_{(idown,j)}}{\Delta Z_0} \tag{76b}$$

$$idown = \begin{cases} i & \left(q_{x\ (i-1/2,j)} \geq 0\right) \\ i\text{-}1 & \left(q_{x\ (i-1/2,j)} < 0\right) \end{cases} \tag{76c}$$

Here, the subscript *idown* represents the location of the Z value at a point immediately downdrift of q_x (**Figure 14**). A similar method can be used for the y-component of q. Here, the thickness of the sand layer ΔZ_0, from which the

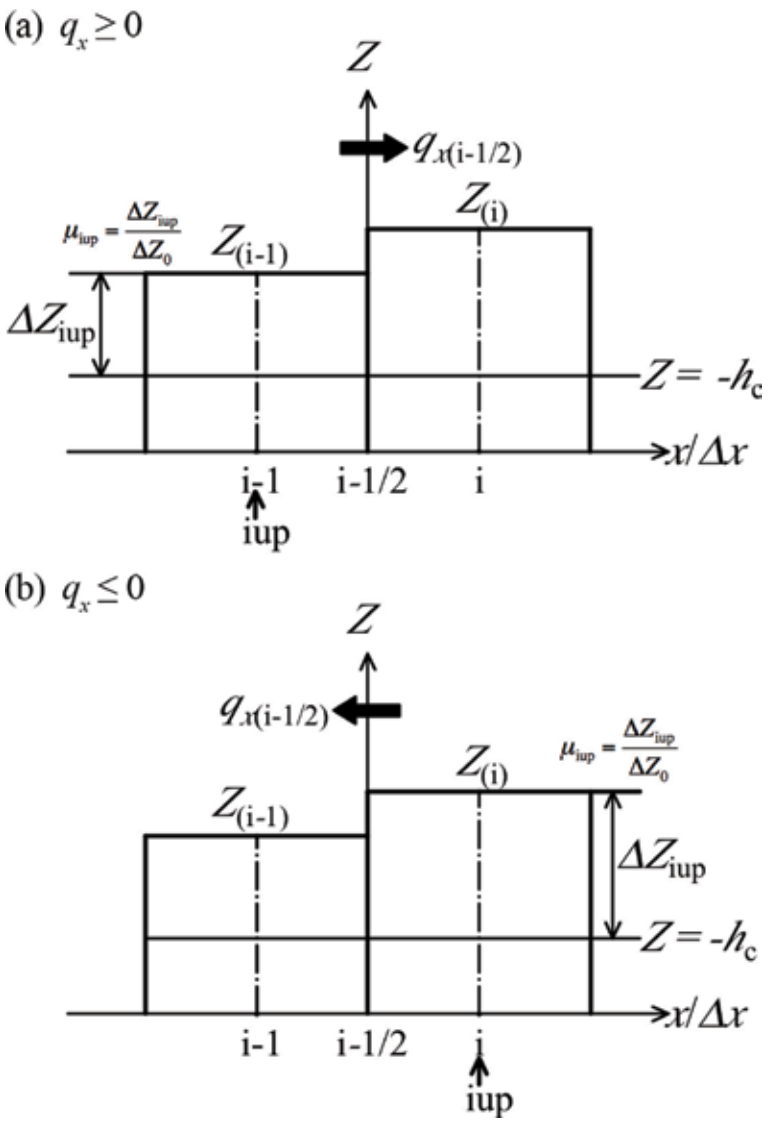

Figure 13.
Method selecting Z value near h_c depending on the direction of sand transport q_x when calculating reduction coefficient μ of sand transport rate.

reduction in sand transport begins, in Eq. (72) was empirically determined. In the calculation in Chapter 3 using the Type 1 BG model, ΔZ_0 is determined using Eq. (77), considering that the reduction of sand transport begins when the slope angle coincides with the angle of the slope in a right-angled triangle whose base has a length of one mesh and whose height is equal to the depth difference, similarly to [2, 6]:

$$\Delta Z_0 = \frac{1}{2}\tan\beta_c \cdot \Delta L \quad (\ \Delta L = \min(\Delta x, \Delta y)\ ) \tag{77}$$

In the other calculation, ΔZ_0 is selected as a value within the following range:

$$\Delta Z_0 = (0.05\text{-}0.2)h_c. \tag{78}$$

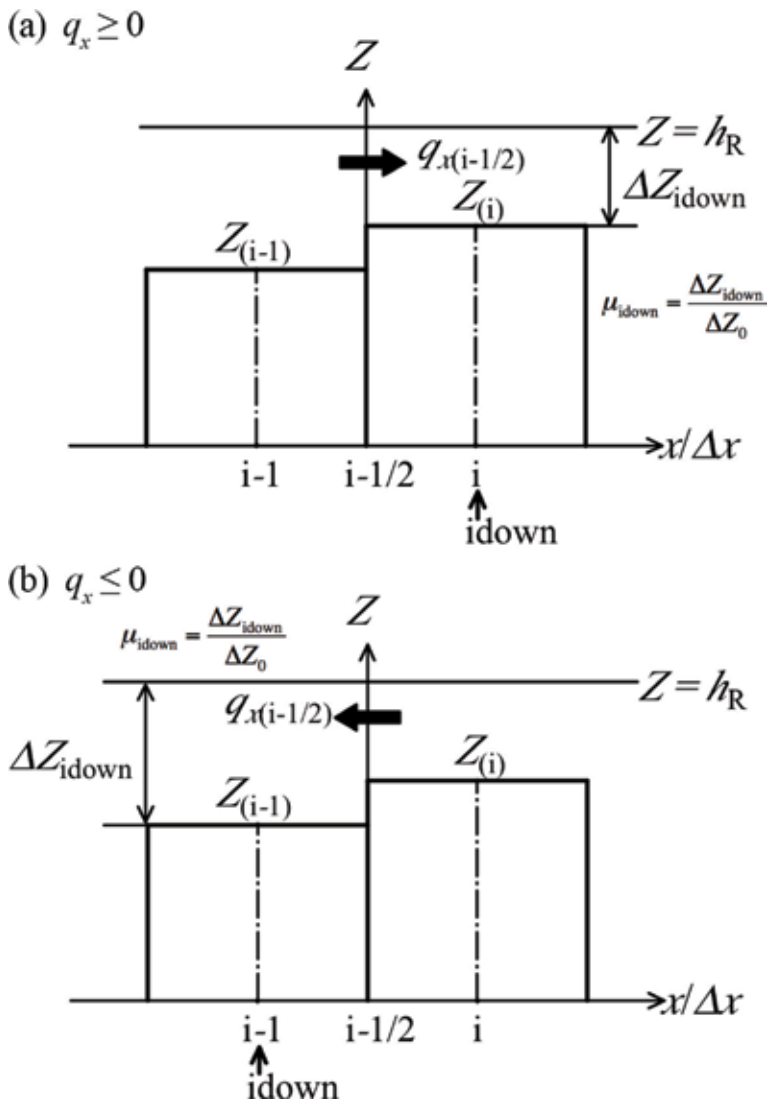

Figure 14.
Method selecting Z value near h_R depending on the direction of sand transport q_x when calculating reduction coefficient μ of sand transport rate.

3.4 Procedure for calculating cross-shore sand movement due to the effect of gravity

Regarding the seaward sand movement in regions above h_R and deeper than h_c, the falling of sand to the deep sea bottom when the local slope exceeds the slope of the angle of repose of sand was evaluated by calculating the sand transport flux due to the gravity [35]. In this calculation, the sand transport flux $\vec{q_g}$ due to the effect of gravity on a steep slope is calculated by Eq. (79) (**Figure 15**), given the slope of the angle of repose of sand.

$$\vec{q_g} = A_g(\tan\beta - \tan\phi)\left(-\vec{e_n}\right)(\tan\beta \geq \tan\phi) \tag{79}$$

Here, $\vec{e_n}$ is the unit vector normal to the contour lines (shoreward), where n is the local coordinate taken along the direction normal (shoreward) to the contour lines, $\tan\beta = \left|\overrightarrow{\nabla Z}\right|$ is the local slope, and $\tan\phi$ is the slope of the angle of repose of sand particle. Here, we assume $\tan\phi = 1/2$. Sand transport with flux $\vec{q_g}$ takes place when the local slope exceeds the slope of the angle of repose of sand, the direction of $\vec{q_g}$ is down the slope and normal to the contour lines, and the strength is proportional to the deviation between the local slope and the slope of the angle of repose with proportionality coefficient A_g. Thus, Eq. (79) expresses the effect of the seabed slope, that is, the steeper the seabed slope, the larger the sand transport. Moreover, when the local slope is gentler than the slope of the angle of repose, $\vec{q_g}$ is set to 0.

Using Eq. (80), Eq. (79) can be written as Eq. (81):

$$\overrightarrow{\nabla Z} = \tan\beta \ \vec{e_n} = \partial Z/\partial n \tag{80}$$

$$\vec{q_g} = A_g(\tan\phi/\tan\beta - 1)\,\overrightarrow{\nabla Z} \quad (\tan\beta \geq \tan\phi) \tag{81}$$

Eq. (81) can be expressed by the basic expression for sand transport of Eq. (57), as mentioned earlier, and the coefficients A_1, A_2, and A_3 of each term of Eq. (57) are given by

$$A_1 = A_3 = 0 \tag{82a}$$

$$A_2 = A_g(\tan\phi/\tan\beta - 1)\ . \tag{82b}$$

Accordingly, $\vec{q_g}$ can be evaluated in the same manner as Eq. (57) using the coefficients given by Eq. (82), assuming that the coefficient A_g is known. Since sand transport due to the effect of gravity is much faster than that due to waves, a large value can be selected for A_g. However, when an excessively large value is employed for A_g, it is difficult to stably carry out the numerical calculation. Here, A_g is designated as the maximum value in a range, in which the numerical simulation can stably proceed as follows.

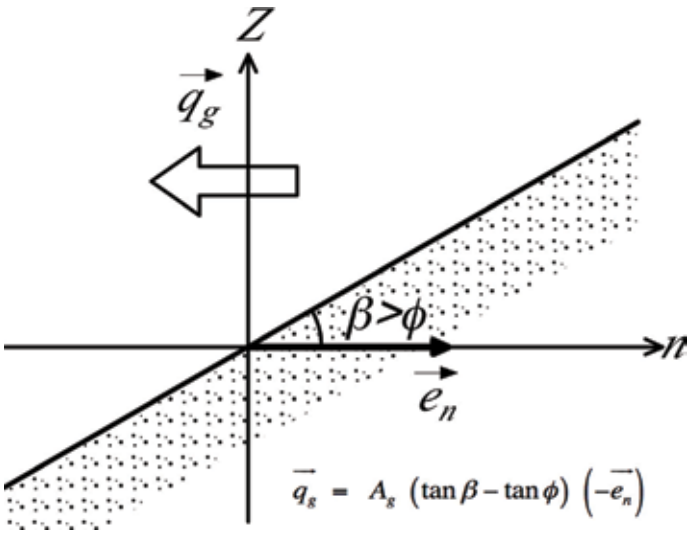

Figure 15.
Seaward sand transport due to gravity when local slope exceeds slope of repose angle.

First, $\vec{q_g}$ in Eq. (79) is reduced to Eq. (83) using Eq. (80), and the cross-shore sand transport component q_n becomes Eq. (84). Assuming the one-dimensional problem in the n-direction, Eq. (84) is substituted into the continuity equation of Eq. (85), and we obtain the one-dimensional diffusion equation of Eq. (86) in the n-direction with a diffusion coefficient of A_g. To solve Eq. (86) using the explicit finite-difference method, Eq. (87) must be satisfied as the stability condition of Eq. (86):

$$\vec{q_g} = A_g(\tan\phi - \partial Z/\partial n)\ \vec{e_n} \tag{83}$$

$$q_n = \vec{e_n} \bullet \vec{q_g} = A_g(\tan\phi - \partial Z/\partial n) \tag{84}$$

$$\frac{\partial Z}{\partial t} = -\frac{\partial q_n}{\partial n} \tag{85}$$

$$\frac{\partial Z}{\partial t} = A_g \frac{\partial Z^2}{\partial n^2} \tag{86}$$

$$\Delta t \le 0.5 \frac{(\Delta n)^2}{A_g} \tag{87}$$

Here, Δn is the mesh interval along the n-axis and Δt is the time interval. Although Eq. (87) is normally used to determine the upper limit of Δt given A_g and Δn, here it is employed as a relationship to determine the upper limit of A_g given Δn and Δt. Eq. (87) can be rewritten as Eq. (88) to provide a stability condition for A_g. Thus, the right term of Eq. (88) gives the upper limit of A_g:

$$A_g \le 0.5 \frac{(\Delta n)^2}{\Delta t} \tag{88}$$

The coefficient A_g that ensures the stability of Eq. (89) is given:

$$A_g = R_S \frac{(\Delta L)^2}{\Delta t} \tag{89a}$$

$$R_S = 0.2 \tag{89b}$$

$$\Delta L = \min(\Delta x, \Delta y)\ . \tag{89c}$$

Finally, $\vec{q_g}$ is calculated in the same manner as Eq. (57) using Eqs. (82) and (89). In the numerical simulation, sand transport fluxes due to both waves and the effect of gravity are calculated at each time step, and the larger value at a location is employed as in Eq. (90):

$$\vec{q} = \begin{cases} \vec{q_g} & \left(\text{if } \left|\vec{q_g}\right| > \left|\vec{q}_{\text{due to waves}}\right| \right) \\ \vec{q}_{\text{due to waves}} & (\text{otherwise}) \end{cases} \tag{90}$$

Author details

Takaaki Uda[1*], Masumi Serizawa[2] and Shiho Miyahara[2]

1 Public Works Research Center, Tokyo, Japan

2 Coastal Engineering Laboratory Co., Ltd., Tokyo, Japan

*Address all correspondence to: uda@pwrc.or.jp

IntechOpen

© 2018 The Author(s). Licensee IntechOpen. Distributed under the terms of the Creative Commons Attribution - NonCommercial 4.0 License (https://creativecommons.org/licenses/by-nc/4.0/), which permits use, distribution and reproduction for non-commercial purposes, provided the original is properly cited. CC BY-NC

References

[1] Ozasa H, Brampton AH. Model for predicting the shoreline evolution of beaches backed by seawalls. Coastal Engineering. 1980;**4**:47-64

[2] Serizawa M, Uda T, San-nami T, Furuike F, Kumada K. Improvement of contour-line change model in terms of stabilization mechanism of longitudinal profile. In: Coastal Sediments'03; 2003. pp. 1-15

[3] Uda T, Kawano S. Development of a predictive model of contour line change due to waves. In: Proceedings of the JSCE, No. 539/II-35; 1996. pp. 121-139 (in Japanese)

[4] Horikawa K, editor. Nearshore Dynamics and Coastal Processes. Tokyo: University of Tokyo Press; 1988. 522p

[5] Sakai K, Uda T, Serizawa M, Kumada T, Kanda Y. Model for predicting three-dimensional sea bottom topography of statically stable beach. In: Proceedings of the 30th ICCE; 2006. pp. 3184-3196

[6] Uda T. Japan's Beach Erosion - Reality and Future Measures. 2nd ed. Singapore: World Scientific; 2017. 530p

[7] Bagnold RA. Mechanics of marine sedimentation. In: Hill MN, editor. The Sea. Vol. 3. New York: Wiley; 1963. pp. 507-528

[8] Bailard JA, Inman DL. An energetics bedload model for a plane sloping beach: Local transport. Journal of Geophysical Research. 1981;**86**(C3):2035-2043

[9] Mase H. Multidirectional random wave transformation model based on energy balance equation. Coastal Engineering Journal, JSCE. 2001;**43**(4): 317-337

[10] Dally WR, Dean RG, Dalrymple RA. A model for breaker decay on beaches. In: Proceedings of the 19th ICCE; 1984. pp. 82-97

[11] Goda Y. Random Seas and Design of Maritime Structures. Tokyo: University of Tokyo Press; 1985. 323p

[12] Shimizu T, Kumagai T, Watanabe A. Improved 3-D beach evolution model coupled with the shoreline model (3D-SHORE). In: Proceedings of the 25th ICCE; 1996. pp. 2843-2856

[13] Uda T, Serizawa M. Model for predicting formation of bay barrier in flat shallow sea. In: Coastal Sediments' 11; 2011. pp. 1176-1189

[14] Dronkers J. Dynamics of Coastal Systems. Singapore: World Scientific; 2005. 519p

[15] Komar PD. Beach Processes and Sedimentation. London: Prentice Hall International; 1998. 544p

[16] San-nami T, Uda T, Serizawa M, Miyahara S. Prediction of devastation of natural coral cay by human activity. In: Proceedings of the Coastal Dynamics 2013, Paper No. 138; 2013. pp. 1427-1438

[17] Wilson BW. Numerical prediction of ocean waves in the North Atlantic for December, 1959. Deutsche Hydrografische Zeitschrift. 1965;**3**: 114-130

[18] Goda Y. Revisiting Wilson's formulas for simplified wind-wave prediction. Journal of Waterway, Port, Coastal, and Ocean Engineering. 2003; **129**(2):93-95

[19] Tung T, Stive MJF, van de Graaff J, Walstra DJR. Morphological behavior of seasonal closure of tidal inlets. In: Proceedings of the Coastal Sediments '07; 2007. pp. 1589-1600

[20] Beck TM, Kraus NC. Ebb-Tidal delta development where before there was none, Shark River Inlet, New Jersey. In: Proceedings of the Coastal Sediments 2011; Miami, Florida. Vol. 1; 2011. pp. 458-471

[21] Serizawa M, Uda T, San-nami T, Furuike K, Ishikawa T. Model for predicting formation of dynamically stable ebb tidal delta off tidal inlet. In: Proceedings of the 31st ICCE; 2008. pp. 2291-2302

[22] Uda T, Serizawa M, San-nami T, Ishikawa T. Prediction of formation of dynamically stable ebb tidal delta and measures for preventing offshore sand loss. In: Proceedings of the 32nd ICCE, sediment. Vol. 73; 2010. pp. 1-10. http://journals.tdl.org/ICCE/article/view/1047/pdf_163

[23] Serizawa M, Uda T, San-nami T, Furuike K. Three-dimensional model for predicting beach changes based on Bagnold's concept. In: Proceedings of the 30th ICCE; 2006. pp. 3155-3167

[24] Bailard JA. An energetics total load sediment transport model for a plane sloping beach. Journal of Geophysical Research. 1981;**86**(C11):10938-10954

[25] Bowen AJ. Simple models for nearshore sedimentation; beach profiles and longshore bars. McCann SB, editor. The Coastline of Canada, The Geological Survey of Canada. 1980;**80**(10):1-11

[26] Zanuttigh B. Numerical modelling of the morphological response induced by low-crested structures in Lido di Dante, Italy. Coastal Engineering. 2007; **54**:31-47

[27] Kuroiwa M, Shibutani Y, Matsubara Y, Mase H. A coastal area model considering sand nourishment process. In: Proceedings of the 34th Conference on Coastal Engineering; Seoul, Korea; 2014. 13p

[28] Watanabe A, Maruyama K, Shimizu T, Sakakiyama T. Numerical prediction model of three-dimensional beach deformation around a structure. Coastal Engineering Journal (Coastal Engineering Journal in Japan). 1986;**29**: 179-194

[29] Watanabe A, Shimuzu T, Kondo K. Field application of a numerical model of beach topography response. In: Proceedings of the Coastal Sediments'91; ASCE Press; 1991. pp. 1814-1928

[30] Kuroiwa M, Kamphuis JW, Kuchiishi T, Matsubara Y, Noda H. Medium-term Q-3D coastal area model with shoreline change around coastal structures. In: Proceedings of the ICCE, No. 29; ASCE; 2004. pp. 2194-2206

[31] Ding Y, Wang SSY, Jia Y. Development and validation of a quasi three-dimensional coastal morphological model. Journal of Waterway, Port, Coastal, and Ocean Engineering. ASCE. 2006;**132**(6): 462-476

[32] Larson M, Kraus NC. Numerical model of longshore current for bar and trough beaches. Journal of Waterway, Port, Coastal, and Ocean Engineering. 1991;**117**(4):326-347

[33] Uda T, Gibo M, Ishikawa T, Miyahara S, San-nami T, Serizawa M. Change in carbonate beach triggered by construction of a bridge on Irabu Island and its simulation using BG model. In: Proceedings of the 7th International Conference of Asian and Pacific Coasts, 2013. pp. 24-31

[34] Ikeno M, Shimizu T, Kobayashi E, Ishii T, Saito T. Application of 3-D beach deformation numerical model to a field site of sandy beach including exposed rock area around a harbor. In: Proceedings of the 28th International Conference on Coastal Engineering; 2002. pp. 2994-3006

[35] Serizawa M, Uda T, San-nami T, Furuike K. Prediction of depth changes on *x-y* meshes by expanding contour-line change model. Annual Journal of Coastal Engineering, JSCE. 2003;**50**: 476-480. (in Japanese)

Chapter 4

Prediction of Typical Beach Changes Owing to Human Activities

Takaaki Uda, Masumi Serizawa and Shiho Miyahara

Abstract

Beach changes related to human activities, such as the effect of construction of groynes and detached breakwaters on a coast with prevailing longshore sand transport, and offshore sand mining, which have engineering importance, were predicted using the Types 1 and 2 BG model. When a long port breakwater is extended, a large wave-shelter zone is formed and dominant longshore sand transport is induced from outside to inside the wave-shelter zone, resulting erosion outside the wave-shelter zone and accretion inside the wave-shelter zone. These beach changes were also predicted using the Type 2 BG model with the evaluation of the effect of a jetty extended at the port entrance to reduce sand deposition inside the port.

Keywords: beach changes, groynes, detached breakwater, offshore sand mining, port breakwater, wave-shelter zone, longshore sand transport

1. Introduction

Beach changes triggered by human activities, such as the construction of groynes and detached breakwaters as a measure against beach erosion, dredging in navigation channel, and offshore sand mining, have been predicted using the Type 1 BG model in previous papers [1–3]. Also, beach changes on the nearby coast triggered by the repeated dredging operation of the anchorage ground in a port were calculated in [1–3]. These results described are commonly observed on many coasts and important in practical coastal engineering, so that these issues were studied again in this chapter by the numerical simulations using the Types 1 and 2 BG model.

Groynes have been used for a long time as one of the most common measures to build statically or dynamically stable shoreline by reducing longshore sand transport on a coast with prevailing longshore sand transport. The effect of the groynes in controlling longshore sand transport strongly depends upon its point depth h in comparison with the depth of closure h_c. If h is greater than h_c, almost all longshore sand transport is blocked, whereas if h is smaller than h_c, a part of longshore sand transport can be transported downcoast, turning around the tip of the groyne. The effect of the construction of the groynes, therefore, was investigated in Section 2 using the Type 1 BG model on a coast with prevailing longshore sand transport under the condition that h is smaller than h_c, which permits passage of part of longshore sand transport offshore of the groynes.

IntechOpen

Detached breakwaters have also been widely employed in Japan as one of the measures against beach erosion. Normally, detached breakwaters have been constructed to reduce the wave energy reaching the shoreline, and wave dissipation by the offshore breakwaters will induce sand accumulation behind the detached breakwaters, resulting in the formation of a cuspate foreland. In such a condition, longshore sand transport is induced from outside to inside the wave-shelter zone as a result of the formation of a wave-shelter zone, resulting in erosion outside the wave-shelter zone and accretion inside the wave-shelter zone [1, 3]. This induced longshore sand transport owing to the wave-sheltering effect of the breakwater can be evaluated by Ozasa and Brampton's method [4], in which an additional term of longshore sand transport owing to the longshore change in the breaker height is included as in Type 2 BG model. Moreover, when they are constructed on a coast with prevailing longshore sand transport, often severe downcoast erosion occurs. Therefore, the difference in the effect of the construction of the detached breakwaters was investigated in Section 3 using the Type 2 BG model when waves were incident from the direction normal to the shoreline and obliquely incident.

In the past, offshore sand mining has been extensively carried out in Japan, particularly in the Western Japan, which triggered beach erosion in the vicinity of the offshore holes produced by sand mining [1]. The offshore mining in the depth zone, the depth of which is comparable to the depth of closure, exerts significant impact to the nearby coasts. Such beach changes can be also predicted using the Type 1 BG model. The impact of the offshore sand mining to the nearby coast and sand dune was numerically predicted in Section 4.

In the coastal zone development, a long breakwater of the commercial or fishing port has been constructed at many coasts, forming a large wave-shelter zone on the lee of the offshore breakwater. In this case, beach changes inside and outside the wave-shelter zone of an oblique port breakwater are triggered, similarly to the case of detached breakwaters. These beach changes were predicted in Section 5 using the Type 2 BG model.

When a long port breakwater is extended, longshore sand transport from outside the wave-shelter zone to inside the wave-shelter zone occurs, and sand refills in the navigation channel. The ordinary way for maintaining the channel is the dredging. However, the repetition of the dredging operation of the navigation channel accelerates sand loss on the nearby coast, unless dredged sand is returned to the beach. In the previous work [1], this issue was analyzed using the Type 1 BG model. In Section 6, the mechanism of sand deposition inside the wave-shelter zone after the overall dredging inside the port was predicted by Type 2 BG model, and the effect of a jetty preventing sand from depositing inside the port was predicted.

2. Beach changes around groynes

2.1 Calculation conditions

A calculation domain of 2000 m length and 600 m width in the longshore and cross-shore directions, respectively, was adopted. Assume that two impermeable groynes were installed at an interval of 500 m on a straight coast with the parallel contours and the initial slope of 1/20 and that waves were obliquely incident relative to the normal to the initial shoreline at a breaker angle of 10° (**Figure 1**(**a**)). The point depth of two groynes, the berm height h_R, and the depth of closure h_c were assumed to be 5, 3, and 10 m, respectively. The point depth (5 m) of the groynes is smaller than the depth of closure, so that part of littoral drift can turn around the tip of the groynes. As the incident waves, waves with a breaker height of H_b = 3 m were assumed, and this breaker height was given at each point in the calculation

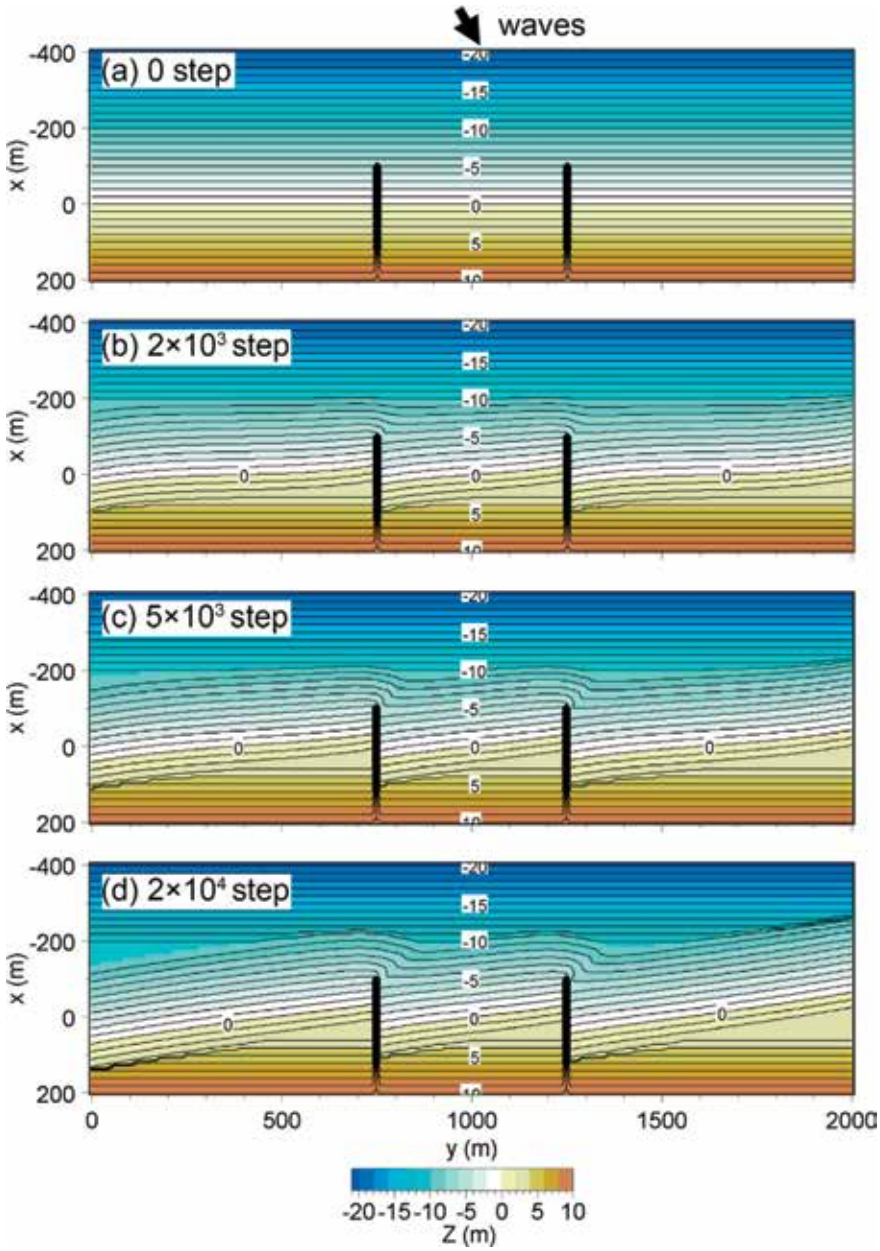

Figure 1.
Prediction of topographic changes around two groynes installed on coast with parallel contours under oblique wave incidence.

domain. The equilibrium slope was the same as the initial slope of $\tan\beta_c = 1/20$. The numerical calculation was carried out using the Type 1 BG model. The other calculation conditions, such as the coefficients of sand transport, mesh size, time intervals, and boundary conditions, are summarized in **Table 1**.

2.2 Calculation results

Subsequent topographic changes and sand transport flux around two groynes installed on a coast with parallel contours under oblique wave incidence are shown in **Figures 1** and **2**. By 2×10^3 steps, the contours upcoast (downcoast) of the groynes advanced (receded) owing to the longshore sand transport toward the positive

Calculation methods	Type 1 BG model
Wave conditions	Incident waves: H_b = 3 m, wave direction θ_w = 10°
Berm height	h_R = 3 m
Depth of closure	h_c = 10 m
Equilibrium slope	$\tan\beta_c$ = 1/20
Depth distribution of sand transport	Cubic equation (Uda and Kawano [5])
Angle of repose slope	$\tan\beta_g$ = 1/2
Coefficients of sand transport	Coefficient of longshore and cross-shore sand transport K_1 = 0.2 Coefficient of Ozasa and Brampton [4] term K_2 = 0.0
Mesh size	$\Delta x = \Delta y$ = 10 m
Time intervals	Δt = 0.05 h
Duration of calculation	1.5×10^3 h (3×10^4 steps)
Boundary conditions	Shoreward and landward ends q_x = 0 Right and left boundaries q_y = 0
Remarks	Lower minimum of 0.5 was set for $\lvert\cos\alpha_b\rvert$ in calculation of P value (Eq. (4) in Chap. 2) to avoid local discontinuity in topography

Table 1.
Calculation conditions.

y-direction (**Figure 1(b)**). Because the groyne insufficiently blocked rightward longshore sand transport, part of longshore sand transport turned around the tip of the groynes, as shown in **Figure 2(a)**, resulting in meandering of offshore contours (**Figure 1(b)**). With time, the meandering of contours offshore of the groynes became more prominent, whereas parallel contours were formed between the groynes as well as the formation of a scarp downcoast of the groynes (**Figure 1(c)** and **(d)**). The sand transport flux offshore of the tip of the groyne still continues after 5×10^3 and 2×10^4 steps with gradual decrease in the intensity. In the meantime, the accretion and erosion zones upcoast and downcoast of the groyne, respectively, expanded, as shown in **Figure 2(b)** and **(c)**. These topographic changes between the groynes including the meandering of contours offshore of the groynes are commonly observed in the field or in a movable bed experiment [1, 3], and such characteristics were successfully reproduced by the Type 1 BG model. **Figure 3** shows the shoreline changes around two groynes. The straight shoreline at the initial stage changed stepwise with time, and the shoreline was stabilized so as for the shoreline to be normal to the wave direction.

The prediction of the meandering of offshore contours became possible only if a stabilization mechanism of the longitudinal profile is taken into account. **Figure 4** shows a schematic diagram of sand transport in the vicinity of a groyne. Consider two contours with the depths h_1 and h_2 and that the cross-shore distance between h_1 and h_2 is a. In addition, consider the extension of a groyne with a point depth between h_1 and h_2, and assume that the shoreward contour advances or retreats by b upcoast and downcoast of the groyne, respectively. If the seabed slope in the longitudinal profile was equal to the equilibrium slope before the beach changes, we obtain the relations for the equilibrium slope and the beach slope after the beach changes:

$$\tan\beta_c = (h_2 - h_1)/a \tag{1}$$

$$\tan\beta = (h_2 - h_1)/(a - b). \tag{2}$$

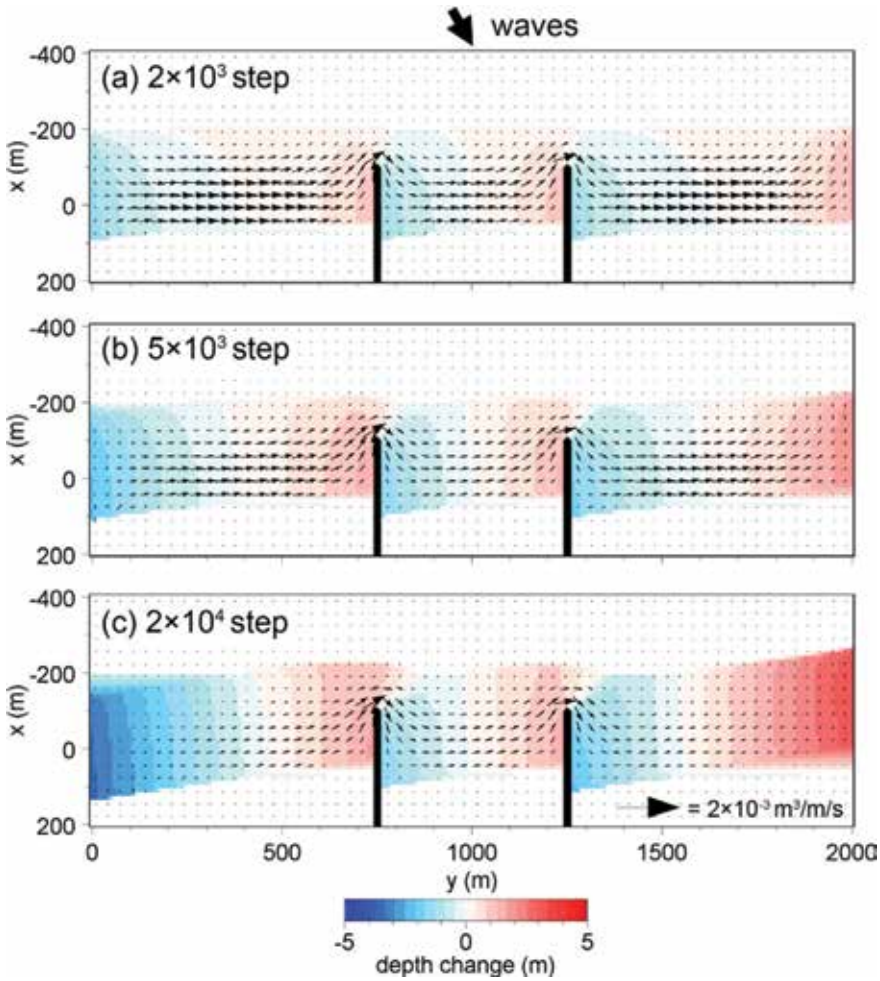

Figure 2.
Topographic changes and sand transport flux around two groynes installed on coast with parallel contours under oblique wave incidence.

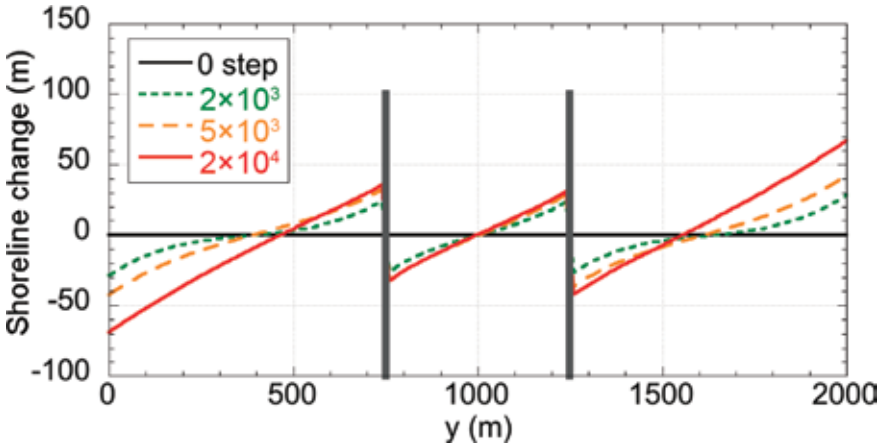

Figure 3.
Shoreline changes around two groynes with time.

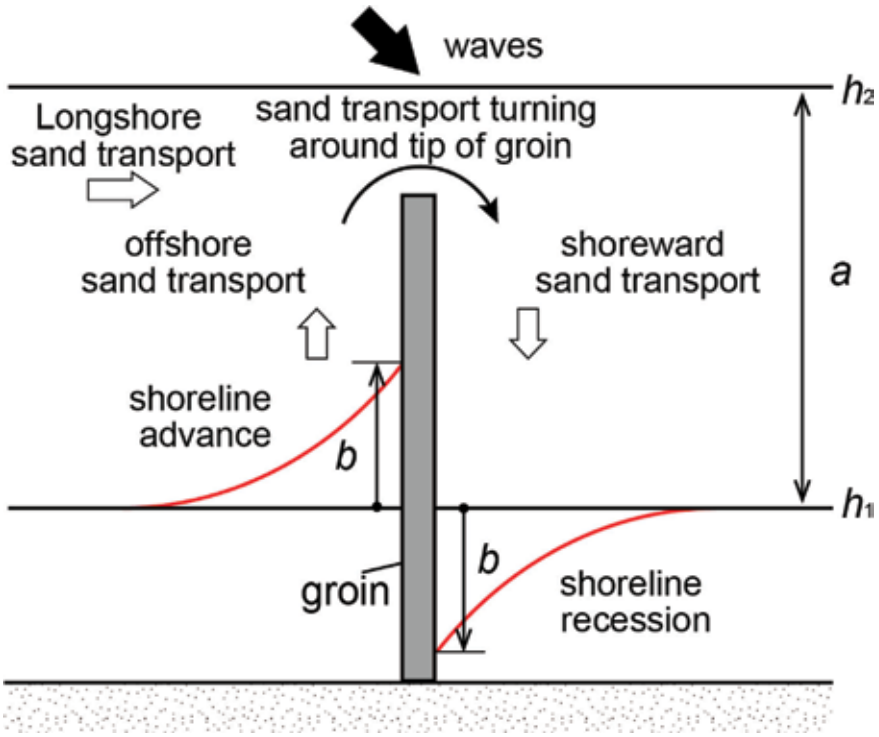

Figure 4.
Schematic diagram of sand transport in vicinity of a groyne.

Eliminating h_1 and h_2 from Eqs. (1) and (2), we obtain Eq. (3).

$$\tan\beta = a/(a - b)\tan\beta_{c.} \quad (3)$$

In other words, the longitudinal slope increases greater than the equilibrium slope upcoast of the groyne, resulting in offshore sand transport. Similarly, the local seabed slope decreases downcoast of the groyne, as in Eq. (4), and shoreward sand transport arises, because the local slope becomes smaller than the equilibrium slope.

$$\tan\beta = a/(a + b)\tan\beta_{c.} \quad (4)$$

Thus, after the construction of the groyne, some specific contour line advances (retreats) upcoast (downcoast) because of the obstruction of longshore sand transport, causing the steeper (gentler) slope. This resulted in the offshore (shoreward) sand transport, and sand transport turning around the tip of the groyne may take place (**Figure 4**). Because of the effects of the cross-shore and longshore sand transport offshore of the groyne, sand deposited near the shoreline upcoast is transported offshore near the tip of the groynes. The meandering of the contour lines offshore of the groynes corresponds to this motion of sand.

3. Beach changes around detached breakwaters

3.1 Calculation conditions

A calculation domain of 2000 m length and 600 m width in the longshore and cross-shore directions, respectively, was adopted, similarly to the groyne case. Assume that two permeable detached breakwaters of 250 m length and the wave transmission

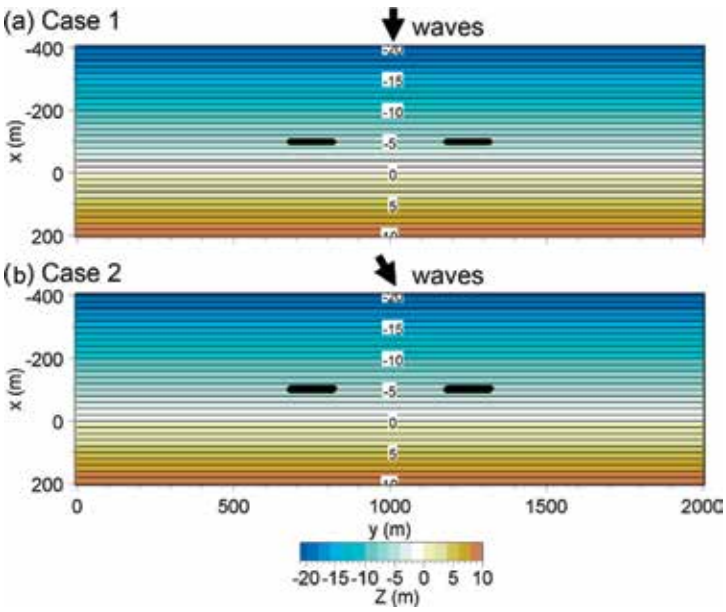

Figure 5.
Initial topography for calculating topographic changes around two detached breakwaters in Cases 1 and 2.

coefficient of K_t = 0.3 were placed 100 m offshore of the initial shoreline on a straight coast with parallel contours and the initial slope of 1/20. The interval of two detached breakwaters was set 350 m. As the incident wave direction, two directions were considered, i.e., waves were incident from the direction normal to the shoreline in Case 1, as shown in **Figure 5(a)** and obliquely incident relative to the normal to the initial shoreline at a breaker angle of 10° in Case 2, as shown in **Figure 5(b)**.

The wave-sheltering effect of the detached breakwaters was evaluated using the angular spreading method for irregular waves, given the directional spreading parameter S_{max} = 10 for wind waves [1], and the wave field was assumed to be constant over time. The berm height h_R and the depth of closure h_c were assumed to be 3 and 10 m, respectively, in both cases. The detached breakwaters were set at a depth of 5 m shallower than the depth of closure, so that part of littoral drift could pass through the area offshore of the detached breakwaters, when waves were obliquely incident relative to the normal to the shoreline. As the incident waves, waves with a breaker height of H_b = 3 m were assumed. The wave height was reduced on the lee of the detached breakwaters along with the change in wave direction because of the wave-sheltering effect of the detached breakwaters. These effects were evaluated by the angular spreading method for irregular waves [1], i.e., the wave energy flux was reduced by the multiplication of the square of the diffraction coefficient at each point, i.e., $(EC_g)_b' = K_d^2(EC_g)_b$, and the wave direction at each point was assumed to be the diffracted wave direction of θ_d ($\theta_w' = \theta_d$). In addition, K_dH_b was employed for the wave height included in the Ozasa and Brampton's term [4]. The equilibrium slope was the same as the initial slope of $\tan\beta_c$ = 1/20. The other calculation conditions are summarized in **Table 2**.

3.2 Calculation results

3.2.1 Case 1

Figure 6 shows the wave field around detached breakwaters when waves were incident from the direction normal to the initial shoreline in Case 1. The symmetric wave-shelter zones were formed on the lee of the detached breakwaters. The wave-calm zone was formed near the shoreline, which may induce sand deposition behind the

Calculation methods	**Angular spreading method for irregular waves** [1] **Type 2 BG model**
Wave conditions	Incident waves: H_b = 3 m, wave direction θ_w = 0° and 10° in Cases 1 and 2, respectively, S_{max} = 10, $(EC_g)_b' = K_d^2 (EC_g)_b$, $\theta_w' = \theta_d$, $H_b' = K_d H_b$ for Ozasa and Brampton [4] term; K_d, diffraction coefficient; θ_d, diffracted wave direction
Berm height	h_R = 3 m
Depth of closure	h_c = 10 m
Equilibrium slope	$\tan\beta_c = 1/20$
Depth distribution of sand transport	Cubic equation (Uda and Kawano [5])
Angle of repose slope	$\tan\beta_g = 1/2$
Coefficients of sand transport	Coefficient of longshore sand transport K_x = 0.2 Coefficient of cross-shore sand transport K_y/K_x = 1.0 Coefficient of Ozasa and Brampton [4] term $K_2 = 1.62K_y$
Mesh size	$\Delta x = \Delta y$ = 10 m
Time intervals	Δt = 0.05 h
Duration of calculation	1.5×10^3 h (3×10^4 steps)
Boundary conditions	Shoreward and landward ends $q_x = 0$ Right and left boundaries $q_y = 0$
Other remarks	Wave transmission coefficient of detached breakwater: K_t = 0.3
Remarks	Lower minimum of 0.5 was set for $\lvert\cos\alpha_b\rvert$ in calculation of P value (Eq. (4) in Chap. 2) to avoid local discontinuity in topography

Table 2.
Calculation conditions.

detached breakwaters. **Figures 7** and **8** show the topographic changes and sand transport flux around two detached breakwaters in Case 1. Symmetric cuspate forelands were formed behind the detached breakwaters, and concave contours were formed in the opening of the detached breakwaters because of the formation of symmetric wave field. The response of the topographic changes behind the detached breakwaters was very quick, and the cuspate forelands were formed with time, as shown in **Figure 7(a)**,

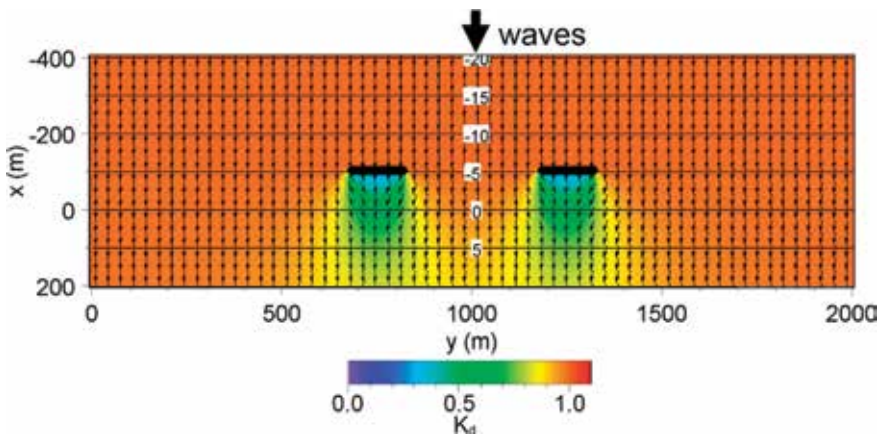

Figure 6.
Wave field around two detached breakwaters in Case 1 calculated using angular spreading method for irregular waves.

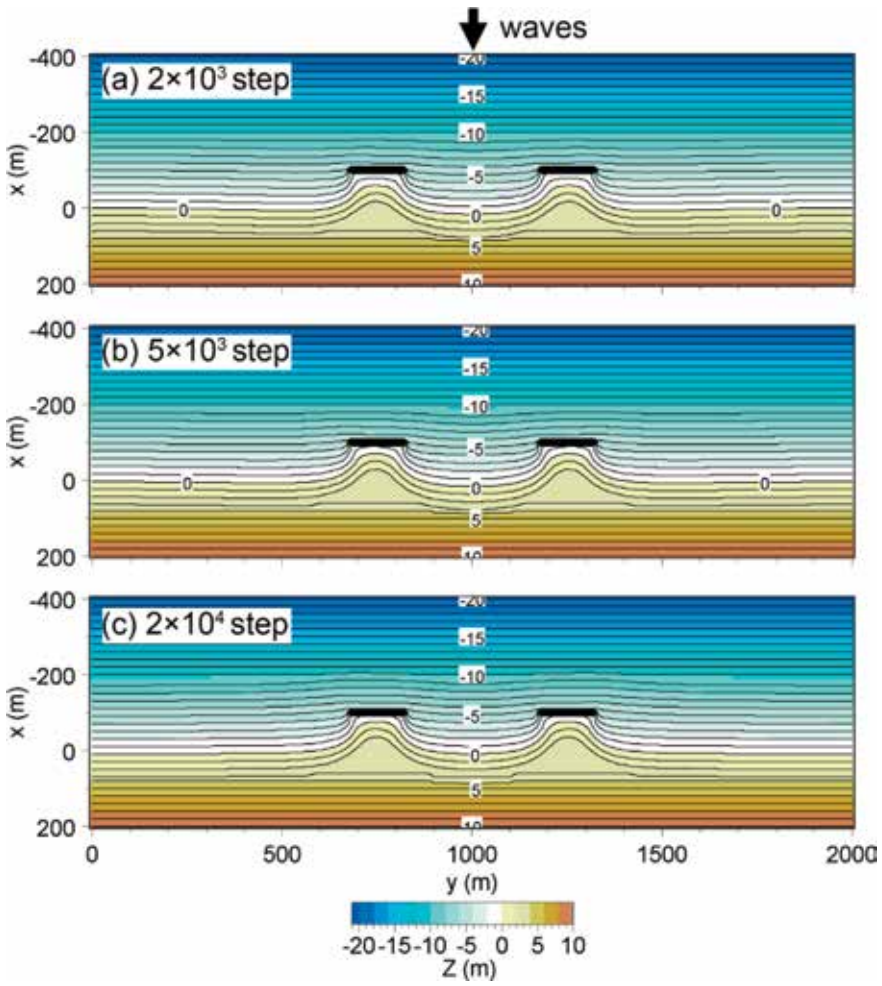

Figure 7.
Predicted topographies around two detached breakwaters in Case 1.

(b), and **(c)**. The sand transport flux decreased its intensity with the formation of cuspate forelands, as shown in **Figure 8(a)**, **(b)**, and **(c)**. **Figure 9** shows the shoreline changes around two detached breakwaters with time. The shoreline outside of the wave-shelter zone of the detached breakwaters receded, even though the amount of the shoreline recession was not so large, whereas the shoreline on the lee of the detached breakwaters markedly advanced because of the wave-sheltering effect of the detached breakwaters. It is concluded that the construction of detached breakwaters induces the concentrated accumulation of sand behind the detached breakwaters.

The response of the topographic changes behind the detached breakwaters was very quick, and the cuspate forelands were formed with time, as shown in **Figure 7(a)**, **(b)**, and **(c)**. The sand transport flux decreased its intensity with the formation of cuspate forelands, as shown in **Figure 8(a)**, **(b)**, and **(c)**.

3.2.2 Case 2

Similarly, **Figure 10** shows the wave field around detached breakwaters when waves were obliquely incident from the direction relative to the normal to the initial shoreline at a breaker angle of 10° in Case 2. Although the wave-shelter zones were also formed on the lee of the detached breakwaters, more wave energy was transported from the

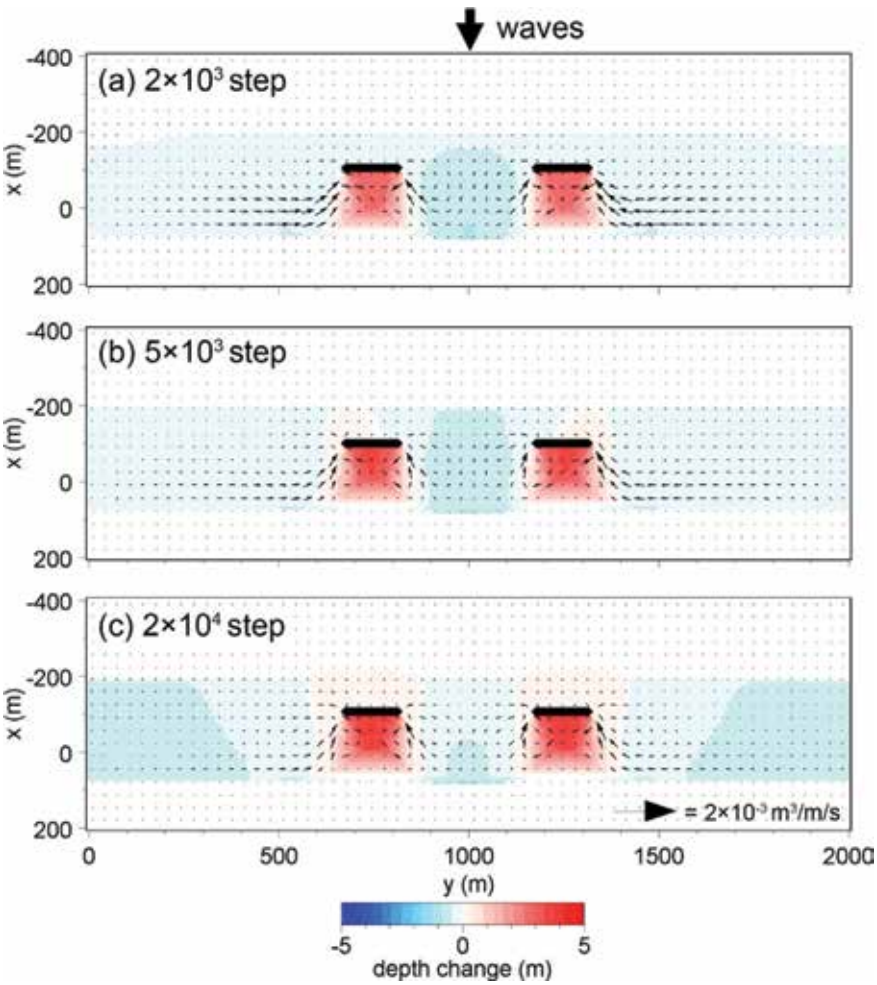

Figure 8.
Topographic changes and sand transport flux around two detached breakwaters in Case 1.

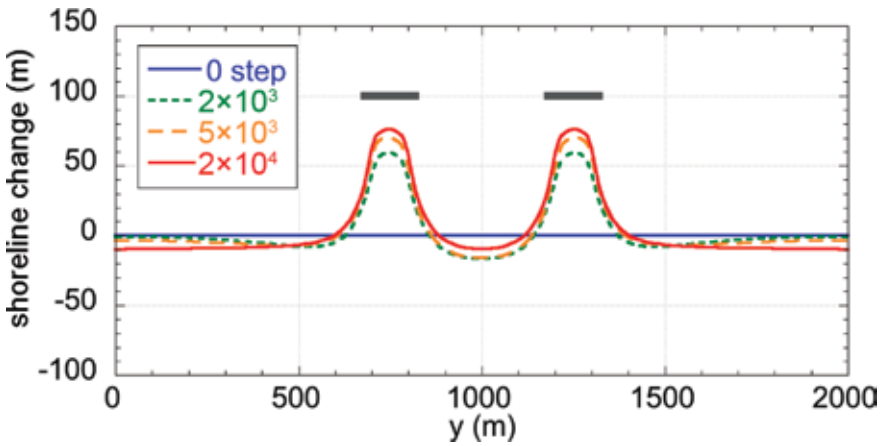

Figure 9.
Shoreline changes around two detached breakwaters in Case 1.

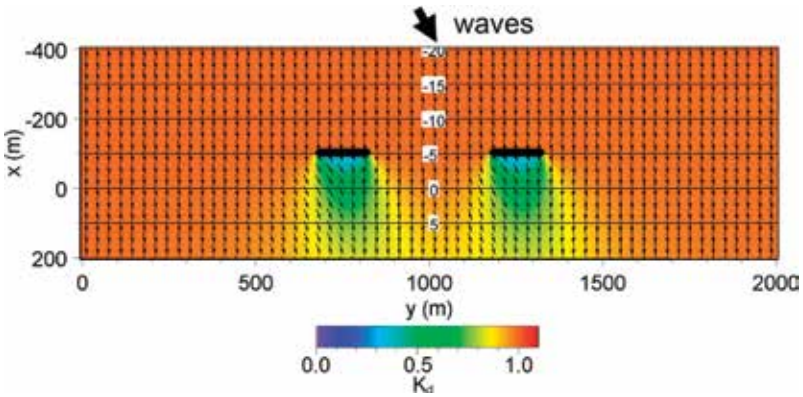

Figure 10.
Wave field around two detached breakwaters calculated using angular spreading method for irregular waves in Case 2.

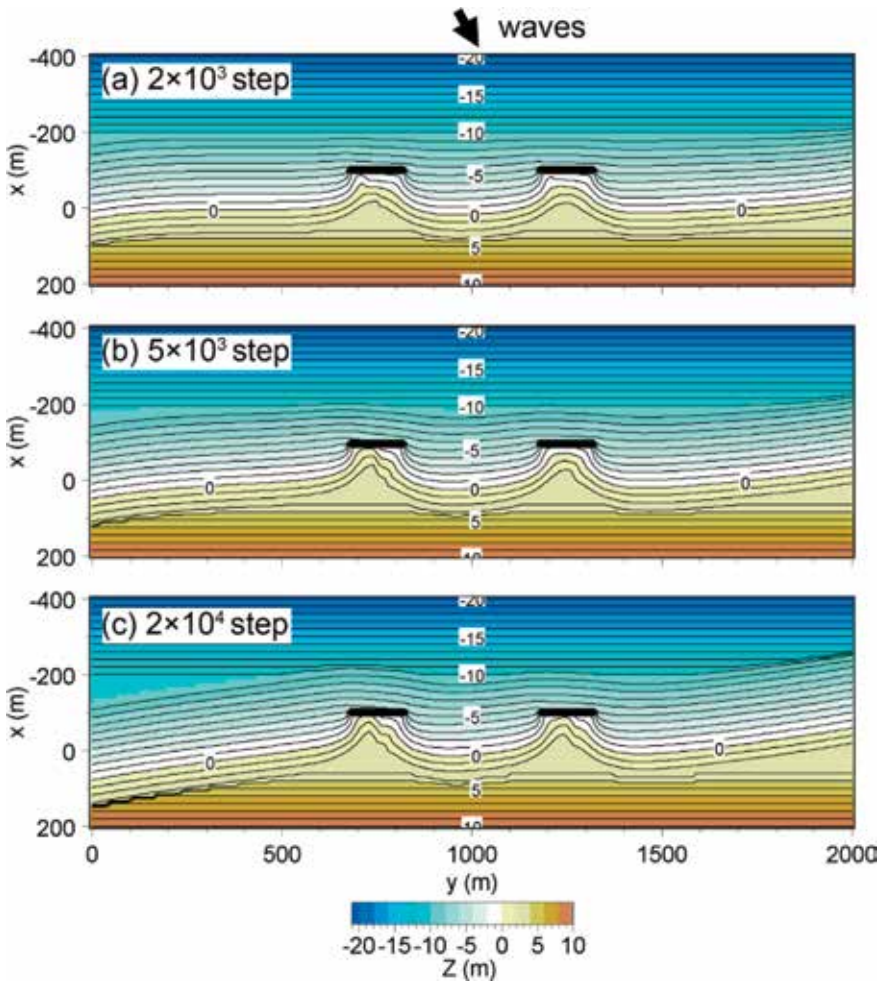

Figure 11.
Predicted topographies around two detached breakwaters in Case 2.

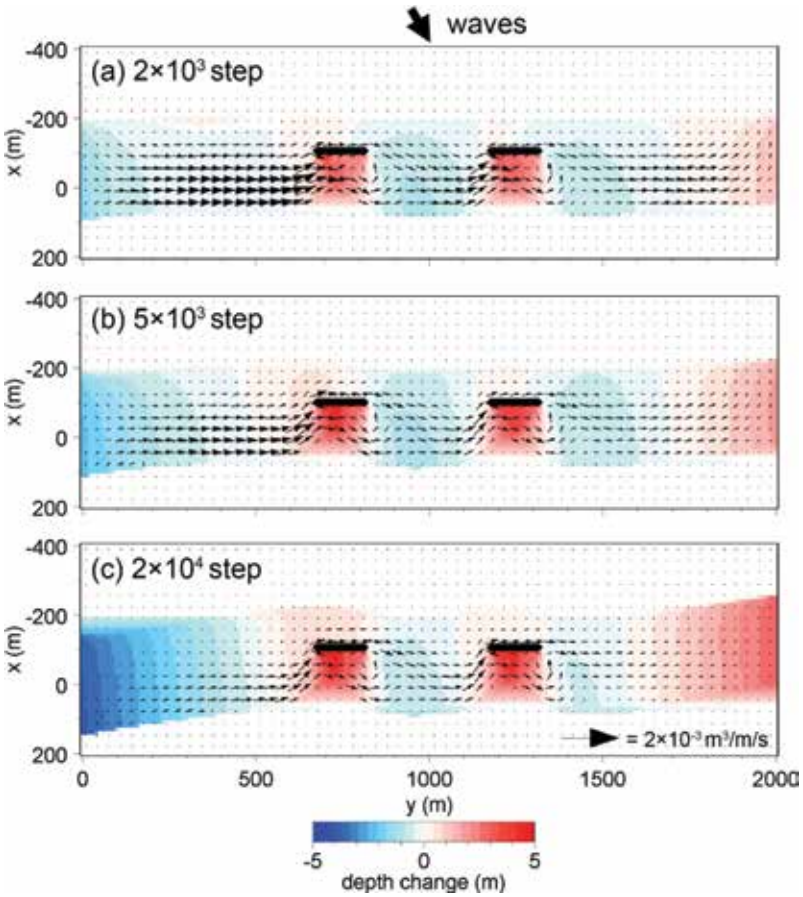

Figure 12.
Topographic changes and sand transport flux around two detached breakwaters in Case 2.

left on the lee of the detached breakwaters because of oblique wave incidence from the counterclockwise direction. The topographic changes and sand transport flux around two detached breakwaters in Case 2 are shown in **Figures 11** and **12**. Cuspate forelands were formed behind each detached breakwater after 2×10^3 steps, and concave contours were formed in the opening of the detached breakwaters (**Figure 11(a)**). Also, sand was transported rightward even offshore of the detached breakwaters (**Figure 12(a)**, **(b)**, and **(c)**), resulting in the meandering of contours offshore of the detached breakwaters,

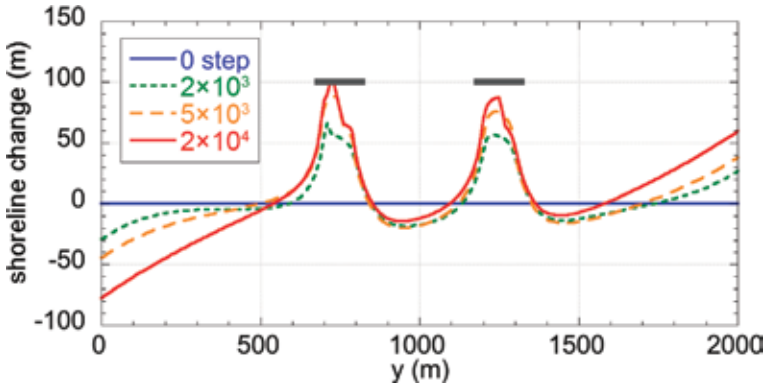

Figure 13.
Shoreline changes around two detached breakwaters in Case 2.

as shown in **Figures 11(b)** and **(c)**. **Figure 13** shows the shoreline changes around two detached breakwaters with time under oblique wave incidence. The shoreline upcoast of the detached breakwaters receded, whereas the shoreline downcoast of the detached breakwaters advanced because of the passage of part of longshore sand transport offshore of the detached breakwaters. Thus, it is concluded that sand is gradually transported downcoast by longshore sand transport under the condition that waves are obliquely incident to the direction normal to the shoreline, when permeable detached breakwaters were constructed on a coast.

4. Beach changes caused by offshore sand mining

4.1 Calculation conditions

Beach changes caused by sand mining offshore of a pocket beach was predicted using the Type 1 BG model. A calculation domain of 2000 m length and 600 m width in the longshore and cross-shore directions, respectively, was adopted,

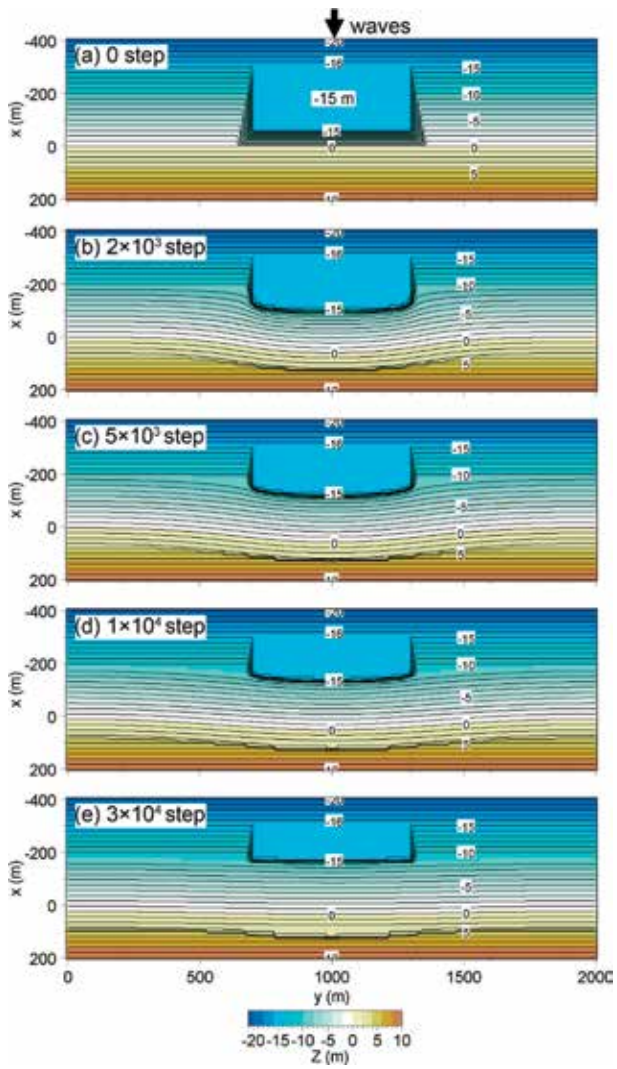

Figure 14.
Topographic changes around a hole excavated offshore of sandy beach with parallel contours.

similarly to the groyne case. Assume that the breaker height of H_b = 3 m and waves were assumed to be incident normal to the shoreline on a straight coast with a uniform seabed slope of 1/20. In the calculation, this constant breaker height was assumed anywhere in the calculation domain. Offshore mining was assumed to be carried out up to a depth of 15 m in a 600-m long and 300-m wide rectangular zone in the depth range between the shoreline and 15 m depth (**Figure 14(a)**). The excavated depth of the dredging hole at its center was large (reaching as deep as 15 m) relative to the original seabed, and h_R and h_c were assumed to be 3 and 10 m, respectively. The other calculation conditions are summarized in **Table 3**.

4.2 Calculation results

Figure 14 shows the refilling process of sand into the dredging hole under waves. The contour lines shallower than h_c of 10 m depth retreated around the dredging hole, and the dredging hole was gradually refilled over time because of the falling of sand through the landward steep slope. Sand refill began soon after dredging after 2×10^3 steps, and a concave shoreline was formed landward of the dredging hole, and a scarp began to be formed (**Figure 14(b)**). The dredging hole was further refilled due to wave action with time, as shown in **Figure 14(c)**. Since part of the sand on the sand dune was transported to the hole, the beach was severely eroded landward of the hole, resulting in the formation of a scarp of over 3 m height (**Figure 14(c)**). The size of the dredging hole decreased considerably as well as the longshore expansion of the eroded zone landward of the dredging hole after 10^4 steps (**Figure 14(d)**). Finally, the offshore dredging hole was refilled by 3×10^4 steps, and the remains of a dredging hole were left in the offshore zone together with the formation of a high scarp on the sand dune landward of the dredging hole (**Figure 14(e)**). It is concluded that a dredging hole is smoothed out with time in the region undergoing the dominant wave action, but a steep slope formed on the sand dune landward of the berm top has been left for a long time.

Calculation methods	**Type 1 BG model**
Wave conditions	Incident waves: H_b = 3 m, wave direction θ_w = 0°
Berm height	h_R = 3 m
Depth of closure	h_c = 10 m
Equilibrium slope	$\tan\beta_c$ = 1/20
Depth distribution of sand transport	Cubic equation (Uda and Kawano [5])
Angle of repose slope	$\tan\beta_g$ = 1/2
Coefficients of sand transport	Coefficient of longshore and cross-shore sand transport K_1 = 0.2 Coefficient of Ozasa and Brampton [4] term K_2 = 0.0
Mesh size	$\Delta x = \Delta y$ = 10 m
Time intervals	Δt = 0.05 h
Duration of calculation	1.5×10^3 h (3×10^4 steps)
Boundary conditions	Shoreward and landward ends, q_x = 0 Right and left boundaries, q_y = 0
Remarks	Lower minimum of 0.5 was set for $\lvert\cos\alpha_b\rvert$ in calculation of P value (Eq. (4) in Chap. 2) to avoid local discontinuity in topography

Table 3.
Calculation conditions.

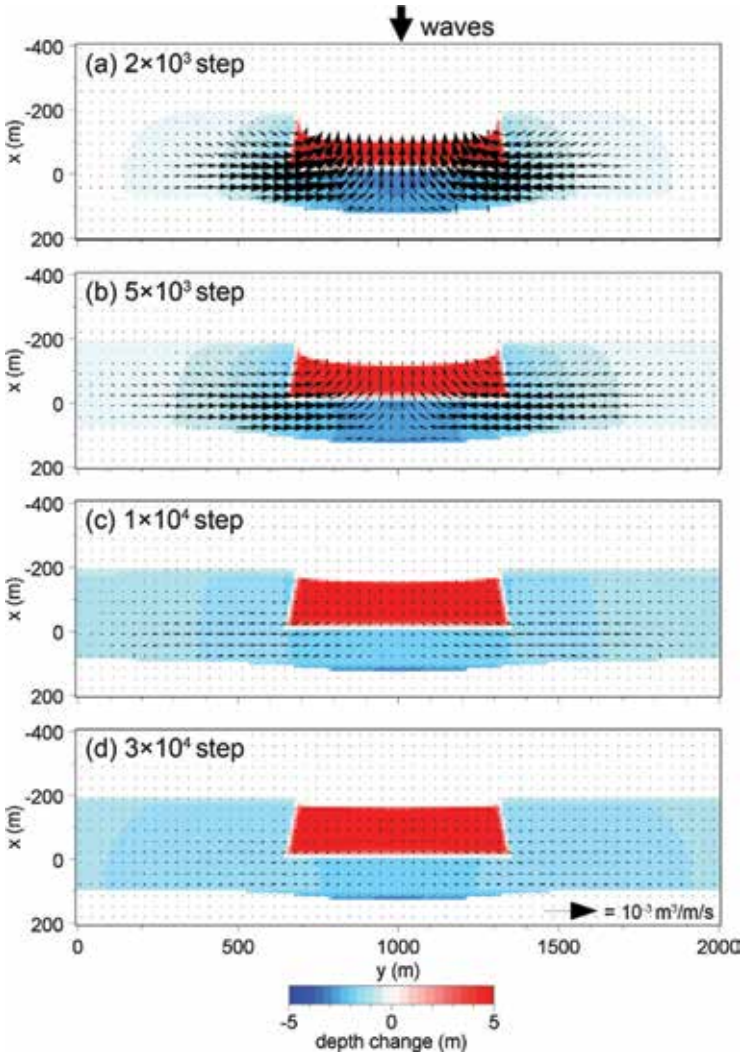

Figure 15.
Bathymetric changes and sand transport flux around a dredging hole excavated offshore of sandy beach with parallel contours.

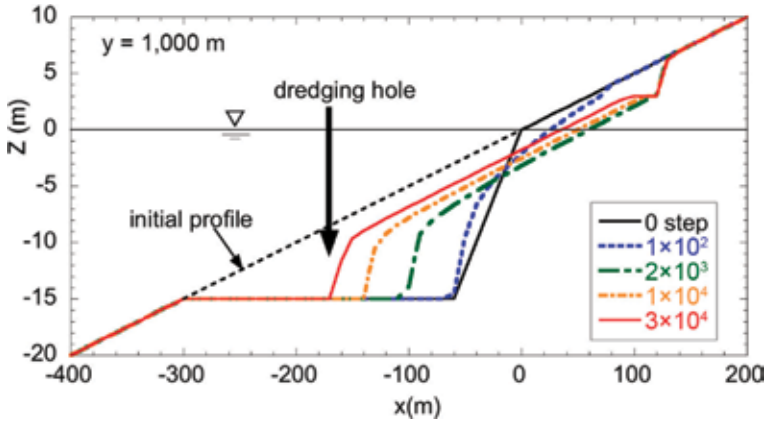

Figure 16.
Change in longitudinal profile with time along transect y = 1000 m.

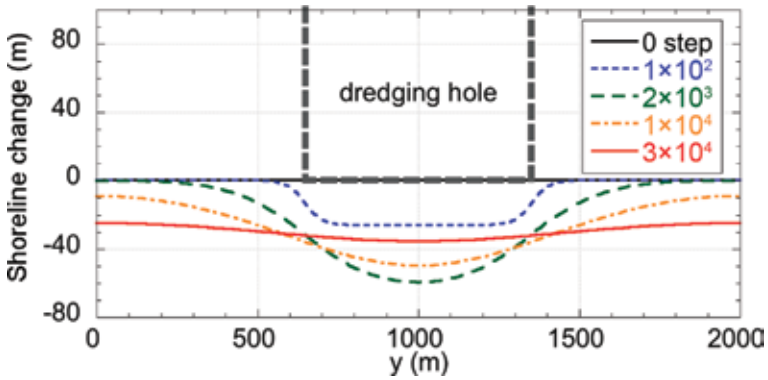

Figure 17.
Shoreline changes around a dredging hole with time.

The sand transport fluxes corresponding to the bathymetries at each step shown in **Figure 14** are shown in **Figure 15**. At the initial stage, strong fluxes toward the dredging hole from the nearby area were generated (**Figure 15(a)**), and these fluxes ceased with time as the dredging hole was refilled, as shown in **Figures 15(b)**, **(c)**, and **(d)**. The topographic changes can be realized from the change in longitudinal profile through the center line of the hole (**Figure 16**). At the initial stage, the landward slope of the dredging hole was so steep that sand was refilled from the shoreward slope, forming a steep slope with angle of repose of sand in the zone deeper than the depth of closure.

The shoreline changes around a dredging hole with time can be drawn as in **Figure 17**. After 100 steps, the shoreline immediately behind the offshore dredging hole retreated. With time, the shoreline recession zone expanded alongshore. Note that the offshore sand mining in a zone shallower than h_c affects the beach in the entire zone together with the formation of a high scarp on the sand dune.

5. Beach changes associated with extension of oblique port breakwater

5.1 Calculation conditions

A calculation domain of 2000 m length and 600 m width in the longshore and cross-shore directions, respectively, was adopted to predict beach changes associated with the extension of an oblique breakwater on a coast with parallel contours. **Figure 18**

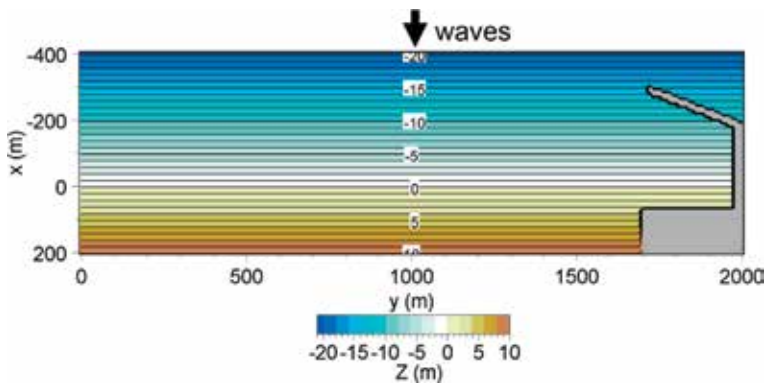

Figure 18.
Initial topography of coast with parallel contours and setup of an oblique breakwater.

Calculation methods	**Type 2 BG model** **Angular spreading method for irregular waves** [1]
Wave conditions	Incident waves: H_b = 3 m, wave direction θ_w = 0°, S_{max} = 10, $(EC_g)_b' = K_d^2 (EC_g)_b$, $\theta_w' = \theta_d$, $H_b' = K_d H_b$ for Ozasa and Brampton [4] term; K_d, diffraction coefficient; θ_d, diffracted wave direction
Berm height	$h_R' = K_d h_R$ (h_R = 3 m), K_d: diffraction coefficient
Depth of closure	$h_c' = K_d h_c$ (h_c = 10 m), K_d: diffraction coefficient
Equilibrium slope	$\tan\beta_c$ = 1/20
Depth distribution of sand transport	Cubic equation (Uda and Kawano [5])
Angle of repose slope	$\tan\beta_g$ = 1/2
Coefficients of sand transport	Coefficient of longshore sand transport K_x = 0.2 Coefficient of cross-shore sand transport K_y/K_x = 1.0 Coefficient of Ozasa and Brampton [4] term $K_2 = 1.62K_y$
Mesh size	$\Delta x = \Delta y$ = 10 m
Time intervals	Δt = 0.05 h
Duration of calculation	10×10^3 h (5×10^4 steps)
Boundary conditions	Shoreward and landward ends q_x = 0 Right and left boundaries q_y = 0
Remarks	Lower minimum of 0.5 was set for $\lvert\cos\alpha_b\rvert$ in calculation of P value (Eq. (4) in Chap. 2) to avoid local discontinuity in topography

Table 4.
Calculation conditions.

shows the initial topography of the coast and the setup of an oblique breakwater, which was constructed at the right corner of the calculation domain. The wave field which was affected by the extension of the breakwater was determined by the angular spreading method for irregular waves [1], assuming that waves with the breaker height of H_b = 3 m were incident normal to the shoreline on a straight coast with a uniform seabed slope of 1/20. The wave field was assumed to be constant over time. The wave-sheltering effect of an oblique breakwater was evaluated similarly to the method in the case of the detached breakwater, as described in Section 3.

In the calculation of beach changes, h_R and h_c were assumed to be 3 and 10 m, respectively, in the zone without the wave-sheltering effect far from the oblique

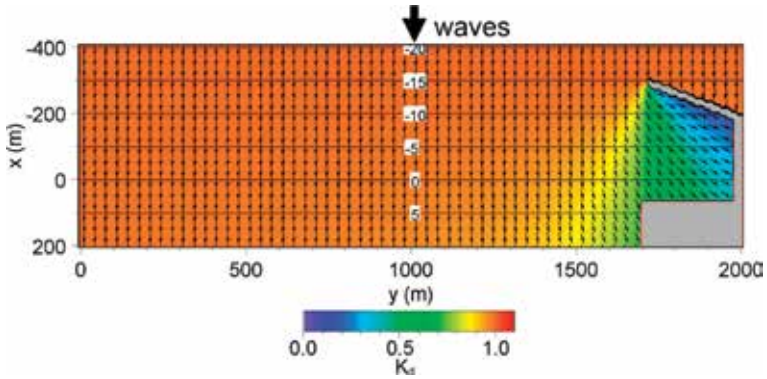

Figure 19.
Wave field around an oblique breakwater.

breakwater. In the wave-shelter zone, the berm height h_R' was estimated from h_R multiplied by the diffraction coefficient K_d ($h_R' = K_d h_R$). Similarly, the depth of closure h_c' was estimated from h_c multiplied by the diffraction coefficient K_d ($h_c' = K_d h_c$). The equilibrium slope was set 1/20. The calculation conditions are summarized in **Table 4**.

5.2 Calculation results

Figure 19 shows the wave field around an oblique breakwater. Owing to the wave-diffraction effect of the oblique breakwater, the wave-shelter zone expanded to the lee of the breakwater. The longshore change in wave height owing to the wave-sheltering effect of the breakwater caused rightward longshore current

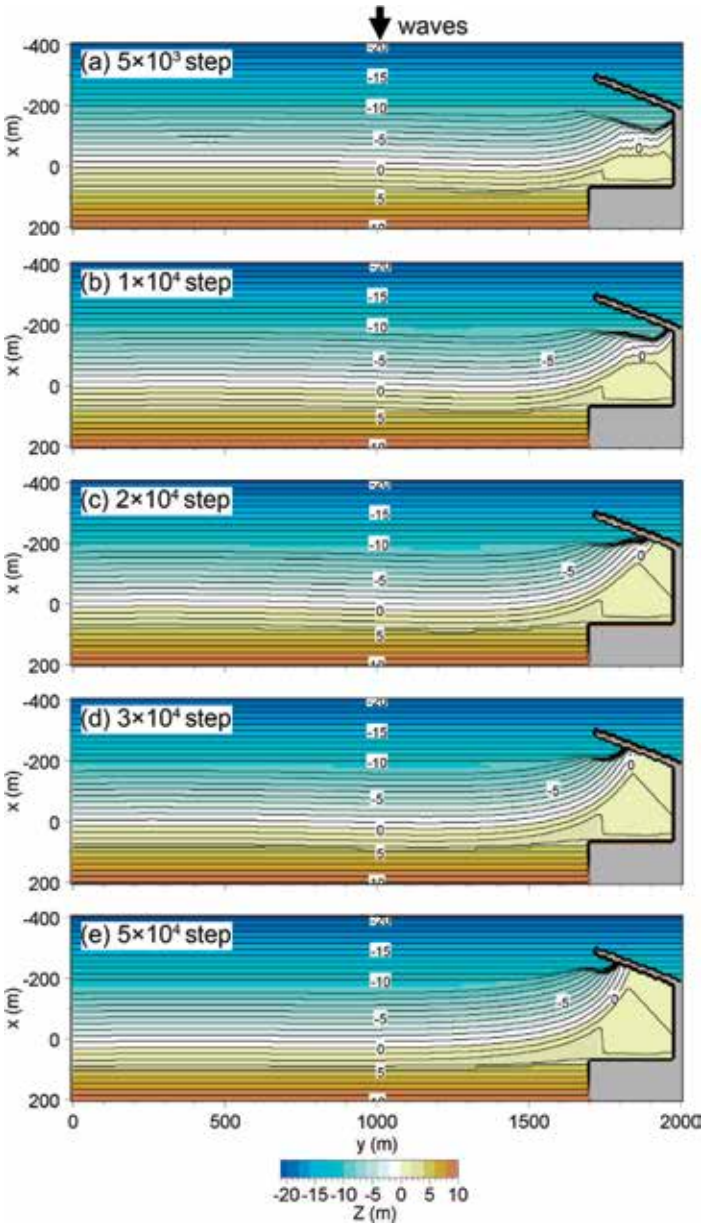

Figure 20.
Successive deposition of sand inside the wave-shelter zone produced by extension of a long port breakwater.

(longshore sand transport), resulting in erosion outside the wave-shelter zone and sand deposition inside the wave-shelter zone. **Figure 20** shows the topographic changes around an oblique breakwater at each step. Owing to the occurrence of longshore sand transport from outside to inside the wave-shelter zone, sand was deposited on the lee of the breakwater after 5×10^3 steps, and sand fell down into the deep area immediately landward of the breakwater while forming a steep slope of angle of slope of sand (**Figure 20(a)**). In contrast, beach erosion far from the breakwater was gradual. With time, sand deposition behind the oblique breakwater continued, and a large amount of sand was deposited inside the port with filling

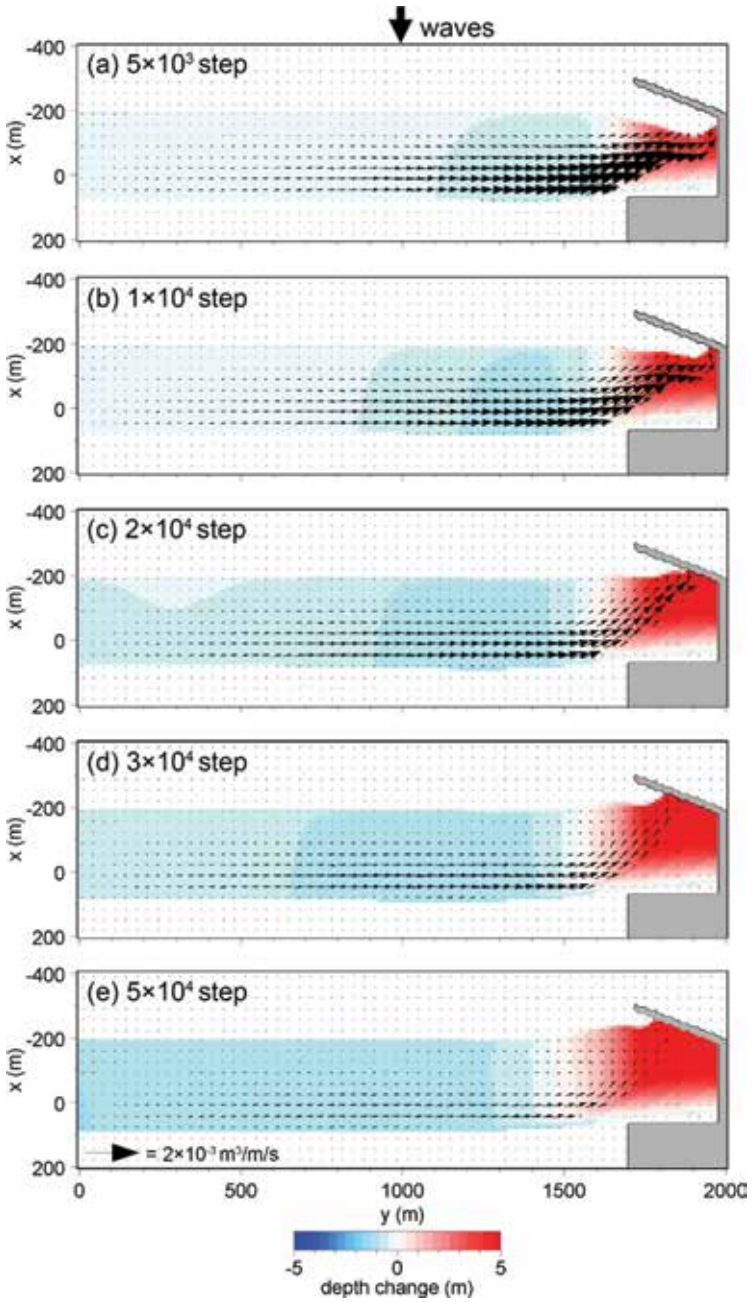

Figure 21.
Topographic changes and sand transport flux around an oblique breakwater.

up of the whole area up to 5×10^4 steps, as in the successive changes in topography shown in **Figure 20**.

As regards the sand transport flux at each stage, strong rightward longshore sand transport was induced in the area shoreward of the tip of the oblique breakwater, and the sand transport flux diminished with the sand accumulation inside the wave-shelter zone, as shown by the successive changes in sand transport flux in the vicinity of the port breakwater in **Figure 21**. In reality, such sand deposited on the lee of the wave-shelter zone of the breakwater would have been removed in general to maintain the navigation channel. In such a case, the shoreline recession outside the wave-shelter zone significantly increases, because total amount of sand on the nearby coast decreases by repeated removal of sand.

The shoreline recession and advance outside and inside the wave-shelter zone of an oblique breakwater are shown in **Figure 22**. A large amount of sand was deposited in the wave-shelter zone, resulting in a large shoreline advance, whereas outside the wave-shelter zone, the shoreline recession was much smaller than that inside the wave-shelter zone.

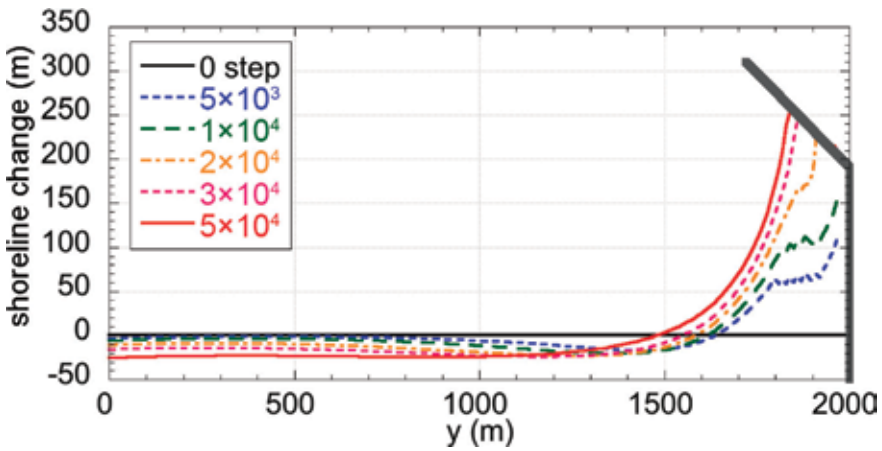

Figure 22.
Shoreline recession and advance outside and inside wave-shelter zone, respectively, formed by an oblique breakwater.

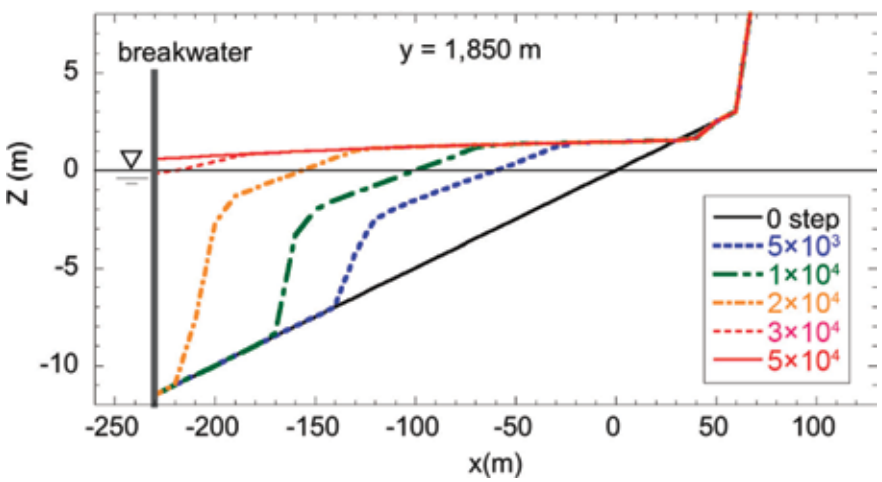

Figure 23.
Change in longitudinal profile along transect y = 1850 m.

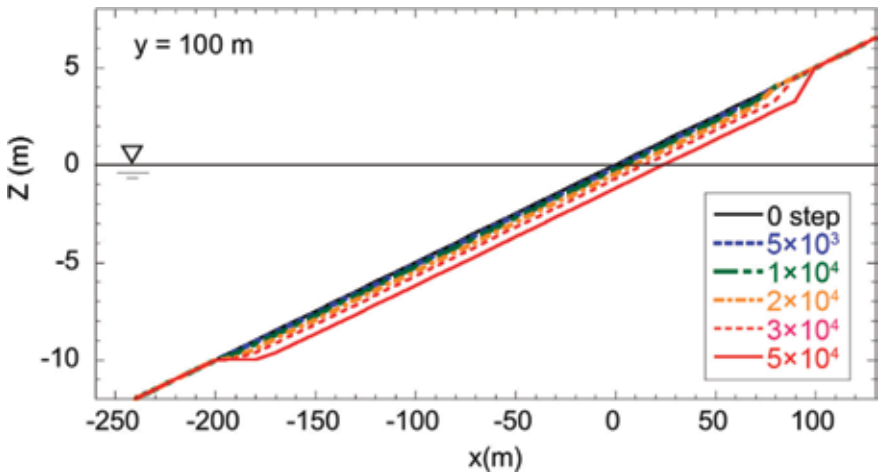

Figure 24.
Change in longitudinal profile along transect y = 100 m.

Figures 23 and **24** show the change in longitudinal profiles along transects y = 1850 m in the accumulation area and y = 100 m in the eroded area outside the wave-shelter zone. A large amount of sand was deposited immediately behind the breakwater with the formation of steep slope of the angle of slope. In contrast, far from the wave-shelter zone, the longitudinal profile retreated parallelly, and a scarp was formed on the backshore.

6. Sand deposition inside a port surrounded by an oblique breakwater and a jetty

6.1 Calculation conditions

A calculation domain of 2000 m length and 600 m width in the longshore and cross-shore directions, respectively, was adopted, similarly to that in the former cases. **Figure 25** shows the initial topography of the coast and the setup of an oblique breakwater, which was constructed at the right corner of the calculation

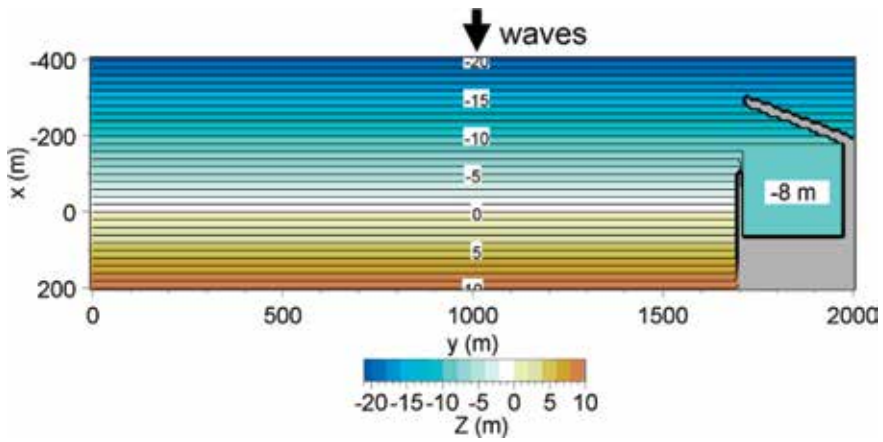

Figure 25.
Initial topography of coast and setup of oblique breakwater and jetty.

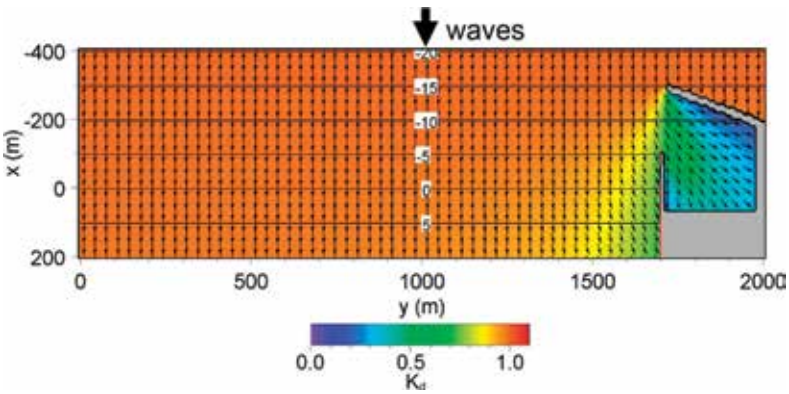

Figure 26.
Wave field around port breakwater and a jetty.

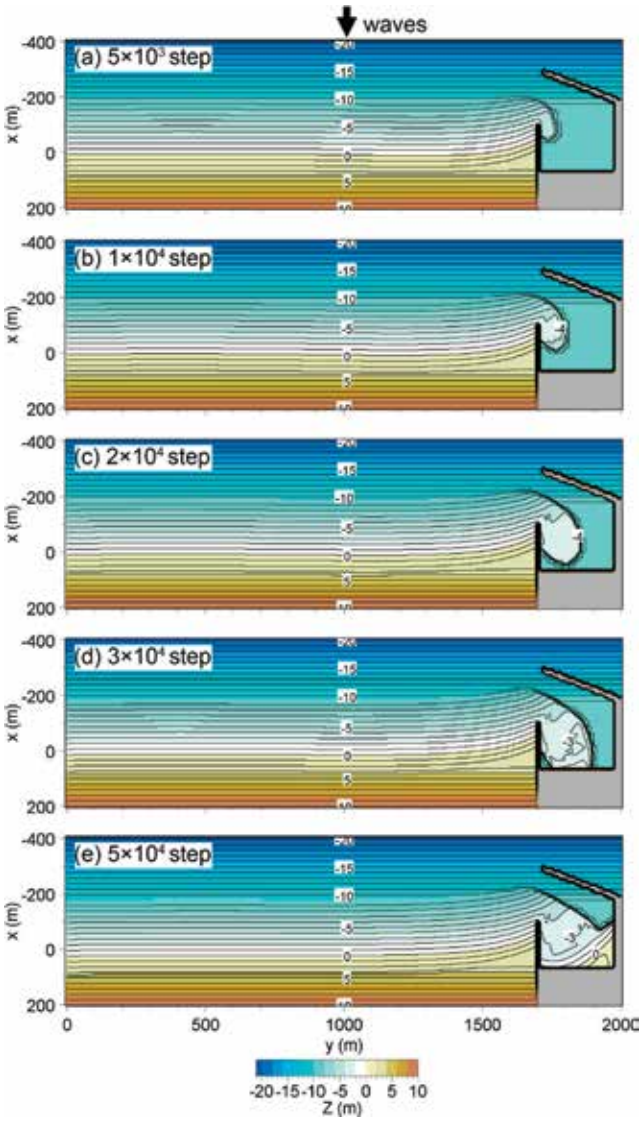

Figure 27.
Successive beach changes inside port and erosion on the nearby coast.

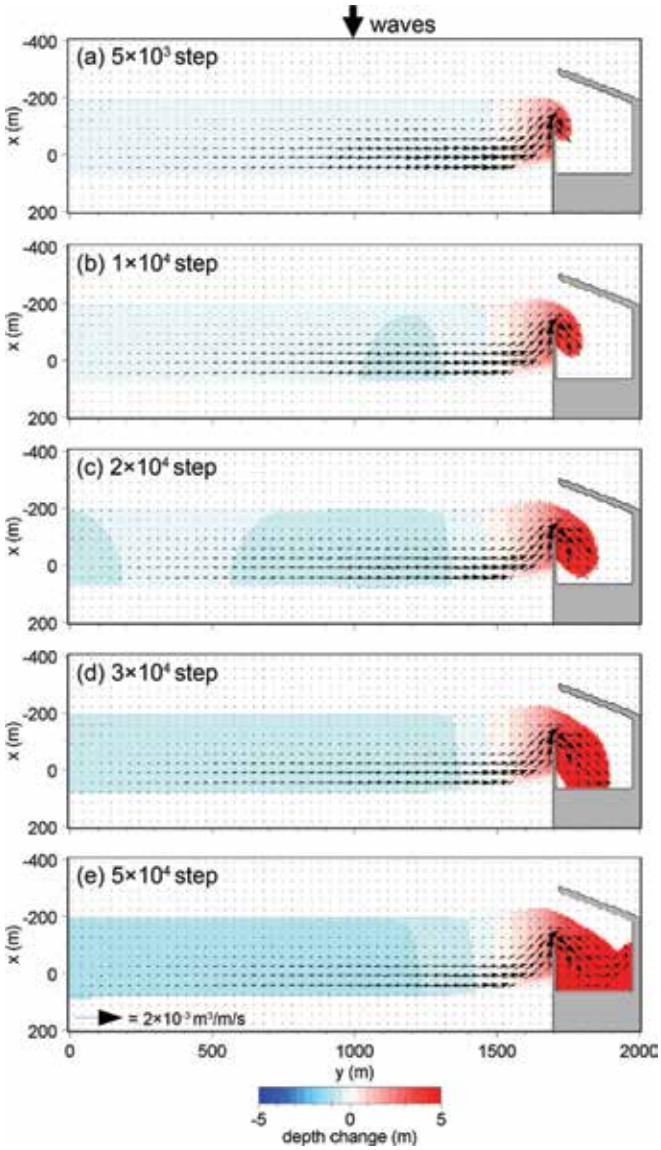

Figure 28.
Sand transport flux corresponding to beach changes shown in ***Figure 27****.*

domain, together with a jetty with a point depth of 5 m to prevent sand from depositing inside the port. At the initial stage, the depth of the port is maintained as a constant depth of 8 m, and an impermeable jetty separates the sandy beach of a slope of 1/20 and the port area. The wave field which will be affected by the extension of the breakwater was determined similarly by the angular spreading method for irregular waves [1], assuming that waves with a breaker height of H_b = 3 m were incident normal to the shoreline on a straight coast. The wave-sheltering effect of an oblique breakwater was evaluated similarly to the method in the case of the detached breakwater, as described in Section 3. In the calculation of beach changes, h_R and h_c were assumed to be 3 and 10 m, respectively, in the zone without the wave-sheltering effect far from the oblique breakwater. In the wave-shelter zone, the berm height h_R' and the depth of closure h_c' were calculated by the same method described in Section 5 ($h_R' = K_d h_R$ and $h_c' = K_d h_c$).

Figure 26 shows the wave field around the port with a jetty at the mouth of the port. Because of the wave-sheltering effect of the breakwater, longshore sand transport toward the wave-shelter zone was induced. The calculation conditions in this case are the same as in Section 5 (**Table 4**).

6.2 Calculation results

Figure 27 shows the successive beach changes inside the port and erosion on the nearby coast. Rightward longshore sand transport took place because of the wave-sheltering effect of the oblique breakwater, and such sand transport turned around the tip of the jetty, causing the sand deposition immediately right of the jetty. Gradual deposition of sand inside the port was well predicted, as shown in **Figure 27(a)-(e)**. The shape of the sand deposition area was similar to a sand spit with a flat top and steep slope around the sand deposition area. **Figure 28** shows the sand transport flux corresponding to the beach changes shown in **Figure 27** at each step. Strong sand transport occurred around the tip of the impermeable jetty, and such

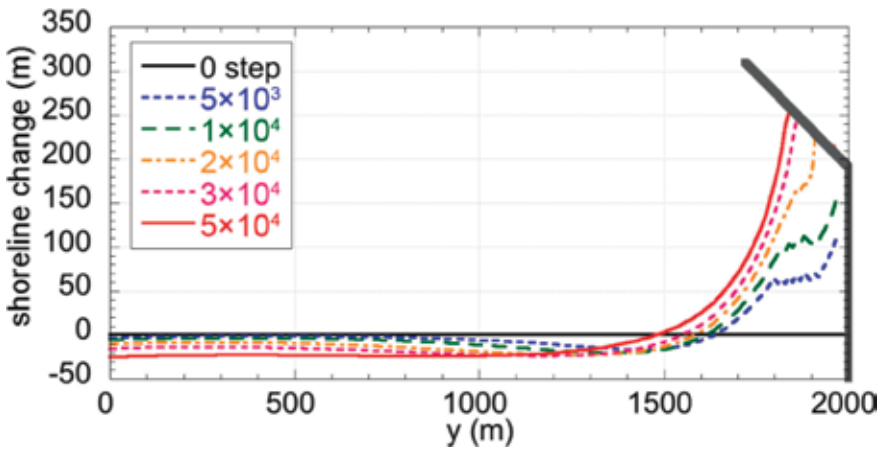

Figure 29.
Shoreline changes around port.

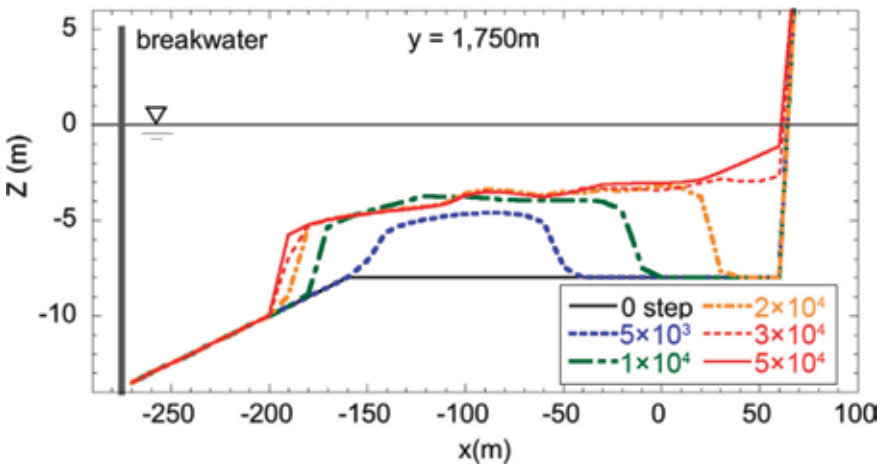

Figure 30.
Changes in longitudinal profiles along transect y = 1750 m.

sand transport flux continued for a long time, regardless of the time steps, as shown in **Figures 28(a)-(e)**. Finally, erosion occurred over a widespread area even in the area far from the offshore breakwater, whereas a large amount of sand accumulated behind the breakwater.

The shoreline changes around the port can be drawn as in **Figure 29**. The shoreline recession continued with time, even though accretion area did not increase. This is because a large amount of sand was deposited in the port area with a large water depth. Finally, the changes in longitudinal profiles along transect y = 1750 m across the sand deposition area and transect y = 100 m across the erosion zone are shown in **Figures 30** and **31**, respectively. Along transect y = 1750 m, sand deposition zone with a flat depth of approximately 3 m expanded over time. In contrast, in the erosion zone, longitudinal profiles retreated parallel each other.

The effect of a jetty extended at the entrance of the port in preventing sand from depositing inside the port can be evaluated in terms of the volume of sand deposited inside the port with/without a jetty. **Figure 32** shows the change in sand volume

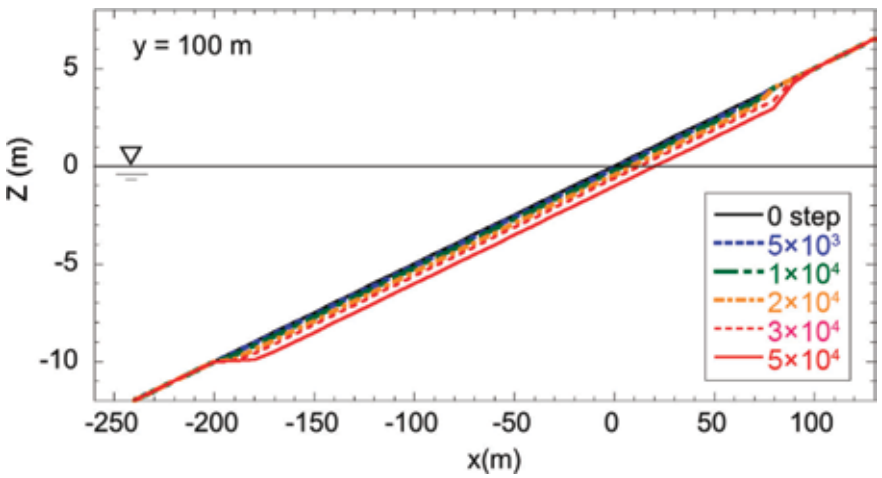

Figure 31.
Changes in longitudinal profiles transect y = 100 m.

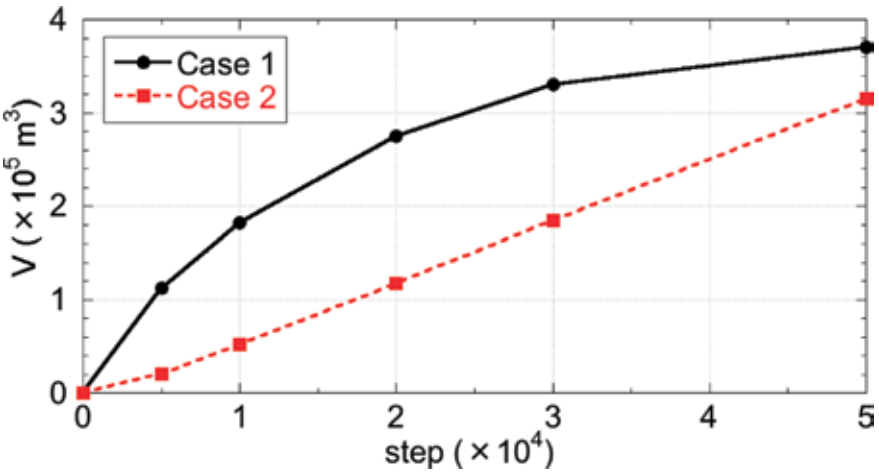

Figure 32.
Change in sand volume accumulated inside port in Cases 1 and 2.

accumulated inside the port. At the initial stage, the rate of sand deposition in Case 1 without a jetty was very rapid compared with that in Case 2, but the difference between two cases decreased with time.

7. Conclusions

In Chapter 3, beach changes when groynes, detached breakwaters, and an oblique breakwater were constructed on a coast with parallel contours were predicted using the Types 1 and 2 BG model together with the prediction of the beach changes when offshore sand mining was carried out. The Types 1 and 2 BG model became a useful tool to solve these beach changes, which were frequently encountered in practical engineering. The Type 2 BG model that was employed in the present study was successfully used for the prediction of lakeshore changes associated with the extension of an offshore breakwater [6], and the prediction of the beach changes caused by not only the imbalance in longshore sand transport but also ground subsidence on south Kujūkuri Beach [7]. Such results can be referred in the original papers [6, 7].

As another application of the Type 2 BG model, the mechanism of sand deposition inside a fishing port was predicted in [8], and the Type 2 BG model was used for the prediction of beach changes triggered by the construction of a causeway on a coral reef coast on Miyako Island, Okinawa, in [9].

Author details

Takaaki Uda[1*], Masumi Serizawa[2] and Shiho Miyahara[2]

1 Public Works Research Center, Tokyo, Japan

2 Coastal Engineering Laboratory Co., Ltd., Tokyo, Japan

*Address all correspondence to: uda@pwrc.or.jp

IntechOpen

© 2018 The Author(s). Licensee IntechOpen. Distributed under the terms of the Creative Commons Attribution - NonCommercial 4.0 License (https://creativecommons.org/licenses/by-nc/4.0/), which permits use, distribution and reproduction for non-commercial purposes, provided the original is properly cited. BY–NC

References

[1] Uda T. Japan's Beach Erosion–Reality and Future Measures. 2nd ed. Singapore: World Scientific; 2017. 530 p

[2] Serizawa M, Uda T, San-nami T, Furuike K. Three-dimensional model for predicting beach changes based on Bagnold's concept. In: Proceedings of 30th ICCE; 2006. pp. 3155-3167

[3] Serizawa M, Uda T, San-nami T, Furuike K, Ishikawa T. BG-model predicting three-dimensional beach changes based on Bagnold's concept and applications. In: Proceedings of 4th International Conference on Asian and Pacific Coasts 2007; 2007. pp. 1165-1179

[4] Ozasa H, Brampton AH. Model for predicting the shoreline evolution of beaches backed by seawalls. Coastal Engineering. 1980;**4**:47-64

[5] Uda T, Kawano S. Development of a predictive model of contour line change due to waves. In: Proceedings of JSCE, No. 539/II-35; 1996. pp. 121-139. (in Japanese)

[6] Uda T. Numerical simulation of formation of cuspate foreland behind an offshore breakwater built in a lake. In: 8th International Conference on Asian and Pacific Coasts (APAC 2015), Procedia Engineering. Vol. 116; 2015. pp. 478-485

[7] Uda T, Yoshida R, Todoroki T. Beach changes triggered by imbalance of longshore sand transport and ground subsidence on south Kujukuri Beach. In: Coastal Sediments'15, CD-Rom, No. 34; 2015. pp. 1-14

[8] Ohki Y, Uda T, Miyahara S, Serizawa M, San-nami T, Sumita A. Analysis of mechanism of sand deposition inside a fishing port using BG model. In: Proceedings of the 7th International Conference on Asian and Pacific Coasts 2013; 2013. pp. 32-39

[9] Uda T, Gibo M, Ishikawa M, Miyahara S, San-nami T, Serizawa M. Change in carbonate beach triggered by construction of a bridge on Irabu Island and its simulation using BG model. In: Proceedings of the 7th International Conference on Asian and Pacific Coasts 2013; 2013. pp. 24-31

Chapter 5

Beach Changes on Coast Subject to Waves and Seaward or Shoreward Strong Currents

Takaaki Uda, Masumi Serizawa and Shiho Miyahara

Abstract

Beach changes on a coast subject to waves and seaward or shoreward strong currents were predicted using the Type 7 and 8 BG models. The formation of an ebb tidal delta subject to strong ebb tidal currents was studied first, taking the Imagire-guchi inlet connecting Lake Hamana with the Pacific Ocean as an example, and the long-term evolution of the tidal inlet was investigated using the bathymetric survey data. Then, the formation of a dynamically stable ebb tidal delta was predicted. Regarding the beach changes on a coast subject to waves and shoreward strong currents, the Type 8 was applied to the Kaike coast, where an artificial reef was constructed in place of a detached breakwater, resulting in the occurrence of strong shoreward currents over the artificial reef. A stable cuspate foreland behind a detached breakwater disappeared after the conversion of a detached breakwater into an artificial reef, suggesting that the artificial reef was less effective in sand deposition effect than the detached breakwater. Such beach changes were numerically predicted.

Keywords: ebb tidal delta, Lake Hamana, Imagire-guchi inlet, artificial reef, Kaike coast

1. Introduction

In predicting beach changes on a coast subject to not only waves but also seaward or shoreward strong currents, the effect of both waves and strong currents must be taken into account. As the beach changes on a coast subject to waves and seaward strong currents, the formation of an ebb tidal delta under strong ebb tidal currents at an inlet was considered, taking the Imagire-guchi inlet connecting Lake Hamana with the Pacific Ocean, as an example, and the long-term evolution of the tidal inlet was studied using the bathymetric survey data. The past studies have revealed that the jetty at this inlet blocks predominant westward longshore sand transport, causing downcoast erosion. However, not only shoreline changes but also complicated, large-scale 3-D beach changes have occurred around this tidal inlet due to the strong ebb tidal currents along with the action of rough waves from the Pacific Ocean. Sand supplied from upcoast has flowed out to the offshore zone, forming a large ebb tidal delta. In the comprehensive management of the coast, the loss of sand into the offshore zone is of importance, but the quantitative prediction of the bathymetric changes around this tidal inlet was difficult in the past because of the combined action of waves and tidal currents. In Section 2, bathymetric changes between 1978 and 2005 around this inlet, for which the characteristics of tidal currents have been

IntechOpen

measured by Syamsidik et al. [1], were investigated, and the evolution of an ebb tidal delta and bathymetric changes were predicted using the Type 7 BG model [2, 3].

It is well known that strong shoreward currents are induced by the wave breaking on the artificial reef, i.e., a kind of submerged breakwater, resulting in significant beach changes around the artificial reef. In Section 3, the Kaike coast was adopted as an example, where an artificial reef was reconstructed in place of a detached breakwater and then strong shoreward currents were induced over the artificial reef, causing significant beach changes around the artificial reef. The beach changes associated with the conversion from the detached breakwater to an artificial reef on this coast were measured, and the Type 8 BG model was used to predict beach changes [4]. It was concluded that a stable cuspate foreland behind a detached breakwater disappeared after the conversion of a detached breakwater into an artificial reef, implying that the artificial reef was less effective in sand deposition effect than the detached breakwater.

2. Prediction of formation of dynamically stable ebb tidal delta

2.1 General condition of Imagire-guchi jetty

A jetty had been built at the Imagire-guchi inlet to stabilize the tidal inlet and to enhance the safety of the navigation of fishing boats in Maisaka fishing port located inside the lake, as shown in **Figure 1** [2].

This jetty blocked predominant westward longshore sand transport, causing accretion upcoast and downcoast erosion, and a part of sand supplied from the upcoast has transported offshore by ebb tidal currents, forming a large ebb tidal delta and causing loss of a part of foreshore sand. The bathymetric changes associated with the extension of Imagire-guchi jetty were studied based on the bathymetric survey data in the previous work [2]. The channel connecting Lake Hamana with the Pacific Ocean and the parallel jetty shown in **Figure 1** had already been built by 1964. By 1973, an oblique jetty of 200 m length had been extended at the tip of the east jetty; this oblique jetty forced the direction of ebb tidal currents clockwise, and this accelerated the southwestward development of the foreset slope together with the blockage of westward

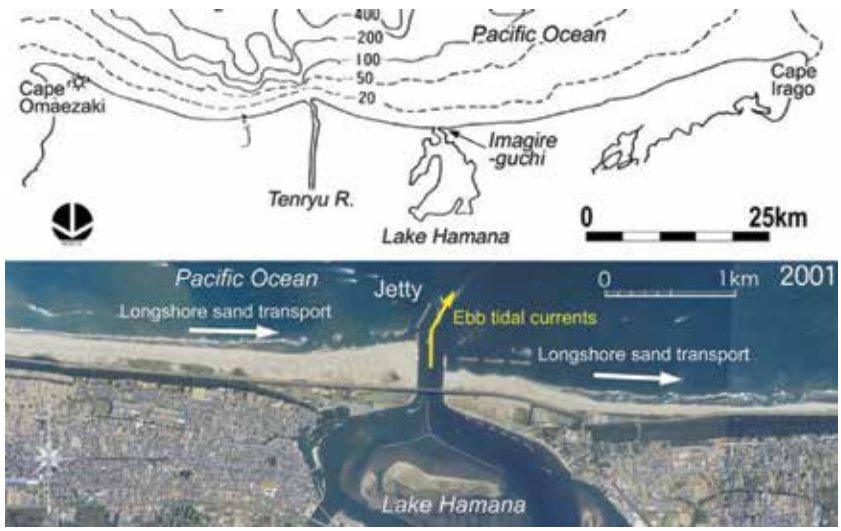

Figure 1.
Location of Imagire-guchi inlet on Enshu-nada coast.

longshore sand transport [2]. Furthermore, two detached breakwaters had been built by 1990 and another by 1994 west of the inlet. Finally, the present shoreline, as shown in **Figure 1**, was formed around the Imagire-guchi inlet.

2.2 Calculation conditions

The evolution of ebb tidal delta offshore of Imagire-guchi jetty was predicted using the Type 7 BG model. To this purpose, the coastal domain was discretized in 2-D elements with dimensions Δx and Δy. Given the initial topography, H_b, α_b, h_c, h_R, the equilibrium slope, and various conditions of the ebb tidal currents, sand transport fluxes due to waves and the ebb tidal currents were calculated from Eqs. (43) and (45) in Chapter 2, respectively. Finally, the sum of them was obtained from Eq. (42) in Chapter 2, and the beach changes after Δt were calculated from the continuity equation of the sand. These calculations were repeated.

For the boundary conditions, sand transport across the boundary was set to be 0 at the structural boundary. **Figure 2** shows the initial bathymetry. Although both actions of waves and ebb tidal currents simultaneously occur at the tidal inlet, it was assumed that sand supply during the ebb tidal currents was none. In the calculation, the change in wave energy intensity associated with the wave refraction was neglected for simplicity, and we assumed that $\cos\alpha_b = 1$. In addition, the lower-limit depth of bathymetric changes due to tidal currents h_{c2} was assumed to be equal to the depth of closure due to waves, h_c, and the upper-limit depth of bathymetric changes due to tidal currents h_{R2} was taken at the mean sea level. In the calculation of Eq. (48) in Chapter 2, a minimum value of $h_0 = 1$ m was assumed for h.

The distribution of the ebb tidal currents through a tidal inlet is very similar to that of a jet flowing into a still water, which in turn is similar to the distribution of the wave diffraction coefficient of the diffracted waves through the opening of the impermeable breakwaters [2]. Taking this fact into account, the angular spreading method for irregular waves [5] was introduced to calculate the ratio of the velocity K_{V1}, as shown in Eq. (49) in Chapter 2, under a constant depth condition. Assume that the directional spreading of a jetlike flow at the tidal inlet is given by the directional spreading function of wave energy $G(\theta)$ in the angular spreading method and that the ratio of the wave energy, which is given by the square of the wave diffraction coefficient, is equal to the velocity ratio. Then, the reduction of the velocity of a jetlike flow can be evaluated while satisfying the mass conservation condition.

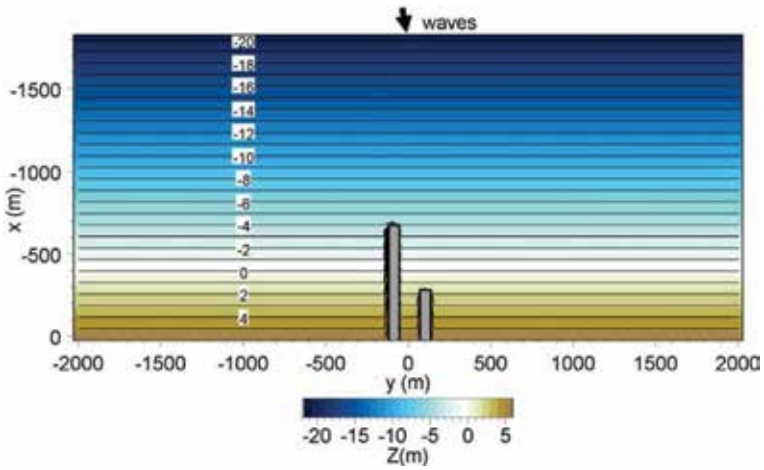

Figure 2.
Initial bathymetry.

When setting the range of the flow direction with respect to the center line of the jetlike flow as $\theta = -\theta_{max}$, θ_{max}, θ_{max} becomes $\pi/2$ for the irregular waves, but the range becomes as narrow as $\theta_{max} = 11°$ for a jetlike flow. Furthermore, the diffusivity of a jetlike flow can be evaluated by a parameter A_0 in the angular spreading method [5] expressing the directional distribution function of the wave energy. Finally, regarding the tidal inlet as an opening of the impermeable breakwaters, irregular waves propagating offshore were generated, and the wave diffraction coefficient was calculated using the angular spreading method. The ratio of the wave energy and wave direction of diffracted waves was substituted for the ratio of flow velocity and the direction of the flow, respectively, assuming that θ_{max} and A_0 are 15° and 5, respectively.

In this study, bathymetric survey data collected since 1978 were used to validate the numerical model, and the sand movement around the ebb tidal delta and the formation of dynamically stable topography were investigated. Given the parallel contours before the construction of the jetty as the initial condition, the bathymetry in 1978 was first predicted, and then the bathymetric changes since 1978 were predicted, enabling the comparison of the predicted development of the ebb tidal delta with measurements. During this period, the ebb tidal currents were intensified because of the scouring at the inlet associated with the extension of the jetty. The coefficient of intensity of sand transport due to ebb tidal currents, therefore, was linearly increased over time from $K_R = 0.1$ in 1978 to 0.3 in 2005 in the calculation.

The east jetty at Imagire-guchi is longer than the west jetty, causing the development of oblique ebb tidal currents. The effect of oblique currents between jetties of different lengths was modeled by a jet obliquely emerging from the inlet at an angle of 30° relative to the direction normal to the shoreline, so that the assumed direction of the jet currents coincides with that of the ebb tidal currents measured at Imagire-guchi inlet by Syamsidik et al. [1]. **Figure 3** shows the velocity distribution when ebb tidal currents obliquely flow out of the inlet.

The calculation conditions are summarized in **Table 1**. Assuming that the breaker height H_b was 3 m and the incident angle of waves at the breaking point was $\alpha_b = 10°$, the coefficient of longshore sand transport K_y was adjusted so that the initial longshore sand transport was 2.0×10^5 m^3/year, by which the best fit results for the beach changes were obtained, and the dynamically stable condition was reproduced by setting $K_x = 0.2K_y$, where K_x is the coefficient of cross-shore sand transport. The calculation results were presented in a coordinate system (X, Y), in which the X- and Y-axes were taken to be the longshore and cross-shore directions (positive for offshore), respectively.

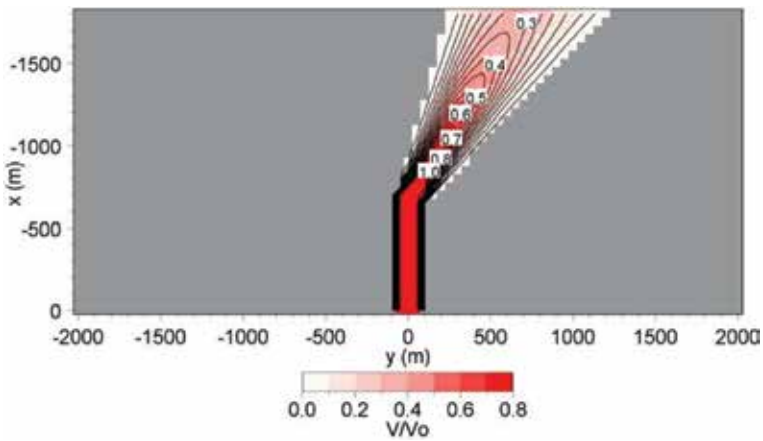

Figure 3.
Example of velocity distribution.

Calculation method	Type 7 BG model
Initial topography	Uniform slope of 1/70
Equilibrium slope	$\tan\beta_c = 1/70$
Slope of angle of repose	$\tan\phi = 1/2$
Wave conditions	H_b = 3 m, breaker angle $\theta_w = 10°$, H_{b0} = 1 m in calculating $(EC_g)_{b0}$
Depth distribution of intensity of longshore sand transport	Uniform
Coefficients of longshore and cross-shore sand transport	$K_y = 0.0105$ and $K_x = 0.2K_y$
Berm height	h_R = 3 m
Depth of closure	h_c = 8 m
Coefficient of sediment transport due to ebb tidal currents	K_R = 0.1–0.3 for reproduction and K_R = 0.3 for prediction
Upper depth of bathymetric changes induced by tidal currents	h_{R2} = 0 m
Lower depth of bathymetric changes induced by tidal currents	h_{c2} = 8 m
Reference depth of inlet	h_0 = 1 m
Minimum depth for the use of correction term of current velocity	h = 1 m
Mesh size	$\Delta x = \Delta y$ = 50 m
Time interval	Δt = 5 hrs
Calculation duration	27 years between 1978 and 2005 in reproduction, 10 years in prediction
Boundary conditions	$q_x = 0$ at landward and offshore boundaries $dq_y/dy = 0$ at side boundaries

Table 1.
Calculation conditions.

2.3 Calculation results

Figure 4 shows the results of the numerical simulation of the formation of the ebb tidal delta with the sand transport flux, given the initial parallel contours and the velocity distribution (**Figures 2** and **3**), and assuming that waves are obliquely incident from the left. The sand was continuously transported westward (rightward in **Figure 4**) along the outer margin of the ebb tidal delta, forming a dynamically stable beach. Finally, an ebb tidal delta with an oblique principal axis developed offshore of the tidal inlet together with the formation of a steep foreset slope in the zone deeper than 10 m depth. Moreover, a pair of circulating sand transport systems developed on both sides of the principal axis of the jetlike offshore sand transport.

Figure 5 shows the bathymetry measured in 2005 and the change in the 8-m-depth contour over time. It is clear that the ebb tidal delta has developed over time. The predicted and measured bathymetric changes between 1978 and 2005 are shown in **Figure 6**. A sand deposition zone was formed along the margin of the ebb tidal delta, whereas erosion occurred in an extensive area around the tip of the jetty. The predicted and measured topographic changes are in good agreement.

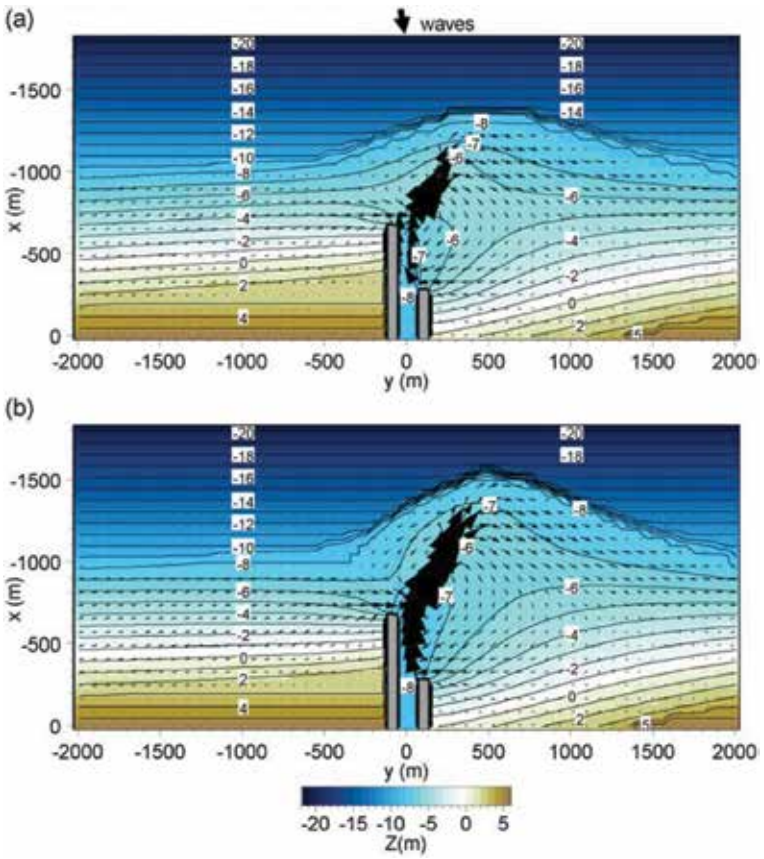

Figure 4.
Predicted bathymetries around Imagire-guchi inlet in 1978 and 2005 (a) Predicted bathymetry in 1978, (b) Predicted bathymetry in 2005.

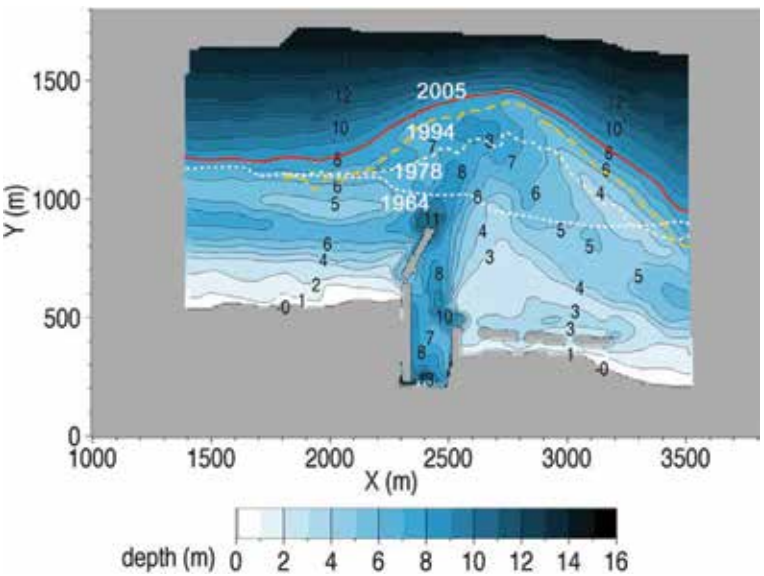

Figure 5.
Measured bathymetry in 2005 and change in 8 m contour over time [3].

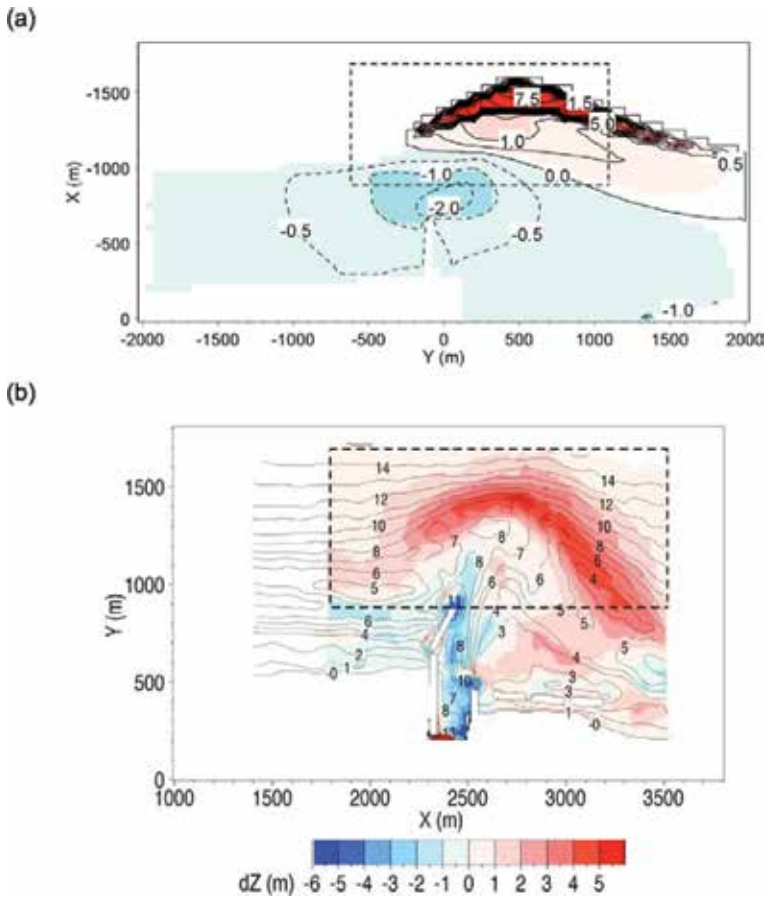

Figure 6.
Measured and predicted bathymetric changes between 1978 and 2005 [3] (a) predicted, (b) measured.

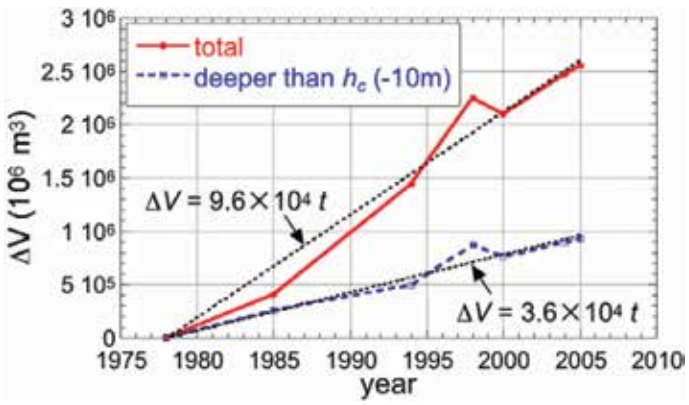

Figure 7.
Change in sand volume over time in rectangular zone under study [3].

Based on the bathymetric survey data since 1978, the total volume of sand forming the ebb tidal delta and deposited in the zone deeper than h_c of 10 m was calculated. **Figure 7** shows the change in sand volume in a rectangular zone shown by the broken line in **Figure 6**. The total volume of sand increased at a rate of 9.6×10^4 m^3/year,

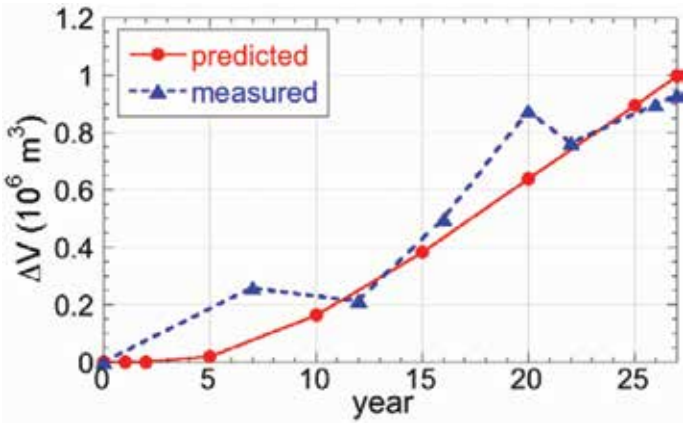

Figure 8.
Predicted and measured volumes of sand transported offshore into the zone deeper than 10 m [3].

3.6×10^4 m^3/year of which was transported offshore into the zone deeper than 10 m. The predicted and measured volumes of sand transported offshore into the zone deeper than 10 m can be compared as in **Figure 8**, and both results agree well.

3. Prediction of beach changes around artificial reef built on Kaike coast

3.1 General conditions

The Kaike coast with a 20-km stretch is the marginal coast along the Yumigahama Peninsula in Miho Bay in Tottori Prefecture, Japan, as shown in **Figure 9**. This peninsula has developed as a tombolo by the deposition of sand supplied from the Hino River owing to the wave-sheltering effect of the Shimane Peninsula. After the World War II, beach erosion along the Kaike coast occurred owing to the decrease in sand supply from the Hino River. A famous Kaike spa is located near the shoreline immediately west of the Hino River mouth, and, therefore, the beach around this spa was protected by groynes in the 1960s. Then, 12 detached breakwaters were constructed between 1971 and 1982 as a measure against beach erosion, and soon

Figure 9.
Location of Kaike coast facing the Sea of Japan [4].

Figure 10.
Aerial photograph of beaches around 12 detached breakwaters on Kaike coast taken in 2003 [4].

after the construction of the detached breakwaters, tombolos were formed behind the detached breakwaters.

Figure 10 shows the aerial photograph in 2003 of the detached breakwaters, in which the number of the breakwaters corresponds to the order of the construction. Although these detached breakwaters and tombolos have been stable until 2003, concrete armor units placed immediately offshore of the shoreline near the spa spoiled the scenic beauty as a recreational beach and extremely narrowed the swimming space, and the foreshore slope was excessively steepened at the opening of the detached breakwaters. Therefore, an artificial reef with crests was constructed in place of the No. 3 detached breakwater in 2005. After the conversion, the tombolo was reduced in size because of the generation of shoreward currents on the artificial reef, and severe scouring occurred at the opening between the artificial reef and the existing detached breakwaters owing to the development of rip currents [4]. Here, the beach changes were predicted using the Type 8 BG model, in which the effect of not only waves but also strong nearshore currents was taken into account, as well as increase in h_c due to the strong currents.

3.2 Beach changes after construction of artificial reef

Figure 11 shows the bathymetry measured in July 2002 before the conversion of the No. 3 detached breakwater into the artificial reef. In 2002, a tombolo was formed behind the Nos. 1, 3, and 5 detached breakwaters owing to their wave-sheltering effect, and semicircular contours were formed at the openings between the detached breakwaters owing to their wave diffraction effects. In addition, the foreshore slope became as steep as 1/7 at the central part of the opening. One of the objectives of converting the detached breakwater into an artificial reef was to create a gentle slope near the shoreline that is considered to be safe for recreational use. The artificial reef had a crown height of 0.5 m below MSL and a width of 40 m, as well as two rows of crests that enhance the wave attenuation effect. Here, HWL and LWL of this coast are +0.36 and − 0.56 m above MSL. After the conversion of the reef, storm waves associated with a low pressure hit the artificial reef in December 2005.

Owing to the wave observation at a depth of 8 m offshore of the artificial reef, storm waves with a maximum significant wave height of 4.5 m and a wave period of 12 s were measured, and storm waves with a wave height of greater than 3 m continued for 30 h. As a result, the tombolo behind the artificial reef was eroded, and the foreshore disappeared (**Figures 12** and **13**). A flat shallow seabed of 2 m depth was formed behind the artificial reef.

Figure 13 shows the bathymetric changes around the artificial reef before and after the construction of the artificial reef. Not only did the tombolo formed behind the detached breakwater disappear, but also a deep scouring hole with a maximum depth of 7 m was formed at the west end of the artificial reef. The local

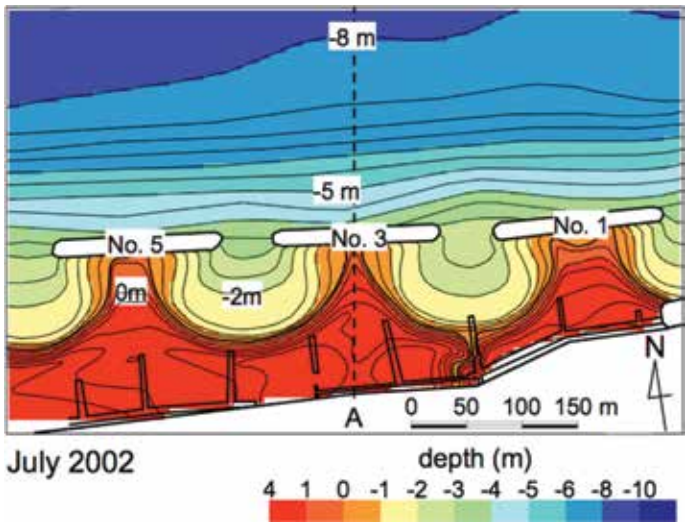

Figure 11.
Bathymetry in July 2002 before conversion of detached breakwater into artificial reef [4].

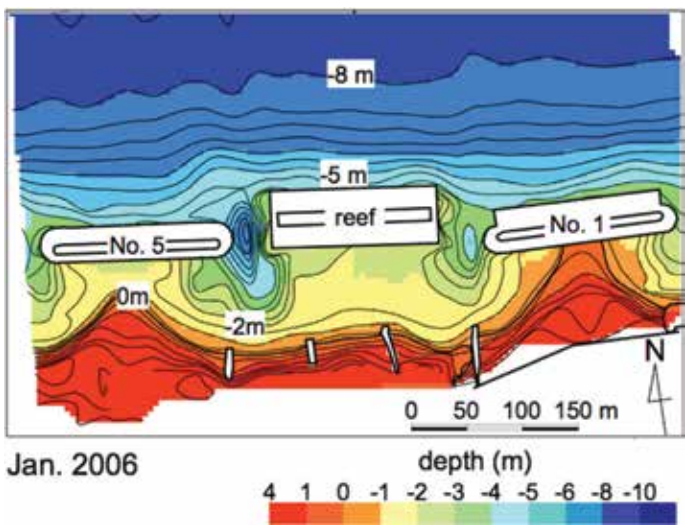

Figure 12.
Bathymetry after storm waves measured in January 2006 [4].

scouring at both ends of the artificial reef showed asymmetry, and the scouring hole at the west opening was larger than that at the east opening. Thus, it is considered that predominant waves were incident from the east, producing westward longshore currents. Furthermore, the tombolo behind the No. 5 detached breakwater west of the artificial reef was eroded and the shoreline retreated, implying the development of westward longshore currents passing through the lee of the No. 5 detached breakwater, which in turn eroded the shoreline on the lee of the No. 5 detached breakwater. Finally, it was found that converting the detached breakwater into an artificial reef caused the disappearance of the tombolo, the local scouring at the opening, and the reduction in the size of the tombolo behind the nearby detached breakwater.

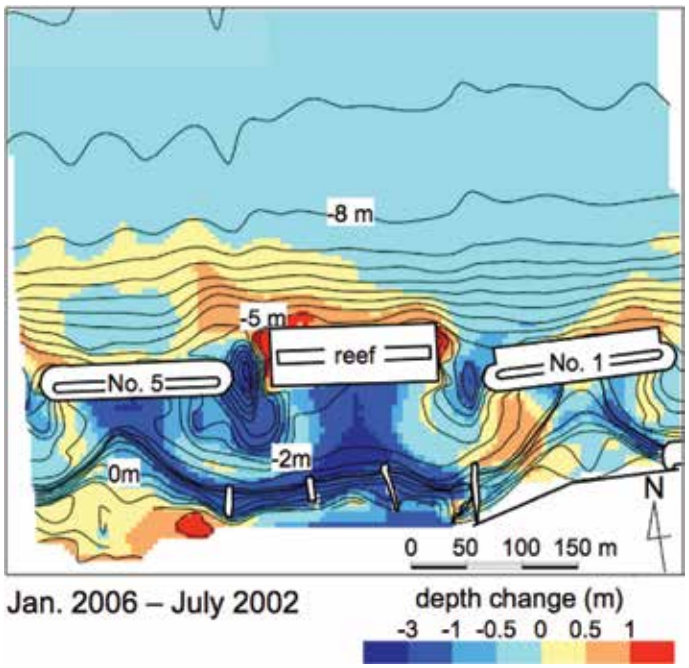

Figure 13.
Bathymetric changes from July 2002 to January 2006 [4].

3.3 Calculation conditions

On the basis of the bathymetric survey data in 2009, a rectangular calculation domain of 1800 m length and 700 m width including the No. 3 detached breakwater, which was later converted into an artificial reef, was adopted. As the initial bathymetry, the condition that tombolos behind the detached breakwaters have sufficiently developed was set (**Figure 14(a)**). The offshore slope was set to be 1/30 in the depth zone between −5 and −8 m and 1/100 deeper than −8 m.

Under these conditions, storm waves with a significant height H_i = 3 m and a period of 8 s were obliquely incident from the right at an angle of θ_i = 10°. The wave field and nearshore currents were recalculated at every 5000 steps of the calculation of the topographic changes. **Table 2** summarizes the detailed calculation conditions. h_R was set to be 3 m, and the equilibrium slope was given as in **Table 2**, depending on the water depth, and the slope of the angle of repose was set to be 1/2.

3.4 Calculation results

3.4.1 Beach changes around detached breakwater and artificial reef

Beach changes owing to a 40-h wave action after all the detached breakwaters were installed were calculated, using the bathymetry in **Figure 14(a)** as the initial bathymetry. The predicted bathymetry and the bathymetric changes are shown in **Figures 14(b)** and **14(c)**. In this case, although the beach was slightly eroded around the detached breakwaters and sand was deposited on the foreshore, beach changes were negligibly small, and the cuspate forelands behind the detached breakwaters were stable, implying that beach changes around the detached breakwaters could be reproduced by the present model.

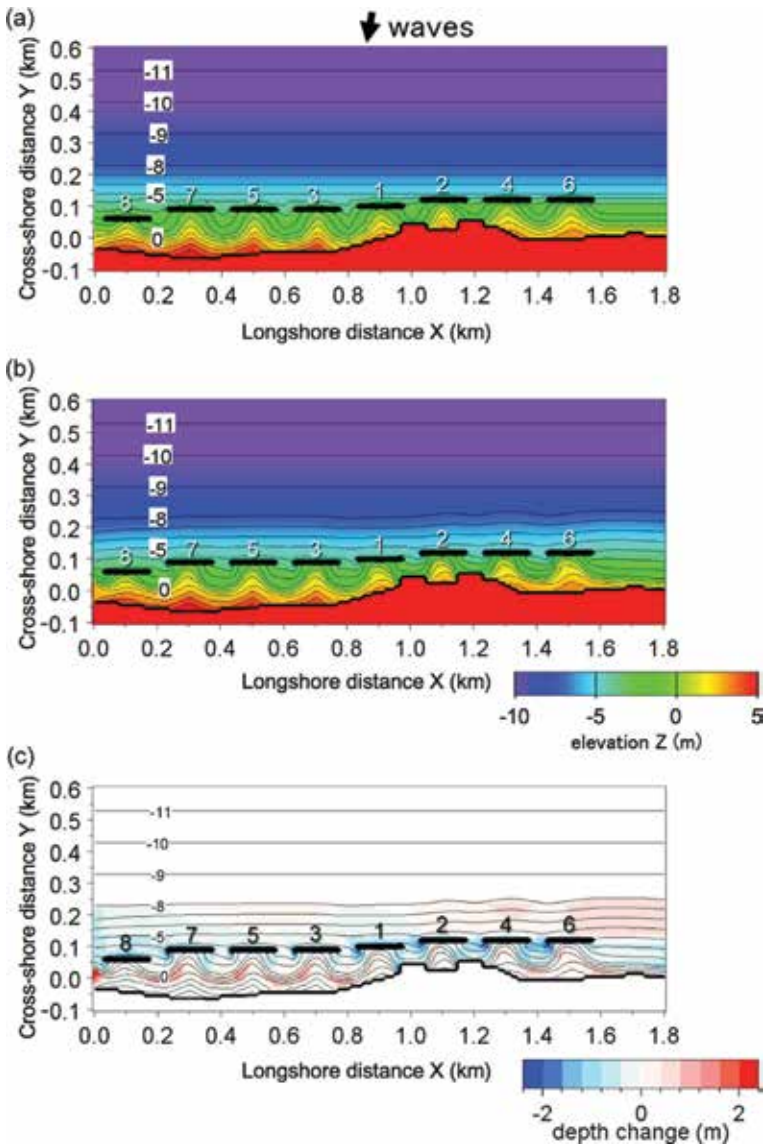

Figure 14.
Predicted bathymetries after a 40-h wave action in case of detached breakwater [4] (a) Initial bathymetry, (b) After 40 hours (10^4 steps), (c) depth changes.

Figure 15(a) shows the initial bathymetry when the No. 3 detached breakwater was converted into an artificial reef. After a 40-h wave action, the tombolo rapidly disappeared, and tombolos with a symmetric shape at the initial stage became asymmetric while inclining leftward behind the No. 5 and No. 7 detached breakwaters west of the artificial reef (**Figure 15(b)**). Also, local scouring occurred at the west end of the artificial reef. The predicted results were in good agreement with the measured results, as shown in **Figure 13**. In the bathymetric changes (**Figure 15(c)**), the beach was eroded not only shoreward of the artificial reef but also near the area between the artificial reef and the No. 5 detached breakwater.

3.4.2 Change in wave field and nearshore currents

The wave field and nearshore currents were compared to investigate the difference between the topographic changes behind the detached breakwater and artificial reef

Calculation model	**Type 8 BG model taking wave and nearshore current fields into account**
Initial bathymetry	Bathymetry before the conversion of the detached breakwater into artificial reef Tombolos were set behind artificial reef Straight parallel contours with beach slope of 1/30 in offshore zone between −5 and − 8 m and that of 1/100 in depth zone deeper than −8 m
Wave conditions	Incident waves: H_I = 3 m, T = 8 s, and wave direction θ_I = −10° relative to normal to initial shoreline
Berm height	h_R = 3 m
Depth of closure	h_c = 2.5H (H: wave height) The increment due to the effect of strong rip currents is evaluated as $h_c = \{1+\alpha(v/u_m)\}h_c$ Here, V = velocity of nearshore currents, u_m = amplitude of seabed velocity due to orbital motion of waves, and a = 0.5 The lower and upper limits of h_c' are 3 and 9 m, respectively
Equilibrium slope	tanβ_c = 1/10 shallower than −1 m tanβ_c = 1/30 between Z = −1 and − 8 m tanβ_c = 1/100 deeper than −8 m
Angle of repose slope	tanϕ = 1/2
Coefficients of sand transport	Coefficient of sand transport due to current $K_c = 7.5 \times 10^{-4}$ Coefficient of sand transport due to wave $K_w = 0.5K_c$
Mesh size	$\Delta x = \Delta y$ = 10 m
Time intervals	Δt = 0.004 h
Duration of calculation	10^4 steps
Boundary conditions	Shoreward and landward ends q_x = 0 and right and left boundaries dq_y/dy = 0
Calculation of wave field	Energy balance Equation [6] • Term of wave dissipation due to wave breaking: Dally et al. [7] model • Mesh size: $\Delta x = \Delta y$ = 10 m • Wave spectrum of incident waves: combination of frequency spectrum of Bretchnider-Mitsuyasu-type and Mitsuyasu-type directional function [8] • Total number of frequency components N_F = 1 and number of directional subdivisions N_θ = 8 • Directional spreading parameter S_{max} = 10 • Coefficient of wave breaking K = 0.17 and Γ = 0.5 • Minimum depth h_{min} = 1 m • Imaginary depth between $Z = -h_0$ and berm height h_R: h_0 = 3 m • Wave energy = 0, where $Z \geq h_R$
Calculation of nearshore currents	• Two-dimensional shallow water momentum equation and continuity Equation [9] • Explicit finite difference method • Mesh size $\Delta x = \Delta y$ = 10 m • Time intervals Δt = 0.014 s • Duration of calculation 5×10^4 steps • Friction coefficient C_f = 0.01 • Lateral diffusion coefficient N = 0.5 [10] • Minimum water depth h_{min} = 1 m
Other remarks	• Γ = 0.55 on crown of artificial reef • Calculation of wave and nearshore currents: every 5000 steps of calculation of beach changes • Wave transmission coefficient of detached breakwater K_t = 0.15

Table 2.
Calculation conditions.

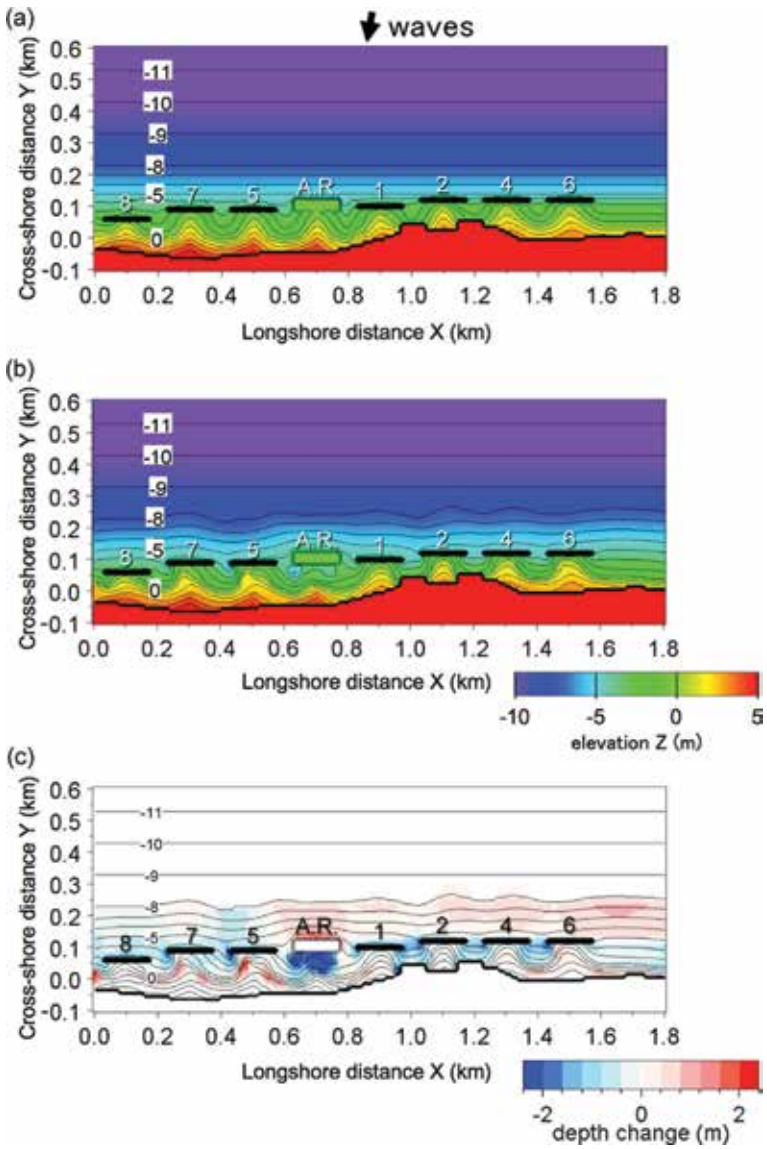

Figure 15.
Predicted bathymetries after a 40-h wave action in case of artificial reef [4] (a) Initial batymetry, (b) After 40 hours (10^4 steps), (c) depth changes.

(**Figures 16** and **17**). Although the wave height distributions around the detached breakwaters and artificial reef are similar, as shown in **Figure 16(a)** and **16(b)**, marked changes can be seen in the nearshore currents. In the case of the detached breakwater, a couple of circulating currents was generated on the lee of the detached breakwaters (**Figure 17(a)**), whereas strong shoreward currents were induced on the reef, and such currents reduced to rip currents obliquely flowing out at the opening between the artificial reef and the existing detached breakwater (**Figure 17(b)**). Because it was difficult for the seawater transported shoreward on the artificial reef to be carried offshore again only by the rip currents, part of the seawater passed through the lee of the detached breakwater and was finally returned to the offshore sea through the openings of the detached breakwaters. The generation of strong shoreward currents on the reef and oblique rip currents in the opening explains the difference between the topographic changes around the detached breakwaters and artificial reef.

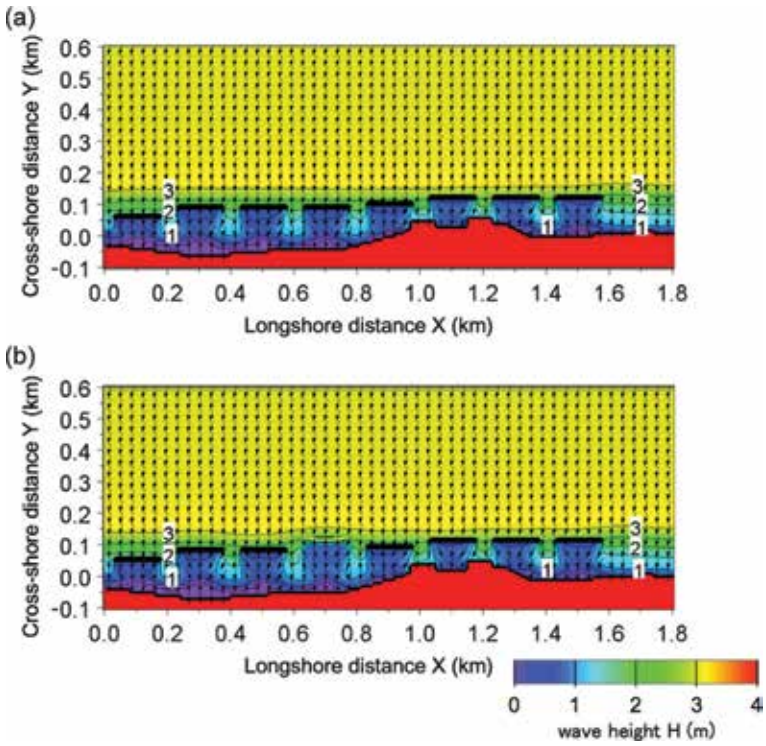

Figure 16.
Wave fields around detached breakwater and artificial reef [4] (a) detached breakwater, (b) artificial reef.

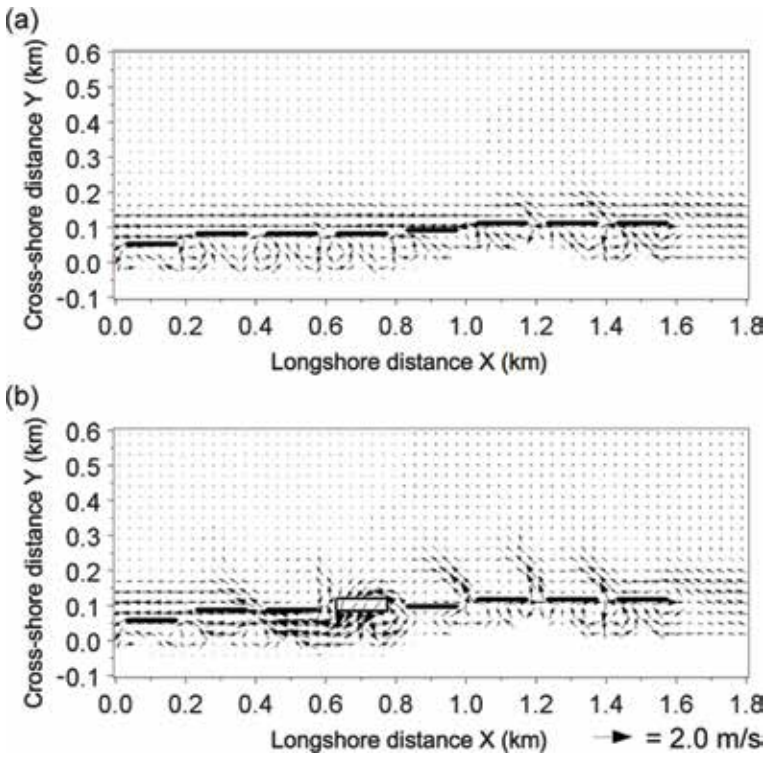

Figure 17.
Nearshore currents around detached breakwater and artificial reef [4] (a) detached breakwater, (b) artificial reef.

4. Conclusions

In Chapter 4, two topics were discussed, and topographic changes were predicted, in which the effects by both waves and strong currents were taken into account: (1) formation of dynamically stable ebb tidal delta (the Type 7 BG model) and (2) beach changes around artificial reef built on Kaike coast (the Type 8 BG model).

1. The development of an ebb tidal delta subject to the actions of waves and strong ebb tidal currents was investigated, taking Imagire-guchi inlet connecting Lake Hamana to the Pacific Ocean as an example. The predicted bathymetric changes were compared with the measured changes, and they were in good agreement.

2. The Type 8 BG model, in which the effect of the sand transport flux due to strong shoreward currents induced by wave breaking on the artificial reef was explicitly included, was used on the Kaike coast, where one of the detached breakwaters was converted into an artificial reef. After the storm, the tombolo behind the artificial reef was eroded, and a local scouring hole was formed in the opening. Given the storm wave conditions, beach changes were predicted. The beach changes were successfully predicted using this model.

3. It was concluded that shoreward currents on the artificial reef and resulted rip currents in the opening played an important role in the beach changes around the artificial reef and that the artificial reef was less effective in sand deposition effect than the detached breakwater.

Acknowledgements

Part of the work described in Chapter 4, i.e., prediction of formation of dynamically stable ebb tidal delta and beach changes around artificial reef built on Kaike coast, was based on the conference paper [3, 4] presented at the 32nd and 33rd Conference on Coastal Engineering in 2010 and 2012, respectively. We would like to express our gratitude for the use of materials.

Author details

Takaaki Uda[1*], Masumi Serizawa[2] and Shiho Miyahara[2]

1 Public Works Research Center, Tokyo, Japan

2 Coastal Engineering Laboratory Co., Ltd., Tokyo, Japan

*Address all correspondence to: uda@pwrc.or.jp

IntechOpen

© 2018 The Author(s). Licensee IntechOpen. Distributed under the terms of the Creative Commons Attribution - NonCommercial 4.0 License (https://creativecommons.org/licenses/by-nc/4.0/), which permits use, distribution and reproduction for non-commercial purposes, provided the original is properly cited. BY–NC

References

[1] Syamsidik, Aoki S, Kato S. Effects of tidal currents and waves on bottom suspended sediment fluxes off two river mouths. Proceedings of 18th International Offshore (Ocean) and Polar Engineering Conference. Vancouver; 2008

[2] Serizawa M, Uda T, San-nami T, Furuike K, Ishikawa T. Model for predicting formation of dynamically stable ebb tidal delta off tidal inlet. In: Proceedings of 31st ICCE. 2008. pp. 2291-2302

[3] Uda T, Serizawa M, San-nami T, Ishikawa T. Prediction of formation of dynamically stable ebb tidal delta and measures for preventing offshore sand loss. In: Proceedings of 32nd ICCE, sediment. 73. 2010. pp. 1-10 https://icce-ojs-tamu.tdl.org/icce/index.php/icce/article/view/1047/pdf_163

[4] Fujiwara H, Uda T, Onishi T, Miyahara S, Serizawa M. Prediction of beach changes around artificial reef using BG model. In: Proceedings of 33rd ICCE, sediment. 77. 2012. pp. 1-12 https://icce-ojs-tamu.tdl.org/icce/index.php/icce/article/view/6532/pdf_533

[5] Uda T. Japan's Beach Erosion: Reality and Future Measures. 2nd ed. Singapore: World Scientific; 2017. 530 p

[6] Mase H. Multidirectional random wave transformation model based on energy balance equation. Coastal Engineering Journal, JSCE. 2001;**43**(4):317-337

[7] Dally WR, Dean RG, Dalrymple RA. A model for breaker decay on beaches. In: Proceedings of 19th ICCE. 1984. pp. 82-97 https://journals.tdl.org/icce/index.php/icce/article/view/3787/3470

[8] Goda Y. Random Seas and Design of Maritime Structures. Tokyo: University of Tokyo Press; 1985. 323 p

[9] Horikawa K. Nearshore Dynamics and Coastal Processes. Tokyo: University of Tokyo Press; 1988. 522 p

[10] Larson M, Kraus NC. Numerical model of longshore current for bar and trough beaches. Journal of Waterway, Port, Coastal, and Ocean Engineering. 1991;**117**(4):326-347

Chapter 6

Formation of Sand Spit and Bay Barrier

Takaaki Uda, Masumi Serizawa and Shiho Miyahara

Abstract

The formation of a sand spit and bay barrier was predicted using the BG model, covering three topics: (1) formation of a bay barrier in flat shallow sea and merging of bay mouth sand spits (Section 2), (2) elongation of a sand spit on a seabed with different water depths (Section 3), and (3) deformation of a sandbar formed at the tip of the Futtsu cuspate foreland owing to a tsunami which propagated into Tokyo Bay after the Great East Japan Earthquake on March 11, 2011 (Section 4). The Type 5 BG model was employed in Section 2, and Type 3 BG model in Sections 3 and 4.

Keywords: sand spit, bay barrier, embayed coasts, Futtsu cuspate foreland

1. Introduction

A barrier island normally develops along the marginal area of a flat shallow sea. Various explanations have been given for the cause of the development of barrier islands: the elongation of a sand spit, the emergence of a longshore bar during the decreasing sea level, and the submergence of a beach ridge during the increasing sea level [1]. Nummedal [2] studied the physical process of the formation of a barrier island and concluded that it is closely related to four factors: the increase in the sea level during the past several thousand years, the longshore distribution of the sand source and the loss of sand, the exchange of sea water across inlets, and the wave energy level. However, the theoretical explanation for the growth of barrier islands as a result of extension of a sand spit was inadequate, and in particular, the effect of the change in water depth to the development of a barrier island was not fully investigated. In Section 2, therefore, this issue was focused. Among the various forms of barrier islands, a bay barrier [3] was taken as an example.

Zenkovich [4] gave an example of a barrier beach closing the bay mouth in a fjord in eastern Kamchatka. The elongation of a sand spit is commonly observed at bay or river mouths, where the direction of the shoreline abruptly changes. Consider a case in which the sand source is located on both sides of a bay. In this case, sand spits are formed near the mouth of a bay by the deposition of sand supplied from upcoast. When the water depth of the bay is sufficiently small, the sandbars can rapidly extend to form a bay barrier enclosing the bay. When the shape of the bay is asymmetrical, the sand spit located offshore has a wave-sheltering effect on the other spit, affecting the topographic changes of the other sand spit, and finally the two spits may merge. Taking these effects into account, the elongation and merging of sand spits at a bay mouth were studied using the Type 5 BG model in Section 2 [5].

IntechOpen

Serizawa and Uda [6] predicted the development of a sand spit using the BG model, and their results were compared with the results of a movable-bed experiment. They successfully explained the formation of a sand spit and a barrier. In their study, however, the effects of the change in water depth of the sand accumulation zone on the formation of the sand spit have not yet been fully investigated. Taking a sand spit and a barrier formed along the west Izu coast in Suruga Bay as the example, these issues were investigated in Section 3 [7].

A 2-m-height tsunami propagated into Tokyo Bay after the Great East Japan Earthquake occurred on March 11, 2011, and a cuspate foreland separating Tokyo Bay and the Uraga Strait was eroded by the current during this tsunami. Although this cuspate foreland has long been stable, decreased sand supply from the south coast has resulted in erosion of the cuspate foreland [8], and the previously straight sandbar had become concave northward with several openings by February 3, 2011 [9]. Then, the tsunami flowed over the sandbar, dispersing the sand and leaving an isolated protruding sandbar. After the tsunami, this sandbar was significantly deformed owing to wave action. The subsequent shoreline changes of this protruding sandbar were measured, and the 3-D beach changes were calculated and compared with the measured shoreline changes in Section 4 [9].

2. Numerical simulation of elongation and merging of bay mouth sand spits

2.1 Formation of bay barriers

Zenkovich [4] showed an example of a barrier beach in a fjord in eastern Kamchatka, which extended at the bay mouth (**Figure 1**). In this bay, downward longshore sand transport developed along the coastline, resulting in the formation of sand spits from both shores; they connected each other; and a barrier beach was formed. Note that the beach is wide at the central part of the bay barrier, whereas it is narrow at the right end. He gave another example of a sand spit formed in a bay mouth (**Figure 2**). **Figures 2A** and **2B** show the sand spits alternately extending from both shores of the bay mouth, and a slender sand spit extended owing to unidirectional longshore sand transport from the right bank, respectively. In another example of a pair of sand spits shown in **Figure 3**, the tips extended on both sides

Figure 1.
Bay barrier closing bay mouth in fjord in eastern Kamchatka [4].

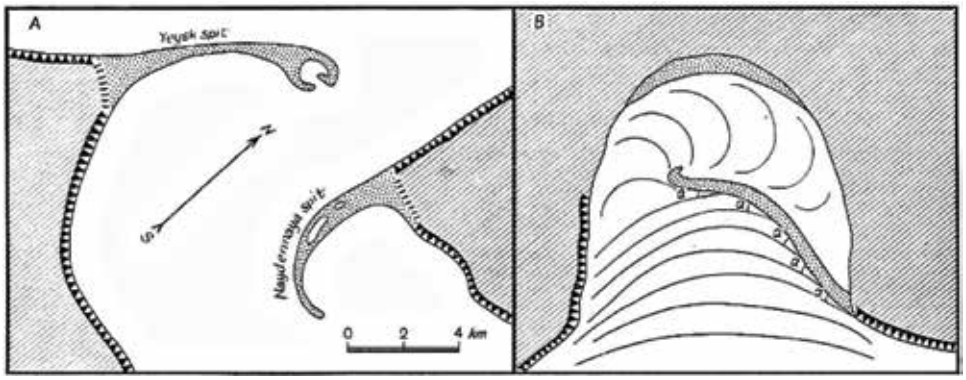

Figure 2.
Schematic diagram of formation of bay mouth sand spits [4].

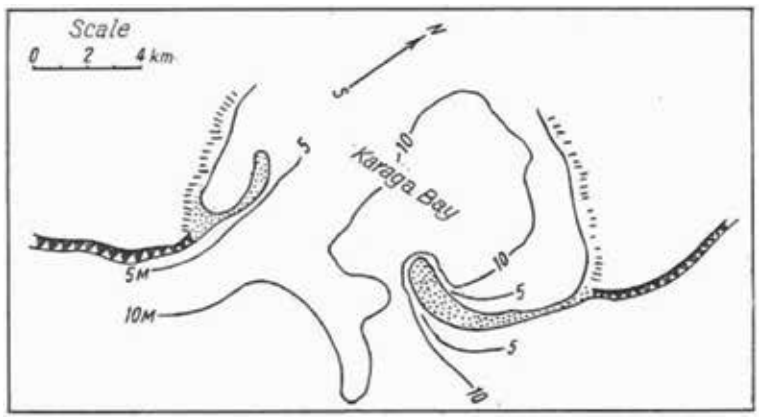

Figure 3.
Example of a pair of sand spits enclosing Karaga Bay [4].

of the bay markedly curved inward, because the water depth at the tips of the sand spits is too larger for the sand spits to extend in a straight line.

2.2 Calculation conditions

A rectangular calculation domain with 600 m length in the longshore and cross-shore directions was considered with a flat solid bed of 3 m depth, and sandy headlands with an initial beach slope of 1/10 and a berm height of 1 m were set at the left corner of this domain. Sand supplied from the headlands is available for the formation of a bay barrier. The beach changes were predicted when multidirectional irregular waves with a significant wave height of 1 m were incident from the direction normal to the y-axis, and the incident wave direction at each time step was randomly determined, so that the probability of occurrence of each wave direction was satisfied. As the probability of occurrence, the directional distribution of wave energy that corresponds to the angular spreading parameter S_{max} = 10 for wind waves was used by employing the angular spreading method for irregular waves [10]. h_c and the equilibrium slope of sand were assumed to be 3 m and 1/10, respectively. **Table 1** summarizes the conditions for calculating the elongation and merging of bay mouth sand spits.

Four cases of calculation were carried out; a slender, rectangular sandy headland was placed at the left end of the calculation domain in Case 1, double sandy headlands with the same shape as that on the left side was placed in Case 2, and two

Calculation method	Type 5 BG model
Incident wave height H	1 m
Berm height h_R	1 m
Depth of closure h_c	3 m
Equilibrium slope tan β_c	1/10
Coefficients of sand transport	Longshore and cross-shore sand transport coefficient K_s = 0.2
Mesh size	$\Delta x = \Delta y$ = 10 m
Time interval	Δt = 1 hrs
Duration of calculation	2×10^4 hrs (2×10^4 steps)
Boundary conditions	Shoreward and landward ends $q_x = 0$ Right and left boundaries $q_y = 0$

Table 1.
Conditions for calculating elongation and merging of bay mouth sand spits.

sandy headlands were placed asymmetrically in Case 3. Furthermore, in Case 4, the formation of a barrier island closing three bays was predicted.

2.3 Calculation results

2.3.1 Single sandy headland (Case 1)

Figure 4 shows the calculation results up to 5000 hr in Case 1. A spatial imbalance in longshore sand transport occurred near the corner, causing erosion to the left of the corner, because waves were incident from the negative x-direction, and the shoreline orientation changed by 90° at the corner (**Figure 4(a)**). The eroded sand was transported rightward, resulting in the formation of sand spit A at the corner (**Figure 4(b)**). Simultaneously, shoreline undulation started to develop owing to the high-angle wave instability [11] along the shoreline extending parallel to the direction of wave propagation, and a small sand spit A' was formed. With time, the sand spit A was significantly elongated, producing a wave-shelter zone on the lee of the sand spit (**Figure 4(c)**). Although sand spits independently developed near the head and foot of the sandy headland at the initial stage, the wave-sheltering effect of sand spit A became dominant with increasing size of the sand spit, and the sand spit A' was subject to the wave-sheltering effect of sand spit A (**Figure 4(c)**). Finally, it disappeared, and sand spit A simply elongated rightward (**Figures 4(d)**, **4(e)**, and **4(f)**). This elongation of a single sand spit well explains the mechanism of the extension of sand spits given by Zenkovich [4], as schematically shown in **Figure 2**.

2.3.2 Deformation of symmetric sandy headlands on both sides of a bay (Case 2)

Figure 5 shows the results in Case 2, in which sandy headlands were symmetrically arranged on both sides of the bay with a distance of 320 m between them (**Figure 5(a)**). The sandy headland on the left, therefore, was subjected to the wave-sheltering effect from that on the right and vice versa. When waves were incident from the negative x-direction under these conditions, three small-scale sand spits had developed along the shoreline on both sides of the sandy headlands after 1000 hrs, together with the elongation of two slender sand spits, one on each side of the bay mouth (**Figure 5(b)**). By 2000 hrs, the two sand spits at the bay mouth had further extended, and the opening width was narrowed to 60 m (**Figure 5(c)**). Because waves were obliquely incident

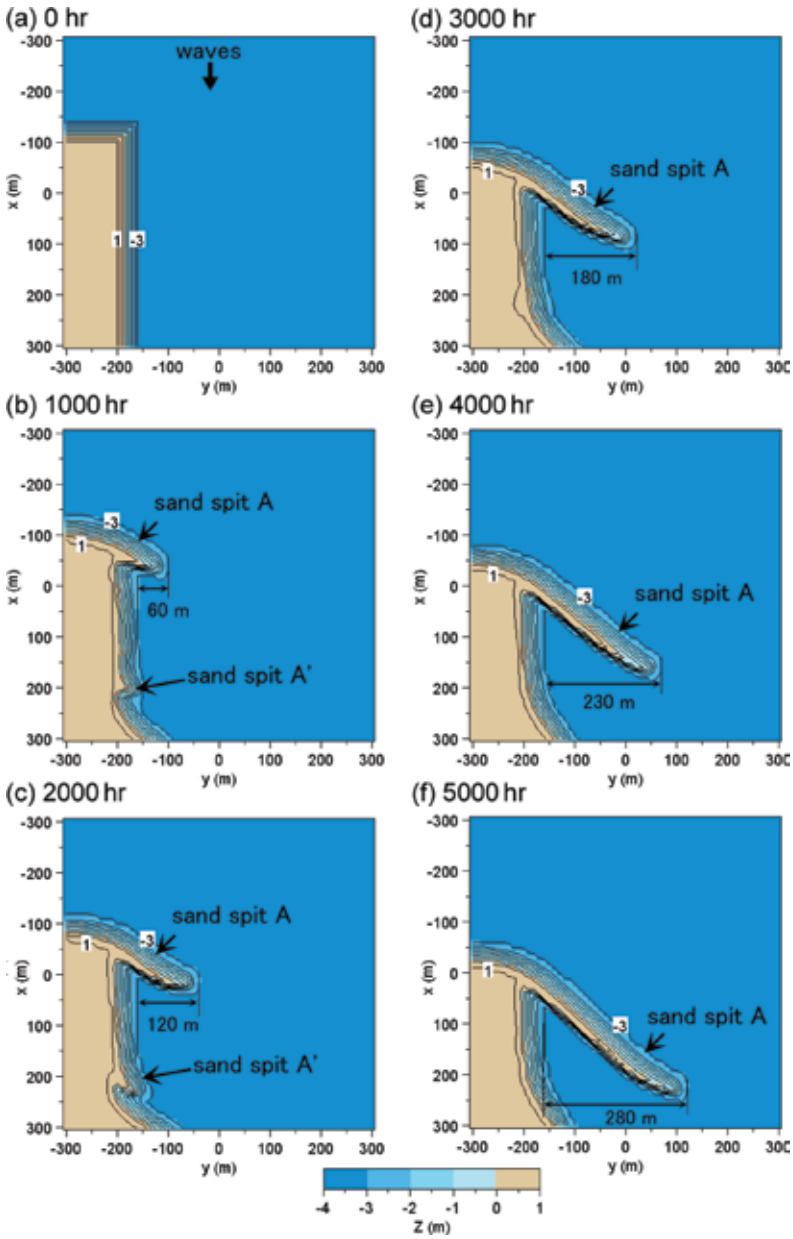

Figure 4.
Calculation results for elongation of sand spit along the shoreline on the right side of sandy headland (Case 1) [5].

to the sand spits on both sides of the sandy headlands through the opening, these sand spits further developed. The size of the three sand spits increased until 2000 hrs (**Figure 5(c)**). After 3000 hrs, the two sand spits that extended from both sides had connected to form a bay barrier. Because the bay mouth was completely closed by the bay barrier (**Figure 5(d)**), the sand spits that formed along the shoreline on both sides of the sandy headlands were left intact.

Longshore sand transport from the sandy headlands to the concave shoreline still prevailed even after the complete closure of the bay mouth by the bay barrier, and the beach width at the central part of the bay barrier increased with time (**Figures 5(e)**-**5(h)**). Comparing the shape of the bay barrier after 4000 hrs, as shown in **Figure 5(f)**, with **Figure 1**, the calculation results illustrating the

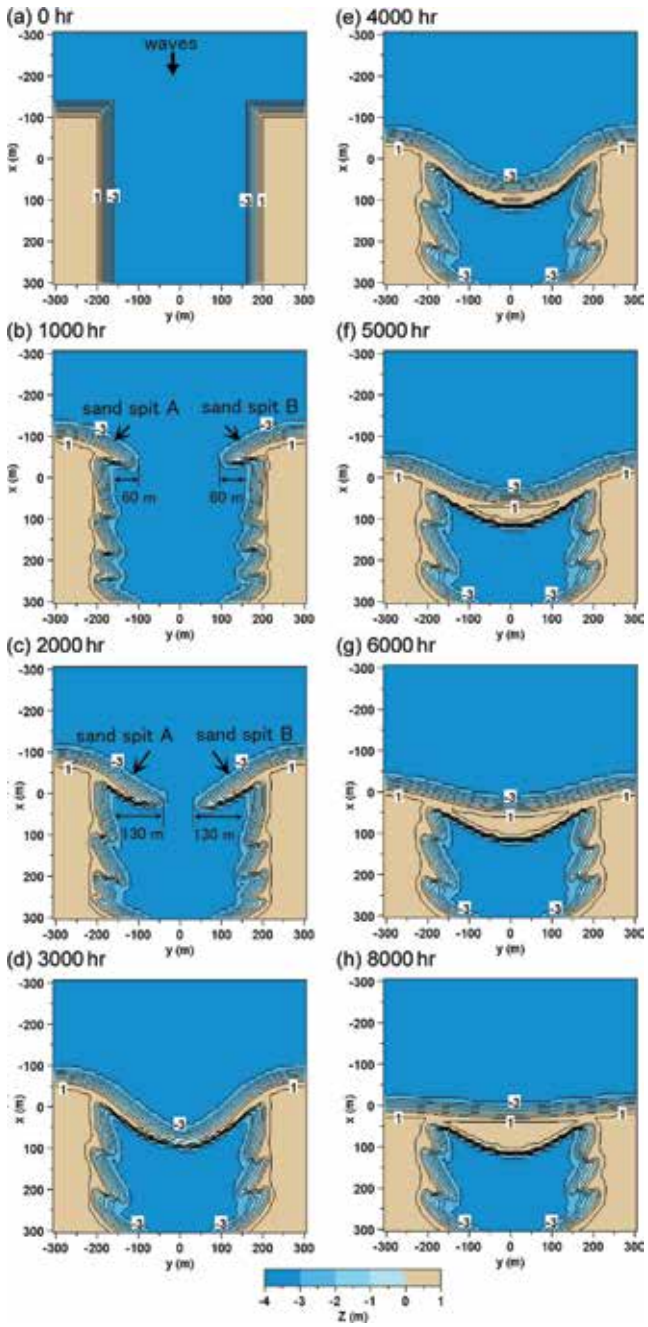

Figure 5.
Calculation results for elongation of bay mouth bar between two sandy headlands separating a bay (Case 2: symmetric arrangement) [5].

development of a bay barrier and a wide beach at the central part of the bay barrier are in good agreement with the photograph in [4].

2.3.3 Deformation of asymmetric sandy headlands on both sides of a bay (Case 3)

When waves were incident from the negative x-direction, the wave-sheltering effect of the left sandy headland on the right headland became stronger because of the protrusion of the left headland (**Figure 6(a)**). After 1000 hrs, the sand spits had

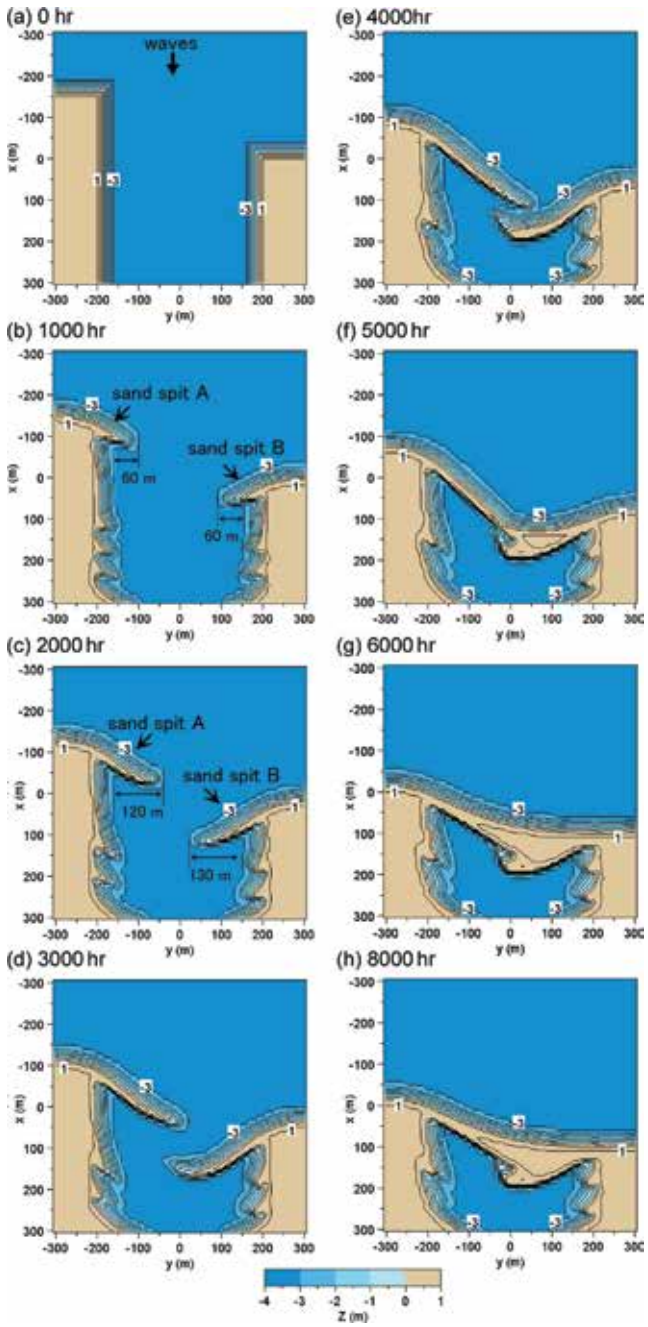

Figure 6.
Calculation results for elongation of bay mouth bar between two sandy headlands separating a bay (Case 3: asymmetric arrangement) [5].

started to form on both sides of the sandy headlands (**Figure 6(b)**). Here, the sand spits are denoted as sand spits A and B, respectively. At this stage, the elongation length of sand spits A and B was 60 m. With further wave action, sand spits A and B became markedly elongated to 120 and 130 m, respectively, after 2000 hrs (**Figure 6(c)**). Sand spit B was 10 m longer than sand spit A because of the larger wave-sheltering effect of sand spit A. After 3000 hrs, sand spit B had further elongated, and the tip of the sand spit curved and approached the tip of sand spit A (**Figure 6(d)**). After 4000 hrs, sand spit B had stopped elongating, because it had entered the wave-shelter

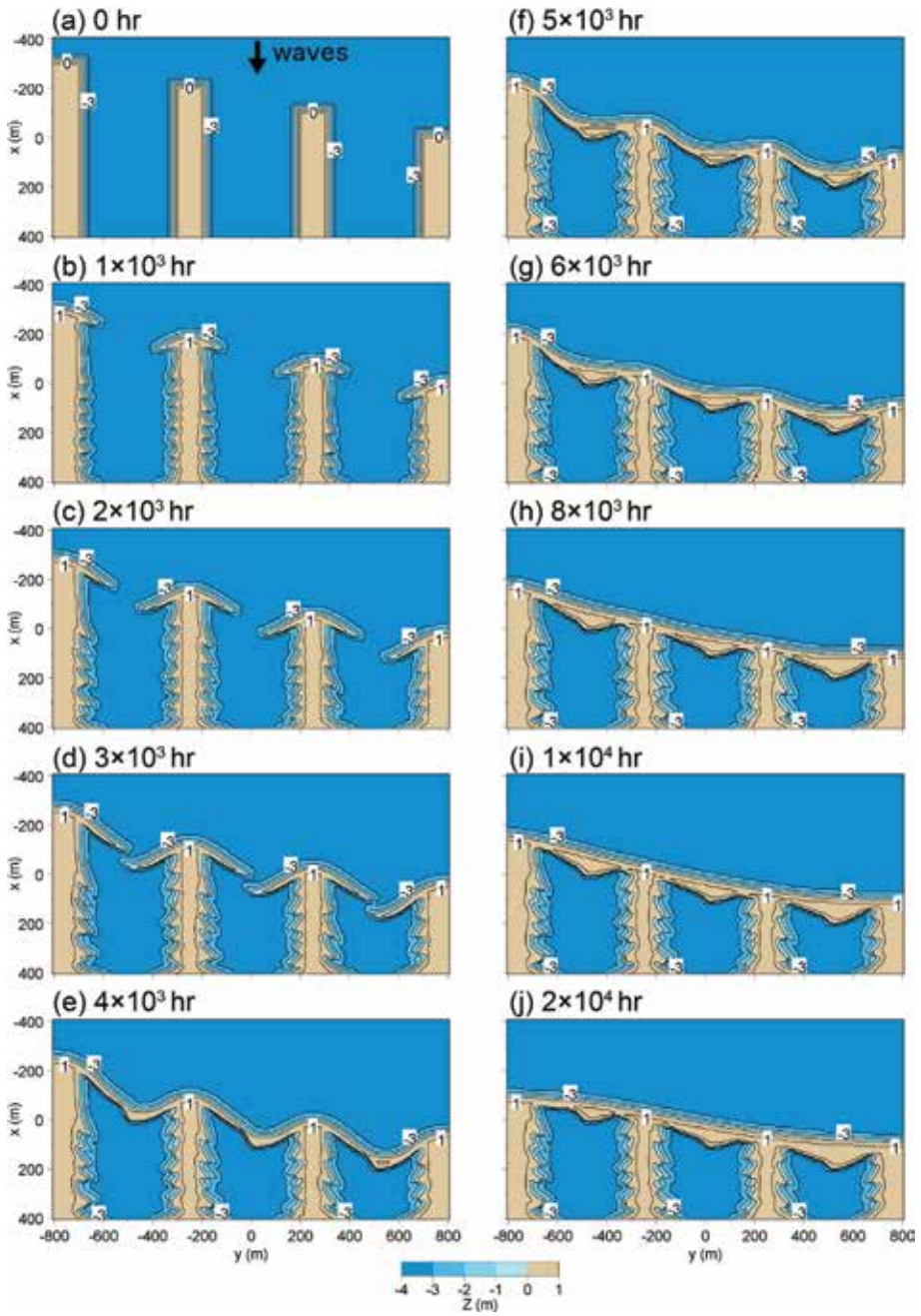

Figure 7.
Formation of embayed coasts closed by a barrier island (Case 4).

zone of sand spit A, and the tip of sand spit A became connected to sand spit B owing to successive sand deposition near the tip of sand spit A (**Figure 6(e)**). After 5000 hrs, a bay barrier had formed by the connection of the two sand spits A and B (**Figure 6(f)**). Because the shoreline protruded at this stage, the shoreline further retreated up to 8000 steps, and the shoreline inclination was reduced (**Figure 6(h)**).

In Case 3, the width of the bay increased by the deposition of sand at the tip of sand spit B, and a bay barrier with a wide shore in the central part was formed after 5000 hrs. With time, the bay barrier continued to develop up to 8000 hrs, although

a protrusion that had formed near the point connecting the two sand spits was left intact. This protrusion was formed when sand spit A was superimposed on sand spit B from the offshore side in the period between 4000 and 5000 hrs, which corresponds to the previous beach changes in the evolution process of the bay barrier.

2.3.4 Formation of embayed coasts by extension of a barrier island (Case 4)

Zenkovich [4] illustrated the main stages of the evolution of an embayed coast as in Figure 223 (p. 451) in his book and described that the process is as follows: the first stage is completed when the bays are cut off from the sea by barrier beaches which link up capes and peninsulas that have already retreated slightly as a result of abrasion. Then, as the next stage, all the projections have been cut away, and the coastline has advanced to the heads of the former bays.

In Case 4, the formation of the embayed coasts by the extension of a barrier island as described in Zenkovich [4] was predicted. At the initial stage, four headlands composed of sand were considered with three bays between these headlands, the length of which gradually decreases in the direction of the y-axis (**Figure 7(a)**). Waves were assumed to be incident from the negative x-direction. Successive topographic changes of the embayed coasts over time are shown in **Figure 7**. By 10^3 hrs, short sand spits started to extend from the tips of the headlands (**Figure 7(b)**). With time, these sand spits extended, and they connected each other and merged up to 4×10^3 hrs (**Figures 7(c)**, **7(d)**, and **7(e)**). Because the shoreline of the barrier islands protrudes in front of the headlands at these stages, such projections were eroded away owing to longshore sand transport, resulting in the formation of a straight coastline with time (**Figures 7(f)**-**7(i)**). Finally, three bays closed by a straight barrier island were formed (**Figure 7(j)**). These results are in good agreement with the explanation of the formation of the embayed coasts given by Zenkovich [4].

3. Numerical simulation of elongation of sand spit on seabed with different water depths

3.1 Examples of sand spit and barrier on west Izu coast

Typical examples of the sand spit and barrier can be seen on the west Izu coast (**Figures 8** and **9**) [7]. A recurved sand spit, Mihama Point, of 650 m length extends at the mouth of Heda Bay. The bathymetry in the rectangular area of Heda Bay in **Figure 9** is drawn in **Figure 10**. The water depth at the tip of the sand spit reaches 30 m, which is much greater than the depth of closure of h_c = 10 m in this area, and the slope around the tip of sand spit is very steep. Also, a barrier is located 2.2 km north of the sand spit (**Figures 9** and **11**), separating Myojin Pond from Suruga Bay, and further north, another recurved sand spit, Osezaki Point, of 650 m length extends 3.3 km north of the pond (**Figures 8** and **12**). The development of a sand spit and a barrier in these examples strongly suggests that the water depth of the sand deposition zone is a key factor for the formation of the sand spit and the barrier.

3.2 Calculation conditions

The water depths of the shallow seabed where the sand spit elongates were set to 5, 10, 15, and 20 cm in Cases 1–4, respectively, with a model scale of 1/100. The incident wave height was H_i = 4.6 cm, and the wave period T = 1.27 s. Waves were obliquely incident at an angle of 20° relative to the direction normal to the initial

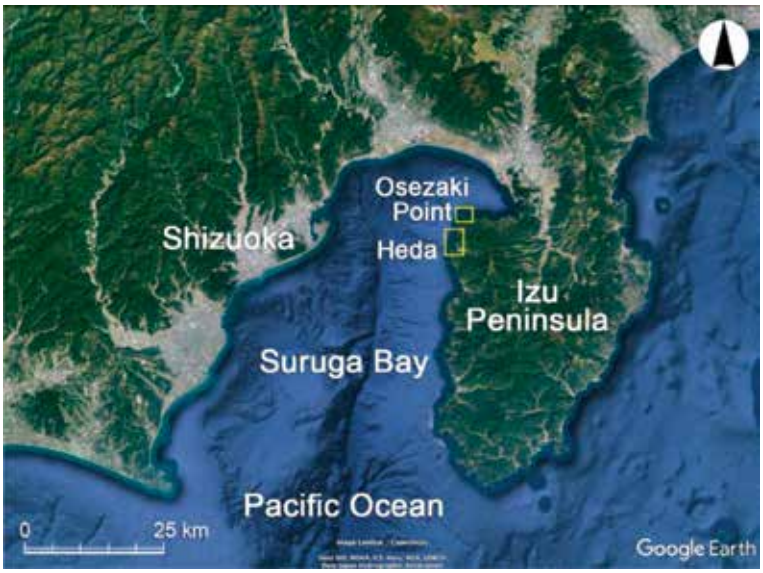

Figure 8.
Location of Heda and Osezaki Points on the west coast of Izu Peninsula.

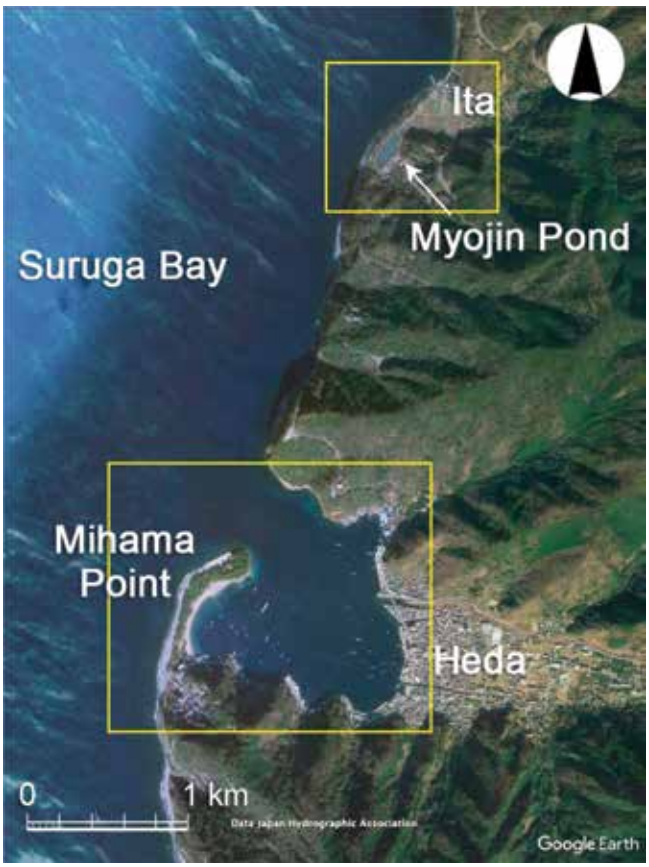

Figure 9.
Satellite image of Mihama Point and Myojin Pond.

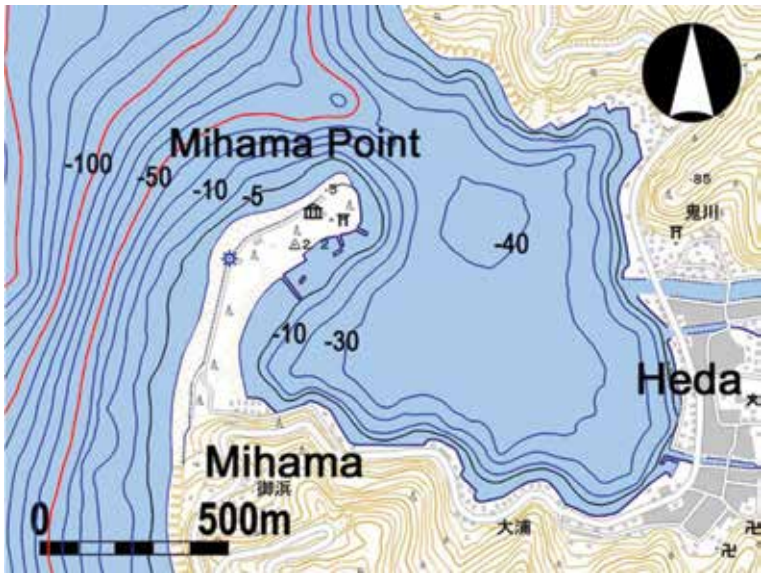

Figure 10.
Bathymetry around Mihama Point [7].

Figure 11.
Aerial photograph of Myojin Pond.

shoreline. The depth of closure was given as $h_c = 2.5H$, where H is the wave height at a point. h_R and the equilibrium slope of sand were assumed as 5 cm and 1/5, respectively, based on the experimental results. The calculation domain was discretized by meshes of 20 cm, and the 8 hrs of calculation (8×10^4 steps) was carried out using the time intervals of $\Delta t = 10^{-4}$ hr. **Table 2** summarizes the conditions for calculating the elongation of a sand spit. The calculation results are shown with the same model scale of 1/100, so that it is easy to compare the results of this study with those given in [6], in which the formation of a spit with a model scale of 1/100 was predicted. The numbers in parentheses in **Table 2** correspond to the experimental conditions.

Figure 12.
Aerial photograph of Osezaki Point taken in 2005.

Calculation method	**Type 3 BG model**
Wave conditions	Incident waves: H_I = 4.6 m (4.6 cm), T = 12.7 s (1.27 s), wave direction θ_I = 20° relative to normal to initial shoreline
Berm height	h_R = 5 m (5 cm)
Depth of closure	h_c = 2.5H (H: wave height)
Equilibrium slope	tanβ_c = 1/5
Angle of repose slope	tanϕ = 1/2
Coefficients of sand transport	Coefficient of longshore sand transport K_s = 0.045 Coefficient of Ozasa and Brampton [12] term K_2 = 1.62K_s Coefficient of cross-shore sand transport K_n = 0.1 K_s
Mesh size	$\Delta x = \Delta y$ = 20 m (20 cm)
Time intervals	$\Delta t = 10^{-3}$ hr. (10^{-4} hr)
Duration of calculation	80 (8) hrs (8×10^4 steps)
Boundary conditions	Shoreward and landward ends, q_x = 0; right and left boundaries, q_y = 0
Calculation of wave field	Energy balance Equation [13] • Term of wave dissipation due to wave breaking: Dally et al. [14] • Wave spectrum of incident waves: directional wave spectrum density obtained by Goda [15] • Total number of frequency components N_F = 1 and number of directional subdivisions N_θ = 8 • Directional spreading parameter S_{max} = 75 • Coefficient of wave breaking K = 0.17 and Γ = 0.3 • Imaginary depth between minimum depth h_0 and berm height h_R: h_0 = 2 m (2 cm) • Wave energy = 0 where $Z \geq h_R$ • Lower limit of h in terms of wave decay due to breaking Φ, 0.7 m (0.7 cm)

Table 2.
Conditions for calculating elongation of a sand spit.

3.3 Calculation results

3.3.1 Formation of sand spit on a flat bottom with constant depth

F**igures 13–16** show the initial topographies with a flat bottom in the sand deposition area and the results after an 8-hr wave action of Cases 1–4. In Case 1 (**Figure 13**), a sand spit rapidly extended along the marginal line of the shallow seabed forming a barrier (**Figure 13(b)** and **13(c)**), because the water depth of the sand deposition zone is much smaller than the depth of closure h_c of 12 cm, and it connected with the other side, leaving a shallow lagoon inside up to 2 hrs (**Figure 13(d)**). After 4 hrs, the width of the sandbar increased because of the sand deposition to the deeper zone from the left boundary while forming a steep slope (**Figure 13(e)**).

In Case 2 (h_0 = 10 cm, **Figure 14**), the elongation velocity of the sand spit decreased compared with that in Case 1 because of the increase in the volume of the sand deposition zone. Simultaneously, the curvature of the shoreline at the tip

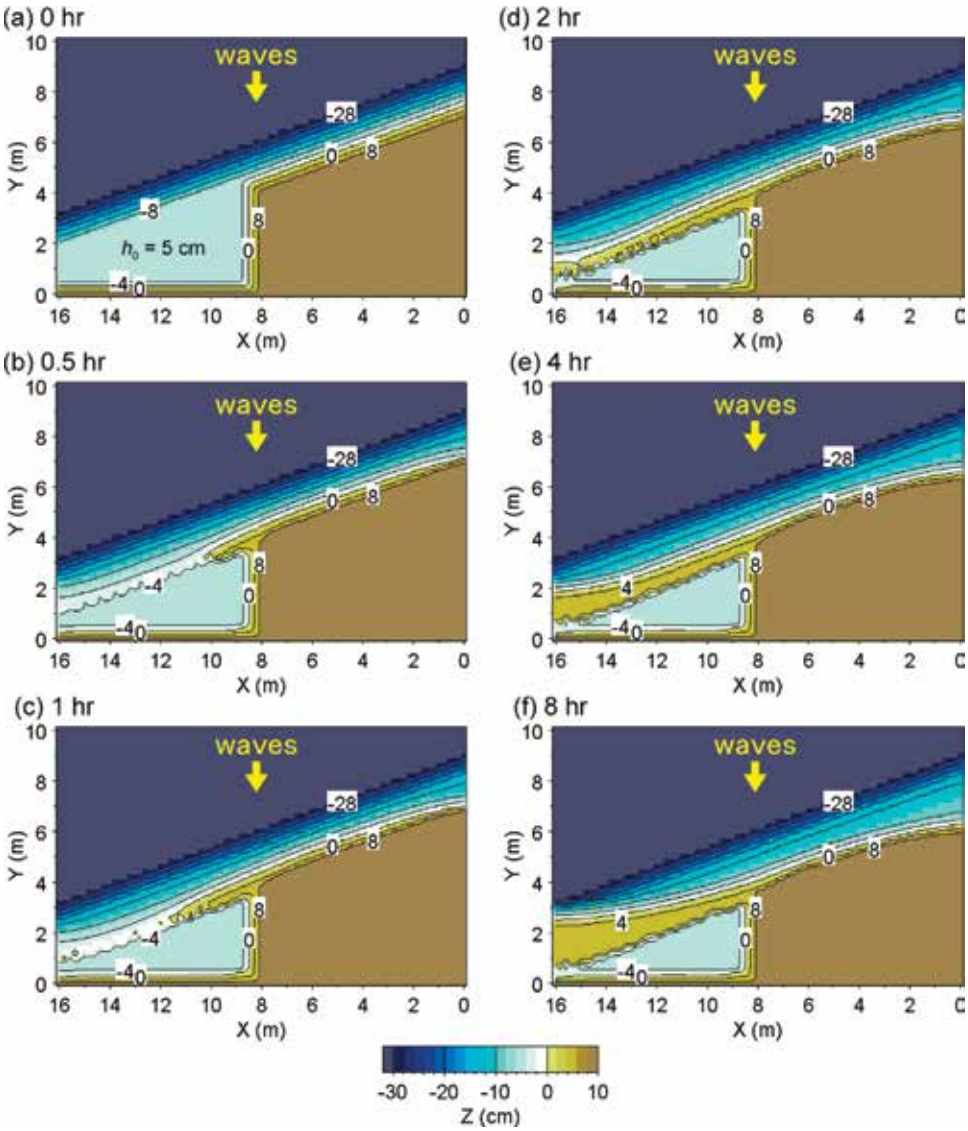

Figure 13.
Formation of sand spit on the flat seabed with 5 cm depth in Case 1 [7].

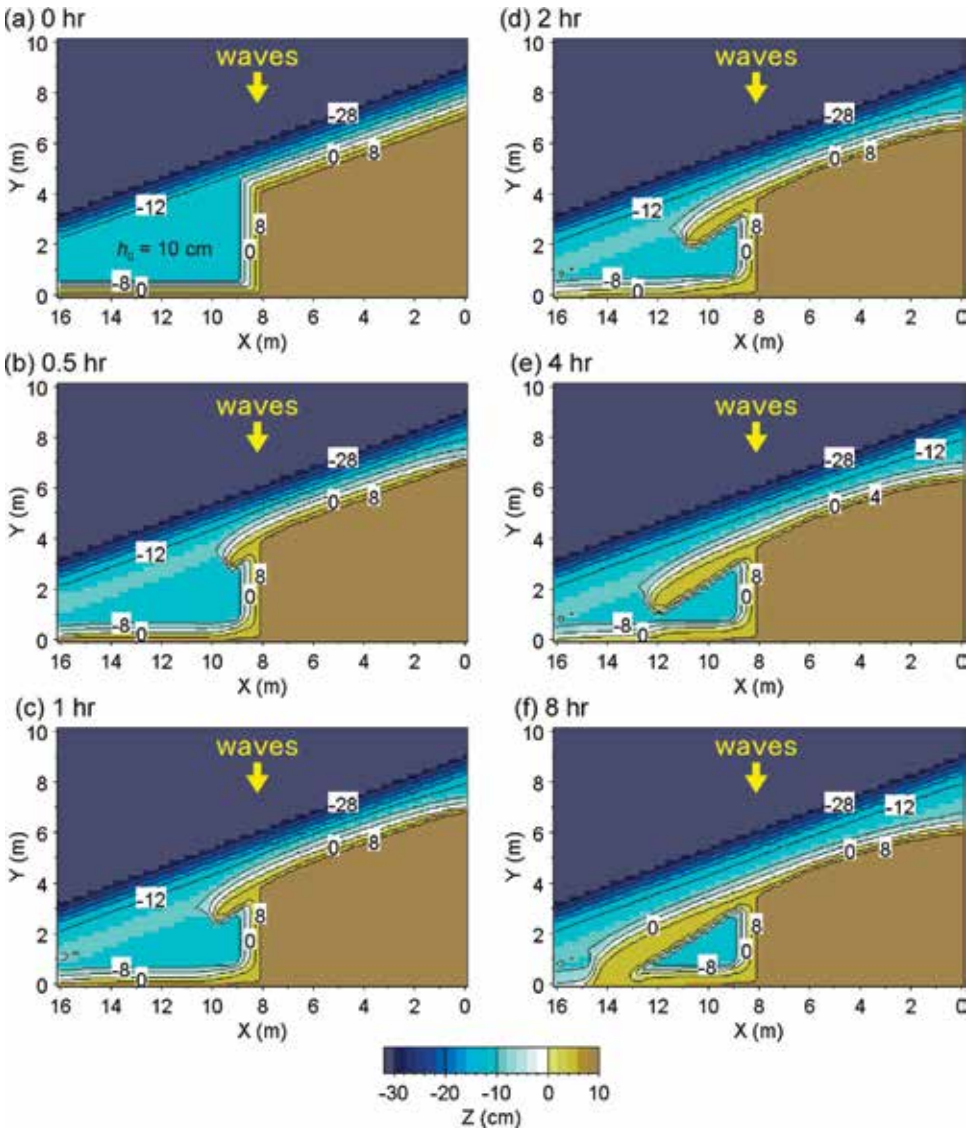

Figure 14.
Formation of sand spit on the flat seabed with 10 cm depth in Case 2 [7].

of the sand spit increased because of the larger wave energy incident to the shallow seabed (**Figures 14(b)**, **14(c)**, and **14(d)**). As a result, the tip of the sand spit approached very close to the X-axis after 4 hrs and connected at X = 14 m after 8 hrs (**Figures 14(e)** and **14(f)**). A cuspate foreland was formed on the opposite side against the sand spit after 4 hrs owing to the wave-sheltering effect of the sand spit, and the area of the lagoon behind the barrier markedly decreased in Case 2 compared with that in Case 1.

In Case 3 (h_0 = 15 cm, **Figure 15**), the elongation velocity and the length of the sand spit further decreased because of successive sand deposition into the deeper zone. When the water depth of a flat bottom is greater than h_c, part of the sand transported from upcoast falls into the zone deeper than h_c, and such sand cannot be transported again by wave action (**Figures 15(b)**, **15(c)**, and **15(d)**), implying that an additional volume of sand is required for the sand spit to extend. It is concluded that the greater the water depth of a flat bottom, the slower the development

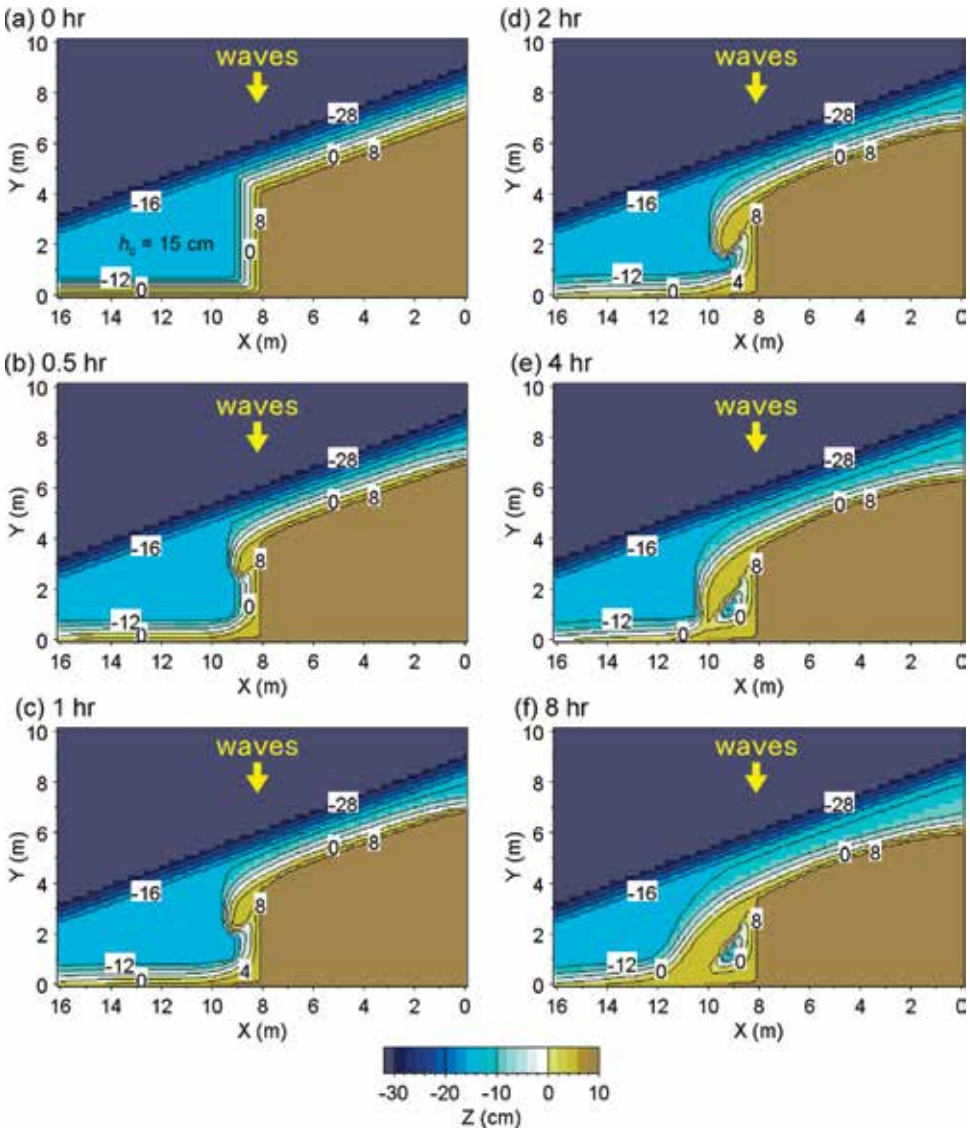

Figure 15.
Formation of sand spit on the flat seabed with 15 cm depth in Case 3 [7].

of a sand spit, even if the same amount of sand is supplied from the upcoast. With the increase in the water depth of the flat bottom, the tip of the sand spit was forced to be bent landward. Moreover, the sand deposited upcoast of the sand spit quickly discharged downcoast after 4 hrs, because the shoreline at the tip of the sand spit smoothly connected to the opposite shore, so that longshore sand transport was able to smoothly reach the downcoast shoreline ((**Figure 15(e)**).

In Case 4 (h_0 = 20 cm, **Figure 16**), the development of the sand spit was depressed, and its size was reduced. Although a small hollow was formed behind the sandbar, no lagoon was formed (**Figures 16(b)**-**16(e)**). **Figure 17** shows the shoreline configurations in Cases 1–4 after 2 hrs. The shoreline upcoast of X = 8 m, i.e., sand source, coincides with each other, suggesting that equivalent longshore sand transport develops in each case. Thus, it is concluded that the sand spit was formed under the condition that a constant volume of sand is supplied from the upcoast. In other words, the difference in the development of the sand spit must be

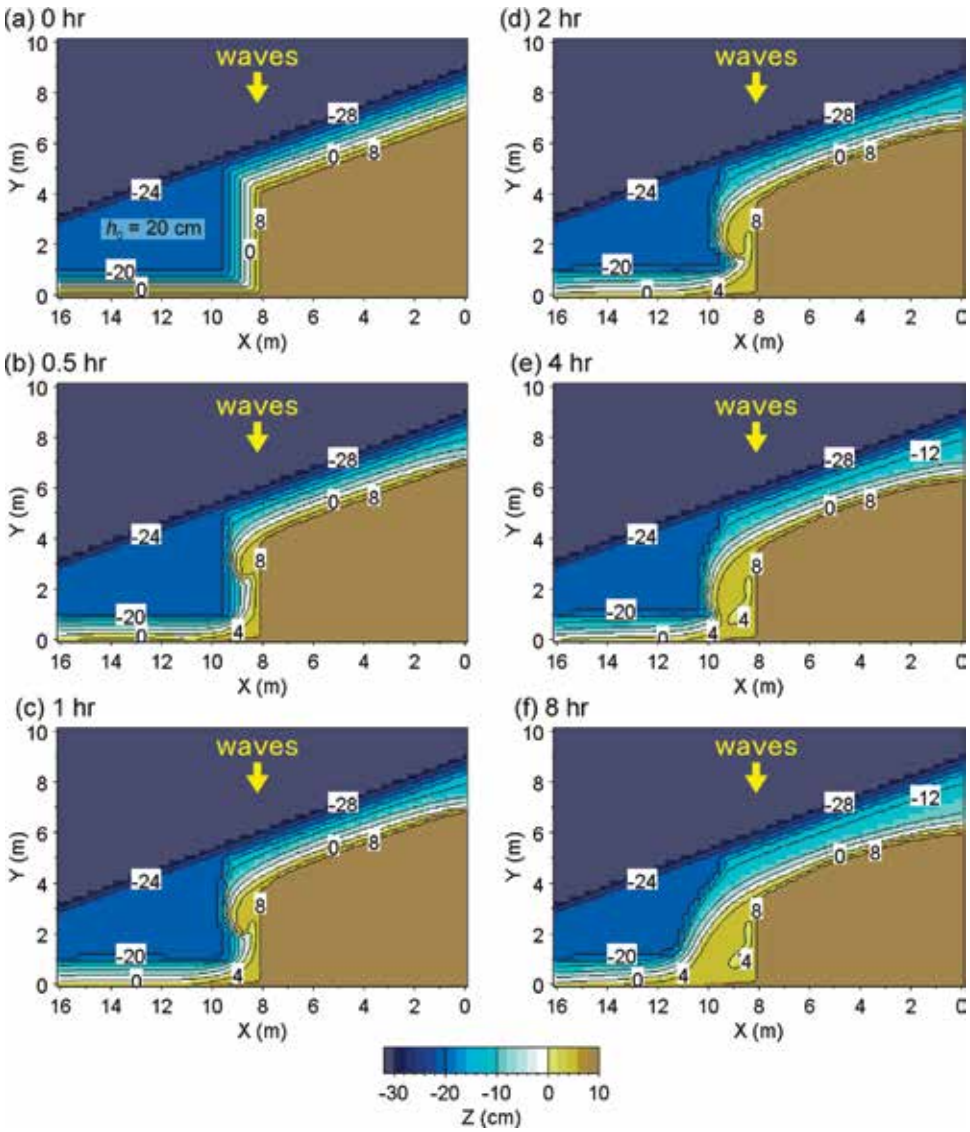

Figure 16.
Formation of sand spit on the flat seabed with 20 cm depth in Case 4 [7].

explained only by the difference in the water depth. With the increase in the water depth, the sand spit was depressed, and a semicircular cuspate foreland was formed instead of a sand spit when the water depth of the flat shallow seabed is 20 cm.

3.4 Discussion

When a constant longshore sand transport Q_0 is supplied from upcoast and a sand spit is formed owing to this sand supply, the elongation velocity of the sand spit is proportional to Q_0/h^2, where h is the water depth of the sand deposition area. The development of the sand spit is remarkable with a smaller water depth of the sand deposition zone. At the same time, sufficient wave energy cannot reach deep into the shallow body of water, inducing the development of a sandbar there, whereas sufficient wave energy can reach the shoreline with a larger water depth, resulting in the increase in the curvature of the shoreline. Mihama Point with a

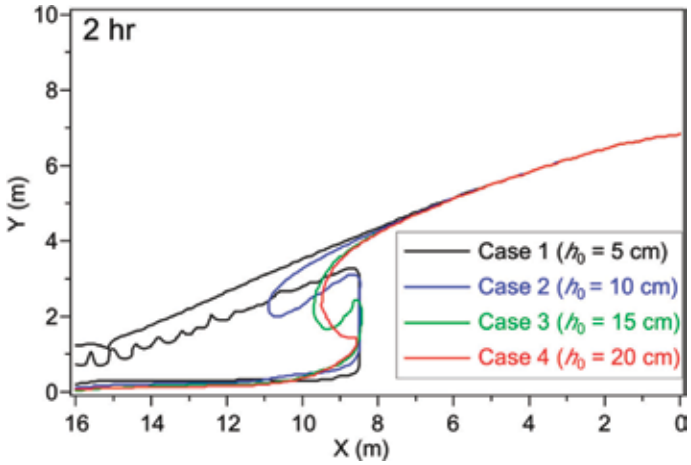

Figure 17.
Shoreline configurations after 2 hrs for Cases 1–4 [7].

large water depth of the sand deposition area, which is much larger than the depth of closure h_c of 10 m, as shown in **Figure 10**, is very similar to the results after 2 hrs in Case 3 (**Figure 15(d)**). The topography of Myojin Pond (**Figure 11**) is similar to that after 8 hrs in Case 2 (**Figure 14(f)**), implying that Myojin Pond was left behind as a shallow pond, as a result of the extension of a barrier island. In case of Osezaki Point that protruded northward at the north end of Izu Peninsula (**Figure 12**), the sand spit extended straight from the turning point of the coastline, and then the tip of the sand spit recurved inward. This feature is similar to the result after 2 hrs in Case 2 with a larger water depth of the flat seabed (**Figure 14(d)**). In addition, regarding the seabed slope, the effect of the change in the seabed slope is equivalent to that of the combination of several flat seabeds as in [7]. Thus, the water depth and seabed slope of the sand deposition area play an important role in the development of a sand spit or a barrier.

4. Numerical simulation of deformation of sandbar formed at the tip of Futtsu cuspate foreland

4.1 Change in sandbar offshore of Futtsu Point owing to the 2011 Great Tsunami

Large topographic changes were first discovered by a field observation on June 11, 2011, at the tip of Futtsu Point (**Figure 18**) [9]. Because a tsunami with 2 m height, which was recorded in the field observation at the south shore of Futtsu Point, hit the foreland on March 11, 2011, the sandbar at the tip of Futtsu Point was discharged by the overflow of this tsunami. The impact of the tsunami to the sandbar can be seen in aerial photographs taken on February 3, 2011, and March 27, 2012, before and after the tsunami, respectively (**Figure 19**). Before the tsunami, a slender, concave sandbar extended from Futtsu Point to Dai-ichikaiho Island. On March 27, 2012, almost all of the sandbar was disintegrated by the tsunami overflow, resulting in the submergence of the sandbar and leaving a small sandbar at the tip of Futtsu Point [9]. Comparing the broken line in **Figure 19(b)**, which shows the shapes of the sandbar before the tsunami and the submerged sandbar on March 27, 2012, it is seen that the sand comprising the sandbar was transported northward, implying that the sandbar was flushed away. In addition, part of the sand was transported by the return flow near the tip of the cuspate foreland.

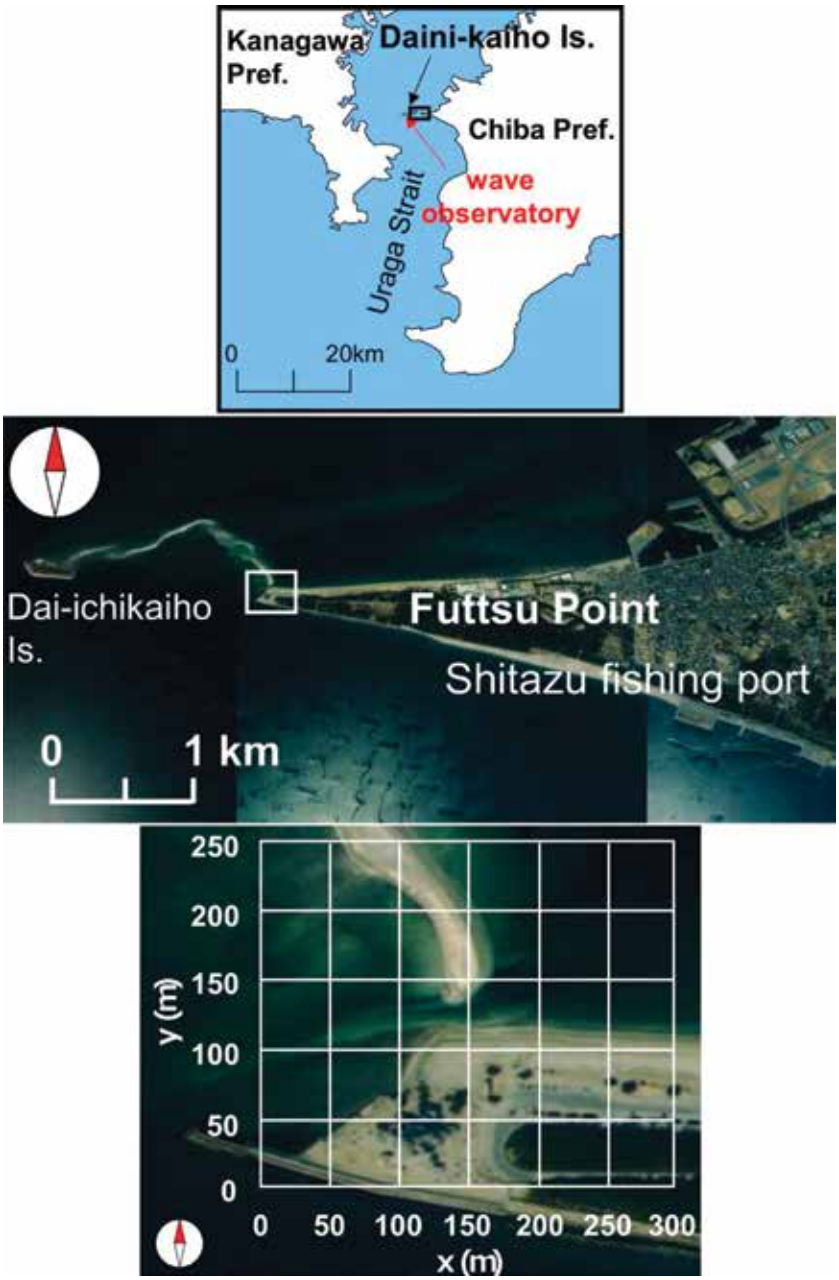

Figure 18.
Location of the study area at the tip of Futtsu Point and coordinate system [9].

4.2 Method of field observation

A rectangular observation area was set up at the tip of Futtsu Point (**Figure 18**), and the shoreline changes in this area were measured using a GPS between June 11, 2011 and October 16, 2012. The shoreline position was measured when the tide level was approximately equal to MSL. The changes in shoreline position were investigated using coordinates (x, y) with reference to a point in the vicinity of the seawall at the tip of Futtsu Point (**Figure 18**), and the berm height and foreshore slope were

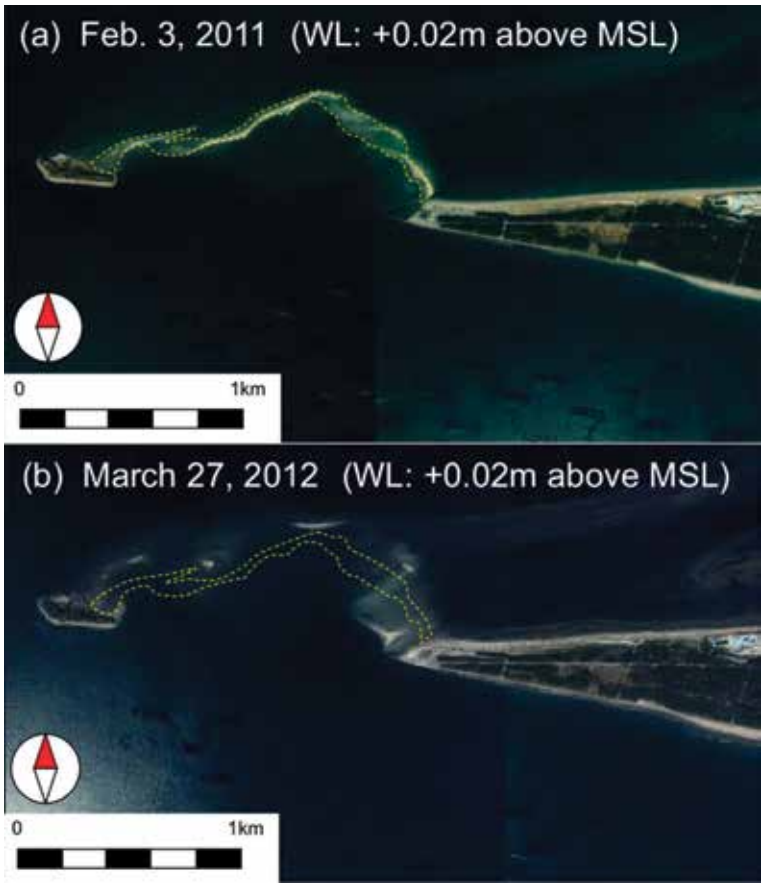

Figure 19.
Aerial photographs of Futtsu Point taken on February 3, 2011, before the tsunami, and March 27, 2012, after the tsunami [9].

measured during low tide on February 26, 2012; the measured berm height was +0.97 m above MSL, and the foreshore slope was 1/8. Wave conditions were investigated using wave observation results offshore of Dainikaiho Island located 2.4 km west of Dai-ichikaiho Island (**Figure 18**).

4.3 Results of field observation

Due to the wave observation offshore of Dainikaiho Island, the wave height normally ranges between 0.3 m in summer and 1 m in winter, and the wave period changes between 3 and 5 s. The important effect upon the deformation of the sandbar at the tip of Futtsu Point is caused by the oblique wave incidence. Monthly changes in wave direction show that predominant wind directions are NNW and SSW, but waves incident from SSW do not affect the beach changes located on the north side of the cuspate foreland, because Futtsu Point extends in the E-W direction. Thus, the deformation of the sandbar primarily depends on the waves incident from NNW.

Figure 20 shows an oblique photograph of a crescent-shaped sandbar formed on the north side on Futtsu Point, taken from an observation tower at the tip of Futtsu Point on June 11, 2011 [9]. The shoreline on the west side of the sandbar

Figure 20.
Oblique photograph of a crescent-shaped sandbar [9].

Figure 21.
Concave shoreline and a sand spit mainly composed of shells [9].

was concave, whereas sand spit A was formed at the east end. **Figure 21** shows a sand spit mainly composed of shells, as denoted by arrow A in **Figure 20**, formed by eastward longshore sand transport along the shoreline of the crescent-shaped sandbar, and the concave shoreline on the lee of the sand spit.

The successive change in shoreline position of this sandbar between June 11, 2011 and February 17, 2012 can be summarized in **Figure 22**. Up to June 11, when the observation began, a crescent-shaped sandbar of 130 m length had developed northward with a concave shoreline on the west side [9]. By July 19, the tip of the sandbar had retreated. Then, the west end of the sandbar was eroded, because wind waves were incident from NNW in July, and the eroded sand was transported eastward, turning around the tip of the sandbar. By September 14, the sandbar had further inclined eastward, and a sand spit was formed on the east side until October 14. After October 14, the entire sandbar eroded out, reducing

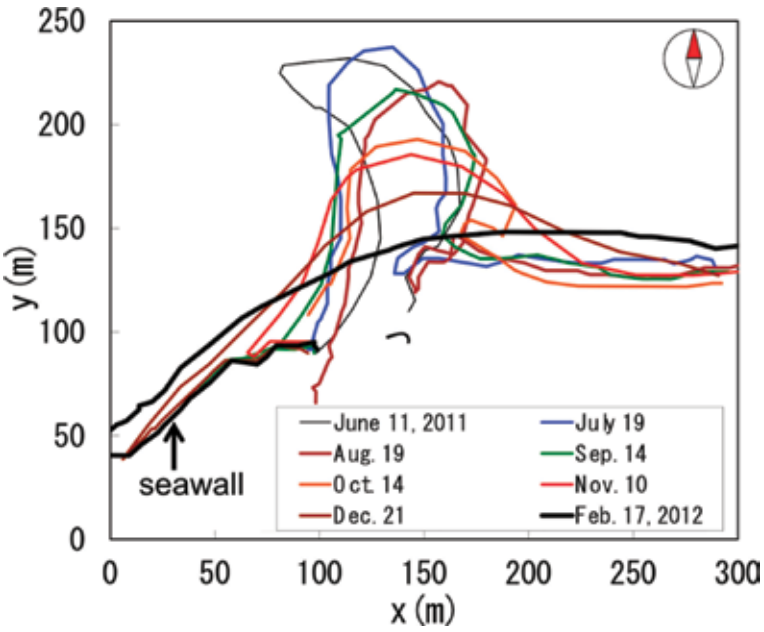

Figure 22.
Overall changes in sandbar between June 11, 2011, and February 17, 2012 [9].

to a sandbar with a smooth shoreline, and diffusion-type shoreline changes occurred. By February 17, a gradually curved shoreline had formed, and the seawall was buried again by sand.

4.4 Numerical simulation using Type 3 BG model

4.4.1 Calculation conditions

Referring to the results of wave observations between June 2011 and January 2012 offshore of Dainikaiho Island (**Figure 18**), we assumed a mean significant wave height of H_i = 0.5 m (T = 4 s). The wave direction and directional spreading parameter S_{max} [15] were determined using a trial-and-error method, so that the measured and calculated shoreline configurations were in good agreement, taking the predominant wave direction of NNW into account [9]. The adopted best-fit wave direction and S_{max} were N17°W and 2, respectively. h_R was assumed to be 1.1 m, as obtained in the field observation on June 11, 2011, and the depth of closure was assumed to be $h_c = 4H$, where H is the local wave height. The equilibrium slope and the slope of the angle of repose were assumed to be 1/7 and 1/2, respectively. As the initial topography, the sandbar topography measured on July 19, 2011, was assumed, when the shoreline configuration was measured in full scale. Because only the shoreline position was measured in the observation, a uniform beach with a foreshore slope of 1/7 was assumed between heights of 1.1 and −2 m. **Table 3** summarizes the conditions for calculating the deformation of a sandbar.

4.4.2 Calculation results

Figure 23 shows the results [9]. Although the initial sandbar on July 19 had a 50 m width and protruded northward by 100 m (**Figure 23(a)**), two protrusions had formed on both sides of the sandbar by August 19 owing to the wave action

Calculation method	Type 3 BG model
Wave conditions	Incident waves: H_I = 0.5 m, T = 4 s Wave direction θ_W = +17.5° (N17.5°W)
Tide level	MSL, 0.0 m
Berm height	h_R = 1.1 m
Depth of closure	$h_c = 4H$ (H: wave height at a local point)
Equilibrium slope	$\tan\beta_c = 1/7$
Coefficients of sand transport	Coefficient of longshore sand transport $K_s = 2 \times 10^{-3}$ Coefficient of sand transport by Ozasa and Brampton [12] term $K_2 = 1.62\ K_s$ Coefficient of cross-shore sand transport $K_n = 0.2\ K_s$
Mesh sizes	$\Delta x = \Delta y$ = 5 m
Time intervals	Δt = 1.2 hr
Total time steps	1×10^4 steps (500 days)
Boundary conditions	Seaward and shoreward ends, $q_x = 0$; right and left ends, $q_y = 0$
Calculation of wave field	Energy balance Equation [13] • Term of wave dissipation due to wave breaking: Dally et al. [14] model • Wave spectrum of incident waves: directional wave spectrum density obtained by Goda [15] • Total number of frequency components N_F = 1 • Number of directional subdivisions N_θ = 8 • Directional spreading parameter S_{max} = 2 • Coefficient of wave breaking K = 0.17 and Γ = 0.3 • Imaginary depth between depth h_0 and berm height h_R, 0.5 m • Lower limit of h in terms of wave decay Φ due to wave breaking, h_{min} = 0.5 m • Wave energy = 0 where $Z \geq h_R$

Table 3.
Conditions for calculating deformation of a sandbar.

from N17°W (**Figure 23(b)**). The calculation result that a small embayment on the eastern foot of the sandbar was enclosed by the sand spit is in agreement with the observed shoreline. However, there is some discrepancy between the measured and observed shorelines in that the measured shoreline is straight on the west side of the sandbar, whereas the calculated shoreline has a small protrusion.

By September 14, the shoreline of the north part of the sandbar significantly retreated with a large inclination toward the east, and the shoreline on the east side was connected by a smooth line with a small hollow (**Figure 23(c)**). By October 14, the shoreline in the north part had markedly retreated, and a sand spit had begun to form on the east side (**Figure 23(d)**). By November 10, the sand spit had elongated and became connected to the other shore, resulting in the formation of a gradually curved shoreline because of the continuous sand supply from the upcoast (**Figure 23(e)**). The protruding sandbar had eroded to form a gradually curving shoreline by December 21, 2011 (**Figure 23(f)**). Thus, the changes in the sandbar that was formed by the 2011 Great East Japan Earthquake tsunami were well predicted using the Type 3 BG model. Also, the subsequent deformation of the sandbar was found to be due to the action of waves incident from the direction of N17°W [9].

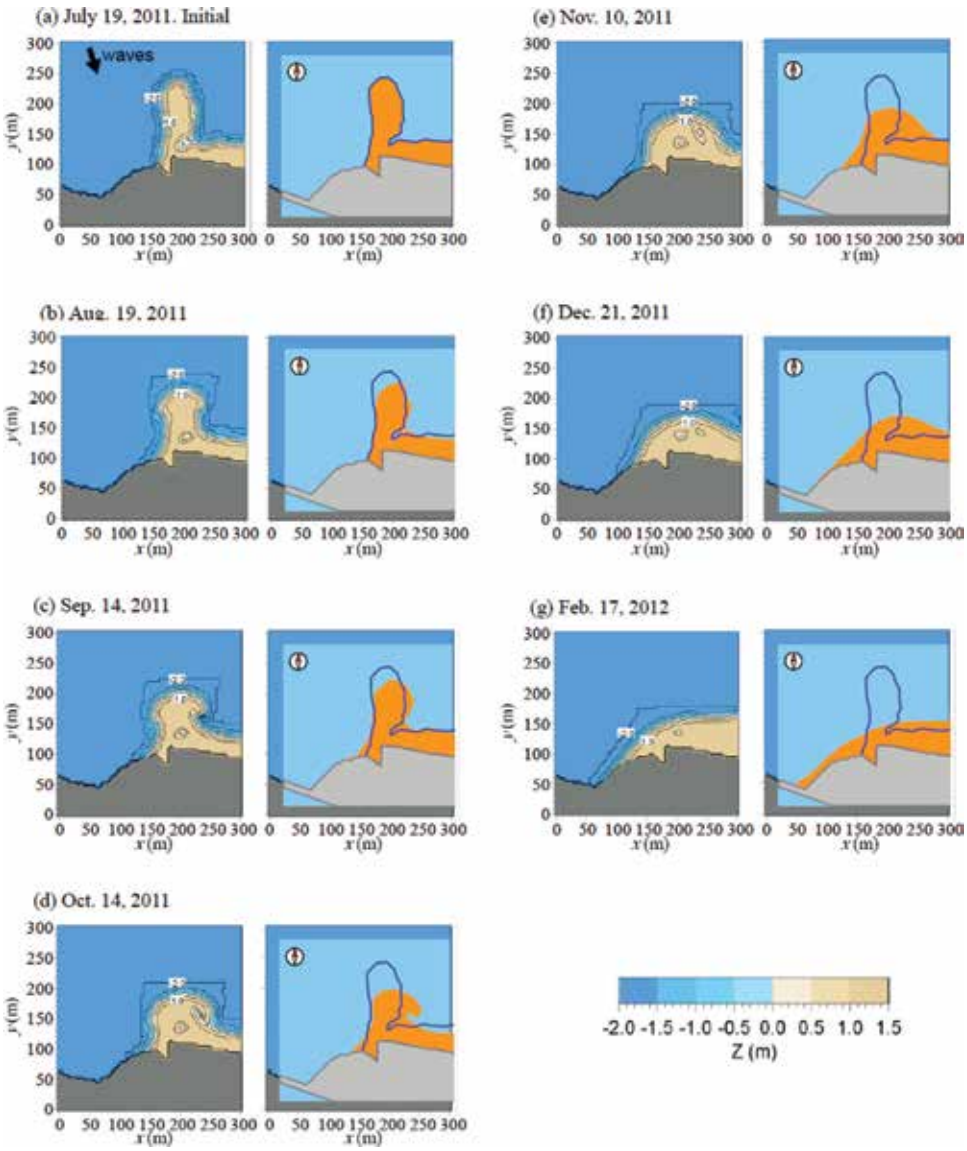

Figure 23.
Calculation results of deformation of sandbar [9].

5. Conclusions

In Chapter 5, three topics were discussed, and topographic changes were predicted using the BG model: (1) formation of a bay barrier in flat shallow sea and merging of bay mouth sand spits (Type 5 BG model), (2) elongation of sand spit on seabed with different water depths (Type 3 BG model), and (3) deformation of a sandbar formed at the tip of the Futtsu cuspate foreland owing to a tsunami which propagated into Tokyo Bay after the Great East Japan Earthquake (Type 3 BG model).

1. The elongation and merging of sand spits formed at a bay mouth of symmetric or asymmetric shape were studied. When a slender sandy headland was placed on the left side of the bay (Case 1), sand spits independently developed near the tip

and the base of the sandy headland at the initial stage. With increasing size of the sand spit formed near the tip of the sandy headland, the wave-sheltering effect increased, and the sand spits that had formed near the base of the sandy headland were subject to the wave-sheltering effect and disappeared. Finally, a single sand spit elongated rightward. The simulation results for the elongation of a single sand spit into a bay and an image in Zenkovich [4] were in good agreement.

2. When double sandy headlands were placed in the calculation domain (Case 2), a bay barrier with a concave shape was formed with a wide beach in the central part of the bay barrier. When the sandy headlands were placed asymmetrically (Case 3), the wave-sheltering effect of the sand spit from the larger headland on the smaller sand spit was significant, and the sand spits merged with each other to form a single bay mouth barrier. In Case 4, the formation of the embayed coasts by the extension of a barrier island as described in Zenkovich [4] was predicted, and the calculation results were in good agreement with the explanation regarding the formation of the embayed coasts given by Zenkovich [4].

3. The development of the sand spit was remarkable with a smaller water depth of the sand deposition zone, because sufficient wave energy cannot penetrate into the shallow body of water. In contrast, sufficient wave energy can reach the shoreline with a larger water depth, resulting in the increase in the curvature of the shoreline.

4. A crescent-shaped sandbar was formed offshore of the Futtsu cuspate foreland by the overflow during the 2011 Great East Japan Earthquake tsunami. The subsequent shoreline changes due to wind waves were investigated by field observation. These topographic changes were studied using the Type 3 BG model. The predicted and measured topographic changes of the crescent-shaped sandbar were in good agreement.

As further applications of the Type 3 BG model, (1) the model was used to predict the elongation of sand spit and profile changes on sloping shallow seabed under waves [16], (2) field observation on the formation of a barrier island as a result of elongation of sand spit was studied in Nabeshima area facing Nakatsu tidal flat in the Suonada Sea, and their formation was numerically predicted using the Type 3 BG model [17]. (3) The deformation of an isolated offshore sandbar on tidal flat and merging with beach owing to waves was also predicted using the Type 3 BG model in [18]. As regard the formation of a sand spit at the river mouth, (4) the rapid formation of a sand spit at a river mouth was measured at the Shimanto River mouth, and the deformation of a sand spit was predicted using Type 3 BG model in [19]. Moreover, (5) the beach changes on a coral cay owing to waves with seasonal change in wave direction was investigated on Embudu Village Island in the Maldives, and the seasonal movement of sand spits was predicted using the Type 3 BG model in [20].

Acknowledgements

Parts of the work described in Chapter 5, i.e., numerical simulations of elongation and merging of bay mouth sand spits, elongation of sand spit on seabed with different water depths, and deformation of sandbar formed at the tip of Futtsu cuspate foreland by the 2011 tsunami, were based on the conference papers [5, 7, 9], respectively, presented at the 34th Conference on Coastal Engineering in 2014. We would like to express our gratitude for the use of materials.

DOI: http://dx.doi.org/10.5772/intechopen.81415

Author details

Takaaki Uda[1*], Masumi Serizawa[2] and Shiho Miyahara[2]

1 Public Works Research Center, Tokyo, Japan

2 Coastal Engineering Laboratory Co., Ltd., Tokyo, Japan

*Address all correspondence to: uda@pwrc.or.jp

IntechOpen

© 2018 The Author(s). Licensee IntechOpen. Distributed under the terms of the Creative Commons Attribution - NonCommercial 4.0 License (https://creativecommons.org/licenses/by-nc/4.0/), which permits use, distribution and reproduction for non-commercial purposes, provided the original is properly cited. BY–NC

References

[1] Schwarz ML. The multiple causation of barrier islands. Journal of Geology. 1971;**79**:91-93

[2] Nummedal D. Barrier Islands. In: Komar PD, editor. Handbook of Coastal Processes and Erosion. Boca Raton, FL: CRC Press; 1983. pp. 77-121

[3] Bird E. Coastal Geomorphology: An Introduction. New York: John Wiley and Sons; 2000. p. 322

[4] Zenkovich VP. Processes of Coastal Development. New York: Interscience Publishers, Div. of John Wiley and Sons, ING; 1967. p. 751

[5] Watanabe S, Uda T, Serizawa M, Miyahara S. Numerical simulation of elongation and merging of bay mouth sand spits using the BG model. In: Proceedings of 34th ICCE; 2014. pp. 1-11. https://journals.tdl.org/icce/index.php/icce/article/view/7105/pdf_409

[6] Serizawa M, Uda T. Prediction of formation of sand spit on coast with sudden change in coastline using improved BG model. In: Proceedings of the Coastal Sediments; 2011. pp. 1907-1919

[7] San-nami T, Uda T, Serizawa M, Miyahara S. Numerical simulation of elongation of sand spit on seabed with different water depth and slopes. In: Proceedings of 34th ICCE; 2014. pp. 1-13. https://journals.tdl.org/icce/index.php/icce/article/view/7112/pdf_415

[8] Uda T, Kanda Y. Beach erosion of Futtsu Point in Chiba Prefecture. Coastal Engineering Journal, JSCE. 1995;**42**:651-655. (in Japanese)

[9] Kobayashi A, Uda T, Serizawa M, Miyahara S, Endo M. Numerical simulation of deformation of sandbar formed at tip of Futtsu cuspate foreland by the 2011 Tsunami. In: Proceedings of 34th ICCE; 2014. pp. 1-11. https://journals.tdl.org/icce/index.php/icce/article/view/7111/pdf_479

[10] Uda T. Japan's Beach Erosion—Reality and Future Measures. 2nd ed. Vol. 530. Singapore: World Scientific; 2017

[11] Ashton A, Murray AB. High-angle wave instability and emergent shoreline shapes: 1. Modeling of sand waves, flying spits, and capes. Journal of Geophysical Research. 2006;**111**:F04011. DOI: 10.1029/2005JF000422

[12] Ozasa H, Brampton AH. Model for predicting the shoreline evolution of beaches backed by seawalls. Coastal Engineering. 1980;**4**:47-64

[13] Mase H. Multidirectional random wave transformation model based on energy balance equation. Coastal Engineering Journal, JSCE. 2001;**43**(4):317-337

[14] Dally WR, Dean RG, Dalrymple RA. A model for breaker decay on beaches. In: Proceedings of 19th ICCE; 1984. pp. 82-97. https://journals.tdl.org/icce/index.php/icce/article/view/3787/3470

[15] Goda Y. Random Seas and Design of Maritime Structures. Vol. 323. Tokyo: University of Tokyo Press; 1985

[16] Miyahara S, Uda T, Serizawa M, San-nami T. Elongation of sand spit and profile changes on sloping shallow seabed. In: 8th International Conference on Asian and Pacific Coasts (APAC 2015). Procedia Engineering. 2015;**116**:245-253

[17] Miyahara S, Uda T, Serizawa M. Field observation and numerical simulation of barrier island formation

as a result of elongation of sand spit and its attachment to opposite shore. In: Proceedings of 35th Conference on Coastal Engineering, Sediment 5; 2016. pp. 1-14. https://icce-ojs-tamu.tdl.org/icce/index.php/icce/article/view/8103/pdf

[18] San-nami T, Uda T, Miyahara S, Serizawa M. Deformation of an isolated offshore sandbar on tidal flat and mergence with beach due to waves, Coastal Sediments '15, CD-Rom, No. 14; 2015. pp. 1-14

[19] Serizawa M, Uda T, Miyahara S. Rapid formation of a sand spit at river mouth and its prediction using BG model. In: Proceedings of 9th International Conference on Asian and Pacific Coasts (APAC2017); 2017. pp. 479-490

[20] Uda T, Serizawa M, Miyahara S. Seasonal movement of sand spits on a coaral cay of Embudu Village Island in the Maldives. In: Proceedings of 9th International Conference on Asian and Pacific Coasts (APAC2017); 2017. pp. 467-478

Chapter 7

Interaction of Sandy Islands

Takaaki Uda, Masumi Serizawa and Shiho Miyahara

Abstract

The formation of land-tied islands as a result of the extension of a cuspate foreland, when waves were incident to several islands composed of sand from two opposite directions, was first investigated, taking a land-tied island offshore of Shodoshima Island in the Seto Inland Sea, Japan, as an example, and their topographic changes were predicted using the Type 5 BG model. Then, the interaction among multiple circular sandy islands on flat shallow seabed owing to waves was investigated, taking the islands in Hingham Bay near Boston Harbor as an example. On the basis of this example, topographic changes were also predicted using the Type 5 BG model.

Keywords: land-tied island, interaction of islands, Shodoshima Island, multiple islands, Hingham Bay

1. Introduction

When waves are incident to a sandy beach from two opposite directions, a cuspate foreland may develop, and a land-tied island could be formed by the extension of a cuspate foreland. A typical land-tied island can be seen offshore of Shodoshima Island in the Seto Inland Sea, Japan [1]. This land-tied island extends from Bentenjima to Oyoshima Islands with two small islands, Nakayoshima and Koyoshima Islands, between them (**Figures 1** and **2**). The island and mainland are combined by a slender sandbar, which is exposed during low tide, suggesting that wave action from both sides of the sandbar balances each other. The sandbars connecting these islands are popular tourist attractions because of the scenic beauty, and understanding the formative mechanism is important in the study of the preservation of the sandbar. The formation of a land-tied island, however, has not been studied in the previous works except the studies regarding the morphological features of the fully developed land-tied island. In this chapter, field observations were first carried out around Oyoshima Island, and then the elongation of a sandbar of a land-tied island was predicted using the Type 5 BG model while focusing the importance of the wave-sheltering effect of an island affecting to another island into account. Then, the interaction among multiple circular sandy islands on flat shallow seabed owing to waves was investigated, taking the islands in Hingham Bay near Boston Harbor as an example. On the basis of this example, topographic changes were predicted using the Type 5 BG model.

IntechOpen

Figure 1.
Location of study area on the south shore of Shodoshima Island.

Figure 2.
A sandbar of land-tied island extending between Shodoshima and Oyoshima Islands.

2. Prediction of formation of land-tied islands

2.1 Field observations on Oyoshima Island

Field observation on this land-tied island was carried out during low and high tides on April 26 and 27, respectively, in 2013 [1]. In this area, two small isolated

islands, Nakayoshima and Shoyoshima Islands, are also located between the islands (**Figure 2**). The primary study area is the sandbar extending between the Ojima fishing port and Oyoshima Island.

Figures 3 and **4** show views of the sandbar extending from the mainland to Nakayoshima Island, taken from the top of Bentenjima Island (A in **Figure 2**) during low and high tides, facing the south. On the west side of the sandbar, a seabed of a gentle slope covered with gravel extended. Although the top of the sandbar was exposed during low tide, it was immediately below the sea surface during high tide. In addition, the sandbar had developed along the eastern marginal line of a shallow gravel bed of a gentle slope. In contrast, the beach on the east side of the sandbar

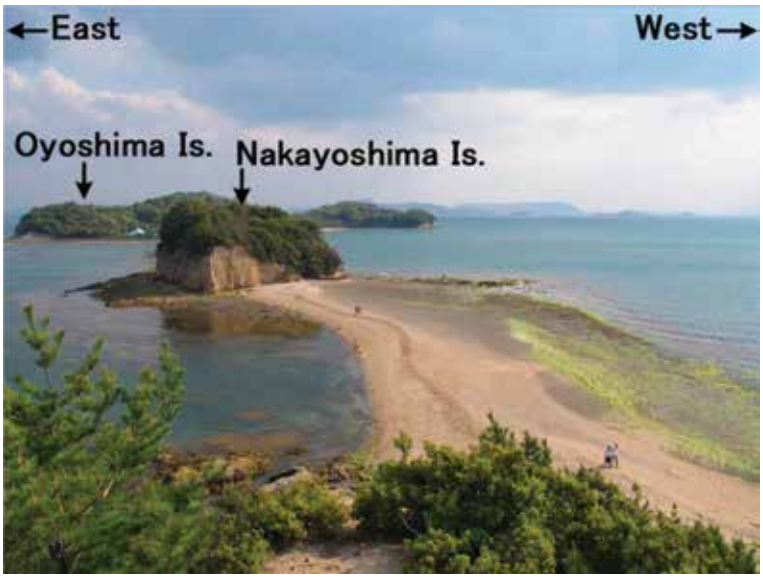

Figure 3.
Oblique photograph of sandbar taken during low tide on April 26, 2013 [1].

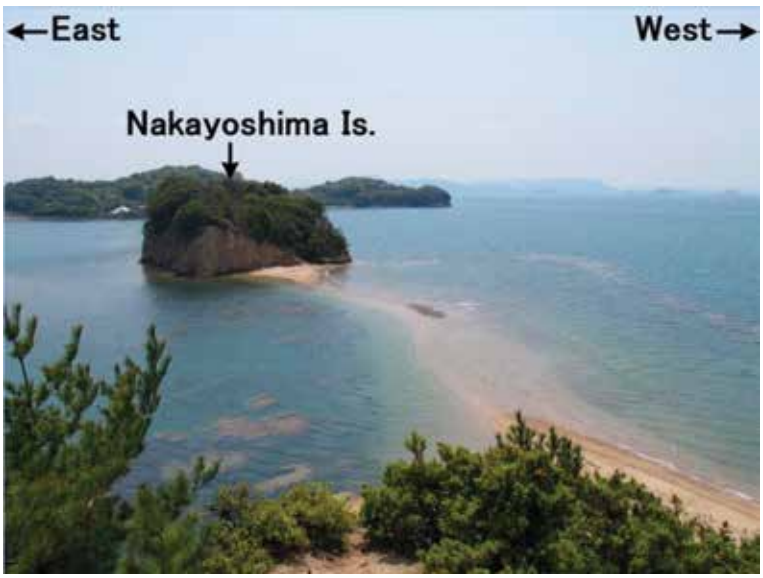

Figure 4.
Oblique photograph of sandbar taken during high tide on April 27, 2013 [1].

Figure 5.
Foreshore slope of 1/6.3 measured at the north side of Nakayoshima Island [1].

had a steep slope with concave shoreline, and exposed rocks covered with seaweed were observed offshore of the sandbar, implying no sand movement.

On Nakayoshima Island, a sea cliff and a wide wave-cut bench can be seen on the east side, in contrast to a lack of abrasion on the west side of the island, implying that the wave intensity from the east is greater than that from the west because of the longer fetch distance to the east (**Figure 2**). The beach material was composed of well-sorted granite sand supplied from sea cliffs composed of unconsolidated granite layers.

The foreshore of the sandbar elongating from the west end of Bentenjima to Nakayoshima Islands was composed of granite coarse sand, and the foreshore slope was 1/6.3 (**Figure 5**). On the east side of Nakayoshima Island, sea cliff and wave-cut bench were formed (**Figure 6**). The sea cliff is the highest at the east end with a gradually decreasing height westward and was composed of a well-weathered granite layer. It was inferred from these observations that Nakayoshima Island itself was a sand source for littoral sediment necessary for forming the land-tied island, and sand is mainly supplied from the east side of the island.

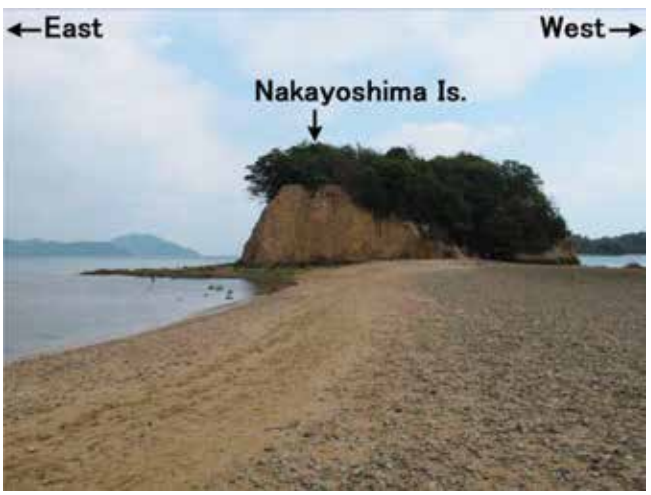

Figure 6.
Sea cliff and wave-cut bench on the east side of Nakayoshima Island [1].

Figure 7.
Sandbar extending between Shoyoshima and Oyoshima Islands [1].

At the south end of Shoyoshima Island, a sandbar extended toward Oyoshima Island (**Figure 7**), and the sandbar extended along the eastern edge of the gravel bed. At the north end of Oyoshima Island (point B in **Figure 2**), granite sand was deposited on the gravel bed composed of andesite (**Figure 8**). Furthermore, although the sandbar of a land-tied island of Oyoshima is convex to the west, the formation of this convex shape is assumed to be due to the greater intensity of the waves from the east relative to that from the west because of the longer fetch distance to the east (**Figure 2**).

2.2 Calculation conditions

Four cases of calculations were carried out. Consider a rectangular area with 600 m length in the longshore and cross-shore directions in Cases 1, 2, and 3 and 2000 and 500 m in longshore and cross-shore directions in Case 4. A flat shallow body of water with a constant depth of 3 m was assumed. Irregular waves were assumed to

Figure 8.
Sandbar extending between Oyoshima and Shoyoshima Islands [1].

be incident from the upper and lower sides of the calculation domain, and the topographic changes associated with the formation of a land-tied island were predicted using the Type 5 BG model [1]. Two sand sources were placed on both sides of the calculation domain in Cases 1 and 2, which had different probabilities of the occurrence of waves from two opposite directions, 1:1 and 1:0.5 in Cases 1 and 2, respectively. In Case 3, two sand sources were alternately placed on both sides of the calculation domain with the same probability of the occurrence of waves from two opposite directions as in Case 1. In Case 4, a sand source modeling a sea cliff on Nakayoshima Island was set at the center of the calculation domain with three small islands on each side of the sand source. To model the sand supply from the sea cliffs, the sand deficit was supplied at each step to maintain the topography of the sand source over time.

The wave direction at each step was randomly determined given the probability of the occurrence of the wave direction, similarly to the method given by San-nami et al. [2]. As the probability distribution of the occurrence of waves incident from two opposite directions, the energy distribution for multidirectional irregular waves with a directional spreading parameter of S_{max} = 10 was used. **Table 1** summarizes the conditions for calculating land-tied islands. In the calculation, waves were incident with a probability from all the directions on both sides of a land-tied island. The wave-sheltering effect increases around an island or the sandbar, and this enhances the sand deposition in the wave-shelter zone, and, in turn, sand deposition further increases the wave-sheltering effect (positive feedback).

2.3 Calculation results

When sand sources were set on both sides of the calculation domain and irregular waves with a significant wave height of 1 m were incident from the upper and lower sides of the calculation domain with the same probability of occurrence as in Case 1, a pair of cuspate forelands extended, and then a straight sandbar was formed (**Figure 9**). In Case 2 with the asymmetric probability of occurrence of 1:0.5, two cuspate forelands oriented downward were formed at the initial stage. They approached each other, and after 1.2×10^4 h, a sandbar was formed with a convex upper shoreline (**Figure 10**). Thus, when the probability of occurrence of waves was different, the effect of the asymmetric wave incidence was left in the asymmetric form of a cuspate foreland and a land-tied island. These results are in good agreement with the measured results, where the sandbar connecting

Calculation method	**Type 5 BG model**
Incident wave height H	1 m
Berm height h_R	1 m
Depth of closure h_c	3 m
Equilibrium slope tan β_c	1/10
Coefficients of sand transport	Longshore and cross-shore sand transport coefficient K_s = 0.2
Mesh size	$\Delta x = \Delta y$ = 10 m
Time interval	Δt = 2 h
Duration of calculation	8×10^4 h (4×10^4 steps)
Boundary conditions	Shoreward and landward ends $q_x = 0$ Right and left boundaries $q_y = 0$

Table 1.
conditions for calculating land-tied islands.

DOI: http://dx.doi.org/10.5772/intechopen.81416

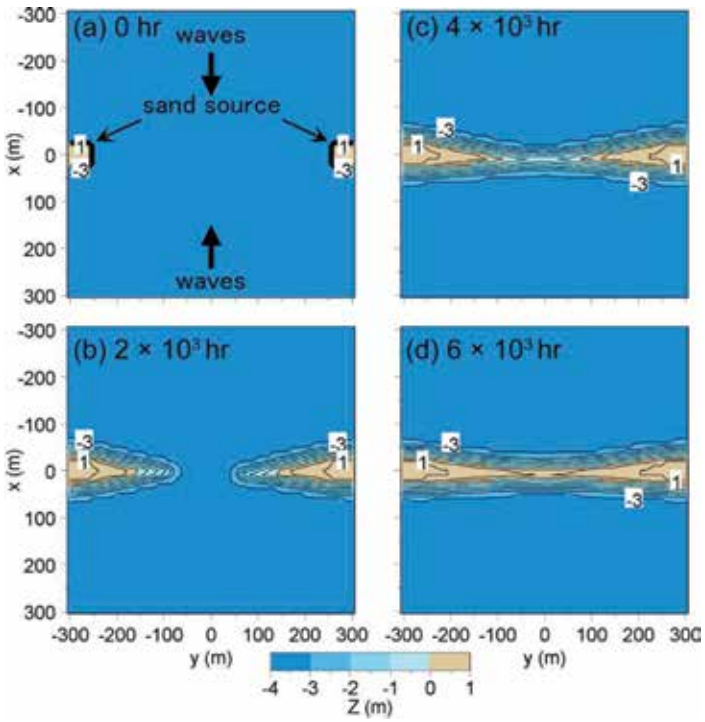

Figure 9.
Calculation results of Case 1 [1].

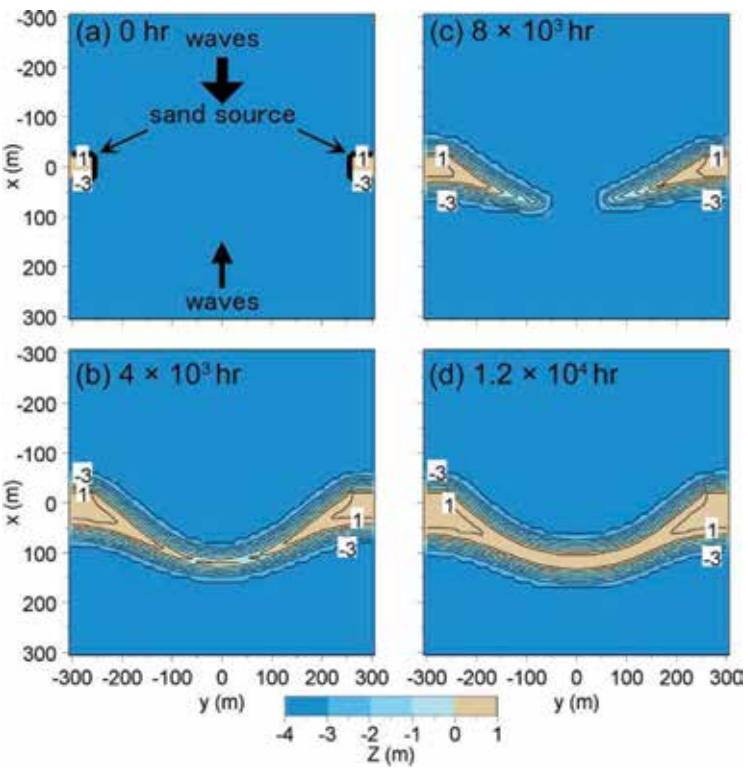

Figure 10.
Calculation results of Case 2 [1].

Bentenjima and Oyoshima Islands had a concave shape on the east side, as shown in **Figure 2**, implying that the wave intensity from the east is greater than that from the west.

When two sand sources were alternately placed on both sides of the calculation domain as in Case 3, the cuspate forelands on both sides pulled at each other owing to the wave-sheltering effect and the sandbars connected. Finally, an oblique cuspate foreland was formed after 2×10^4 h (**Figure 11**). In Case 4, the elongation of a sandbar was predicted, as shown in **Figure 12**. A slender sandbar extended from the sand source behind the islands owing to the wave-sheltering effect of islands a and a′ after 8×10^3 h, and the sand deposition zone extended toward islands b and b′ after 1.6×10^4 h. The tip of the sandbar reached the ends of islands b and b′ after 2.4×10^4 h, and the sandbar extended beyond islands b and b′ up to 3.2×10^4 h. Finally, the sandbar reached islands c and c′ located at both ends of the calculation domain after 4×10^4 h. The connection of the small islands by a slender sandbar convincingly explains the elongation of the sandbar connecting Oyoshima Island.

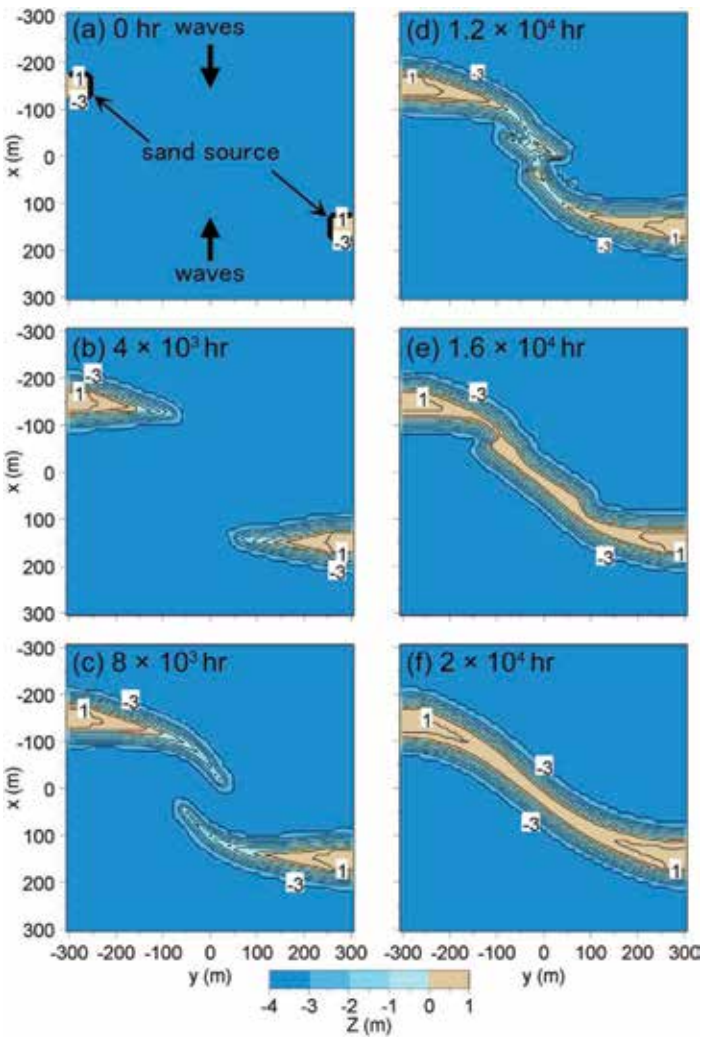

Figure 11.
Calculation results of Case 3 [1].

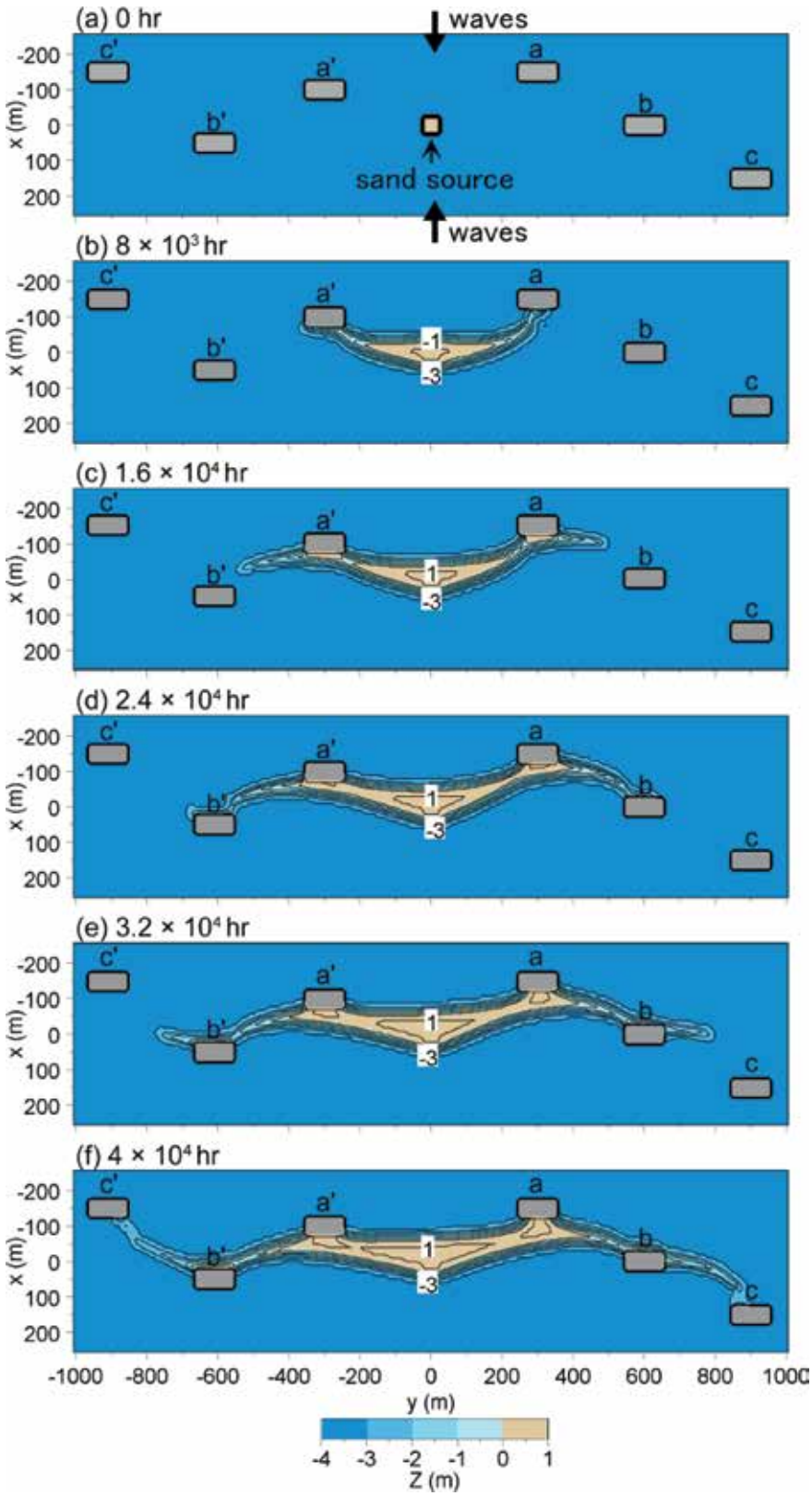

Figure 12.
Calculation results of Case 4 [1].

3. Interaction among multiple circular sandy islands on flat shallow seabed owing to waves

3.1 Connected islands in Hingham Bay in Massachusetts

Figure 13 shows the satellite image of Hingham Bay near Boston Harbor, where Davis and Fitzgerald [3] investigated the formation of Nantasket Beach, and the enlarged images of rectangular areas 1 and 2 in **Figure 13** are shown in **Figures 14** and **15** [3]. In area 1, small island A is seemed to connect to another island B with a slender sandbar, resulting in the formation of Rainsford Island. Similarly, in area 2, four small islands A, B, C, and D connected each other by slender sandbars, resulting in the formation of Peddocks Island. These examples imply that a sandbar may extend in a shallow water body among the islands and small islands may connect with each other by a slender sandbar, suggesting the importance of the wave-sheltering effect of islands themselves.

3.2 Calculation conditions

To investigate the deformation and interaction of multiple islands composed of sand by wave action in a shallow sea, the circular sandy islands were set on a plane solid seabed with a water depth of 2 m, and the beach changes were predicted in Cases 1 and 2 [4]. In both cases, wave incidence from the direction ranging between 0° and 360° with the same probability was assumed. In Case 3, the formation of Peddocks Island in Hingham Bay, as shown in **Figure 15**, was predicted. Since Peddocks Island is assumed to be composed of four islands, four circular islands with the radii of 250 m (A and B), 400 m (C), and 150 m (D) were assumed as the initial condition. The elevation of these islands and water depth surrounding the islands were assumed to be 1 and 2 m, respectively, with the same beach slope of 1/10 and wave conditions as those in Cases 1 and 2. Waves are assumed to be incident to these islands from all the directions with the same probability.

The incident wave height $H_{1/3}$ was assumed to be 1 m. Taking into consideration that the beach changes occur in extremely shallow water, the depth distribution

Figure 13.
Satellite image of Hingham Bay in Massachusetts.

Figure 14.
Satellite image of area 1 (Rainsford Island) in Hingham Bay.

Figure 15.
Satellite image of area 2 (Peddocks Island) in Hingham Bay.

of the sand transport was assumed to be uniform. The conditions for calculating deformation and interaction of multiple islands are summarized in **Table 2**.

3.3 Calculation results

3.3.1 Interaction of sandy islands of symmetric form

In Case 1, the wave-sheltering effect was induced by the sandy islands themselves [4]. Consider two sandy islands with the origin at points of $(x, y) = (0, 200)$

Calculation method	Type 5 BG model
Incident wave height $H_{1/3}$	1 m
Berm height h_R	1 m
Depth of closure h_c	2 m
Equilibrium slope tan β_c	1/10
Coefficients of sand transport	Coefficient of longshore and cross-shore sand transport K_s = 0.2
Mesh size	$\Delta x = \Delta y$ = 10 m
Time intervals	Δt = 1 h
Duration of calculation	3.5×10^4 h (3.5×10^4 steps)
Boundary conditions	Shoreward and landward ends $q_x = 0$ Right and left boundaries $q_y = 0$

Table 2.
Conditions for calculating deformation and interaction of multiple islands.

and (0, −200) and with the radius of 100 m (**Figure 16**). It is assumed that the two islands have the same size; the elevation and beach slope of the islands are 1 m and 1/10, respectively; and the two islands exist in a shallow sea of 2 m depth. Waves are assumed to be incident to these islands from all the directions with the same probability.

Under these conditions, island A is subject to the wave-sheltering effect by island B when waves are incident from the direction of the positive y-axis as in **Figure 17** [4]. Similarly, island B is subject to the wave-sheltering effect by island A when waves are incident from the direction of the negative y-axis. In contrast, when waves are incident from $\pm x$-axis direction, the wave field around islands A and B is not subject to the wave-sheltering effect of either island. Because waves are incident from all the directions around the islands, if the wave direction has a $\pm y$ component, island A or B is subject to the wave-sheltering effect by island B or A, respectively. Since the offshore breakwater is located at a fixed position, the offshore breakwater creates a stationary wave-shelter zone behind the structure, whereas in the case of multiple islands, the islands producing the wave-sheltering effects themselves may deform, resulting in a temporal change in the wave-sheltering effect. These are the major differences in both cases [4].

Under the conditions mentioned above, slender sandbars started to extend from the islands in the direction opposite to each other between the islands (**Figure 16**). After 2×10^3 steps, the sandbars extended from islands A and B almost connected with each other (**Figure 16(c)**), and the two islands became a single island with a neck in the center until 5×10^3 steps (**Figure 16(d)**). As time further elapsed, the neck in the center gradually disappeared, and the island was reduced to an elliptic form. After 2×10^4 steps, an island of almost elliptic form was formed with a center at a point of $(x, y) = (0, 0)$ (**Figure 16(f)**).

3.3.2 Interaction of two sandy islands of asymmetric form

In Case 2, the islands of different sizes were considered [4]. Because the wave-sheltering effect of a large island is more effective than that of a small island, asymmetric beach changes may occur. Two circular sandy islands A and B both centered at points of $(x, y) = (0, 200)$ and $(0, -200)$ and with radii of 100 m (A) and 50 m (B) were considered (**Figure 18**). The elevation of the islands and water depth surrounding the islands were assumed to be 1 and 2 m, respectively, with the same beach slope of 1/10 and wave conditions as those in Case 1.

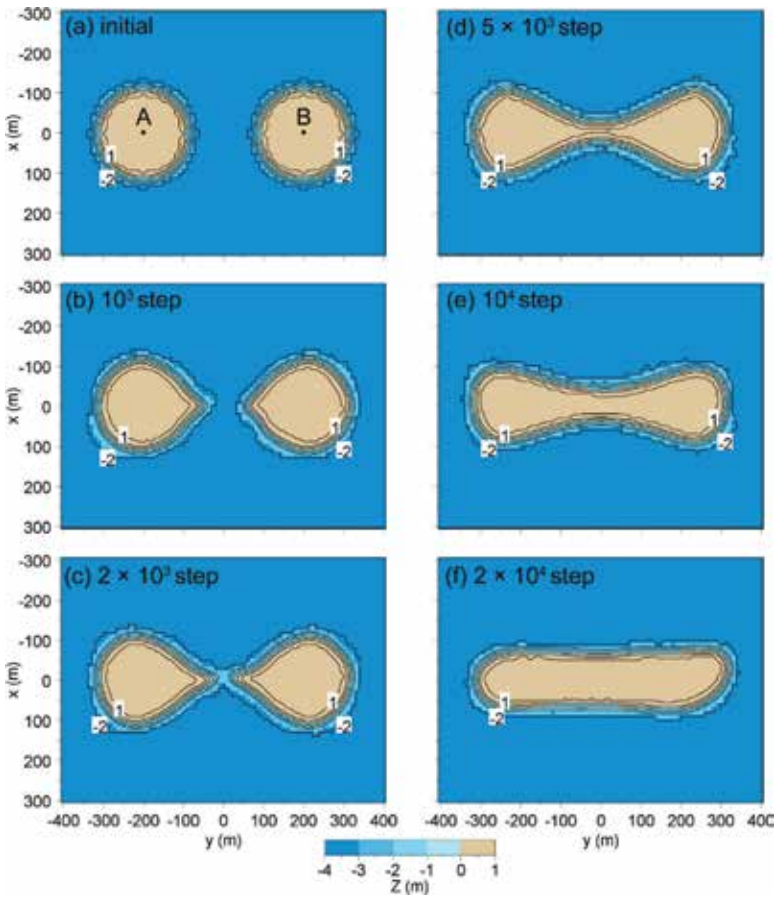

Figure 16.
Deformation and interaction of two symmetric islands composed of sand [4].

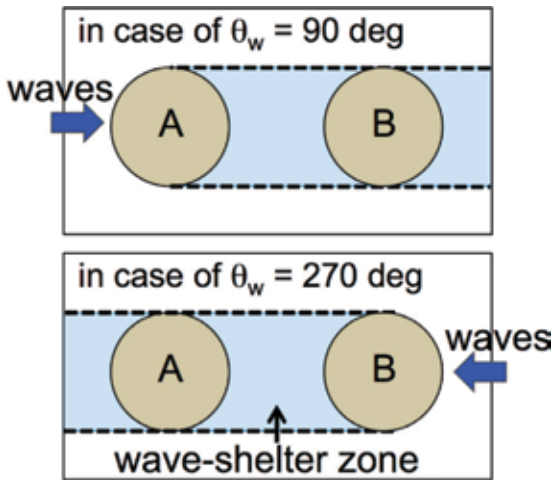

Figure 17.
Schematic view of wave-shelter zone behind two islands of same size under alternate wave incidence [4].

Under these conditions, island A is subject to the wave-sheltering effect of island B when waves are incident from the direction of the positive *y*-axis, but the wave-sheltering effect is relatively weak because of the smaller size of island B (**Figure 19**) [4].

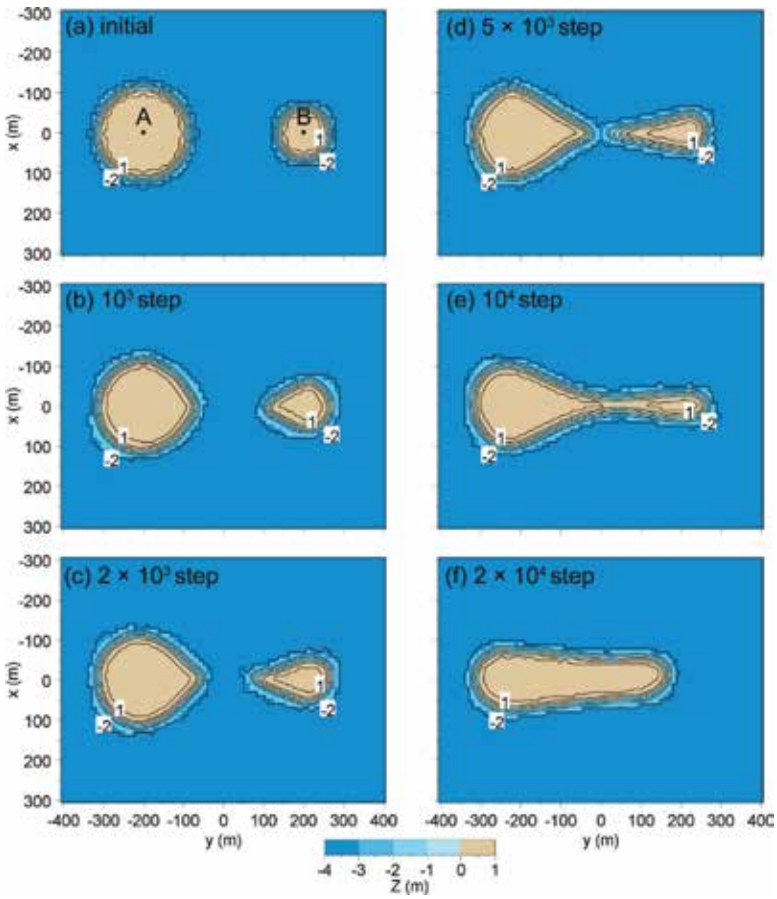

Figure 18.
Deformation and interaction of two asymmetric sandy islands [4].

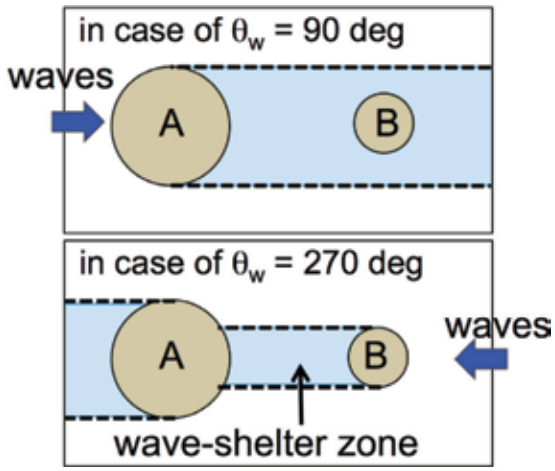

Figure 19.
Schematic view of wave-shelter zone behind small and large islands under alternate wave incidence [4].

On the other hand, when waves are incident from the direction of the negative y-axis, island B is subject to the stronger wave-sheltering effect of island A because of the larger size of island A than island B. Since waves are incident from all the directions around the

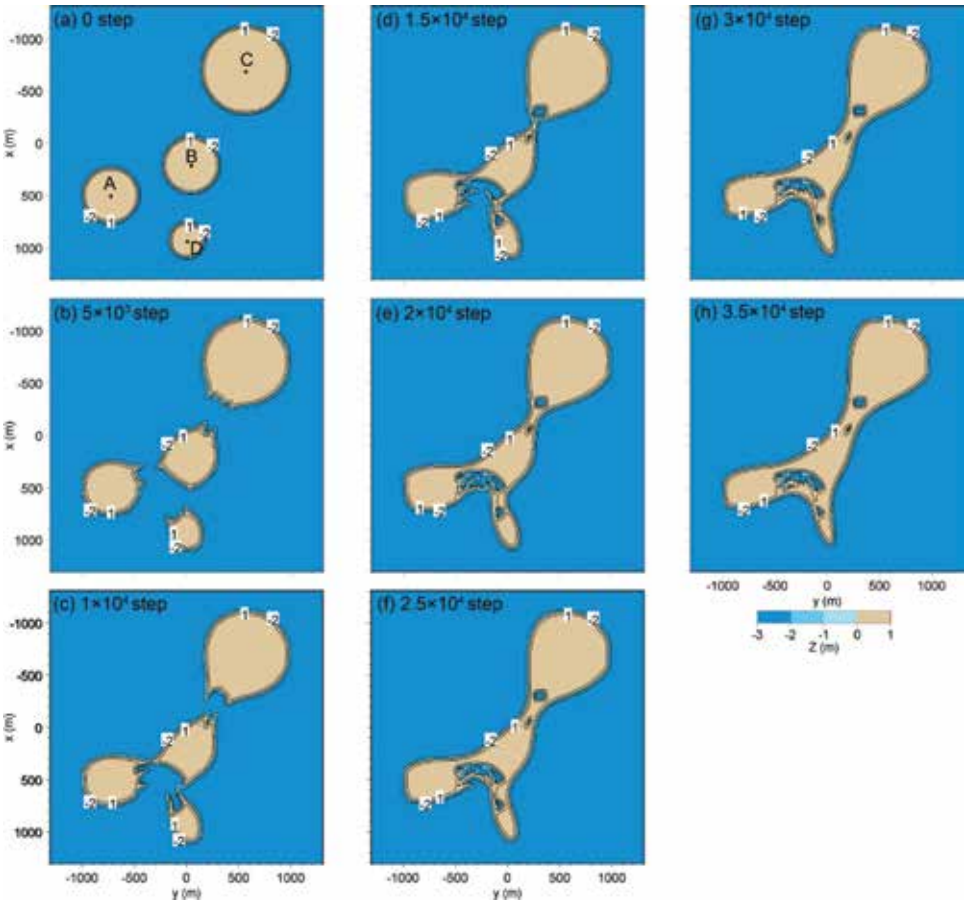

Figure 20.
Numerical simulation of formation of Peddocks Island in Hingham Bay.

islands, if the wave direction has a ± y component, island A or B is subject to the wave-sheltering effect by island B or A, respectively, but the wave-sheltering effect always becomes asymmetric.

The cuspate foreland started to extend in opposite directions between the islands, resulting in the larger cuspate foreland of island B to island A because island B is subject to the stronger wave-sheltering effect of island A (**Figure 18**) [4]. After 5×10^3 steps, the two islands extended and almost connected with each other (**Figure 18**(**d**)). After 10^4 steps, a slender sandbar, the width of which decreases rightward, was formed (**Figure 18**(**e**)). After a large number of time steps, the island became elliptical in shape, and the center of the island moved as a whole near the point of $(x, y) = (-100, 0)$ leftward compared with in Case 1 that the size of the islands is equivalent. Thus, the wave-sheltering effect of the islands themselves played an important role in the deformation of the islands located in shallow sea.

3.3.3 Prediction of formation of Peddocks Island in Hingham Bay

Figure 20 shows the results of the calculation. Four circular islands at the initial stage started to pull each other, and slender sandbars started to extend between the islands by 10^4 steps (**Figure 20**(**c**)). After 1.5×10^4 steps, four islands connected each other owing to the extension of a slender sandbars (**Figure 20**(**d**)). After 2×10^4 steps, the width of the sandbars increased (**Figure 20**(**e**)), and up to 3.5×10^4 steps,

four islands connected each other (**Figure 20**(**h**)), similar to the case of Peddocks Island, as shown in **Figure 15**. Although a small closed water body is left in **Figure 15** between islands A and B, the formation of such a closed water body was successfully predicted, as shown in **Figure 20**.

4. Conclusions

In Chapter 6, three topics were discussed, and topographic changes were predicted using the Type 5 BG model: (1) formation of land-tied islands, (2) interaction among multiple circular sandy islands on flat shallow seabed owing to waves, and (3) prediction of formation of Peddocks Island in Hingham Bay.

1. Field observation was carried out around the land-tied islands of Oyoshima, and the elongation of a sandbar connecting land-tied islands was successfully predicted by the Type 5 BG model when the wave direction at each step was randomly determined given the probability of occurrence of the wave direction [1]. It was concluded that the wave-sheltering effect of the islands and the shallowness of the body of water were key factors for the extension of a slender sandbar and the formation of a land-tied island.

2. The deformation and interaction of multiple sandy islands in a flat shallow sea offshore of Nantasket Beach in Massachusetts [3] were investigated, and the 3-D beach changes and interactions of these multiple islands were successfully predicted.

3. Peddocks Island in Hingham Bay was assumed to be composed of four circular islands at the initial stage with the radii of 250 m (A and B), 400 m (C), and 150 m (D). Then, the present form of Peddocks Island was predicted using the Type 5 BG model. The shape of Peddocks Island as well as the formation of a closed water body between small islands was successfully predicted.

As further application of the Type 5 BG model to the prediction of beach changes, the model was used to predict the elongation and connection of sandbars located offshore of Krabi in Thailand under waves [5].

Acknowledgements

Parts of the contents described in Chapter 6, that is, (1) prediction of formation of land-tied islands and (2) interaction among multiple circular sandy islands on flat shallow seabed owing to waves, are based on the articles [1, 4] presented at the 34th Conference on Coastal Engineering, Seoul, Korea (2014). We would like to express our gratitude for the use of materials.

DOI: http://dx.doi.org/10.5772/intechopen.81416

Author details

Takaaki Uda[1*], Masumi Serizawa[2] and Shiho Miyahara[2]

1 Public Works Research Center, Tokyo, Japan

2 Coastal Engineering Laboratory Co., Ltd., Tokyo, Japan

*Address all correspondence to: uda@pwrc.or.jp

IntechOpen

© 2018 The Author(s). Licensee IntechOpen. Distributed under the terms of the Creative Commons Attribution - NonCommercial 4.0 License (https://creativecommons.org/licenses/by-nc/4.0/), which permits use, distribution and reproduction for non-commercial purposes, provided the original is properly cited. BY–NC

References

[1] Miyahara S, Uda T, Serizawa M. Prediction of formation of land-tied islands. In: Proceedings of 34th ICCE; 2014. pp. 1-14. https://journals.tdl.org/icce/index.php/icce/article/view/7108/pdf_412

[2] San-nami T, Uda T, Serizawa M, Miyahara S. Prediction of devastation of natural coral cay by human activity. In: Proceedings of Coastal Dynamics 2013, Paper No. 138; 2013. pp. 1427-1438

[3] Davis RA, FitzGerald DM. Beaches and Coasts. Malden: Blackwell; 2004. p. 419

[4] Serizawa M, Uda T, Miyahara S. Interaction between two circular sandy islands on flat shallow seabed owing to waves. In: Proceedings of 34th ICCE; 2014. pp. 1-12. https://journals.tdl.org/icce/index.php/icce/article/view/7106/pdf_410

[5] Uda T, Serizawa M, Miyahara S. Development of sandbars around islands offshore of Krabi in Thailand and their prediction. In: Proceedings of 36th Conference on Coastal Engineering; 2018 (in press)

Chapter 8

Formation of Cuspate Foreland

Takaaki Uda, Masumi Serizawa and Shiho Miyahara

Abstract

The formation of a cuspate foreland when waves were incident from two opposite directions was investigated, taking a cuspate foreland extending at the northeast end of Graham Island in British Colombia of Canada and the cuspate forelands formed at the tip of Hon Bip Island north of Nha Trang, Vietnam, as the examples. The formation of such a cuspate foreland was predicted using the Type 4 BG model. Then, the development of multiple sand spits with rhythmic shapes in a shallow water body was investigated, taking the Sea of Azov in Russia as the example. Furthermore, the development of sand spits and cuspate forelands with rhythmic shapes was predicted, assuming that the waves were obliquely incident at angles of 60° relative to the direction normal to the shoreline or at angles of ±60° with probability p_1:p_2 = 0.50:0.50, 0.60:0.40, 0.65:0.35, 0.70:0.30, 0.75:0.25, and 0.80:0.20.

Keywords: cuspate foreland, sand spits, Sea of Azov, Graham Island, Hon Bip Island, rhythmic shapes, shoreline instability, wave-sheltering effect

1. Introduction

A sand spit is a dynamically changing topography formed by the successive deposition of littoral sand when waves are obliquely incident at a large angle relative to the direction normal to the shoreline [1, 2]. A cuspate foreland is another topography protruding into the sea, and it could be formed when waves are incident from two opposite directions, and a cuspate foreland of symmetric or asymmetric shape could be formed depending on the probability of the occurrence of incident waves. Ashton et al. [2] and Ashton and Murray [3] developed a model for predicting the formation of cuspate forelands with rhythmic shapes when waves were obliquely incident from two opposite directions at an angle greater than approximately 45° relative to the direction normal to the shoreline. The present authors also proposed a model for predicting the topographic changes of cuspate forelands with rhythmic shapes using the BG model [4, 5]. However, there were no studies on the formation of a cuspate foreland when waves were incident from two completely opposite directions. Therefore, the morphological characteristics of the cuspate foreland located at the northeast end of Graham Island in British Colombia of Canada and the cuspate forelands formed at the tip of Hon Bip Island north of Nha Trang, Vietnam, were investigated, and then the development of a cuspate foreland when waves were obliquely incident from two opposite directions was predicted using the Type 4 BG model in Section 2 [6].

Zenkovich [1] showed that multiple sand spits with rhythmic shapes may develop in shallow bodies of water, such as the Azov Sea, and called them the Azov-type spits. **Figure 1** shows the satellite image of multiple sand spits with rhythmic shapes developed in t17, the Azov Sea in Russia, and an enlarged image

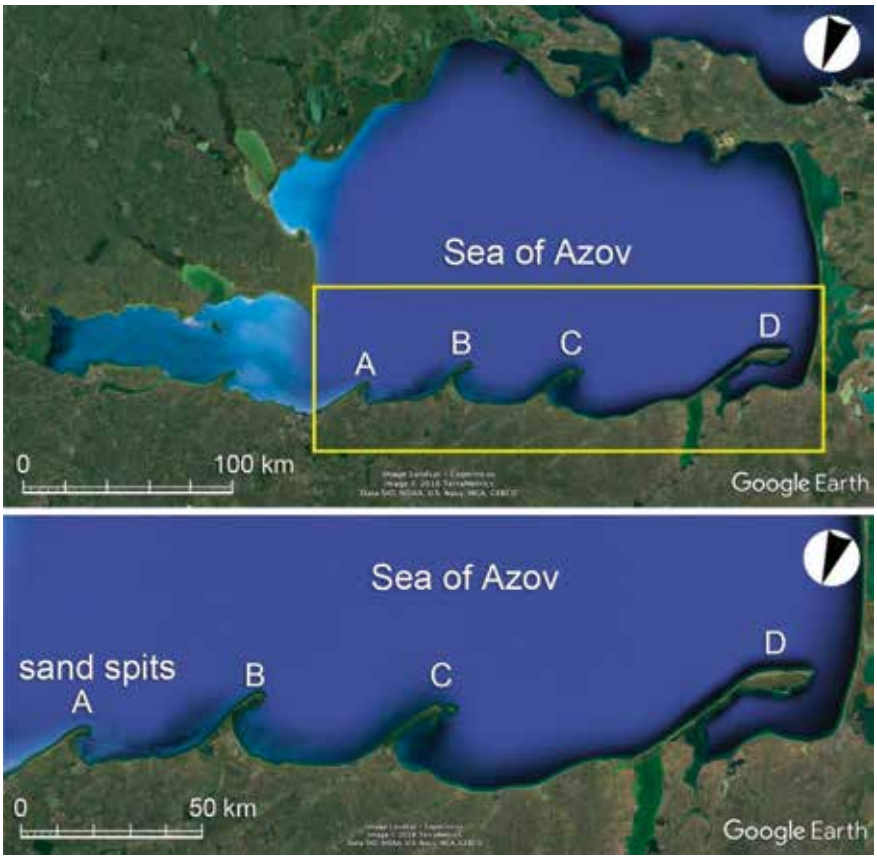

Figure 1.
Multiple sand spits with rhythmic shapes developed in Sea of Azov in Russia [5].

of the rectangular area in **Figure 1**. He concluded that shoreline instability may occur when waves are obliquely incident at an angle larger than 45°, and the wave-sheltering effect due to the sand spits themselves plays an important role in the development of sand spits. Ashton et al. [2] adopted this mechanism and successfully modeled the shoreline instability, and this mechanism was called high-angle wave instability [3]. Littlewood et al. [7] predicted the shoreline of log-spiral bays using their model. In Section 3, we predicted the development of sand spits and cuspate forelands when waves were obliquely incident at an angle larger than 45°, given a small perturbation in the initial topography, and showed that the three-dimensional (3-D) beach changes of sand spits and cuspate forelands with rhythmic shapes can be predicted using the Type 4 BG model [4, 5]. van den Berg et al. [8] predicted the development of sand waves caused by high-angle wave instability using equations similar to that of our model, but not the development of sand spits or cuspate forelands.

2. Model for predicting formation of a cuspate foreland

2.1 Cuspate foreland extending at northeast end of Graham Island

A large cuspate foreland extends at the northeast end of Graham Island in British Colombia of Canada, as shown in **Figure 2** [6, 9]. Graham Island is located north of Moresby Island with a narrow channel separating these islands. The

coastlines of these islands face the Pacific Ocean to the west and extend for 300 km in the SE-NW direction. At the north end of Graham Island, Dixon Entrance of 46 km width is located, and the cuspate foreland extends east of the entrance along with Hecate Strait on the south side. The primary and secondary wave directions are from NW and SSE, respectively, from these geometrical conditions [6].

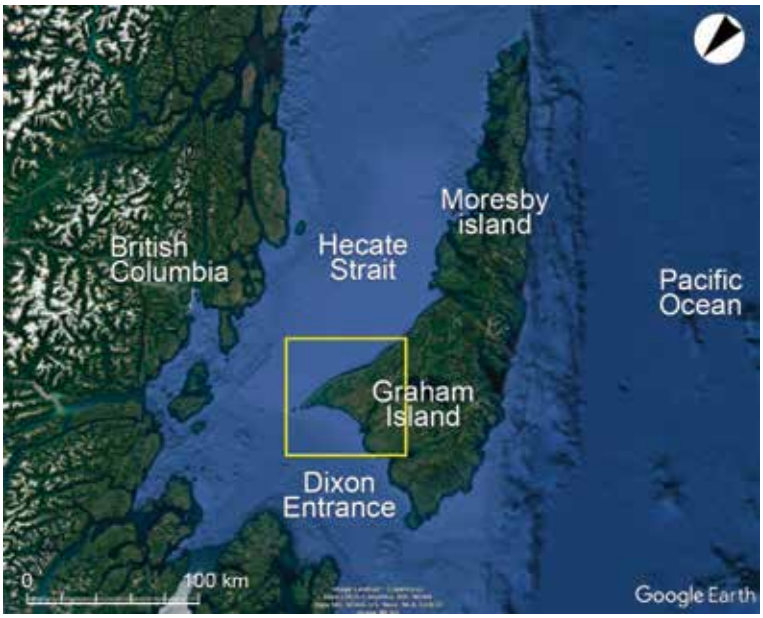

Figure 2.
Location of cuspate foreland at northeast end of Graham Island in Canada.

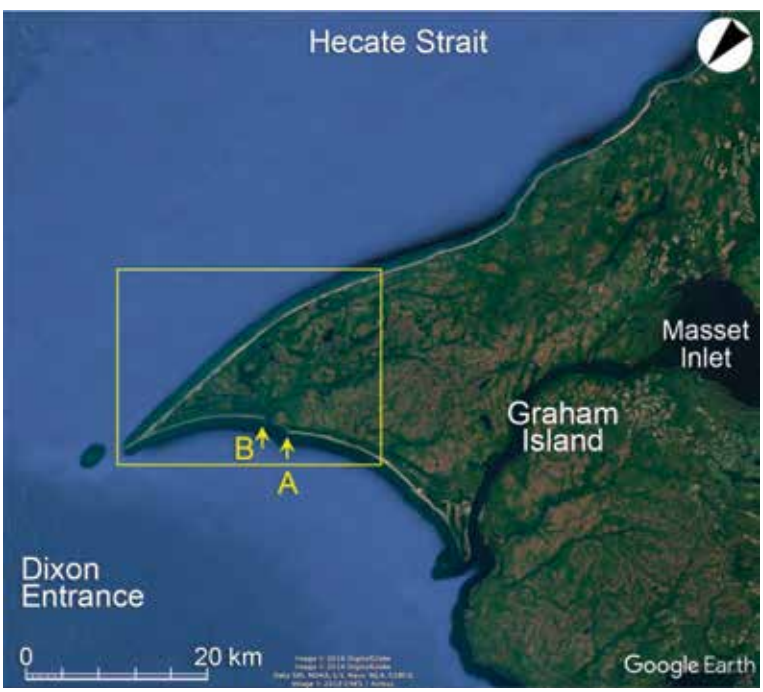

Figure 3.
Enlarged satellite image of cuspate foreland (rectangular area in ***Figure 2****).*

Figure 4.
*Enlarged satellite image of sand ridges and a closed water body C (rectangular area in **Figure 3**).*

Figure 3 shows an enlarged satellite image of the rectangular area in **Figure 2**; the entire coastline west of the foreland has a concave shape, and a hooked shoreline is formed east of points A and B. This means that longshore sand transport toward the tip of the cuspate foreland prevails because of the waves incident from the Pacific Ocean via Dixon Entrance located northwest of the foreland. Furthermore, a number of beach ridges run in parallel with the present shoreline east of point B, as shown in **Figure 4**, which is an enlarged satellite image of the rectangular area in **Figure 3**, implying that sand transported northeastward was deposited to form the cuspate foreland. In contrast, no beach ridges develop along the east coastline extending in the S–N direction, and a number of sand dunes have been formed by the SE wind at an angle of 40° relative to the direction normal to the mean coastline [6]. The development of these sand dunes clearly demonstrates that the coast along the eastern side of the foreland is subjected to the action of the wind waves incident from SE, resulting in the predominance of northward longshore sand transport toward the tip of the foreland. All these conditions of longshore sand transport promote the development

Figure 5.
Hon Bip Island in Van Phong Bay in Vietnam.

Figure 6.
Enlarged satellite images of areas A and B in ***Figure 5****.*

of the cuspate foreland. Moreover, water bodies enclosed inland of the cuspate foreland can be seen near point C in **Figure 4**, which is assumed to be closely related to the formative mechanism of a cuspate foreland.

2.2 Land-tied islands and cuspate foreland on Hon Bip Island

Hon Bip Island is located in Van Phong Bay north of Nha Trang, Vietnam. In the vicinity of this island, a land-tied island and a cuspate foreland are formed [10], similarly to the cases on Yoshima Island offshore of Shodo Island [11]. **Figure 5** shows a satellite image of Hon Bip Island. A shallow sea extends on the southwest

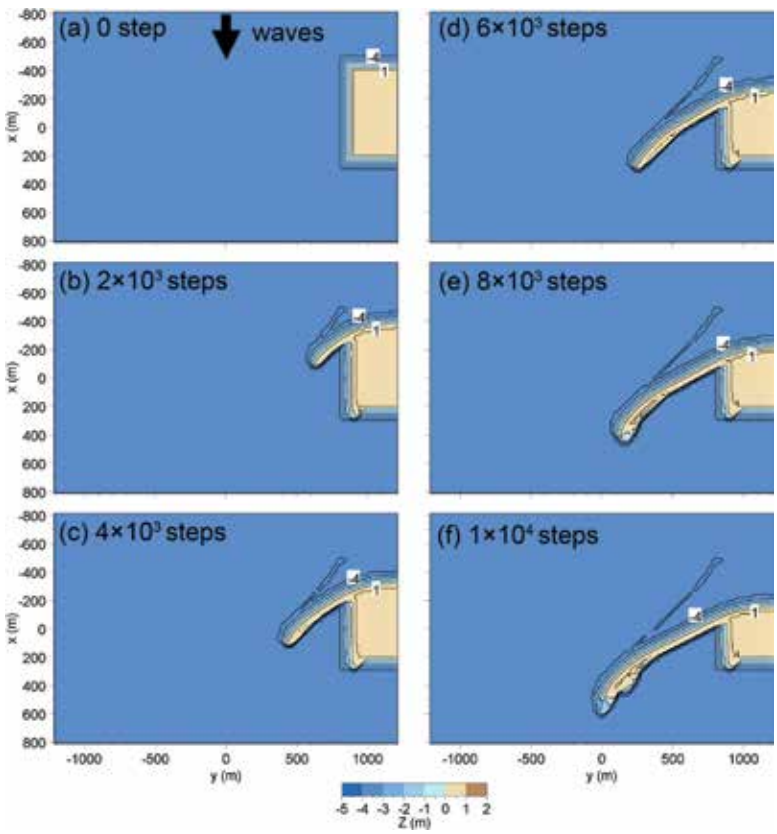

Figure 7.
Extension of single sand spit in Case 1.

side of this island, and slender islands of 0.7 and 1.07 km lengths exist, and sand bars of 0.53 and 0.20 km lengths connecting the islands extend to form a land-tied island. Furthermore, from the southwest end of the islands, a small-scale cuspate foreland extends westward. **Figure 6** shows the enlarged satellite images of areas A and B, shown in **Figure 5**. The cuspate foreland extends straight in a shallow sea between the islands in area A. In contrast, a deep bay approaches the cuspate foreland from the east in area B, resulting in the formation of a bay-shaped shoreline on the east side of the cuspate foreland. Thus, the cuspate foreland can extend in the shallow sea between the islands owing the wave-sheltering effect of the islands.

2.3 Calculation conditions

To predict the formation and deformation of a cuspate foreland, the Cartesian coordinates of (x, y) were introduced, and a rectangular area of 2.4 km width and 1.6 km length was adopted as the calculation domain (**Figure 7(a)**). The water depth was assumed to be a constant of 4 m, and a sandy beach with 1 m height and 1/20 slope was set along the rectangular shoreline as the initial condition. The incident wave height was assumed to be 1 m. Four cases of calculation were carried out; a single wave from the $-x$-axis in Case 1, waves with the equivalent probability of 0.5 incident from two opposite directions in Case 2, and waves incident from two opposite directions with the probabilities of $p_1 = 0.75$ from the $-x$-axis (downward) and $p_2 = 0.25$ from the $+x$-axis (upward) in Case 3. In addition, in Case 4, the

Calculation method	Type 4 BG model
Wave conditions	Incident waves: H_I = 1 m, T = 4 s, wave direction θ_I = 0°, and 180° relative to x-axis
Berm height	h_R = 1 m
Depth of closure	h_c = 4 m
Equilibrium slope	$\tan\beta_c = 1/20$
Angle of repose slope	$\tan\phi = 1/2$
Coefficients of sand transport	Coefficient of longshore sand transport K_s = 0.2 Coefficient of Ozasa and Brampton [12] term $K_2 = 1.62K_s$ Coefficient of cross-shore sand transport $K_n = K_s$
Mesh size	$\Delta x = \Delta y$ = 20 m
Time intervals	Δt = 0.5 h
Duration of calculation	10^4 h (2×10^4 steps)
Boundary conditions	Shoreward and landward ends, $q_x = 0$; right and left boundaries, $q_y = 0$
Calculation of wave field	Energy balance equation [13] • Term of wave dissipation due to wave breaking: Dally et al. [14] model • Wave spectrum of incident waves: directional wave spectrum density obtained by Goda [15] • Total number of frequency components N_F = 1 and number of directional subdivisions N_θ = 8 • Directional spreading parameter S_{max} = 25 • Coefficient of wave breaking K = 0.17 and Γ = 0.3 • Imaginary depth between minimum depth h_0 (0.5 m) and berm height h_R • Wave energy = 0 where $Z \geq h_R$ • Lower limit of h in terms of wave decay due to breaking, 0.5 m

Table 1.
Conditions for calculation of formation of a cuspate foreland.

extension of cuspate forelands, their connection and merging in a shallow water body between two islands were numerically simulated. The wave direction was determined using random numbers when waves were incident from two opposite directions. **Table 1** summarizes the conditions for the calculation of the formation of a cuspate foreland.

2.4 Calculation results

First, the formation of a single sand spit in Case 1 is shown in **Figure 7** in which a single wave was incident from the $-x$-axis. The beach on the exposed side was eroded, and sand was transported obliquely by longshore sand transport, and a single sand spit extended (**Figure 7(b)–(f)**). As the sand spit extended, a wave-shelter zone was formed behind the sand spit itself, so that no beach changes occurred behind the sand spit except the downdrift corner of the initial rectangular sandy island.

When waves were incident from two completely opposite directions with the same probability, as in Case 2, sand spits were soon formed at the right corners of the rectangular sand mound (**Figure 8(b)**) [6]. Then, the sand spits that independently

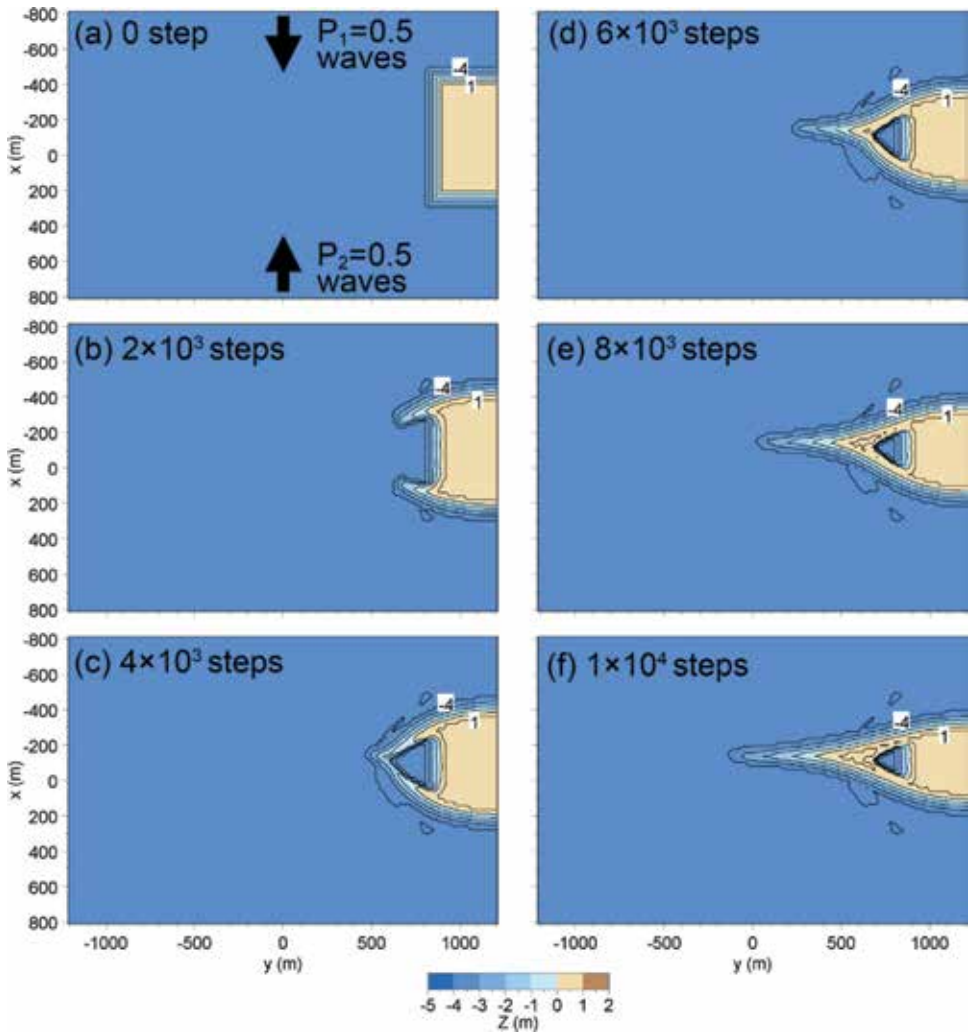

Figure 8.
Extension of cuspate foreland in Case 2.

developed at each corner were pulled to each other and connected because of the wave-sheltering effect of a sand spit at one side to the other (**Figure 8(c)**). Finally, a triangular, completely closed water body was formed at the central part after 6×10^3 steps (**Figure 8(d)**). The size of the closed water body gradually decreased over time because of the deposition of sand owing to cross-shore sand transport, although the tip of the foreland continued to extend leftward, as shown in **Figure 8 (e** and **f)**. These results are in good agreement with the measured at the northeast end of

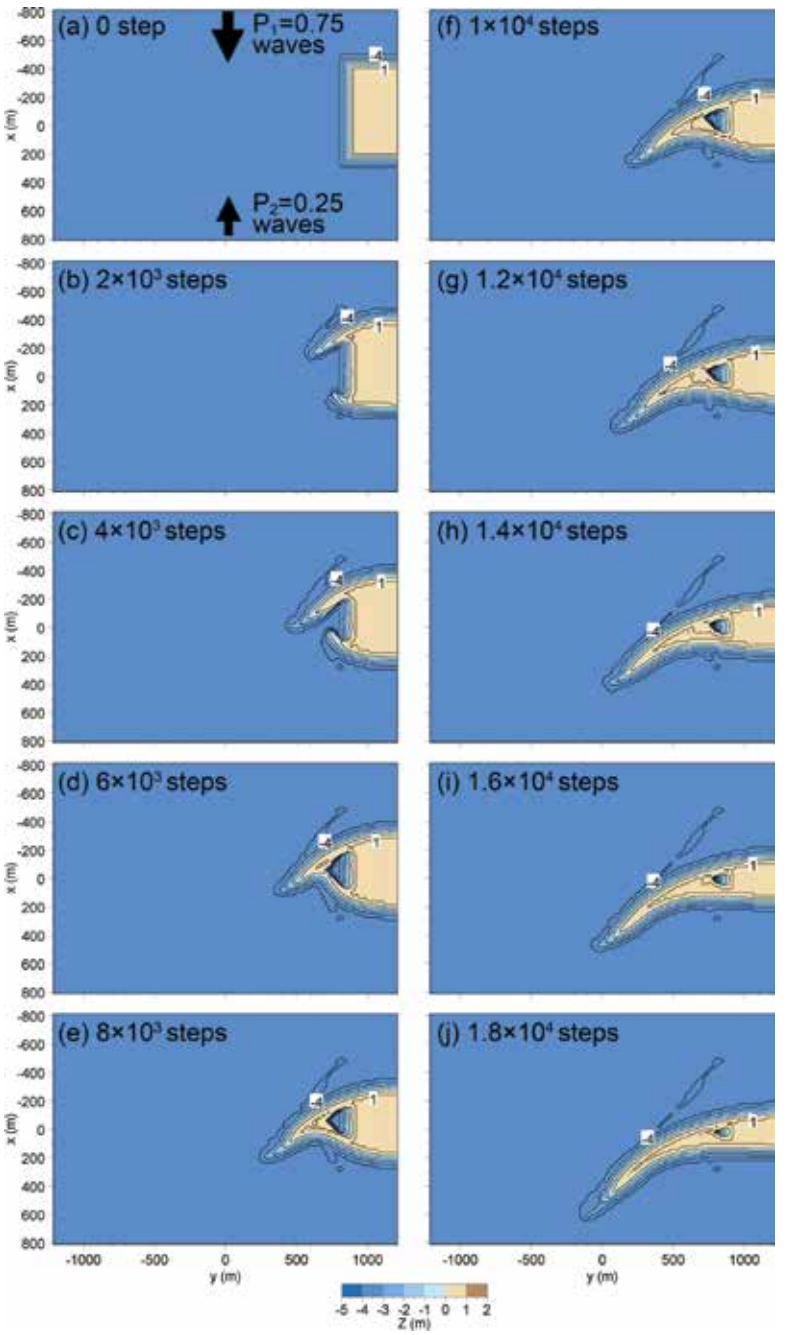

Figure 9.
Extension of cuspate foreland in Case 3.

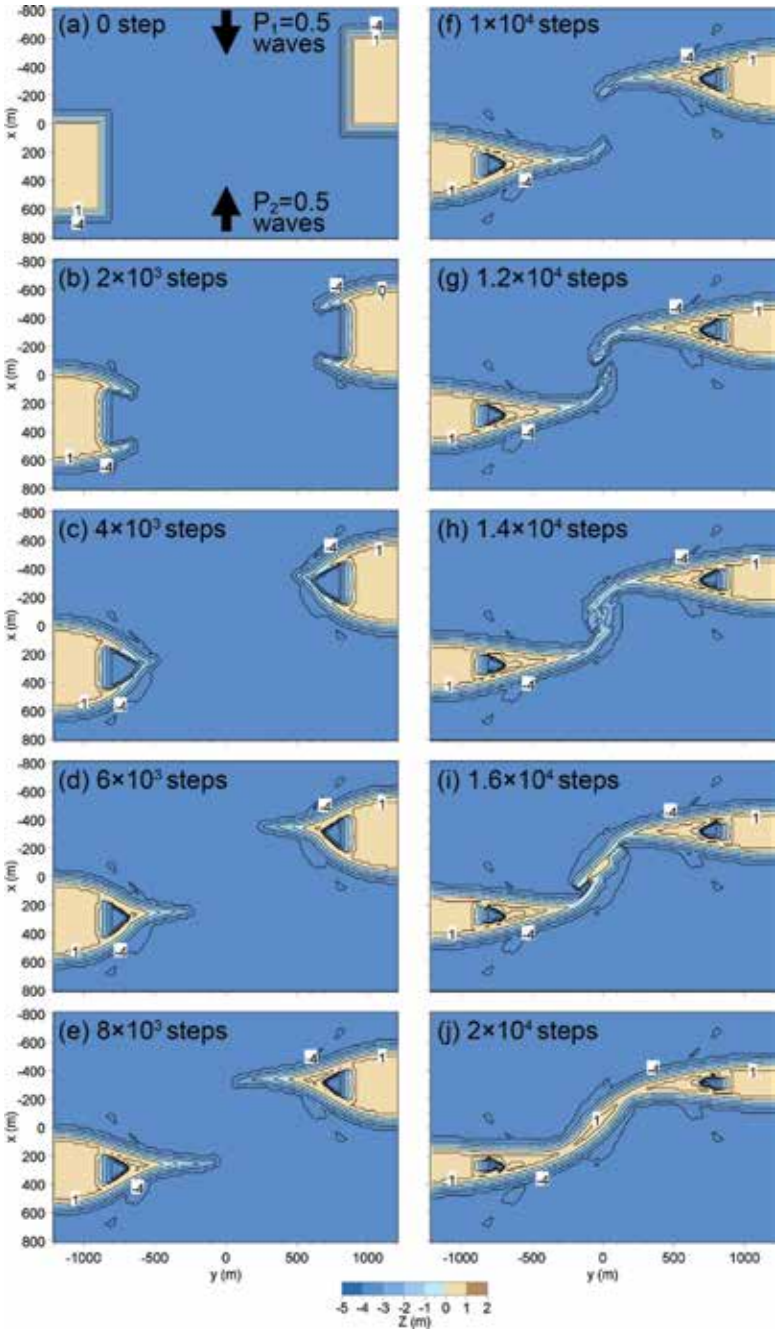

Figure 10.
Extension, connection, and merging of two cuspate forelands (Case 4).

Graham Island in terms of the formation of a closed water body in the central part of the cuspate foreland, as shown in **Figure 4**.

When waves were incident from two opposite directions with different probabilities as in Case 3, an asymmetric cuspate foreland developed (**Figure 9**). At the initial stage, there existed a rectangular sand mound (**Figure 9(a)**). A cuspate foreland on the upper side elongated faster than that on the lower side because of a larger probability of waves, as shown in **Figure 9 (b** and **c)**, and a distorted closed water body was formed in the central part up to 6 × 10^3 steps (**Figure 9(d)**). Then, the cuspate

foreland further extended over time, and the size of this distorted closed water body decreased (**Figure 9(f)**–**(i)**). By 1.8×10^4 steps, a triangular closed water body was almost buried with sand with the recession of the upside shoreline, reducing the size (**Figure 9(j)**).

In Case 4, two sandy islands were set on both sides of the calculation domain, and waves were randomly incident from the $\pm x$-directions with the same probability of 0.5, as shown in **Figure 10**. The cuspate forelands started to elongate from both ends of the sandy islands toward the y-axis and became a flatter shape owing to the action of the waves incident from the $\pm x$-axis directions after 2000 steps (**Figure 10(b)**). Two triangular closed water bodies were formed on both sides up to 4×10^3 steps (**Figure 10(c)**). The cuspate forelands further developed after 6×10^3 steps (**Figure 10(d)**). After 8×10^3 steps, the tips of the slender cuspate forelands extending from the ends of the two islands had pulled each other, and their tips started to bend inward (**Figure 10(e)**). After 1.2×10^4 steps, cuspate forelands at the tips were about to connect (**Figure 10(g)**), and they were almost connected to each other after 1.4×10^4 steps, resembling shaking hands (**Figure 10(h)**). Then, the two islands were connected to each other, and a smooth shoreline was formed after 2×10^4 steps (**Figure 10(j)**).

3. Development of sand spits and cuspate forelands with rhythmic shapes

3.1 Calculation conditions

Ashton and Murray [3] showed that the generation of shoreline instability closely depended on the probability of occurrence of wave directions; sand spits, cuspate bumps, and sand spits with hooked shoreline developed in the case that the probability of occurrence of a unidirectional wave was high, the probability of occurrence of waves incident from two directions was equivalent, and waves were incident from two directions with different probabilities, respectively. The calculation conditions in this study were determined referring their results [4, 5]. As the wave conditions, H_i = 1 m and T = 4 s were assumed considering the formation of sand spits in a shallow lagoon. The wave direction was assumed to be obliquely incident at an angle of 60° and at angles of ±60° with probability p_1:p_2 = 0.50:0.50, 0.60:0.40, 0.65:0.35, 0.70:0.30, 0.75:0.25, and 0.80:0.20, and the wave direction at each step was determined from the probability distribution [4, 5].

Consider a shallow lake with a flat solid bed of 4 m depth, and the initial beach slope and a berm height were assumed to be 1/20 and 1 m, respectively. At the initial stage, a small random perturbation with an amplitude of ΔZ = 0.5 m was added to the slope. The calculation domain was a rectangle of 4 km length and 1.2 km width, and a periodic boundary condition was set at both ends. h_c, the equilibrium slope, and the repose slope were assumed to be 4 m, 1/20, and 1/2, respectively. The calculation of the wave field was carried out every 10 steps in the calculation of beach changes. The detailed conditions for the calculation of development of sand spits and cuspate forelands with rhythmic shapes are summarized in **Table 2**.

3.2 Calculation results

3.2.1 Oblique wave incidence at an angle of 60°

Figures 11 and **12** show the calculation results of the development of sand spits from infinitesimal perturbation and the bird's eye view of the same results.

Calculation method	Type 4 BG model
Wave conditions	Incident waves: H_i = 1 m, T = 4 s, and wave direction θ_I = 60° relative to direction normal to initial shoreline
Berm height	h_R = 1 m
Depth of closure	h_c = 4 m (still water depth)
Equilibrium slope	$\tan\beta_c$ = 1/20
Angle of repose slope	$\tan\phi$ = 1/2
Coefficients of sand transport	Coefficient of longshore sand transport K_s = 0.2 Coefficient of Ozasa and Brampton term [12] $K_2 = 1.62K_s$ Coefficient of cross-shore sand transport $K_n = K_s$
Mesh size	$\Delta x = \Delta y$ = 20 m
Time intervals	Δt = 0.5 h
Duration of calculation	2.75×10^4 h (5.5×10^4 steps)
Boundary conditions	Shoreward and landward ends, q_x = 0; right and left boundaries, periodic boundary
Calculation of wave field	Energy balance equation [13] • Term of wave dissipation due to wave breaking: Dally et al. [14] model • Wave spectrum of incident waves: directional wave spectrum density in Goda [15] • Total number of frequency components N_F = 1 and number of directional subdivisions N_θ = 8 • Directional spreading parameter S_{max} = 25 • Coefficient of wave breaking K = 0.17 and Γ = 0.3 • Imaginary depth between depth h_0 (0.5 m) and berm height h_R • Wave energy = 0 where $Z \geq h_R$ • Lower limit of h in terms of wave decay due to wave breaking, 0.5 m

Table 2.
Conditions for calculation of development of sand spits and cuspate forelands with rhythmic shapes.

The small perturbation applied to the slope at the initial stage developed into 11 cuspate forelands within 5×10^3 steps (**Figures 11(b)** and **12(b)**), and the shoreline projection increased with time together with the rightward movement. Because of the periodic boundary condition at both ends, the cuspate forelands that moved away through the right boundary reentered the calculation domain through the left boundary [4, 5]. After 10^4 steps, the shoreline protrusion increased and developed as slender sand spits (**Figures 11(c)** and **12(c)**). After 2×10^4 steps, the small-scale sand spits located adjacent to each other had merged into large-scale sand spits and disappeared, resulting in the formation of six sand spits (**Figures 11(d)** and **12(c)**).

Two reasons for the above changes are considered [1, 2, 4, 5]. (1) Of the two sand spits of different scales, the small sand spits move faster than the large ones in the absence of the wave-sheltering effect, and then the small sand spits catch up and merge with the large ones. (2) On the lee of sand spits with an elongated neck, a wave-shelter zone is formed, and the velocity of the small sand spits is reduced in the zone because of low wave energy, resulting in the stoppage of the movement of the sand spits and in the merging of small sand spits with larger spits. Furthermore, the sand spits developed and protruded, because (1) their tip is semicircular, meaning that the angle between the direction normal to the shoreline

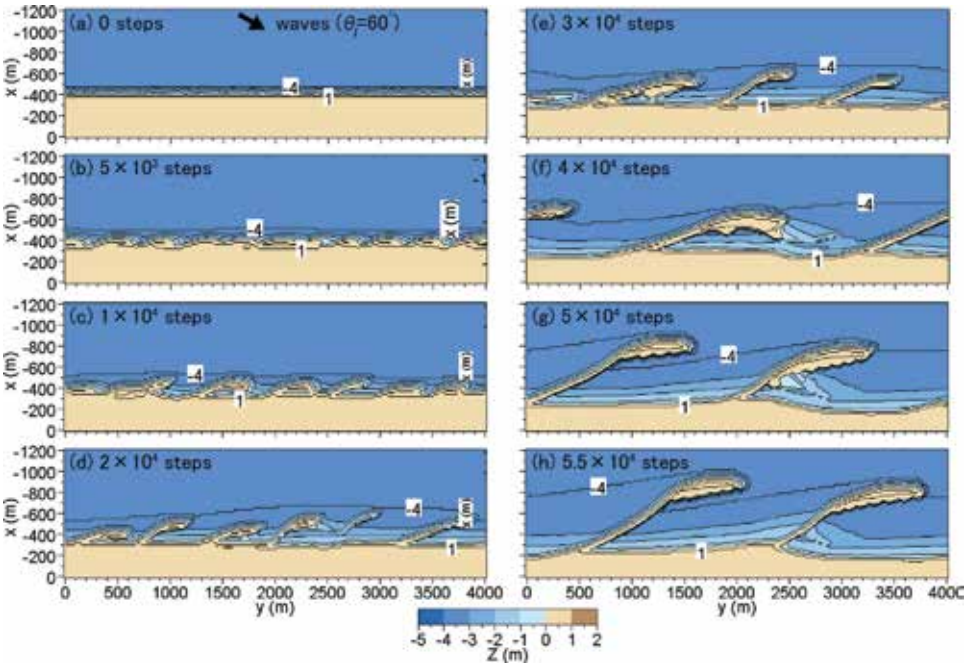

Figure 11.
Development of sand spits from infinitesimal perturbation when waves are obliquely incident at an angle of 60° [4, 5].

and the wave direction exceeds 45° at a point along the shoreline, and the shoreline protrusion occurs at such a point owing to high-angle wave instability. (2) In a wave-shelter zone, sand transport is significantly reduced, whereas it is enhanced near the tip of the sand spits, and thus, the derivative of the sand transport rate takes a maximum value near the boundary between the tip of the sand spits and the wave-shelter zone, inducing the protrusion of sand spits.

After 3×10^4 steps, the small sand spits located in the wave-shelter zone of the large-scale sand spits had stopped moving and merged into the large-scale sand spits, resulting in a decrease in the number of sand spits (**Figures 11(e)** and **12(e)**). After 4×10^4 steps, the number of sand spits decreased to two, and the tip of the sand spits approached close to the original shoreline, permitting the downcoast passage of the sand (**Figure 11(f)**). Two large-scale sand spits were formed up to 5×10^4 steps, and the offshore contour of −4 m depth obliquely extended toward the tip of the sand spit (**Figures 11(g)** and **12(f)**). These features are in good agreement with those measured around sand spits in lakes and bays [16].

3.2.2 Oblique wave incidence at angles of ±60° with probability of 0.50:0.50

When waves were obliquely incident at angles of ±60° with probability of 0.50:0.50, triangular cuspate forelands had developed after 10^4 steps (**Figures 13** and **14**). In this case, symmetric cuspate forelands were formed, and small-scale cuspate forelands disappeared and merged with larger cuspate forelands [4, 5]. Because of the same probability of the occurrence of both wave directions, no net longshore sand transport and no unidirectional movement of the sand body occurred. After 2×10^4 steps, the number of triangular cuspate forelands had been reduced to five (**Figures 13(d)** and **14(c)**), and they further continued to develop with the merging of small-scale cuspate forelands. After 4×10^4 steps, four symmetric cuspate forelands had developed (**Figures 13(f)** and **14(e)**).

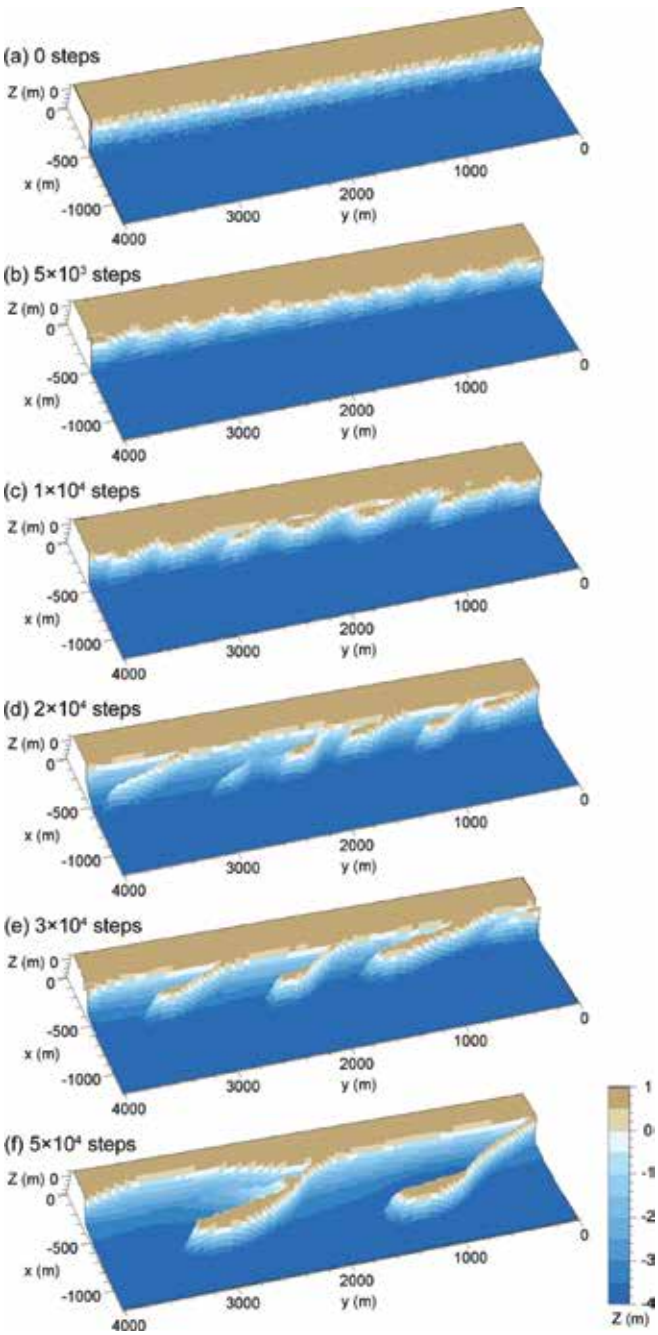

Figure 12.
Bird's eye view of the development of sand spits.

3.2.3 Oblique wave incidence at angles of ±60° with different probabilities

Waves were obliquely incident at angles of ±60°, and the probability of occurrence of waves was changed as 0.60:0.40, 0.65:0.35, 0.70:0.30, 0.75:0.25, and 0.80:0.20, i.e., the condition that rightward longshore sand transport gradually increased with the change in probability.

In case with probability of 0.60:0.40, symmetric cuspate forelands that slightly inclined rightward have developed (**Figure 15**) [5]. Because of the rightward net

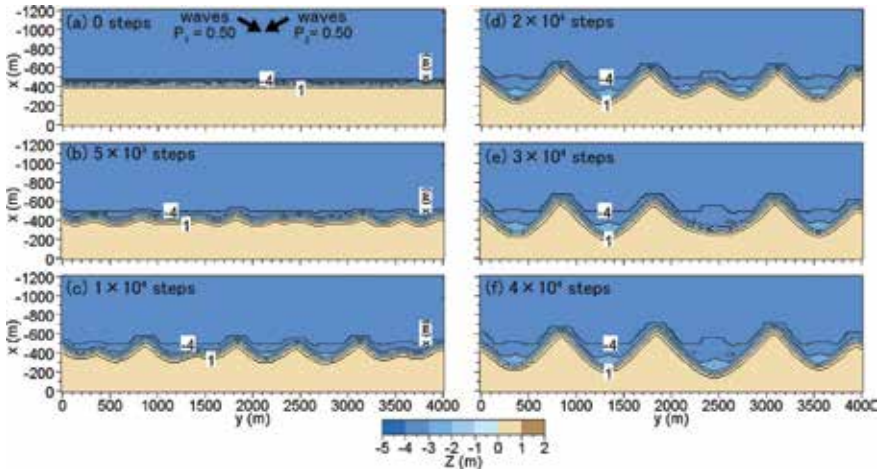

Figure 13.
Formation of cuspate forelands when waves were obliquely incident at angles of ±60° with probability of 0.50:0.50 [4, 5].

longshore sand transport, cuspate forelands developed while moving rightward. The shoreline left of the tips of cuspate forelands extended straight, whereas the shoreline curvature increased immediately right of the tips, forming a hooked shoreline. The contour of 4 m depth extended toward the tips of the forelands while obliquely intersecting with the shoreline left of the tip of the foreland, and then it extended parallel to the shoreline from the tip of the foreland with a large curvature.

In case with probability of 0.65:0.35, the steepness of the cuspate forelands increased after 2×10^4 steps, and a hooked shoreline inclined rightward had formed, because the probability of occurrence of waves incident from the left increased (**Figure 16(a)**) [4, 5]. After 3×10^4 steps, sand spits were formed at the tips of the cuspate forelands (**Figure 16(b)**), and a shallow bay was formed between the apexes, and sand spits obliquely extended rightward from the tips of the cuspate forelands with a larger angle than that in **Figure 13** until 4×10^4 steps (**Figure 16(c)**). In particular, the calculation results obtained after 4×10^4 steps and the case in a lagoon facing the Chukchi Sea shown in **Figure 1** are in good agreement.

In case with probability of 0.70:0.30, sand spits had already developed after 2×10^4 steps (**Figure 17(a)**), and these sand spits further elongated downcoast after 3×10^4 steps (**Figure 17(b)**), and sand spits with a narrow neck at the connecting point to the land and a long head were formed until 4×10^4 steps (**Figure 17(c)**) [5]. The number of sand spits reduced to two from four in the case with probability of 0.70:0.30. Similarly, in case with probability of 0.75:0.25, a slender sand spit started to develop after 2×10^4 steps (**Figure 18(a)**), and the sand spit with a narrow neck had elongated rightward after 3×10^4 steps (**Figure 18(b)**). After 4×10^4 steps, sand spits with a long, slender neck had developed (**Figure 18(c)**). Although contours shallower than 3 m depth extended parallel to the shoreline, while forming the main body of the sand spits, the contour of 4 m depth had an embayment downcoast of the sand spits [5]. Finally, in the case for probability of 0.80:0.20, many sand spits with a head extending in parallel with the original shoreline were formed close to the coastline after 2×10^4 steps, because the probability of occurrence of waves from the left markedly increased (**Figure 19(a)**). After 3×10^4 steps, the lengths of sand spits had further increased, but the head of sand spits extended parallel to the coastline similar to the development of longshore sand bars (**Figure 19(b)**).

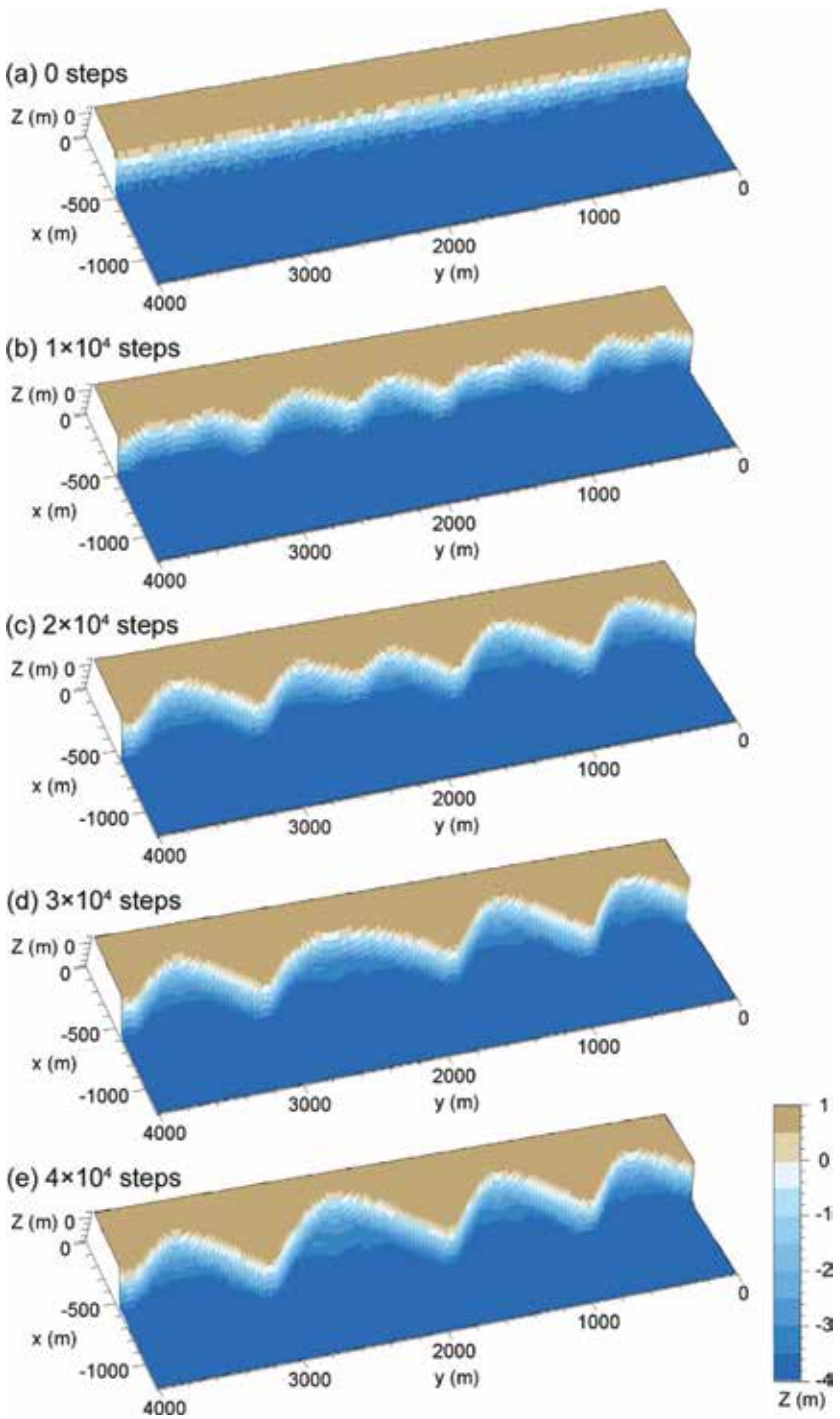

Figure 14.
Bird's eye view of the development of cuspate forelands.

Thus, symmetric cuspate forelands were formed when waves were obliquely incident at angles of ±60° with an equivalent probability of the occurrence of waves. With probability of 0.60:0.40, the asymmetry of cuspate forelands increased, and sand spits started to form after 2×10^4 steps with a probability of 0.65:0.35.

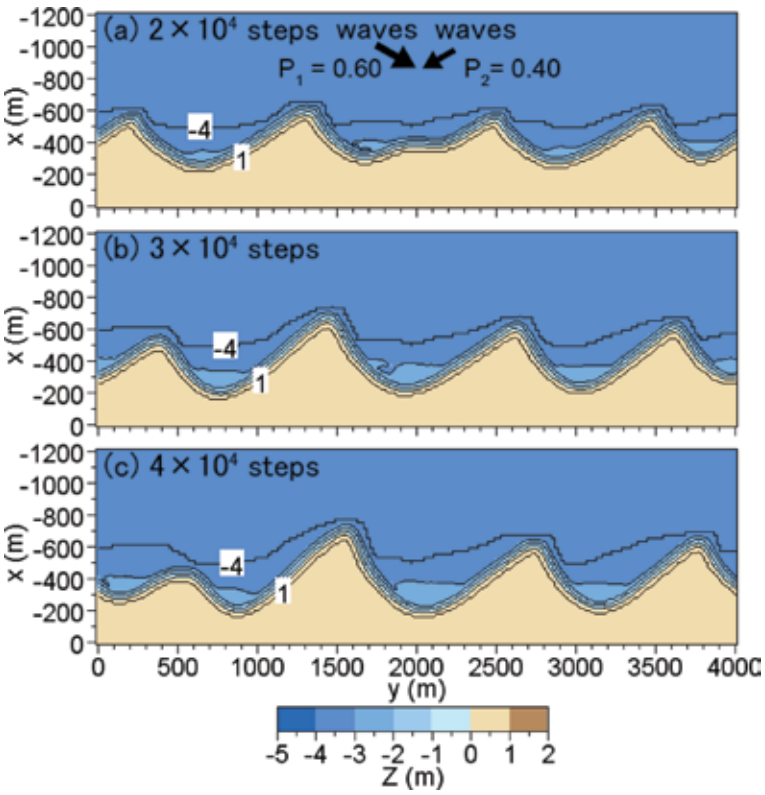

Figure 15.
Formation of cuspate forelands when waves were obliquely incident at angles of ±60° with probability of 0.60:0.40 [5].

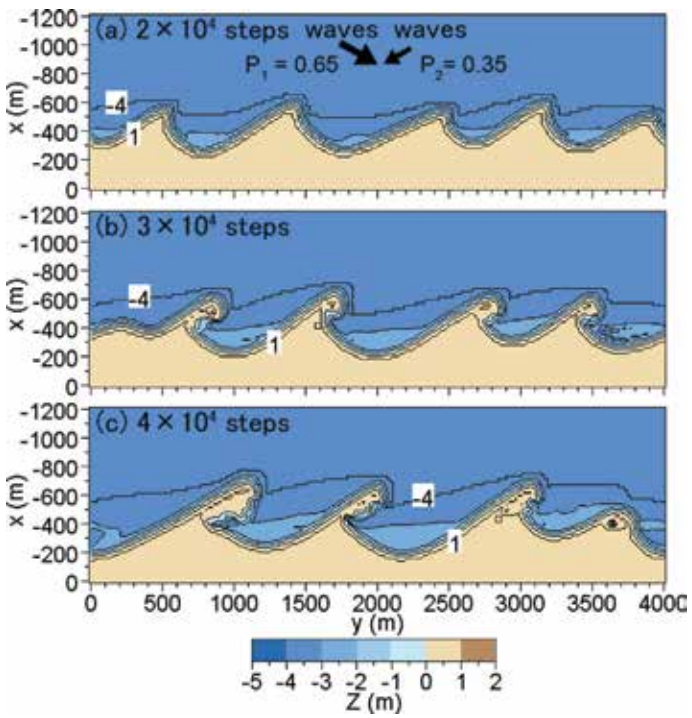

Figure 16.
Formation of cuspate forelands when waves were obliquely incident at angles of ±60° with probability of 0.65:0.35 [4, 5].

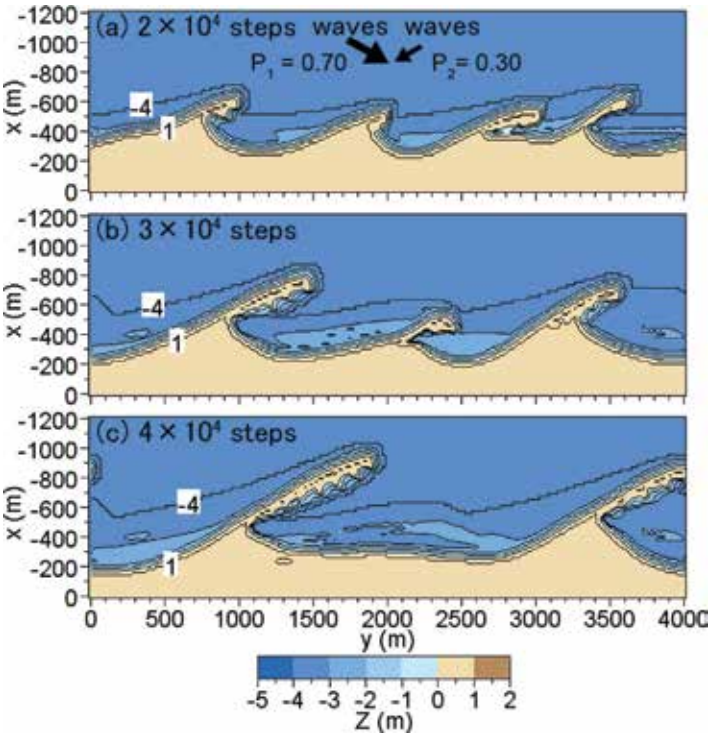

Figure 17.
Formation of cuspate forelands when waves were obliquely incident at angles of ±60° with probability of 0.70:0.30 [5].

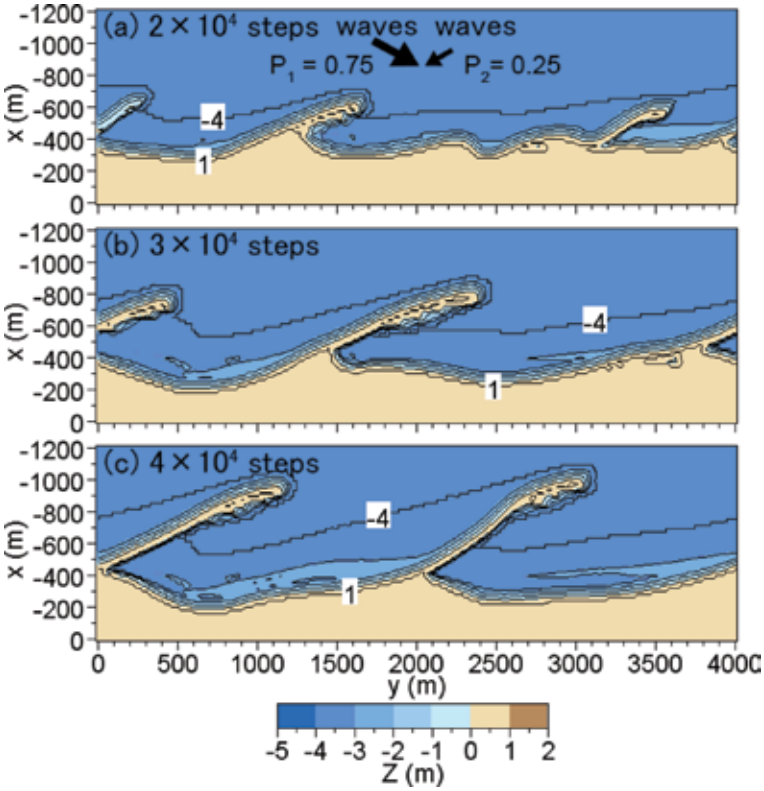

Figure 18.
Formation of cuspate forelands when waves were obliquely incident at angles of ±60° with probability of 0.75:0.25 [5].

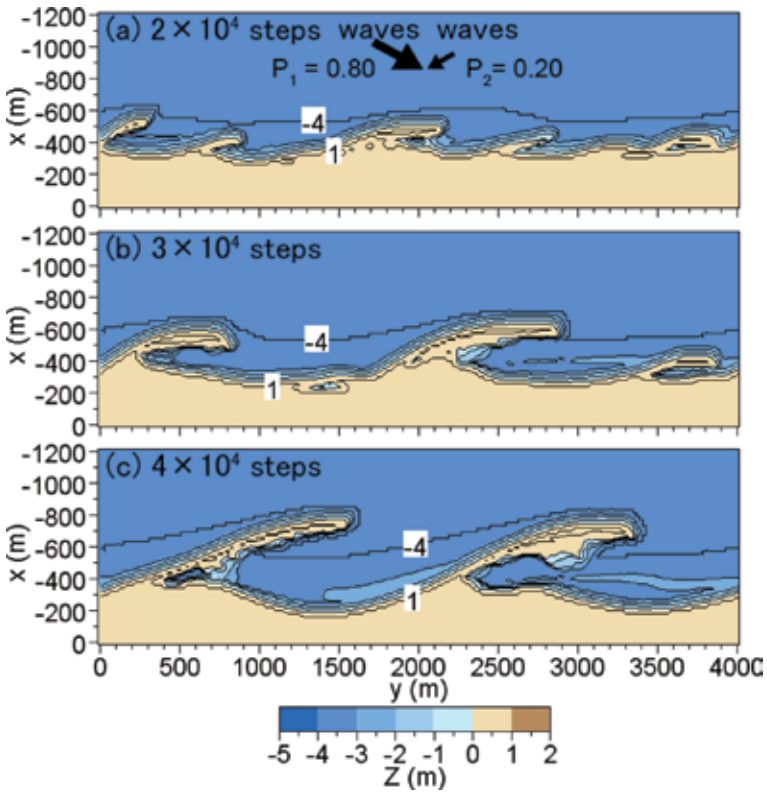

Figure 19.
Formation of cuspate forelands when waves were obliquely incident at angles of ±60° with probability of 0.80:0.20 [5].

Increasing probabilities of occurrence of waves from the left, sand spits with a head extending parallel to the original shoreline developed [5]. In all cases of the development of sand spits, a narrow neck was formed at the connecting point to the land, a general characteristic of the topography around a sand spit [1]. Thus, the mechanism based on the high-angle wave instability and the evolution of 3-D beach changes was explained well by the Type 4 BG model. Although the size of the sand spits formed along the north shore of the Azov Sea is much larger than that of the calculation results, the geometrical configurations of the calculated results are in good agreement with the measured results. Sand spits A, B, C, and D (**Figure 1**) have been formed mainly by waves obliquely incident from the east. The sand spit D located at the west end has a long, slender neck; this feature is in good agreement with the calculation results of the sand spit formed under the incidence of unidirectional waves (**Figure 11(h)**). In addition, the width and length of the neck of the sand spit become thick and short in the order of sand spits C, B, and A, along with the development of a hooked shoreline behind each sand spit. These conditions are very similar to those for the development of sand spits when waves were incident from two directions with different probabilities.

The shape of the sand spit A is very similar to that of the sand spit second from the right end in **Figure 16(c)** calculated with probability of 0.65:0.35, and that of the sand spit C is similar to that located at right end in **Figure 17(b)** calculated with probability of 0.70:0.30 [5]. On the north shore of the Azov Sea, an easterly wind is considered to be predominant, and sand spit D located at the west end could receive sufficiently large wave energy from the east because of a long fetch distance, whereas the wave action from the west is weak because of short fetch distance. As a result, wave action from the

east became stronger, and the sand spit with a narrow, slender neck was considered to be formed. In contrast, for the sand spit A, the fetch distance from the east was so short that the wave action from the east was weakened, whereas wave action from the west was strengthened because of a long fetch distance. In addition, the increase in the fetch distance of the easterly wind was considered to cause the increase in the scale of the sand spit. Here, the development of sand spits and cuspate forelands with rhythmic shapes was predicted, when waves were obliquely incident at large angles relative to the direction normal to the shoreline. Similarly, the effects of anthropogenic factors on development of sand spits and cuspate forelands with rhythmic shapes can be predicted using Type 4 BG model, as described in [5]. Moreover, the Type 4 BG model can be applied to predict the interaction and merging of cuspate forelands formed at the end of multiple sandy islands under the condition that waves are incident from two completely opposite directions [17] and the shoreline variation at tip of cuspate foreland in response to change in wave direction when waves are cyclically incident from two completely opposite directions [18]. The formation of recurved sand spit when waves are cyclically incident from two different directions can be also predicted [19].

4. Conclusions

In Chapter 7, two topics were discussed and topographic changes were predicted using the Type 4 BG model: (1) formation of a cuspate foreland and (2) development of sand spits and cuspate forelands with rhythmic shapes.

1. The morphology of the cuspate foreland located at the northeast end of Graham Island and the cuspate forelands formed at the tip of Hon Bip Island was investigated, and the Type 4 BG model was used to predict the development of a cuspate foreland for waves incident from two opposite directions. It was concluded that not only the cuspate foreland with a sharp tip was formed but also a closed water body remained near the tip of the foreland.

2. The development of sand spits and cuspate forelands with rhythmic shapes was predicted using the Type 4 BG model. A single sand spit elongated when a single wave direction from the $-x$-axis was assumed, whereas a symmetric cuspate foreland was formed when waves with the same probabilities were incident from two opposite directions, and an asymmetric cuspate foreland was formed with different probabilities. Zenkovich [1] qualitatively explained these features using a schematic diagram, but here, these features observed in the field were successfully explained using the BG model.

Author details

Takaaki Uda[1*], Masumi Serizawa[2] and Shiho Miyahara[2]

1 Public Works Research Center, Tokyo, Japan

2 Coastal Engineering Laboratory Co., Ltd., Tokyo, Japan

*Address all correspondence to: uda@pwrc.or.jp

IntechOpen

© 2018 The Author(s). Licensee IntechOpen. Distributed under the terms of the Creative Commons Attribution - NonCommercial 4.0 License (https://creativecommons.org/licenses/by-nc/4.0/), which permits use, distribution and reproduction for non-commercial purposes, provided the original is properly cited. BY–NC

References

[1] Zenkovich VP. Processes of Coastal Development. New York: Interscience Publishers, Div. of John Wiley and Sons, Inc; 1967. p. 751

[2] Ashton A, Murray AB, Arnault O. Formation of coastline features by large-scale instabilities induced by high angle waves. Nature. 2001;**414**:296-300

[3] Ashton A, Murray AB. High-angle wave instability and emergent shoreline shapes: 1. Modeling of sand waves, flying spits, and capes. Journal of Geophysical Research. 2006;**111**:F04011. DOI: 10.1029/2005JF000422

[4] Serizawa M, Uda T, Miyahara S. Prediction of development of sand spits and cuspate forelands with rhythmic shapes caused by shoreline instability using BG model. In: Proc. 33rd ICCE, sediment. 35. 2012. pp. 1-11. http://journals.tdl.org/icce/index.php/icce/article/view/6534/pdf_534

[5] Uda T, Serizawa M, Miyahara S. Development of sand spits and cuspate forelands with rhythmic shapes and their deformation by effects of construction of coastal structures (Chap. 19). In: Awrejcewicz J, editor. Computational and Numerical Simulations. Rijeka: InTech; 2014. pp. 419-450. http://www.intechopen.com/books/computational-and-numerical-simulations/development-of-sand-spits-and-cuspate-forelands-with-rhythmic-shapes-and-their-deformation-by-effect#article-front

[6] Serizawa M, Uda T, Miyahara S. Model for predicting formation of a cuspate foreland. In: Coastal Sediments'15, CD-Rom No. 65. 2015. pp. 1-14

[7] Littlewood R, Murray AB, Ashton AD. An alternative explanation for the shape of 'log-spiral' bays. In: Coastal Sediments'07. 2007. pp. 341-350

[8] van den Berg N, Falqués A, Ribasz F. Long-term evolution of nourished beaches under high angle wave conditions. Journal of Marine Systems. 2011;**88**(1):102-112

[9] Scheffers AM, Scheffers SR, Kelletat DH. The coastlines of the World with Google Earth. In: Coastal Research Library. Vol. 2. New York: Springer; 2012. p. 293

[10] Uda T, Serizawa M, Miyahara S. Formation of cuspate foreland in field subject to wave-sheltering effect of islands. In: Proc. 35th Conf. Coastal Eng., sediment. 4. 2016. pp. 1-14. https://icce-ojs-tamu.tdl.org/icce/index.php/icce/article/view/8102/pdf

[11] Miyahara S, Uda T, Serizawa M. Prediction of formation of land-tied islands. In: Proc. 34th ICCE. 2014. pp. 1-14. https://journals.tdl.org/icce/index.php/icce/article/view/7108/pdf_412

[12] Ozasa H, Brampton AH. Model for predicting the shoreline evolution of beaches backed by seawalls. Coastal Engineering. 1980;**4**:47-64

[13] Mase H. Multidirectional random wave transformation model based on energy balance equation. Coastal Engineering Journal, JSCE. 2001;**43**(4):317-337

[14] Dally WR, Dean RG, Dalrymple RA. A model for breaker decay on beaches. In: Proc. 19th ICCE. 1984. pp. 82-97. https://journals.tdl.org/icce/index.php/icce/article/view/3787/3470

[15] Goda Y. Random Seas and Design of Maritime Structures. Tokyo: University of Tokyo Press; 1985. 323 p

[16] Uda T, Yamamoto K. Beach erosion around a sand spit—an example of Mihono-Matsubara sand spit. In: Proc. 24th ICCE. 1994. pp. 2726-2740. https://journals.tdl.org/icce/index.php/icce/article/view/5141/4819

[17] Miyahara S, Uda T, Serizawa M. Interaction and mergence of cuspate forelands formed at end of multiple sandy islands under waves. In: Proc. 36th Conf. Coastal Eng. 2018. In press

[18] Miyahara S, Uda T, Serizawa M. Shoreline variation at tip of cuspate foreland in response to change in wave direction. In: Proc. 9th Int. Conf. on Asian and Pacific Coasts (APAC2017). 2017. pp. 455-466

[19] Serizawa M, Uda T, Miyahara S. Prediction of formation of recurved sand spit using BG model. In: Proc. 36th Conf. Coastal Eng. 2018. In press

Chapter 9

Segmentation and Merging of Closed Water Bodies by Wind Waves

Takaaki Uda, Masumi Serizawa and Shiho Miyahara

Abstract

The segmentation and merging of elongated shallow water body with a large aspect ratio by wind waves were predicted using the Type 6 BG model. The deformation of a circular lake by wind waves was also studied when a straight seawall cutting a part of the water body was constructed in a lake for land reclamation, together with the investigation on the effect of the construction of detached breakwaters to the surrounding lakeshore. Finally, the formation of oriented lakes, groups of lake basins with a common long-axis orientation found in vast areas of the Arctic Coastal Plain, was predicted using the Type 6 BG model.

Keywords: segmentation, merging, elongated water body, wind waves, circular lake, detached breakwater, oriented lakes

1. Introduction

In a shallow water body, topographic changes may take place owing to wind waves. In the ordinary case, the wave incidence angle relative to the direction normal to the shoreline is small, but in a narrow water body with a large aspect ratio, it may exceed 45°, and the shoreline may become unstable owing to the mechanism of high-angle wave instability [1–3]. Cuspate forelands that develop from both shores of a narrow water body may connect with each other, resulting in the segmentation of the water body into smaller rounded lakes [4–6]. Typical examples can be seen in a water body facing the Chukchi Sea in Russia, as shown in **Figure 1** [7], where the sizes of the water bodies formed by the segmentation differ from each other depending on the size of the original water body. In **Figure 2**, an enlarged image of the rectangular area in **Figure 1**, another segmentation of the shallow lake can be seen, in which the lakeshore is at a primitive stage of development, and cuspate forelands alternately develop from both shores. Regarding these phenomena, the division and reduction of a fetch distance owing to the formation of a large shoreline protrusion and the resulting change in the wave field become key factors. Ashton et al. [1, 5] successfully modeled the development of shoreline irregularities into cuspate spits owing to the instability mechanism only using longshore sand transport formula. Serizawa et al. [8] also explained them by the numerical simulation using the BG model. In this study, 3D beach changes during the segmentation of a shallow water body into small lakes were first predicted using the Type 6 BG model [7, 9, 10] in Section 2.

IntechOpen

Figure 1.
Example of segmentation of a shallow water body facing the Chukchi Sea in Russia.

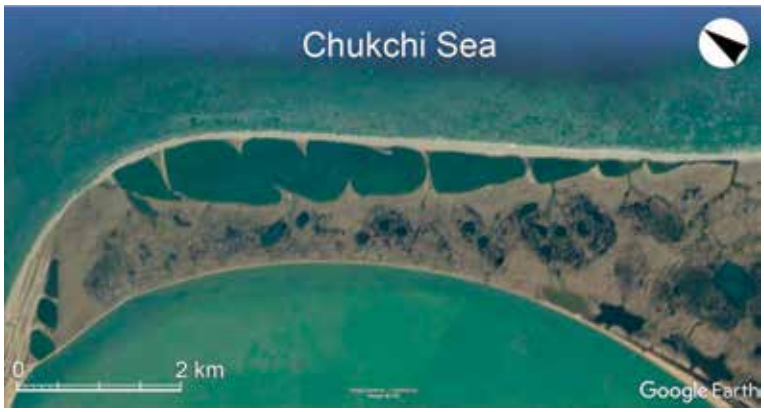

Figure 2.
Enlarged image of rectangular area in ***Figure 1****.*

The second case relates to the deformation of a circular lake. Because a circular lake is completely stable for the wind waves generated when wind blows from all directions with the same probability of occurrence and intensity, no lakeshore changes occur unless the landform changes are exerted, but when a seawall or detached breakwaters are constructed at part of the lake, the wave field will change, causing the lakeshore changes [11]. In Section 3, the deformation of a circular lake by wind waves was studied when a straight seawall cutting part of the water body was constructed in a lake, together with the investigation on the effect of the construction of detached breakwaters to the surrounding lakeshore in Section 4.

In vast areas of the Arctic Coastal Plain, oriented lakes, groups of lake basins with a common long-axis orientation, can be found [12]. Oriented lakes in permafrost regions were originally thermokarst features [13]. The shape of oriented lakes in North America is often elliptical with their long axis generally aligned in the N-NW direction, perpendicular to the direction of the prevailing summer winds. The initial cause of the formation of a thaw lake or depression may be the random melting of ground ice or subsidence of the ground followed by the accumulation of water in the depression. Mackay [14] developed a mathematical model that relates the lake shape with the resultant wind vectors and the square of the velocity and

attempted to analyze the equilibrium forms of lakes that might be produced by winds of today. However, the precise mechanism of the lake orientation remained unexplained. So, the formative mechanism of oriented lakes was investigated using the Type 6 BG model in Section 5 [15].

2. Numerical simulation of 3D segmentation of elongated water body

2.1 Formation of alternate cuspate forelands in a lake

Lake Kitaura located in the Kanto Plains, Japan, is a shallow lagoon with a water area of 35.2 km^2 and 25 km length (**Figure 3**), which is surrounded by the Kashima and Namekata Tablelands with an elevation as low as 40 and 30 m, respectively. Wind, therefore, can blow over the surface of this shallow water body without significant sheltering effect by the local topographies. Referring the wind rose measured at the center of Lake Kasumigaura located 10 km west of Lake Kitaura, the predominant wind directions are NNE, N, and NE, which are close to the direction of the principal axis of Lake Kitaura, resulting in the generation of strong wind waves [7, 9, 10].

In **Figure 3**, many cuspate forelands alternately develop along both shores of the lake. Because the location of the cuspate forelands in the central part of the lagoon coincides with that of ridges extending toward the lake, it is assumed that no cuspate forelands have been formed owing to the shoreline instability, whereas

Figure 3.
Formation of alternate cuspate forelands in Lake Kitaura.

cuspate forelands develop independent of the location of the ridges in the northern and southern rectangular areas (**a** and **b**) shown in **Figure 3**. **Figure 4** (**a** and **b**) show the enlarged aerial photographs of these areas. In these areas, the cuspate forelands alternately develop similarly to the example in a shallow lagoon facing the Chukchi Sea in Russia.

2.2 Calculation conditions

Consider a shallow water body with a flat, solid bed of 3 m depth. The lakeshore was assumed to have a berm of 1 m height and a uniform slope of 1/20. A random noise with an amplitude of $\Delta Z = 0.1$ m was added to the slope between $Z = -3$ and 1 m in the initial profile. Assuming that the wind velocity was 20 m/s and wind blew from all the directions with the same probability and intensity, the wind direction at each step was randomly determined based on a probability distribution function. The depth distribution of longshore sand transport $\varepsilon(Z)$ was assumed to be uniform over the depth. **Table 1** summarizes the conditions for the calculation of the segmentation of a narrow water body.

2.3 Calculation results

Figure 5 shows the segmentation of a narrow slender water body of 4.5 km length and 0.64 km width (aspect ratio = 7) into small lakes. Sandbars with irregular shapes such as cuspate spits had started to develop along the shoreline after 5000 steps (**Figure 5(b)**). The protruded shoreline produced a wave-shelter zone downcoast, causing a decrease in longshore sand transport, whereas it increased at the tip of the protrusion. Thus, small-scale sandbars were absorbed into a larger sandbar, and the size of the sandbar increased by 1×10^4 steps (**Figure 5(c)**). These results explain the formative mechanism of alternate sandbars observed in the water bodies facing the Chukchi Sea and Lake Kitaura.

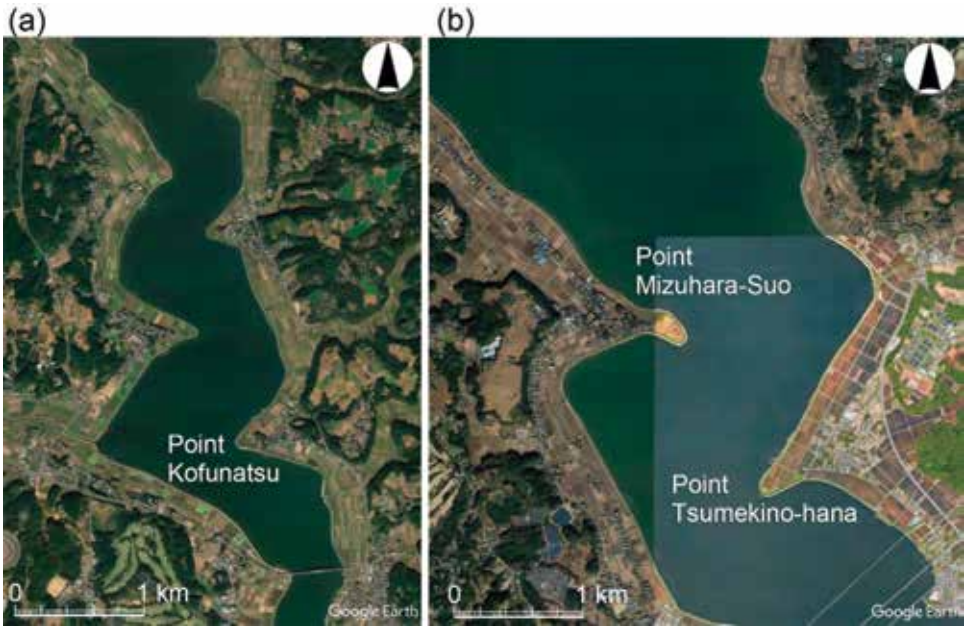

Figure 4.
Aerial photographs of the northern and southern parts, a and b, of Lake Kitaura.

By 2×10^4 steps, the sandbars on both shores connected with each other result in the segmentation of the elongated water body into three smaller, elliptic lakes (**Figure 5(e)**). The segmentation continued with time, and the shape of the lake became rounded (**Figure 5(f)**). After 3×10^4 steps, the three lakes had started to become circular (**Figure 5(g)**), and the three rounded lakes were formed by 10^5 steps (**Figure 5(h)**). The segmentation of the elongated water body into three lakes was similar to that as in [5], but the 3D beach changes including the formation of sandbars with a hound's tooth pattern were possible to predict in this study.

Calculation method	**Type 6 BG model**
Wind velocity	20 m/s
Berm height h_R	1 m
Depth of closure h_c	3 m
Equilibrium slope $\tan\beta_c$	1/20
Coefficients of sand transport	Longshore and cross-shore sand transport coefficient K_s = 0.2
Mesh size	$\Delta x = \Delta y$ = 20 m
Time intervals	Δt = 10 h
Duration of calculation	10^6 h (10^5 steps)
Boundary conditions	Shoreward and landward ends $q_x = 0$ Right and left boundaries $q_y = 0$

Table 1.
Conditions for calculation of segmentation of a narrow water body.

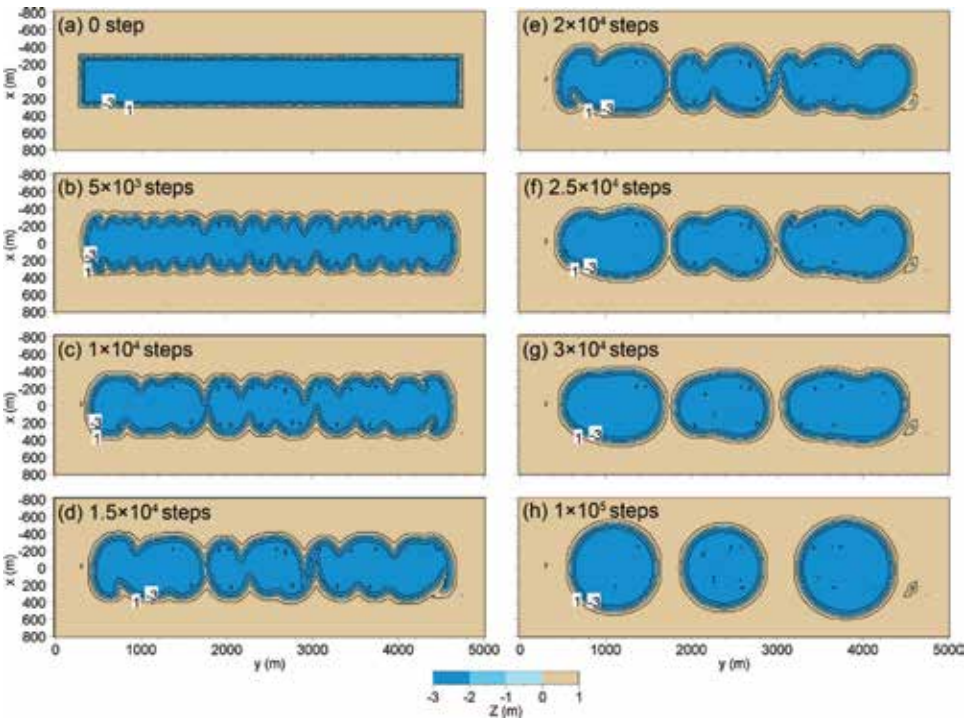

Figure 5.
Segmentation of a slender lake of 4.5 km length and 0.64 km width (aspect ratio = 7) into small lakes.

3. Effect of land reclamation and construction of detached breakwaters in a circular lake

3.1 Calculation conditions

A circular lake of 1.2 km radius was considered, and part of the circular lake was cut off by a seawall extending along $y = -600$ m to investigate the effect of the land reclamation on the nearby lakeshore [11], as shown in **Figure 6**. The depth of a circular water body was assumed to be 3 m, and a sandy beach with a berm height of 1 m and a uniform slope of 1/20 was set along the peripheral shoreline of a lake. Wind velocity was assumed to be 20 m/s, and wind blew from all directions with the same probability of occurrence and intensity in all cases. The wind direction in each step was set using random numbers. The depth distribution of sand transport was assumed to be given by a uniform distribution throughout the depth. **Table 2** summarizes the conditions for the calculation of deformation of a circular lake.

3.2 Calculation results

When a seawall was constructed in a part of the lake, the wave field changed, inducing the lakeshore changes, as shown in **Figure 6**. The shape of the lake was more rounded after 2×10^5 steps (**Figure 6(b)**) relative to the initial shape shown in **Figure 6(a)**. **Figure 7** shows the seabed difference after 2×10^5 steps with reference to the initial topography. Note that the shoreline receded on the opposite shore against the seawall after the construction of the seawall and the lake shape became more rounded. The mechanism of these lakeshore changes can be explained using a schematic diagram as illustrated in **Figure 8**.

Set points C on ark AB and C′ at a point where a straight line connecting point C with the center of the circular lake intersects the shoreline of the water body. Set the fetch distance between points C and C′ to be F1. Then, a straight line tangent to the circle is drawn at point C, and the fetch distance in each direction divided at the same angular intervals is drawn (**Figure 8**). The numbers 2–9 and 2′–9′ are located on the right and left half of the circular lake, respectively. When wind blows from

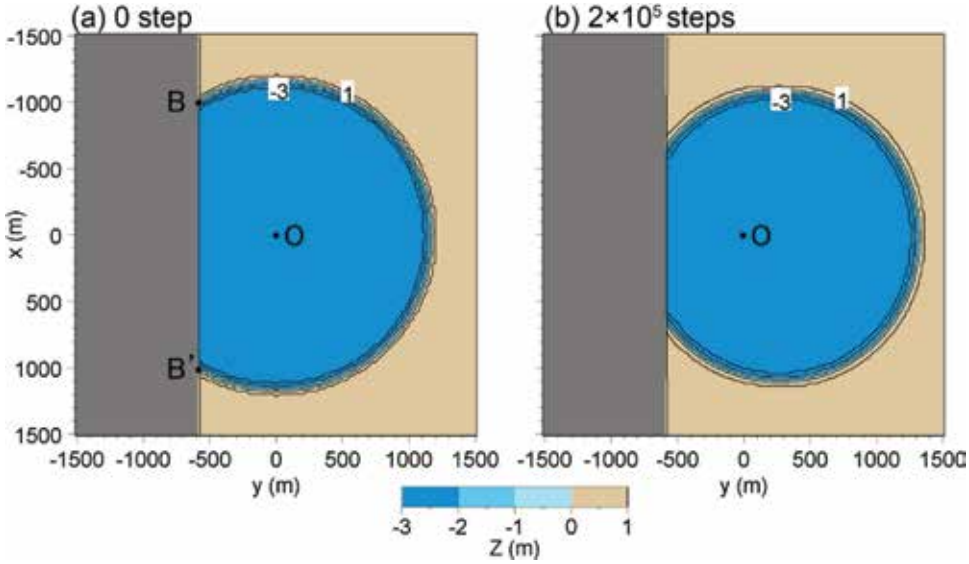

Figure 6.
Change in circular lake cut off by a straight seawall.

Calculation method	Type 6 BG model
Wind velocity	20 m/s
Berm height h_R	1 m
Depth of closure h_c	3 m
Equilibrium slope $\tan\beta_c$	1/20
Coefficients of sand transport	Longshore and cross-shore sand transport coefficient K_s = 0.2
Mesh size	$\Delta x = \Delta y$ = 20 m
Time intervals	Δt = 5 h
Duration of calculation	10^6 h (2×10^5 steps)
Boundary conditions	Shoreward and landward ends $q_x = 0$ Right and left boundaries $q_y = 0$

Table 2.
Conditions for calculation of deformation of a circular lake.

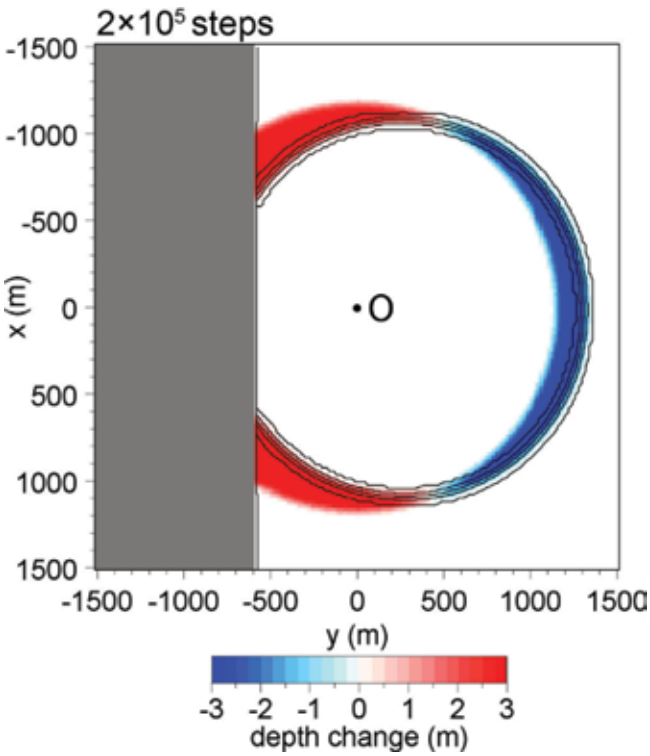

Figure 7.
Seabed differences after 2 × 10^5 steps with reference to initial topography.

the directions between fetch F2 and fetch F9, which extend radially, rightward longshore sand transport is generated with respect to the direction normal to the shoreline at point C, because wind waves are incident from the counterclockwise direction. In contrast, when wind blows from the directions between fetch F2' and fetch F9', leftward longshore sand transport is generated at point C. Longshore sand transport is 0 under the wave incidence from fetch F1 because of the wave incidence normal to the shoreline.

The sum of longshore sand transport owing to waves along fetch F2 and F2' is also 0 because of symmetry of wave incidence. On the other hand, because the

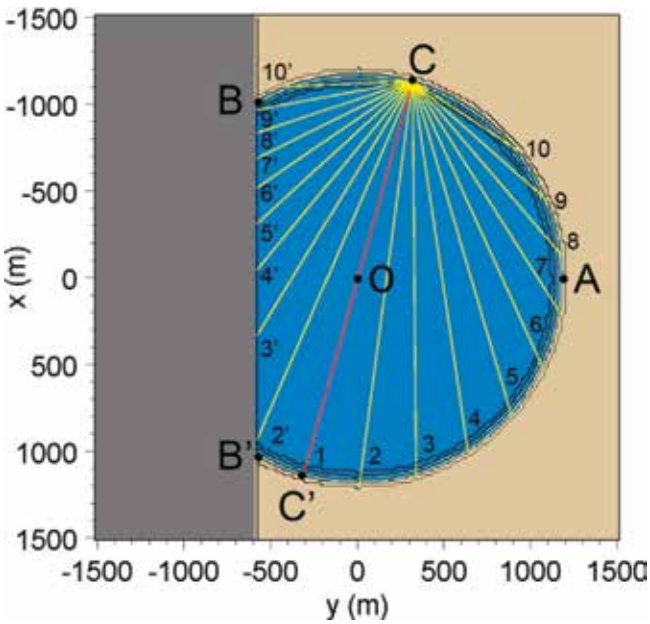

Figure 8.
Change in fetch distances owing to land reclamation.

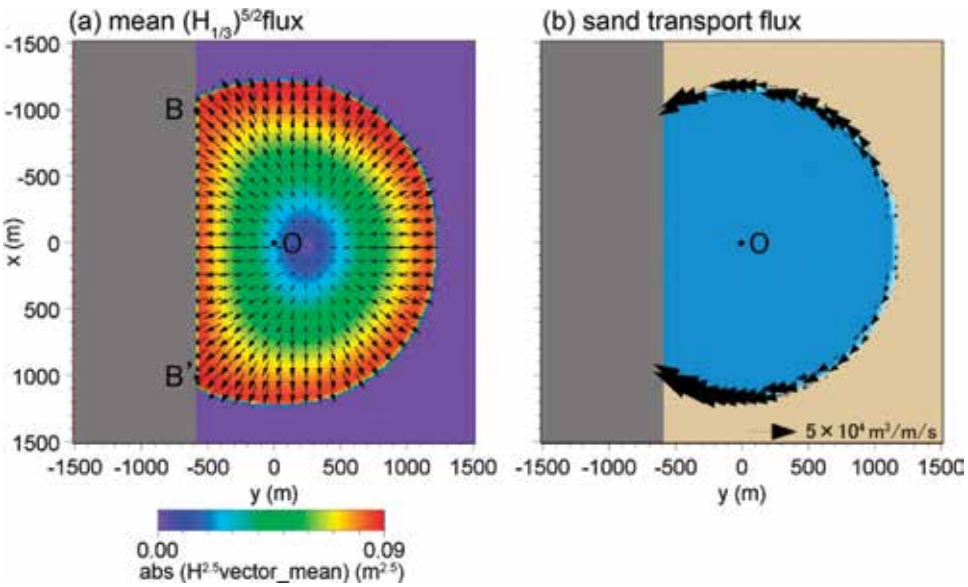

Figure 9.
Mean $(H_{1/3})^{5/2}$ flux and sand transport flux averaged over 1000 steps.

relations F3' ≤ F3, F4' ≤ F4, ..., and F9' ≤ F9 are satisfied in **Figure 8**, the sum of longshore sand transport from the direction between fetch F2' and F9' is always smaller than that from the directions between fetch F2 and fetch F9. As a result, longshore sand transport toward the reclaimed land becomes larger than that toward the opposite direction at point C, resulting in shoreline recession on the opposite side of the reclaimed land and sand deposition near the reclaimed land. When the area of the water body on the left and right sides of line CC' is compared, the action of waves incident from the large water body is stronger, resulting in increase in longshore sand transport.

Mean energy flux of waves $(H_{1/3})^{5/2}$ is weak in the central part of the lake, and increases near the shoreline (**Figure 9(a)**). Moreover, along the shoreline in the upper and lower halves of the water body, waves are obliquely incident counterclockwise and clockwise to the direction normal to the shoreline, respectively. Although longshore sand transport is small on the shore opposite to the reclaimed area, it increases with the proximity to the reclaimed land (**Figure 9(b)**), and the lakeshore changes are triggered by this spatial imbalance of longshore sand transport.

4. Prediction of lakeshore changes after construction of detached breakwaters in a lake

4.1 Calculation conditions

When several detached breakwaters are constructed along the lakeshore, characteristic lakeshore changes can be seen along the lakeshore, because a lake has a closed system of littoral drift. Here, a circular lake of 1 km radius was considered, and six detached breakwaters with 400 m length and offshore distance of 400 m are assumed to be constructed in a lake. The depth of a circular water body was assumed to be 3 m, and a sandy beach with a berm height of 1 m and a uniform slope of 1/20 was set along the peripheral shoreline of a lake. Wind velocity was assumed to be 20 m/s, and wind blew from all directions with the same probability of occurrence and intensity. The wind direction in each step was set using random numbers. **Table 3** summarizes the conditions for the calculation of the lakeshore changes when detached breakwaters were constructed in a circular lake.

4.2 Calculation results

When detached breakwaters were constructed in a lake at the same time, the wave-shelter zones were formed behind the detached breakwaters, and cuspate forelands had started to be formed by 10^4 steps (**Figure 10(b)**). Up to 2×10^4 steps, the shoreline of all forelands connected to the detached breakwaters forms tombolos, as shown in **Figure 10(c)**. Finally, six pocket beaches were formed between

Calculation method	**Type 6 BG model**
Wind velocity	20 m/s
Berm height h_R	1 m
Depth of closure h_c	3 m
Equilibrium slope $\tan\beta_c$	1/20
Coefficients of sand transport	Longshore and cross-shore sand transport coefficient K_s = 0.2
Mesh size	$\Delta x = \Delta y$ = 20 m
Time intervals	Δt = 10 h
Duration of calculation	10^6 h (10^5 steps)
Boundary conditions	Shoreward and landward ends $q_x = 0$ Right and left boundaries $q_y = 0$

Table 3.
Conditions for the calculation of the lakeshore changes when detached breakwaters were constructed in a circular lake.

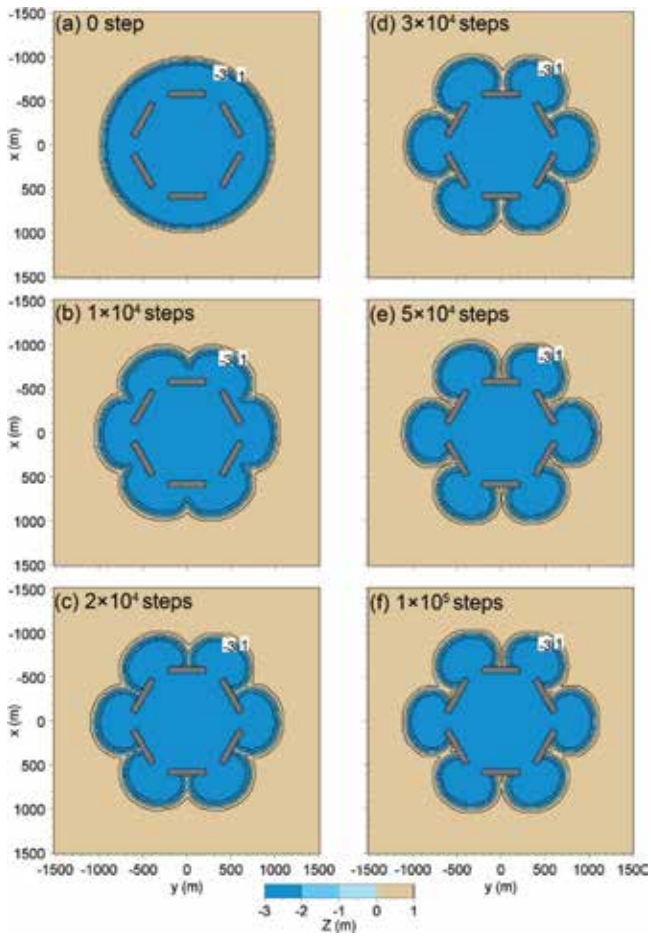

Figure 10.
Formation of cuspate forelands behind six detached breakwaters installed in a circular lake of 1 km radius.

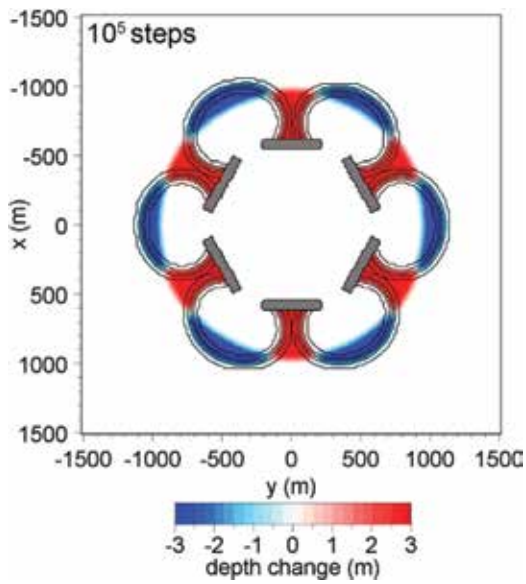

Figure 11.
Seabed difference after 10^5 steps with reference to initial topography.

detached breakwaters after 10^5 steps and stabilized, as shown in **Figure 10(f)**. **Figure 11** shows the seabed difference after 10^5 steps with reference to the initial topography. Sand deposition behind the detached breakwaters and shoreline recession in the openings of the detached breakwaters were triggered by the construction of detached breakwaters, and symmetrical topographic changes took place owing to the symmetrical arrangement of detached breakwaters.

5. Prediction of formation of oriented lakes

5.1 Examples of oriented lakes

In the Arctic Coastal Plain, typical examples of oriented lakes can be found from the satellite images [12]. **Figure 12** shows the satellite image of the coastal lowland at a location (69°13′41.66″N, 160°01′39.84″E) with an elevation of 8 m above MSL, facing the East Siberian Sea in Russia [15]. In this area, many lakes have been formed; three oriented lakes with the principal axis of the NW-SE direction can be seen 20 km west of the Kolyma River, and each lake is separated by a slender sandbar. Seaward of these lakes, many ridges extend in parallel to the shoreline, and the principal axis of these oriented lakes is in parallel to the shoreline [15]. From these characteristics, it is inferred that oriented lakes of this shape could develop, because the strength of the sea breeze is larger than that of the wind blowing from the other direction.

The second example is the oriented lakes west of Point Barrow (70°55′ 32.54″N, 157°27′ 37.11″W) in north Alaska separating the Chukchi and Beaufort Seas (**Figure 13**). In this figure, sand spits and hooked shoreline, which are assumed to have developed owing to the shoreline instability [1–3], run in the SW-NE direction. In **Figure 14**, an enlarged satellite image of the rectangular area in **Figure 13**, a number of oriented lakes can be seen with the direction of the principal axis of N7°W [15]. The direction normal

Figure 12.
Example of oriented lakes in East Siberia.

to this axis is N97°W, and wind of this direction is assumed to have a primary effect to the formation of oriented lakes. This wind direction makes a large angle of 82° to the direction of N15°W normal to the shoreline of the sand spit located at the left end in **Figure 14**. Taking into consideration the fact that wind waves are generated by wind

Figure 13.
Oriented lakes west of Point Barrow in Alaska separating Chukchi and Beaufort Seas.

Figure 14.
*Enlarged satellite image of rectangular area shown in **Figure 13**.*

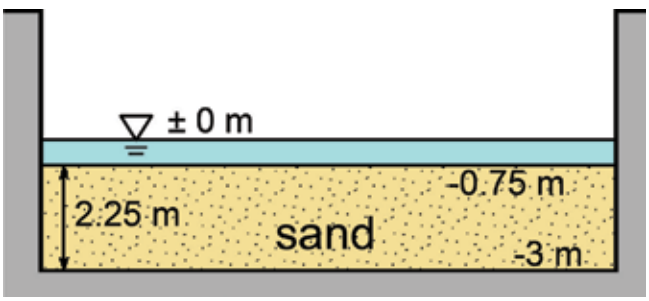

Figure 15.
Cross section of initial lake bed composed of sand.

from this direction, the shoreline instability could occur because of a large wave incidence angle. Thus, in this case, the development of oriented lakes owing to the intensive prevailing wind and the occurrence of the shoreline instability correspond well.

5.2 Calculation conditions

Assuming a shallow lake with a flat sandy bed of 0.75 m depth and the thickness of sand layer of 2.25 m as the initial topography, the development of the oriented lakes was investigated (**Figure 15**). The calculation domain was a square with 2 km length. The lake boundary was given by a solid vertical wall.

At the initial stage, infinitesimal random noise of ΔZ = 0.1 m was added to the lake bed. h_R and h_c were assumed to be 1 and 3 m, respectively. The water depth of the flat shallow lake was shallower than h_c, so that sand deposited on the flat bed at the initial stage could be quickly redistributed by wave action, leading to the formation of a sloping beach. The wind velocity was assumed to be 20 m/s, and an asymmetric (elliptic) probability distribution for the occurrence of wind direction with an aspect ratio of 4 was assumed, such that the principal axis of the probability of occurrence of wind direction was at an angle of 45° to the x-axis (**Figure 16**), although the wind was assumed to blow uniformly from all directions as described in [15], i.e., a symmetric circular distribution. Wind velocity of 20 m/s employed is the one which generates 0.8 m of significant wave height, given the wind fetch distance along the diagonal in the initial lake as 2.8 km. The conditions for the calculation of the formation of oriented lakes are summarized in **Table 4**.

5.3 Calculation results

The calculation results are shown in **Figure 17**. When wind blew obliquely to the shallow body of water of 0.75 m depth, a number of slender small lakes had emerged up to 2×10^3 steps, as shown in **Figure 17(b)**, via the mechanism proposed in [6]. After 5×10^3 steps, these slender small lakes had merged into larger lakes,

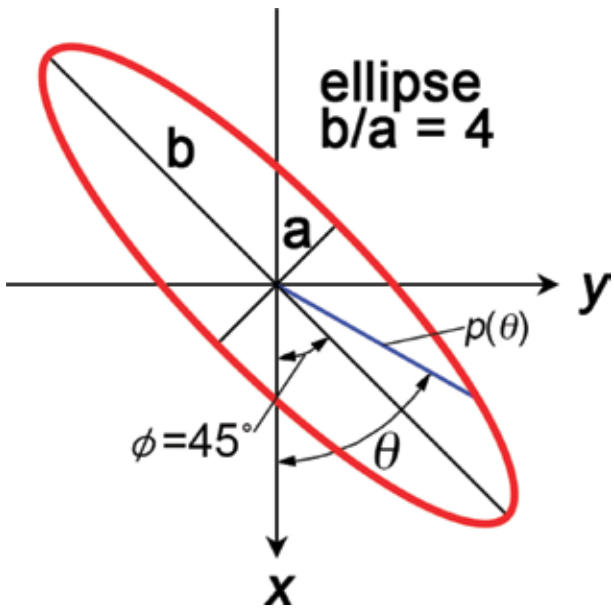

Figure 16.
Probability distribution of occurrence of wind direction.

Calculation method	Type 6 BG model
Wind velocity	20 m/s
Berm height h_R	1 m
Depth of closure h_c	3 m
Equilibrium slope tanβ_c	1/20
Coefficients of sand transport	Longshore and cross-shore sand transport coefficient K_s = 0.2
Mesh size	$\Delta x = \Delta y$ = 20 m
Time intervals	Δt = 5 h
Duration of calculation	10^6 h (2×10^5 steps)
Boundary conditions	Shoreward and landward ends $q_x = 0$ Right and left boundaries $q_y = 0$

Table 4.
Conditions for calculation of formation of oriented lakes.

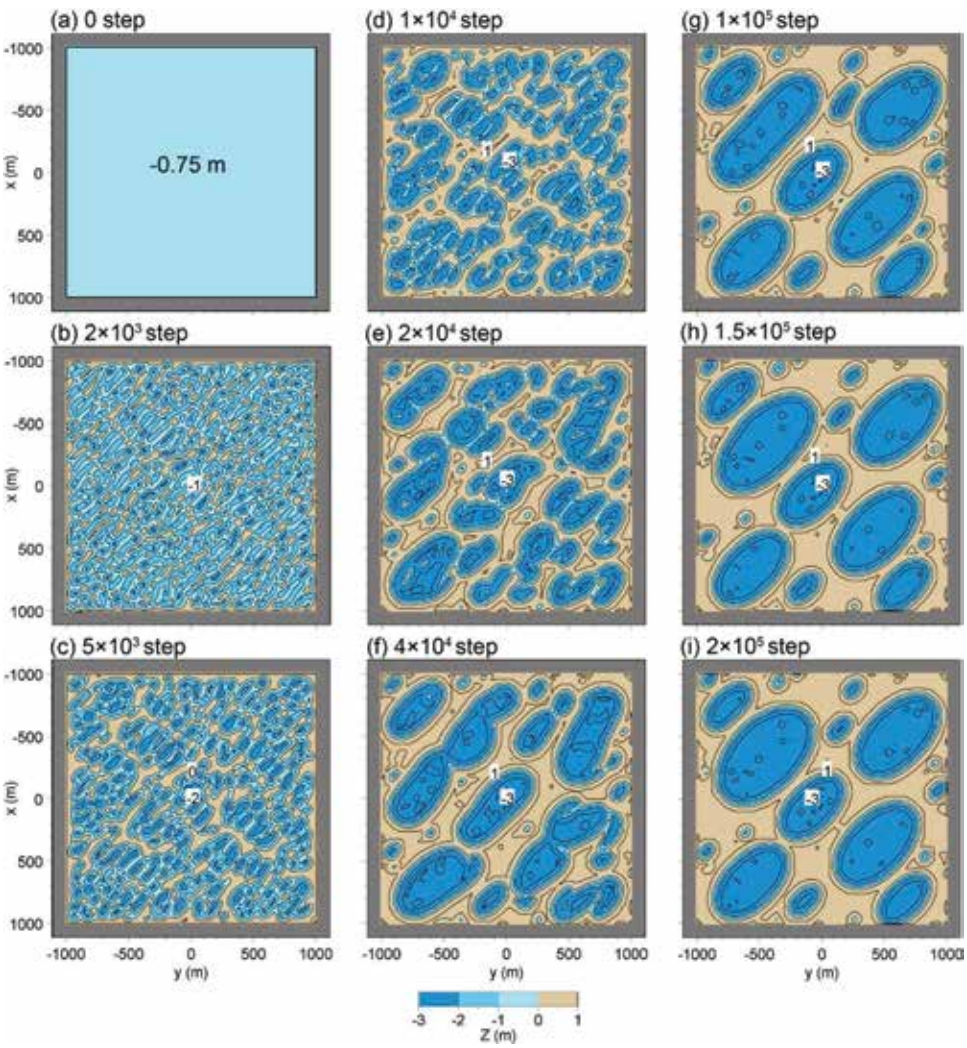

Figure 17.
Prediction of formation of oriented lakes.

and the width of the lakes increased (**Figure 17(c)**). After 10^4 steps, small lakes had further merged into larger lakes, although the shape of the oriented lakes was unclear at this stage (**Figure 17(d)**). After 2×10^4 steps, several lakes similar to the oriented lakes had developed owing to the merging of small lakes with principal axes in parallel with each other (**Figure 17(e)**). After 4×10^4 steps, oriented lakes of almost elliptic shape were formed (**Figure 17(f)**). After 10^5 steps, oriented lakes of elliptic shape were formed with a large aspect ratio (**Figure 17(g)**). It should be noted that the direction of the principal axis of the oriented lakes became normal to the direction of the principal axis of the probability distribution of occurrence of wind, as shown in (**Figure 17(g)**), and the oriented lakes reached a stable form up to 2×10^5 steps shown in (**Figure 17(i)**). The coexistence of the oriented lakes of

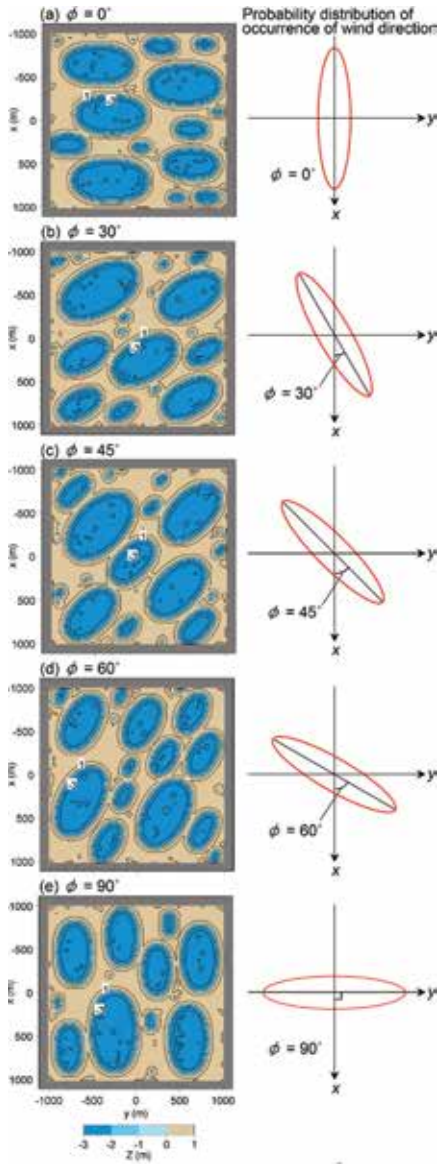

Figure 18.
Change in configuration of oriented lakes up to 2×10^5 steps in response to changes in principal wind direction.

various scales as seen in the results is found in the examples of the oriented lakes (**Figures 12–14**).

Moreover, the change in configuration of the oriented lakes in response to the change in the principal wind direction was investigated by changing the principal wind direction in five cases of Φ = 0, 30, 45, 60, and 90°. In each case, the initial condition and the other calculation conditions were maintained constant except the principal wind direction. The results of the calculation after 2×10^5 steps are shown in **Figure 18**. When the principal wind direction changed counterclockwise, the principal axis of the oriented lakes became normal to the principal wind direction, and the direction of the oriented lakes always became normal to the principal wind direction, as shown in **Figure 18(a)–18(e)**.

6. Conclusions

In Chapter 8, three topics were discussed, and topographic changes were predicted using the Type 6 BG model: (1) 3D segmentation of elongated water body, (2) deformation of a circular lake by wind waves when a straight seawall cutting a part of the water body was constructed or detached breakwaters were constructed in a lake, and (3) prediction of formation of oriented lakes:

1. In a slender water body with a large aspect ratio, the angle between the direction normal to the shoreline and the wave direction exceeds 45° because of a long wind fetch distance along the principal axis, resulting in the emerging of cuspate forelands and the subdivision of a water body. The Type 6 BG model was used to predict such changes in a water body. The calculated results were compared with the ones observed in a water body facing Chukchi Sea and Lake Kitaura, and the 3D subdivision process of a long slender water body was successfully explained.

2. Lakeshore changes triggered by artificial alteration were predicted. When a straight seawall cutting off a circular lake was constructed, the center of the rounded lake approached the seawall, causing the shoreline recession on the opposite shore against the seawall, suggesting that the land reclamation on part of a lake should be careful. Also, the impact of the construction of six detached breakwaters in a lake was investigated. After the construction, lakeshore was subdivided into six pocket beaches fixed by detached breakwaters.

3. When wind blew uniformly from all directions over a water body, a lake with a highly circular shape was formed [6]. In contrast, the shape of the lakes became elliptic when wind blew with an asymmetric probability distribution of occurrence of the wind direction. Thus, the formation of oriented lakes was successfully explained using the Type 6 BG model, and the predicted results and the examples given in [12] were in good agreement. The calculation results clearly indicate that the direction of the principal axis of the oriented lakes became normal to the direction of the principal axis of the probability distribution of occurrence of wind.

Author details

Takaaki Uda[1*], Masumi Serizawa[2] and Shiho Miyahara[2]

1 Public Works Research Center, Tokyo, Japan

2 Coastal Engineering Laboratory Co., Ltd., Tokyo, Japan

*Address all correspondence to: uda@pwrc.or.jp

IntechOpen

© 2018 The Author(s). Licensee IntechOpen. Distributed under the terms of the Creative Commons Attribution - NonCommercial 4.0 License (https://creativecommons.org/licenses/by-nc/4.0/), which permits use, distribution and reproduction for non-commercial purposes, provided the original is properly cited. BY–NC

References

[1] Ashton A, Murray AB, Arnault O. Formation of coastline features by large-scale instabilities induced by high angle waves. Nature. 2001;**414**:296-300

[2] Ashton A, Murray AB. High-angle wave instability and emergent shoreline shapes: 1. Modeling of sand waves, flying spits, and capes. Journal of Geophysical Research. 2006;**111**:F04011. DOI: 10.1029/2005JF000422

[3] van den Berg N, Falqués A, Ribasz F. Long-term evolution of nourished beaches under high angle wave conditions. Journal of Marine Systems. 2011;**88**(1):102-112

[4] Zenkovich VP. Processes of Coastal Development. New York: Interscience Publishers, Div. of John Wiley and Sons, Inc; 1967. p. 751

[5] Ashton A, Murray AB, Littlewood R, Lewis DA, Hong P. Fetch limited self-organization of elongate water bodies. Geology. 2009;**37**:187-190

[6] Uda T, Serizawa M, Miyahara S, Sannami T. Prediction of segmentation and mergence of shallow water bodies by wind waves using BG model. In: Proc. Coastal Dynamics 2013, Paper No. 166. 2013. pp. 1729-1740

[7] Uda T, Serizawa M, Miyahara S. Numerical simulation of three-dimensional segmentation of elongated water body using BG model. In: Proc. 33rd ICCE, Sediment. 65. 2012. pp. 1-11. https://icce-ojs-tamu.tdl.org/icce/index.php/icce/article/view/6533/pdf_448

[8] Serizawa M, Uda T, Miyahara S. Prediction of development of sand spits and cuspate forelands with rhythmic shapes caused by shoreline instability using BG model. In: Proc. 33rd ICCE, Sediment. 35. 2012. pp. 1-11. https://icce-ojs-tamu.tdl.org/icce/index.php/icce/article/view/6534/pdf_534

[9] Serizawa M, Uda T, Miyahara S. Segmentation of water body given probability of occurrence of wind direction by circular or elliptic distribution. In: Proc. 35th Inter. Conf. Coastal Eng., Sediment. 6. 2016. pp. 1-15. https://icce-ojs-tamu.tdl.org/icce/index.php/icce/article/view/8104/pdf

[10] Uda T, Serizawa M, Miyahara S. Segmentation of water body and lakeshore changes behind an island owing to wind waves, Chap. 4. In: Malcangio D, editor. Applications in Water Systems Management and Modeling. Rijeka: IntechOpen; 2018. pp. 49-70. 129 p. https://www.intechopen.com/books/applications-in-water-systems-management-and-modeling/segmentation-of-water-body-and-lakeshore-changes-behind-an-island-owing-to-wind-waves

[11] Serizawa M, Uda T, Miyahara S. Effects of construction of offshore breakwaters on segmentation of a slender water body. In: 8th Int. Conf. on Asian and Pacific Coasts (APAC 2015), Procedia Engineering. Vol. 116. 2015. pp. 502-509

[12] Seppälä M. Wind as a Geomorphic Agent in Cold Climates. Cambridge University Press; 2004. p. 358

[13] Harry DG, French HM. The orientation and evolution of thaw lakes, southwest Banks Island, Canadian Arctic. In: Proceedings, Fourth International Conference on Permafrost. Washington, D. C: Natl. Acad. of Sci; 1983. pp. 456-461

[14] Mackay JR. The Mackenzie Delta Area, N.W.T. Vol. 8. Ottawa, Memoir: Geographical Branch, Mines and Technical Surveys; 1963. 202 p

[15] Uda T, Serizawa M, San-nami T, Miyahara S. Prediction of formation of oriented lakes. In: Proc. 34th ICCE. 2014. pp. 1-12. https://journals.tdl.org/icce/index.php/icce/article/view/7109/pdf_413

List of Symbols

a_0: coefficient in sand transport equation due to unidirectional flow [$m^2\ s^{-1}$]
a_0^+: coefficient in sand transport equation due to shoreward flows of waves [$m^2\ s^{-1}$]
a_0^-: coefficient in sand transport equation due to seaward flows of waves [$m^2\ s^{-1}$]
a_1: coefficient in sand transport equation due to unidirectional flow [$m^2\ s^{-1}$]
a_1^+: coefficient in sand transport equation due to shoreward flows of waves [$m^2\ s^{-1}$]
a_1^-: coefficient in sand transport equation due to unidirectional flow [$m^2\ s^{-1}$]
A: coefficient of sand transport due to waves [$m^2\ s^{-1}$]
A_1, A_2, A_3: coefficients in the basic expression for sand transport equation [$m^2\ s^{-1}$]
A_g: coefficient of sand transport due to the effect of gravity on a steep slope [$m^2\ s^{-1}$]
C_0: coefficient through which the sand transport rate expressed in terms of immersed weight is related to volumetric sand transport rate [$kg^{-1}\ m^2\ s^2$]
C_f: drag coefficient
C_g: wave group velocity [$m\ s^{-1}$]
$D\ (x, y, \theta)$: wave directional spectrum in the (x, y, θ) space [$J\ m^{-4}\ s^{-1}$]
E: wave energy [$J\ m^{-2}\ s^{-1}$]
$(EC_g)_b$: wave energy flux at the breaking point [$J\ m^{-1}\ s^{-2}$]
$(EC_g)_{b0}$: wave energy flux at the breaking point of the reference [$J\ m^{-1}\ s^{-2}$]
$\vec{e_c}$: unit vector in the currents direction
$\vec{e_n} = (\cos\theta_n, \sin\theta_n)$: unit vector normal to contour lines (shoreward)
$\vec{e_u}$: unit vector in the direction of the unidirectional flow
$\vec{e_s} = (-\sin\theta_n, \cos\theta_n)$: unit vector parallel to contour lines
$\vec{e_w} = (\cos\theta_w, \sin\theta_w)$: unit vector in the wave direction
$\vec{e_w^+}$: unit vector in the directions of the shoreward flows of waves
$\vec{e_w^-}$: unit vector in the directions of the seaward flows of waves
F: local fetch distance [m]
f_D: energy dissipation rate due to wave breaking [s^{-1}]
F_w: characteristic value of the intensity of wave action [$J\ m^{-2}\ s^{-2}$]
g: acceleration of gravity [$m\ s^{-2}$] (g = 9.81 $m\ s^{-2}$)
G: intensity of sand transport due to waves [$m^2\ s^{-1}$]
G_x: x-component of intensity of cross-shore sand transport due to waves [$m^2\ s^{-1}$]
G_y: y-component of intensity of cross-shore sand transport due to waves [$m^2\ s^{-1}$]
G_R: intensity of sand transport due to ebb tidal currents [$m^2\ s^{-1}$]
h: water depth [m]
h_0: minimum depth of the imaginary depth h' [m]
h': imaginary depth [m]
h_c: depth of closure [m]
h_c': depth of closure when rip currents develop [m]
h_{c2}: lower limit depth of bathymetric changes due to ebb tidal currents [m]
h_R: berm height [m]
h_{R2}: upper limit height of bathymetric changes due to ebb tidal currents [m]
H: wave height [m]
$H_{1/3}$: significant wave height [m]
H_b: breaker height [m]
i: cell numbers taken in the x-direction at the location of the Z

i_{step}: numbers of time step
i_{up}: cell numbers taken in the x-direction at the location of the Z value at a point immediately updrift of q_x
i_{down} : cell numbers taken in the x-direction at the location of the Z value at a point immediately downdrift of q_x
$I_\varepsilon(Z)$: cumulative function of $\varepsilon(Z)$
j: cell numbers taken in the y-direction at the location of the Z
K: coefficient of the wave-breaking intensity
K_1: coefficient of longshore sand transport
K_2: coefficient of Ozasa and Brampton' term
K_c: coefficients of sand transport due to currents
K_{d}: wave diffraction coefficient
K_n : coefficient of cross-shore sand transport
K_s: coefficient of longshore sand transport
K_R: coefficient of sand transport due to ebb tidal currents
K_V: ratio of the ebb tidal current velocity V to V_0, V/V_0
K_{V1}: ratio of the ebb tidal current velocity V to the flow velocity at the inlet on the plane bottom V_1, V/V_1
K_w: coefficient of sand transport due to waves
K_x: coefficient of cross-shore sand transport
K_y: coefficient of longshore sand transport
n: local coordinate taken along direction normal (shoreward) to contour lines [m]
N_{step}: total number of time step
N_x: number of cells in the x-direction
N_y: number of cells in the y-direction
p: porosity of the sediment ($p = 0.4$)
P: intensity of sand transport [kg s^{-3}]
P_c: intensity of sand transport due to currents [kg s^{-3}]
P_w: intensity of sand transport due to waves [kg s^{-3}]
$\overrightarrow{q} = \left(q_x, q_y\right)$: sand transport fluxes [m^2 s^{-1}]
$\overrightarrow{q^+}$: sand transport due to shoreward flows of waves [m^2 s^{-1}]
$\overrightarrow{q^-}$: sand transport due to seaward flows of waves [m^2 s^{-1}]
$\overrightarrow{q_c} = \left(q_{cx}, q_{cy}\right)$: sand transport fluxes due to nearshore currents [m^2 s^{-1}]
$\overrightarrow{q_g}\left(q_{gx}, q_{gy}\right)$: sand transport due to the effect of gravity on a steep slope [m^2 s^{-1}]
$\overrightarrow{q_R} = \left(q_{Rx}, q_{Ry}\right)$: sand transport fluxes due to ebb tidal currents [m^2 s^{-1}]
$\overrightarrow{q_u} = \left(q_{ux}, q_{uy}\right)$: sand transport fluxes due to unidirectional flow [m^2 s^{-1}]
$\overrightarrow{q_w} = \left(q_{wx}, q_{wy}\right)$: sand transport fluxes due to waves [m^2 s^{-1}]
q_n: cross-shore sand transport [m^2 s^{-1}]
q_s: longshore sand transport [m^2 s^{-1}]
Q_s: total sand transport [m^3 s^{-1}]
s: local coordinates taken along the directions parallel to the contour lines [m]
t: time [s]
$T_{1/3}$: significant wave period [s]
$\tan\beta$: seabed slope $\left(\tan\theta = \left|\overrightarrow{\nabla Z}\right|\right)$
$\tan\beta_{\mathrm{c}}$: equilibrium slope
$\tan\overline{\beta}$: characteristic seabed slope at the breaker point
$\tan\phi$: slope of angle of repose of sand

$\tan\beta_w$: seabed slope measured along direction of wave propagation
U: wind velocity [m s^{-1}]
u_m: amplitude of bottom oscillatory velocity due to waves [m s^{-1}]
u_t: instantaneous flow velocity due to waves [m s^{-1}]
V: velocity of nearshore (ebb tidal) currents [m s^{-1}]
V_0: reference velocity at inlet [m s^{-1}]
V_1: flow velocity of the ebb tidal currents on the plane bottom [m s^{-1}]
(V_x, V_y, V_θ) : wave energy transport velocity vector in the (x, y, θ) space [m s^{-1}]
x: horizontal coordinate [m]
y: horizontal coordinate normal to x [m]
x_w: local coordinate taken along the wave (wind) direction [m]
y_w: local coordinate taken along the direction normal to the wave (wind) direction [m]
Z: seabed elevation with reference to the still water level (Z = 0) [m]
$\overrightarrow{\nabla Z} = (\partial Z/\partial x, \partial Z/\partial y)$: gradient vector of Z
α: angle between the wave direction and the direction normal to the contour lines, ($\alpha = \theta_w$-θ_n) [rad]
α_b: breaker angle [rad]
γ: ratio of breaker height to water depth
Γ: ratio of critical breaker height to water depth on the horizontal bed
Δn: mesh interval along the n-axis [m]
Δt : time interval [s]
Δx: mesh interval along the x-axis [m]
Δx_w: mesh interval along the x_w-axis [m]
Δy: mesh interval along the y-axis [m]
ΔZ_0: thickness of the sand layer from which the reduction in sand transport begins [m]
ΔZ: thickness of the sand layer near h_R or h_c [m]
$\varepsilon(Z)$: depth distribution of the longshore sand transport [m^{-1}]
θ_n: direction normal to the contour lines (shoreward positive) measured counterclockwise from the x-axis [rad]
θ_R: direction of the ebb tidal currents measured counterclockwise from the x-axis [rad]
θ_w: wave direction measured counterclockwise from the x-axis [rad]
μ: reduction coefficient of sand transport rate
ρ: water density [kg m^{-3}] ($\rho = 1.03\times10^3$ kg m^{-3})
ρ_s: sand density [kg m^{-3}] ($\rho_s = 2.65\times10^3$ kg m^{-3})
τ: bottom shear stress [kg m^{-2} s^{-2}]
Φ: wave energy dissipation rate per unit time and unit seabed area [J m^{-2} s^{-2}]
Φ_b: wave energy dissipation rate due to wave breaking at a local point [J m^{-2} s^{-2}]

Authored by Takaaki Uda, Masumi Serizawa and Shiho Miyahara

The authors have developed models for predicting beach changes applicable to various problems on real coasts. One of them is the contour-line-change model to predict long-term beach changes caused by the imbalance in longshore sand transport, which is a kind of N-line model. Because the calculation of the nearshore current is not needed in this model, and the computational load is small, it has an advantage in the prediction of long-term topographic changes on an extensive coast. However, the handling of boundary conditions becomes difficult when offshore coastal structures are constructed in a complicated manner, and in this regard the so-called 3D model has an advantage. Taking this point into account, the authors developed a morphodynamic model (BG model) by applying the concept of the equilibrium slope and the energetics approach, in which depth changes on 2D horizontal grids are calculated.

Published in London, UK
© 2018 IntechOpen
© Shifaaz shamoon / unsplash

IntechOpen

ISBN 978-1-83881-268-3
9 781838 812683